Title
Excited State Dynamics of Isolated Nucleobases and Base Pairs

Author
Siouri, Faady Mohammad

Publication Date
2017

UNIVERSITY OF CALIFORNIA

Santa Barbara

Excited State Dynamics of Isolated Nucleobases and Base Pairs

A dissertation submitted in partial satisfaction of the
requirements for the degree Doctor of Philosophy
in Chemistry

by

Faady Mohammad Siouri

Committee in charge:

Professor Mattanjah S. de Vries, Chair

Professor Martin Moskovits

Professor Steven K. Buratto

Professor Javier Read de Alaniz

June 2017

The dissertation of Faady Mohammad Siouri is approved.

Martin Moskovits

Steven K. Buratto

Javier Read de Alaniz

Mattanjah S. de Vries, Committee Chair

April 2017

Excited State Dynamics of Isolated Nucleobases and Base Pairs

by

Faady Mohammad Siouri

ACKNOWLEDGEMENTS

I would like to express my sincerest gratitude toward numerous individuals at the University of California, Santa Barbara (UCSB), in Orange County, and across the globe. First, I would like to thank Professor Mattanjah de Vries, my research advisor at UCSB. In addition to this role, Dr. de Vries was my mentor who was always available to lend me guidance, my instructor who gave me the opportunity to pursue my research ideas, and my friend who was available to discuss data over American coffee or Arabic tea with sage. Dr. de Vries values the development of the individual just as much as he values the development of research in our lab. I hope to graduate from UCSB not only with his training, but to emulate his decisiveness and patience with my children.

The members of the de Vries group are invaluable in my experience at UCSB. I would like to first thank past group members, Dr. Marshall Ligare and Dr. Shawn Owens. I am thankful for Dr. Ligare's training in all that I do today. In addition to his memorable character, I will also remember how he kindly treated me as if I were his little brother. I wish him and his wife my best and I look forward to when we will meet again. Next, I truly value Dr. Owens' advice, from matters in life to aligning lasers. Dr. Owens is perhaps one of the most patient individuals, and I appreciate our time watching basketball and drinking tea together.

I am much obliged to my current group members of the de Vries lab, Jacob Berenbeim, Sam Boldissar, Gregory Gate, and Michael Haggmark. To my great friend Jacob Berenbeim, thank you for helping me both inside and outside of our lab. I will miss our nights where we grilled giant steaks and watched American football. I cherish our friendship

and I look forward to the day where we may meet in Jerusalem to collaborate on a research project. It is with deep remorse that I thank Sam Boldissar, my dear friend and inspiring colleague who has passed on. You have not only impacted our lives with your ambition, expertise, and innovation, but with your incredible kindness. You will forever be imprinted in our hearts, memories, and research. Finally, I would also like to thank Gregory Gate and Michael Haggmark for all of their help and for our memories playing soccer together.

Next, I realize that I am very fortunate to have picked the best individuals to be on my committee and I would like to express my gratitude toward them. For instance, in addition to his academic support, Professor Martin Moskovits was like a father figure who I talked to when I was stressed. I appreciate that he always found a way to make me laugh. As well, Professor Steve Buratto and Professor Javier Read de Alaniz were like older brothers to me. Specifically, they lent advice and support to me throughout graduate school.

As well, the wonderful staff here at UCSB contributed to my invaluable experience as a graduate student. I especially would like to thank Dr. Alexander Mikhailovsky as he was always available to talk and was very supportive. To Dr. Petra Van Koppen, I appreciate that you believed in me and took part in shaping the person that I am today. Bruce Dunson, Cabe Fletcher, Adrian Shelor, Louis Grace, Mallarie Stevens, Ericka James, Kathy Allain, Mira Lazaro, India Madden, Isoleil Montalvo, Pat Walker, Katie Wright and everyone in the chemistry offices all receive my sincerest thanks too.

My experience as a graduate student would not have been as incredible without the great friends I met at UCSB. Jeff Heckey, Reza Salemmilani, Justin Yoo, Dayton Horvath, Jeremy Robins, Scott Price, Josh Buffon, Jose Navarrete, Hunter Neilson, Jonathan Nelson, Steven Swasey, Tracy Chuong, Sean Cray, Peter Damon, John Eickhoff, and Maxwell Giammona are all friends and colleagues that I cherish.

There are many individuals in Orange County and in Palestine that I am thankful for because of their continued support. First, I would like to acknowledge my undergraduate, research advisor, Professor Nien-hui Ge. While at the University of California, Irvine, she encouraged me to attend graduate school when I initially considered ending my education with a bachelor's degree. My undergraduate research mentors, Dr. Hiroaki Maekawa, Dr. Yuan Feng, and Dr. Yanh Han were also influential in my academic career. I would also like to acknowledge some of my undergraduate instructors and advisors who helped me become the person I am today. Although the list is long, I would like to name few of them, Dr. Alison Gotoh, Dr. Craig Tamooka, Professor Robin De Roo, Professor Lenore Landis, David Dang, Manny Escarrega, and Sara Escarrega, thank you all for encouraging and supporting me. I am grateful for my uncles Rabee, Rebhi, Izz Al-deen, Tayseer, Khairy, Omar, Waleed, Khalid, Ameen, Akram, Maher, Ali, Anwar, Salah, and my aunts Saneya, Rabeeha, Haneya, Salwa, Ola, Najwa, Rifqa, Majeda, and Halah. Coming from a large family, I have more than 150 cousins but I would like to name a few who were really close to me like Mohammad, Falah, Shadi, Dujana, Abed, Omar, Khalid, Ahmad, Mahmoud, Anas, Ghassan, Ihab, Rajae', Shadi, Muhannad, Thaer, Nidal, Imad, Raed, Jabra, Sameer, Sami, Nader, Wael, Osama, Bahjat, Samer, Ziyad, Iyad, Jawad, Rashad, Monther, Izzo, Sufyan, and Loay. I am also grateful for my friends, Ramadam Matari, Shafeeq Arar, Ismael Ady, Rami Mraish, Anas Nassar, Omar Badee, Ali Nakhlah, Mudar Abed- Rubbo, Michael Garrison, Loay Al-bakry, Yahya Mohammad, Yaser Zureid, Abu Nasser Diouri, Marzooq Al-Shobaki, Maher Ismael, Raed Dyab, Bilal Mustafa, Khalid Zuraiqi, Fady Zuraiqi, Jamal Dawudi, Ibrahim Qassas, Jamal Bakhit, Jihad Maswadeh, Adnan Maswadeh, Mohammad Badran, Ahmad Salah, Jamal Sarma, Nidal, Izz, Samer, Ahmed, and many more for their consistent support. Specifically, they knew how to draw a smile on my face and treated me as if I were family.

My best friend Mohammad Tmezi and great friend Nadera Tmezi deserve to have an entire book to be written about them because of their incredible kindness. Whenever I was in need of support, they were present. For instance, Mohammad would impart love, care, and even flash drives, computer parts, laptops, phones, etc. to me. In fact, the very laptop I typed my thesis on was provided by Mohammad. In addition to this generosity, Nadera shared auspices, care, and delicious Arabic food. When I passed my PhD candidacy exam, Mohammad and Nadera graciously threw a memorable, barbeque celebration at Goleta Beach Park. I would like to thank them with all of my heart and I hope that one day we might be fortunate enough to live next to one another.

Since my parents are far away in Palestine, Uncle Saed and his wife Aunt Suegarti have made certain that I have similar love and care here in America. They opened their home up to me with a welcoming smile and the most delicious food. I am also thankful for my cousins Ismael, Amenna and her husband Johnny, Abed, and Abed’s wife and son Alejandra and Said. The years I spent with them were the greatest ever; we shared everything together. I truly love them with all my heart and I wish them all the best.

I saved the best for last, my wife and my family. Malak, you are not just my partner, you are my lover. You are not just my companion, you are my inspiration. You are not just my wife, you are my life. Thank you, my sweetheart. My graduate career has come to a close, and yet, a new and exciting chapter opens with the news of your pregnancy! To my in-laws, you have been the most supportive and generous people I have ever known. Thank you

Uncle Mahmoud, Aunt Ola, Monther, Mutaz, and Ayham for your huge hearts and for loving me.

I thank God everyday for the best grandparents, parents, brothers, and sisters. My family is very supportive and has stood by me every step of the way. I consider myself blessed for having the most generous and loving grandparents. I am grateful for my grandfathers Rabee Siouri and Abed Al-Atheem Katbeh and my grandmothers Rateeba Arafah and Ameena Qwaider. Thank you for everything you have taught me, I am truly a better person for being able to spend time with you and thank you for raising my parents and instilling positive values in them. My father, "Mohammad Yusri" Siouri, is my role model and he encouraged me to pursue a PhD. When I have children, I will treat them the way my father treated me, with love, care, and respect. My mother, Laila Siouri, is not the mother of the year; she is the mother of the century. Whenever I talk to her, I start tearing up because I always miss her. Even though I am thirty years old, I am just a baby when I sleep in her lap. She is my best friend ever and I would do anything to make her happy. My brothers Firas and Waseem are more than brothers, they are my best friends and whenever I am with them, I feel as if we were young again. Much love to my sisters, Nancy, Nahed, Naseem, and Nour. Life has no meaning without them; they are my soul. I am also thankful to their husbands Samer, Osaid, Ashraf, and Mohammad who have flooded me with love and care. Much love to my endearing nephews and nieces, Iyas, Suzan, Yousef, Malak, Owais, Miral, Lana, Mohammad, Masa, and Lujain. I could not have done this without my family and so I dedicate my dissertation to them. I love you all, very much.

.

Curriculum Vitae of Faady Mohammad Siouri

June 2017

Department of Chemistry and Biochemistry
University of California
Santa Barbara, CA 93106

Citizenship: U.S.A
E-mail: fsiouri@chem.ucsb.edu
Telephone: 805-893-4720 (lab)

Education:

University of California Santa Barbara, Santa Barbara CA
Doctor of Philosophy in Physical and Analytical Chemistry, April 2017
GPA 4.00 / 4.00
Thesis Title: "Excited State Dynamics of Isolated Nucleobases and Base Pairs"

University of California Santa Barbara, Santa Barbara CA
Masters of Arts in Physical and Analytical Chemistry, June 2014
GPA 4.00 / 4.00
Thesis Title: "Resonance-Enhanced Multiphoton Ionization to Study the Electronic Structure and Excited State Dynamics of Isolated Thymine and Uracil in the Gas Phase."

University of California Irvine, Irvine CA
Bachelor of Science in Chemistry, June 2011
GPA 3.95 / 4.00

Cypress College, Cypress CA
Associate Degree in Science, June 2009
GPA 3.89 / 4.00

Catholic High School, Ramallah West Bank
High School Diploma, July 2004
GPA 87.4% / 100%

Experience:

Research Experience

Mattanjah de Vries, University of California, Santa Barbara, Chemistry Department.
Graduate Researcher, September 2012 – April 2017

- Constructed a new beam instrument (laser desorption, jet cooling, mass spectrometry instrument) to explore the electronic structure excited state dynamics of base pairs in the gas phase.
- Used resonance-enhanced multiphoton ionization (REMPI) to study the electronic structure and excited state dynamics of isolated nucleobases, nucleobase analogues, and base pairs.
- Used the application of high resolution laser spectroscopy and mass spectrometry to answer some questions on the ancient past of the Mayans.

Anouk M. Rijs, FELIX Laboratory, Radboud University, Nijmegen.
Visiting Researcher, February 22nd – March 4th, & November 15th- December 2nd, 2016

- Used FELIX (Free Electron Laser for Infrared eXperiments) to collect IR spectra for base pairs in the far-IR region.
- Structurally characterized these base pairs with the help of BOMD simulations.
- Studied intermolecular hydrogen-bond vibrations of these base pairs in their ground and excites states.

Nien-hui Ge, University of California, Irvine, Chemistry Department.
Undergraduate Research Assistant, January 2010 - June 2011

- Determine vibrational properties of the amide-I, -II and -A modes in alkyl amide compounds used as models of peptide unit.
- Synthesized amides with different number of methyl groups on the terminal carbon atoms.

Teaching Experience

University of California, Santa Barbara, Chemistry Department.
Teacher Assistant and Lab Instructor, September 2012 – June 2016

- Taught general chemistry laboratory for freshmen and sophomores. (Chem 1AL)
- Taught honors general chemistry laboratory (Chem 2BC)
- Taught environmental chemistry (Chem 123)
- Taught Photochemistry (Chem 118/218)
- Taught Analytical chemistry (Chem 150)

Personal Business

Private Tutor, August 2006 – June 2013

- Tutored high school chemistry, math, and physics
- Tutored college mathematics
- Tutored undergraduate chemistry courses

Dar Al-Ma'refa Middle/High School – Jerusalem

Science, Chemistry, and Physics Teacher, August 2011 – July 2012

- Taught science to sixth, seventh, eighth, and ninth graders.
- Taught chemistry and physics to tenth, eleventh, and twelfth graders.
- Wrote my own chemistry and physics curriculum

Lowell Elementary School - Santa Ana.

CAL Teach, March 2011 – June 2011

- Taught mathematics and science to fifth graders.

University of California, Irvine, Chemistry Department.

Discussion Leader, September 2009 – June 2011.

- Held discussion sessions for thermodynamics, quantum mechanics, statistical mechanics, analytical chemistry, and instrumentation chemistry

Cypress College, Science Department.

Supplemental Instructor, August 2006 – May 2009

- Held chemistry sessions for general chemistry I, general chemistry II, organic chemistry I, and organic chemistry II.
- Held mathematics sessions for Algebra, statistics, calculus I, and calculus II
- Held physics sessions for mechanics and electricity and magnetism.

Work Experience

University of California, Santa Barbara, Chemistry Department.

Lead Teaching Assistant at the Chemistry Department, September 2013 – June 2015

- Observed teaching assistants teaching general chemistry laboratories and provided them with comments and feedback in order to improve their teaching skills.
- Enhanced the quality of instruction in general chemistry labs by providing assistance to the chemistry department's graduate teaching assistants.

Cypress College, Science Department.

Lab Technician Assistant, September 2007 – May 2009

- Prepared chemical solutions for labs to use
- Trained volunteers on how to become proficient in solution chemistry.

Research Projects:

Undergraduate Research

I joined a project which aimed to simulate amide-I/II two-dimensional infrared (2D-IR) spectra of short peptides composed of $C_{\alpha,\alpha}$-dialkylated amino acid residues, and reveal their backbone structure by comparing measured and simulated 2D-IR spectra. One of the important steps to accurately calculate a 2D-IR spectrum is the initial setting of the vibrational properties, such as resonant frequency and transition dipole moment, of the amide modes on each peptide unit along the backbone chain.

My role in this project was to experimentally determine such vibrational properties of theamide-I, -II and -A modes in alkyl amide compounds used as models of peptide unit. To this end, I synthesized nine amides with a different number of methyl groups on the terminal carbon atoms, and characterized them by $_1$H-NMR and mass spectroscopy. Each amide was dissolved in tetrachloroethane to measure a transmission FT-IR spectrum of its monomer form. I analyzed the three amide vibrational bands in the acquired spectra by curve fitting, and investigated how the peak frequencies and the transition dipole moment depend on the number of methyl groups. The acquired information is useful to develop a more sophisticated simulation protocol which takes into account subtle differences of the local environment around a peptide unit.

Graduate Research

The purpose of my research was to use resonance-enhanced multiphoton ionization to study the electronic structure and excited state dynamics of isolated nucleobases and base pairs in the gas phase. This was done using an instrument that combines laser desorption, jet cooling, and mass spectrometry. First, we measured well-resolved vibronic spectra of all the molecules we studied by resonant two-photon ionization (R2PI). Then, we performed double-resonance spectroscopy to further elucidate the structure and excited state dynamics of the target molecules. Because nucleobases typically exist in several tautomeric forms which are isolated under gas phase jet-cooled conditions, we used UV-UV double resonance spectroscopy to determine the number of tautomers present and their origins. IR-UV double resonance spectroscopy was used to obtain tautomer-specific IR spectra. We measured excited state lifetimes of tautomer-selected nucleobases by nanosecond and picosecond pump-probe spectroscopy.

With the use of a free-electron laser, we were able to collect IR spectra for multiple base pairs in the far-IR region (<880 cm^{-1}). Although the far-IR region has been difficult to access both experimentally and computationally, we were able to structurally characterize the molecules with the help of Born–Oppenheimer Molecular Dynamics (BOMD). This far-IR region yields new information because it is characterized by large-scale delocalized vibrations that cannot be observed in the mid-IR region.

Finally, we used R2PI in combination with supersonic jet cooling and mass spectrometry to examine archaeological samples. We studies organic residues within pottery sherds from Maya vessels (600−900 CE) and Mississippian vessels (1100−1200 CE), successfully detecting three molecular markers, caffeine, theobromine, and theophylline, associated with the use of cacao.

<u>Honors and Awards:</u>

- Outstanding Service to the Department of Chemistry and Biochemistry Award, University of California, Santa Barbara, 2015.
- Physical Chemistry Chemical Physics Poster Prize at the 62nd Pacific Conference on Spectroscopy and Dynamics, Royal Society of Chemistry, 2015.
- Phi Lambda Upsilon Award for Outstanding Academic Achievement, University of California, Santa Barbara, 2013.
- Outstanding Teaching Assistant Award in Chemistry, University of California, Santa Barbara, 2013.
- Phi Lambda Upsilon Award for Outstanding Academic Achievement, University of California, Irvine, 2011.
- Magna Cum Laude, University of California, Irvine, 2011
- Golden Key International Honor Society, University of California, Irvine, 2010.
- National Society of Leadership and Success (Sigma Alpha Pi), University of California, Irvine, 2009.
- "Michael Jacob" Honor as the Best Science Student, Cypress College, 2008.
- Deans Honor Roll and President Honor Roll Each Quarter/Semester at Cypress College and University of California, Irvine, 2005-2011.

Fellowships/Scholarships:

- Central Continuing Student Fellowship, University of California, Santa Barbara, 2016-2017
- Philip & Aida Siff Educational Foundation Graduate Fellowship, University of California, Santa Barbara, 2015-2016
- Elliott Family Foundation Scholarship, University of California, Irvine, 2009-2010
- Beall Family Foundation Scholarship, University of California, Irvine, 2009
- "Michael Jacobs" Scholarship for Science/Engineering/Mathematics, Cypress College, 2008

Publications:

1. Marshall Ligare, **Faady Siouri**, Ota Bludsky, Dana Nachtigallova, Mattanjah S. de Vries. *Characterizing the dark state in thymine and uracil by double resonance spectroscopy and quantum computation.* Phys. Chem. Chem. Phys., **17** (37), 24336-24341 (2015)

2. Shawn C Owens, Jacob Berenbeim, Marshall Ligare, Lisa E Gulian, **Faady M Siouri**, Samuel Boldissar, Stuart Tyson-Smith, Gregory Daniel Wislon, Anabel Ford, Mattanjah S De Vries. *Direct Analysis of Xanthine Stimulants in Archeological Vessels by Laser Desorption Resonance Enhanced Multiphoton Ionization*. American Chemical Society., **89** (5), 2838-2843 (2017)

3. **Faady Siouri**, Samuel Boldissar, Jacob Berenbeim, Mattanjah de Vries. *Excited State Dynamics of 6-Thioguanine.* Submitted to the Journal of Physical Chemistry A.

4. Jacob Berenbeim, **Faady Siouri**, Samuel Boldissar, Mattanjah de Vries. *Excited State Dynamics of DNA Base Alternative, Isocytosine.* Submitted to the Journal of the American Chemical Society.

5. **Faady Siouri**, Anouk Rijs, Jerome Mahe, Samuel Boldissar, Kas Houthuijs, Mattanjah S. de Vries. *Structural Characterization of DNA Base Pairs using Far-IR spectra and Born –Oppenheimer Molecular Dynamics (BOMD) Simulations.* In Preparation.

6. **Faady Siouri**, Anouk Rijs, Jerome Mahe, Samuel Boldissar, Kas Houthuijs, Mattanjah d. de Vries. *Intermolecular Hydrogen-Bond Signatures in the Far-IR Region of Guanine-Guanine and Guanine-Cytosine Base-Pairs. Ground State vs Excited State.* In Preparation.

Presentations:

1. Poster Presentation: *Intermolecular Hydrogen Bond Signatures in the Far-IR Region of Guanine-Cytosine Base-Pair Structures,* 2017 Gordon Research Seminar on Gaseous Ions: Structures, Energetics & Reactions (GRS) at Ventura Beach Marriot, CA.

2. Oral Presentation: *Introduction to Undergraduate Research*. 2013-2017 University of California Santa Barbara Chemistry Department, CA. Every quarter, I organized a volunteer seminar where I introduced undergraduates to the different research fields at the University of California, Santa Barbara. The seminar was designed to help students get involved in research as early as possible, explain to them their responsibilities as undergraduate researchers, introduce them to graduate school, and more. After the seminar, I took the students to the de Vries research lab and showed them how a research lab looks like, explained my research and its application, and showed them some laser demonstrations to prove to them that research is also fun.

3. Poster Presentation: *Resonance-Enhanced Multiphoton Spectroscopy of Thymine and Uracil; A High Resolution Probe for Gas Phase Structure and Dynamics*. 2015 62nd Pacific Conference on Spectroscopy and Dynamics at Pacific Grove, CA.

4. Poster Presentation: *Shining Light on Our Origin.* 2014, 2015 University of California Santa Barbara Chemistry Department Recruitment Event, CA.

ABSTRACT

Excited State Dynamics of Isolated Nucleobases and Base Pairs

by

Faady Mohammad Siouri

Environmental conditions such as solar irradiation can induce biochemical reactions and pose a threat to organic molecules necessary in life. How DNA responds to radiation is relevant to human health because radiation damage can affect genetic propagation and lead to cancer. A detailed photochemistry is unraveled by studying the intrinsic properties of individual DNA/RNA building blocks, followed by extrapolation to larger systems such as base pairs via gas phase laser spectroscopy. Moreover, the photodynamics of nucleobases may further our understanding of prebiotic chemistry and its role in developing life as we know it. Electronic structure and excited state dynamics of nucleobases and base pairs have been studied in the past; however, detailed spectroscopy has not been reported for all of them. Moreover, some nucleobase analogues were never studied in the gas phase. As a result, we attempt to build on what was previously established on nucleobases and base pairs and then take a step further to explore a nucleobase analogue.

This work reports studies of electronic structure and excited state dynamics of biological molecules via resonance-enhanced multiphoton ionization in the gas phase. First, we measured well-resolved vibronic spectra of all the molecules we studied by resonant two-photon ionization. Then, we performed double-resonance spectroscopy to further elucidate the structure and excited state dynamics of the target molecules. Because biomolecules typically exist in several tautomeric forms which are isolated under gas phase jet-cooled conditions, we used UV-UV double resonance spectroscopy to determine the number of tautomers present and their origins. We used IR-UV double resonance spectroscopy to obtain tautomer-specific IR spectra. We measured excited state lifetimes of tautomer-selected nucleobases by nanosecond and picosecond pump-probe spectroscopy. Using these methods, we were able to draw a new picture for the dynamics of bare nucloebases thymine and uracil in the gas phase. In the gas phase jet expansion, both molecules were present in the keto form and exhibited long lived excited states. These long lived states have been implicated in the formation of DNA photolesions by causing the formation of a cyclobutane pyrimidine dimer, which can lead to cancers such as melanoma and carcinoma. We also determined that replacing the oxygen in guanine with sulfur results in drastically different dynamics due to the heavy atom effect.

With the use of a free-electron laser, we were able to collect IR spectra for multiple base pairs in the far-IR region (<880 cm^{-1}). Although the far IR region has been difficult to access both experimentally and computationally, we were able to structurally characterize the molecules with the help of Born–Oppenheimer Molecular Dynamics (BOMD). This far-IR region yields new information because it is characterized by large-scale delocalized vibrations that cannot be observed in the mid-IR region.

Finally, we used R2PI in combination with supersonic jet cooling and mass spectrometry to examine archaeological samples. We studies organic residues within pottery sherds from Maya vessels (600−900 CE) and Mississippian vessels (1100−1200 CE), successfully detecting three molecular markers, caffeine, theobromine, and theophylline, associated with the use of cacao.

TABLE OF CONTENTS

Chapter 4. Far IR Spectra and Born-Oppenheimer Molecular Dynamics to Structurally Characterize DNA Base Pairs ………………...……………………………...86

LIST OF FIGURES

Chapter 1

Introduction, Background, and Motivation

Deoxyribonucleic acid (DNA) contains the genetic guidelines for the development and functioning of all living organisms. Ribonucleic acid (RNA) is responsible for reading and decoding the genetic information from DNA into proteins. The basic building blocks of DNA and RNA are called nucleotides. Nucleotides consist of a nucleobase, a five-carbon sugar, and at least one phosphate group. Nucleobases are a group of nitrogen-based molecules that form base pairs and stack upon one another to form a DNA strand. The canonical nucleobases are cytosine, guanine, adenine, thymine, and uracil. Adenine and guanine are purines (consisting of two rings); whereas, cytosine, thymine, and uracil are pyrimidines (consisting of one ring).

Biologically, DNA is obviously significant; however, to gain more detailed information, chemists have used spectroscopy to better understand the interactions of DNA with light. Of special interest is the photochemistry that governs DNA's response to UV radiation as well as its photo- and excited state dynamics [1,2]. The photo damage that causes skin cancer has been found to be one such effect of UV radiation [3]. Furthermore, the photodynamics of DNA may have played a role in prebiotic chemistry and in developing life as we know it. Studies have shown that the biological tautomers of DNA bases have short excited state lifetimes, of the order of 1 ps or less [4–9]. Such short lifetimes prevent intersystem crossing (ISC) to a reactive triplet state; instead, they rapidly decay back to the electronic ground state through internal conversion (IC). This process protects DNA bases against photochemical damage [10]. Presumably, purines and pyrimidines which survived in the harsh environment of the early earth, assembled into macromolecular structures, producing RNA. Back then, the earth was exposed to shorter wavelength UV radiation compared to today. Therefore, the rapid internal conversion to the ground state may have played a major role in prebiotic chemistry. However, the availability of rapid IC pathways depends critically on molecular structure. This dependence results from the fact that the conical intersections that mediate IC occur at molecular geometries that differ strongly from ground state minimum geometries. Therefore the excited state dynamics of nucleobases can differ drastically for different derivatives [11–19], analogues [20–22], and even tautomers [23–25]. Many derivatives and analogues of the canonical nucleobases that could serve as alternative bases lack the UV protection afforded by rapid internal conversion. This difference suggests a possible prebiotic photochemical selection of nucloebases on an early earth.

Studying the excited state dynamics of nucleobases provides valuable information on excited electronic states and molecular structure, both of which play a crucial role in chemical interactions, reactivity, selectivity, and function in biologically active molecules. Moreover, the experimental data can be used to examine and improve theory. New insights in the inter- and intramolecular interactions of the DNA nucleobases, as revealed by studying their photochemistry, have even led to an enhanced understanding of biological and pharmacological functions of the nucleobases. Since the structure of DNA and its base pairs were first described, the hydrogen bonds between base pairs, which govern their structures and the relationship between DNA mutation and base pair tautomerization have been subjects of interest [26–41]. The breaking and re-forming of hydrogen bonds is involved in DNA replication and transcription.

For all reasons mentioned above, the last thirty years have brought about an explosion of information regarding UV photochemistry of isolated nucleobases and their cluster. Recently, studies have focused on nuclobase analogues but most of these studies were theoretical or in solution [42–49]. Each topic often has missing pieces for its' puzzle so in this work we build further on what was previously established on older systems and then take a step further to explore a new system.

This dissertation examines the electronic structure and excited state dynamics of thymine, uracil, and 6-thioguanine. Additionally, we structurally characterize guanine-guanine, guanine-cytosine, and 1methylcytosine-9ethylguanine base pairs. In order to understand the photostability of these molecules, we first measure their absorption spectra and then we probe their excited state dynamics.

In solution, chemical players – single nucleic acids, base pairs, sugars, DNA strands, etc. - can be probed in a biologically relevant environment in which these molecules take on their native structural conformations. However, important higher order dynamics could be hidden due to the multitude of intra-molecular, inter-molecular, and molecular-solvent interactions. On the other hand, gas phase analysis allows for careful study of interaction-free molecules which is necessary in order to distinguish between externally imposed properties and those which are a result of the molecular structure itself. Molecules can exist in a variety of tautometric forms that exhibit different photophysical properties. Unlike gas phase experiments, solution phase experiment lack tautomer selectivity. In this dissertation, we use gas phase spectroscopy to perform all experiments.

The combination of mass spectrometry and gas phase laser spectroscopy provides a powerful tool to perform mass-selected spectroscopy and optically-selected mass spectrometry where the intrinsic properties of nucleobases are studied in a solvent-free environment. We use resonant two-photon ionization (R2PI) to measure the absorption spectra by ionizing a molecule via an intermediate excited state. Tautomer distinction is achieved by means of UV-UV and IR-UV double resonance spectroscopy. Excited state lifetime is estimated using pump-probe spectroscopy.

In chapter 3 we report on the ground state and the dark excited state in isolated uracil and thymine and lifetimes of the dark state for different excitation wavelengths. Cluster formation in a supersonic expansion provides the opportunity to study base pairs and the hydrogen bonding that keeps them together. In chapter 4 we collect the far-IR spectra for G-G, triply and doubly hydrogen-bonded G-C, and 1MeC-9EtG. Then we use DFT-MD BLYP-D3 and static harmonic BLYP-D3 to structurally characterize these base pairs. Intermolecular hydrogen-bonding vibration calculation of the ground state vs the excited state is currently in progress. In chapter 5, we investigate the electronic spectra and excited state dynamics of the guanine analogue, 6-thioguanine. We show that substituting the oxygen in guanine with sulfur results in the two molecules having completely different dynamics and excited state lifetimes due to the heavy atom effect.

Another focus of this dissertation is to use the powerful laser mass spectrometric techniques we have to examine archaeological samples. In appendix 1 we use laser desorption with R2PI spectroscopy to study organic residues within pottery sherds from Maya vessels (600−900 CE) and Mississippian vessels (1100−1200 CE), in order to detect three molecular markers, caffeine, theobromine, and theophylline, associated with the use of cacao. In addition to high molecular specificity, based on both wavelength and mass identification, the high detection sensitivity of this analytical approach allows for direct laser desorption from sherd scrapings, avoiding the need for extracting organic constituents from the sherd matrix. Appendix 2 is supporting information for chapters 3.

We begin by describing our experimental setup and methods in Chapter 2.

References

1. Kleinermanns, K., Nachtigallová, D. & de Vries, M. S. Excited state dynamics of DNA bases. *Int. Rev. Phys. Chem.* **32,** 308–342 (2013).

2. Crespo-Hernández, C. E., Cohen, B., Hare, P. M. & Kohler, B. Ultrafast Excited-State Dynamics in Nucleic Acids. *Chem. Rev.* **104,** 1977–2020 (2004).

3. Diepgen, T. L. & Mahler, V. The epidemiology of skin cancer. *Br. J. Dermatol.* **146,** 1–6 (2002).

4. Daniels, M. & Hauswirth, W. Fluorescence of the Purine and Pyrimidine Bases of the Nucleic Acids in Neutral Aqueous Solution at 300 K. *Am. Assoc. Adv. Sci.* **171,** 675–677 (1971).

5. Callis, P. R. Electronic states and luminescence of nucleic acid systems. *Annu. Rev. Phys. Chem.* **34,** 329–357 (1983).

6. Peon, J. & Zewail, A. H. DNA/RNA nucleotides and nucleosides: direct measurement of excited-state lifetimes by femtosecond fluorescence up-conversion. *Chem. Phys. Lett.* **348,** 255–262 (2001).

7. Kang, H., Jung, B. & Kim, S. K. Mechanism for ultrafast internal conversion of adenine. *J. Chem. Phys.* **118,** 6717–6719 (2003).

8. Lührs, D. C., Viallon, J. & Fischer, I. Excited state spectroscopy and dynamics of isolated adenine and 9-methyladenine. *Phys. Chem. Chem. Phys.* **3,** 1827–1831 (2001).

9. Crespo-Hernández, C. E., Cohen, B., Hare, P. M. & Kohler, B. Ultrafast Excited-State Dynamics in Nucleic Acids. *Chem. Rev.* **104,** 1977–2020 (2004).

10. Broo, A. A theoretical investigation of the physical reason for the very different luminescence properties of the two isomers adenine and 2-aminopurine. *J. Phys. Chem. A* **102,** 526–531 (1998).

11. He, Y., Wu, C. & Kong, W. Decay Pathways of Thymine and Methyl-Substituted Uracil and Thymine in the Gas Phase. *J. Phys. Chem. A* **107,** 5145–5148 (2003).

12. Gengeliczki, Z. *et al.* Effect of substituents on the excited-state dynamics of the modified DNA bases 2,4-diaminopyrimidine and 2,6-diaminopurine. *Phys. Chem. Chem. Phys.* **12,** 5375 (2010).

13. Etinski, M., Fleig, T. & Marian, C. M. Intersystem Crossing and Characterization of Dark States in the Pyrimidine Nucleobases Uracil, Thymine, and 1-Methylthymine [†]. *J. Phys. Chem. A* **113,** 11809–11816 (2009).

14. Trachsel, M. A., Lobsiger, S., Schär, T. & Leutwyler, S. Low-lying excited states and nonradiative processes of 9-methyl-2-aminopurine. *J. Chem. Phys.* **140,** 044331 (2014).

15. Kunitski, M., Nosenko, Y. & Brutschy, B. On the Nature of the Long-Lived ‘Dark’ State of Isolated 1-Methylthymine. *ChemPhysChem* **12,** 2024–2030 (2011).

16. Nir, E., Kleinermanns, K., Grace, L. & de Vries, M. S. On the Photochemistry of Purine Nucleobases. *J. Phys. Chem. A* **105,** 5106–5110 (2001).

17. Malone, R. J., Miller, A. M. & Kohler, B. Singlet Excited-state Lifetimes of Cytosine Derivatives Measured by Femtosecond Transient Absorption. *Photochem. Photobiol.* **77,** 158 (2003).

18. Trachsel, M. A. *et al.* The excited-state structure, vibrations, lifetimes, and nonradiative dynamics of jet-cooled 1-methylcytosine. *J. Chem. Phys.* **145,** 134307 (2016).

19. Brister, M. M. & Crespo-Hernández, C. E. Direct Observation of Triplet-State Population Dynamics in the RNA Uracil Derivative 1-Cyclohexyluracil. *J. Phys. Chem. Lett.* **6,** 4404–4409 (2015).

20. Lobsiger, S., Frey, H.-M. & Leutwyler, S. Supersonic jet UV spectrum and nonradiative processes of the thymine analogue 5-methyl-2-hydroxypyrimidine. *Phys. Chem. Chem. Phys.* **12,** 5032–5040 (2010).

21. Nachtigallová, D. *et al.* The effect of C5 substitution on the photochemistry of uracil. *Phys. Chem. Chem. Phys.* **12,** 4924–4933 (2010).

22. Pollum, M., Martínez-Fernández, L. & Crespo-Hernández, C. E. in *Photoinduced Phenomena in Nucleic Acids I* (eds. Barbatti, M., Borin, A. C. & Ullrich, S.) **355,** 245–327 (Springer International Publishing, 2014).

23. Tomić, K., Tatchen, J. & Marian, C. M. Quantum Chemical Investigation of the Electronic Spectra of the Keto, Enol, and Keto−Imine Tautomers of Cytosine. *J. Phys. Chem. A* **109,** 8410–8418 (2005).

24. Plützer, C. & Kleinermanns, K. Tautomers and electronic states of jet-cooled adenine investigated by double resonance spectroscopy. *Phys Chem Chem Phys* **4,** 4877–4882 (2002).

25. Marian, C. M. The Guanine Tautomer Puzzle: Quantum Chemical Investigation of Ground and Excited States. *J. Phys. Chem. A* **111,** 1545–1553 (2007).

26. Watson, J. D. & Crick, F. H. C. A Structure for Deoxyribose Nucleic Acid. *Nature* **171,** 737–738 (1953).

27. Franklin, R. E. & Gosling, R. G. Molecular Configuration in Sodium Thymonucleate. *Nature* **171,** 740–741 (1953).

28. Watson, J. D. & Crick, F. H. C. Genetical Implications of the structure of Deoxyribonucleic Acid. *Nature* **171,** 964–967 (1953).

29. Löwdin, P.-O. Proton tunneling in DNA and its biological implications. *Rev. Mod. Phys.* **35,** 724 (1963).

30. Hanus, M. *et al.* Correlated ab Initio Study of Nucleic Acid Bases and Their Tautomers in the Gas Phase, in a Microhydrated Environment and in Aqueous Solution. Guanine: Surprising Stabilization of Rare Tautomers in Aqueous Solution. *J. Am. Chem. Soc.* **125,** 7678–7688 (2003).

31. Hanus, M., Kabeláč, M., Rejnek, J., Ryjáček, F. & Hobza, P. Correlated ab Initio Study of Nucleic Acid Bases and Their Tautomers in the Gas Phase, in a Microhydrated Environment, and in Aqueous Solution. Part 3. Adenine. *J. Phys. Chem. B* **108,** 2087–2097 (2004).

32. Bakker, J. M. *et al.* The mid-IR absorption spectrum of gas-phase clusters of the nucleobases guanine and cytosine. *Phys Chem Chem Phys* **6,** 2810–2815 (2004).

33. Kool, E. T., Morales, J. C. & Guckian, K. M. Mimicking the Structure and Function of DNA: Insights into DNA Stability and Replication. *Angew Chem Int Ed Engl* **39,** 990–1009 (2000).

34. Goodman, M. F. Hydrogen bonding revisited: geometric selection as a principal determinant of DNA replication fidelity. *Proc. Natl. Acad. Sci.* **94,** 10493–10495 (1997).

35. Noguera, M., Sodupe, M. & Bertr�n, J. Effects of protonation on proton-transfer processes in guanine?cytosine Watson?Crick base pairs. *Theor. Chem. Acc.* **112,** (2004).

36. Nedderman, A., Stone, M., Williams, D., Lin, P. & Brown, D. Molecular basis for methoxyamine-initiated mutagenesis: 1H magnetic resonance studies of oligonucleotide duplexes containing base-modified cytosine residues. *J Mol Biol* **230,** 1068–1076 (1993).

37. Gorb, L. *et al.* A quantum-dynamics study of the prototropic tautomerism of guanine and its contribution to spontaneous point mutations in Escherichia coli. *Biopolymers* **61,** 77–83 (2001).

38. Podolyan, Y., Gorb, L. & Leszczynski, J. *Ab initio study of the prototropic tautomerism of cytosine and guanine and their contribution to spontaneous point mutations*. (Molecular Diversity Preservation International, 2003).

39. Leszczynski, J. The potential energy surface of guanine is not flat: an ab initio study with large basis sets and higher order electron correlation contributions. *J. Phys. Chem. A* **102,** 2357–2362 (1998).

40. Gorb, L., Podolyan, Y., Dziekonski, P., Sokalski, W. A. & Leszczynski, J. Double-Proton Transfer in Adenine−Thymine and Guanine−Cytosine Base Pairs. A Post-Hartree−Fock ab Initio Study. *J. Am. Chem. Soc.* **126,** 10119–10129 (2004).

41. Tofazzal, H. M. *et al.* Crystallographic studies on damaged DNAs IV. N4-methoxycytosine shows a second face for Watson-Crick base-pairing, leading to purine transition mutagenesis. *Nucleic Acids Res.* **29,** 4949–3954 (2001).

42. Martínez-Fernández, L., González, L. & Corral, I. An ab initio mechanism for efficient population of triplet states in cytotoxic sulfur substituted DNA bases: the case of 6-thioguanine. *Chem. Commun.* **48,** 2134 (2012).

43. Martínez-Fernández, L., Corral, I., Granucci, G. & Persico, M. Competing ultrafast intersystem crossing and internal conversion: a time resolved picture for the deactivation of 6-thioguanine. *Chem. Sci.* **5,** 1336 (2014).

44. Rubin, Y. V., Blagoi, Y. P. & Bokovoy, V. A. 6-Thioguanine luminescence probe to study DNA and low-molecular-weight systems. *J. Fluoresc.* **5,** 263–272 (1995).

45. Reichardt, C., Guo, C. & Crespo-Hernández, C. E. Excited-State Dynamics in 6-Thioguanosine from the Femtosecond to Microsecond Time Scale. *J. Phys. Chem. B* **115,** 3263–3270 (2011).

46. Kuramochi, H., Kobayashi, T., Suzuki, T. & Ichimura, T. Excited-State Dynamics of 6-Aza-2-thiothymine and 2-Thiothymine: Highly Efficient Intersystem Crossing and Singlet Oxygen Photosensitization. *J. Phys. Chem. B* **114,** 8782–8789 (2010).

47. Ashwood, B., Jockusch, S. & Crespo-Hernández, C. Excited-State Dynamics of the Thiopurine Prodrug 6-Thioguanine: Can N9-Glycosylation Affect Its Phototoxic Activity? *Molecules* **22,** 379 (2017).

48. Pollum, M., Martínez-Fernández, L. & Crespo-Hernández, C. E. in *Photoinduced Phenomena in Nucleic Acids I* (eds. Barbatti, M., Borin, A. C. & Ullrich, S.) **355,** 245–327 (Springer International Publishing, 2014).

49. Mai, S. *et al.* The origin of efficient triplet state population in sulfur-substituted nucleobases. *Nat. Commun.* **7,** 13077 (2016).

Chapter 2

Experimental Setup and Methods

The hallmark of the de Vries research laboratory is the ability to perform high resolution spectroscopy on organic molecules using our home-built instrument, conversationally known as the “molecular beam instrument” or the “beam instrument.” A combination of mass spectrometry and gas-phase laser spectroscopy were used for all the experiments performed in this dissertation. This allowed us to perform mass-selected spectroscopy and optically-selected mass spectrometry. In the de Vries research laboratory, we have two fully functional instruments. The first part of this chapter will focus on the older instrument, also known as the “main molecular beam instrument” and the second part will focus on the new instrument, also known as the “second molecular beam instrument.”

2.1 Main Molecular Beam Instrument

Figure 2.1 shows an image of the inside of our molecular beam instrument chamber with a corresponding schematic diagram and experimental setup in Figure 2.2. Briefly, a sample is placed on a translating graphite substrate directly in front of a pulsed molecular beam valve. It is laser desorbed and then entrained in a supersonic molecular beam of an inert gas, at a repetition rate of 10 Hz. The cold, neutral molecules are ionized using pulsed lasers. Ions produced are detected with a reflectron time-of-flight mass spectrometer (reTOF-MS). The timing of all these events is controlled using multi-channel digital delay generators. In the following sections, the instrument and the various spectroscopic techniques will be explained in detail.

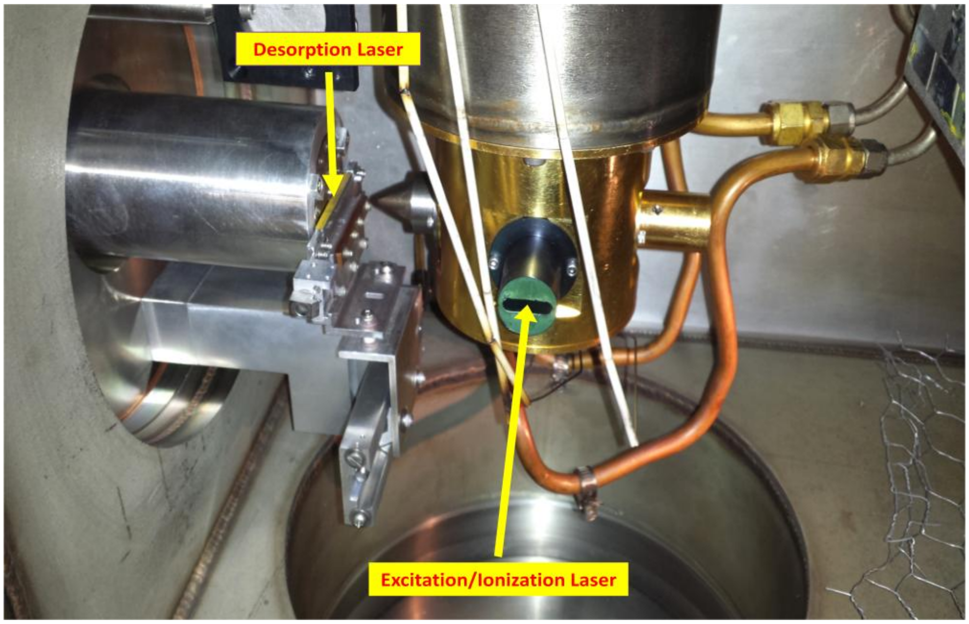

Figure 2.1: An image of the inside of the main molecular beam instrument chamber showing the beam path of both the desorption laser and the excitation/ionization laser. The latter can also be sent from the opposite side of the instrument. The desorption laser strikes the translating sample bar, which can also be adjusted to go up or down for signal optimization.

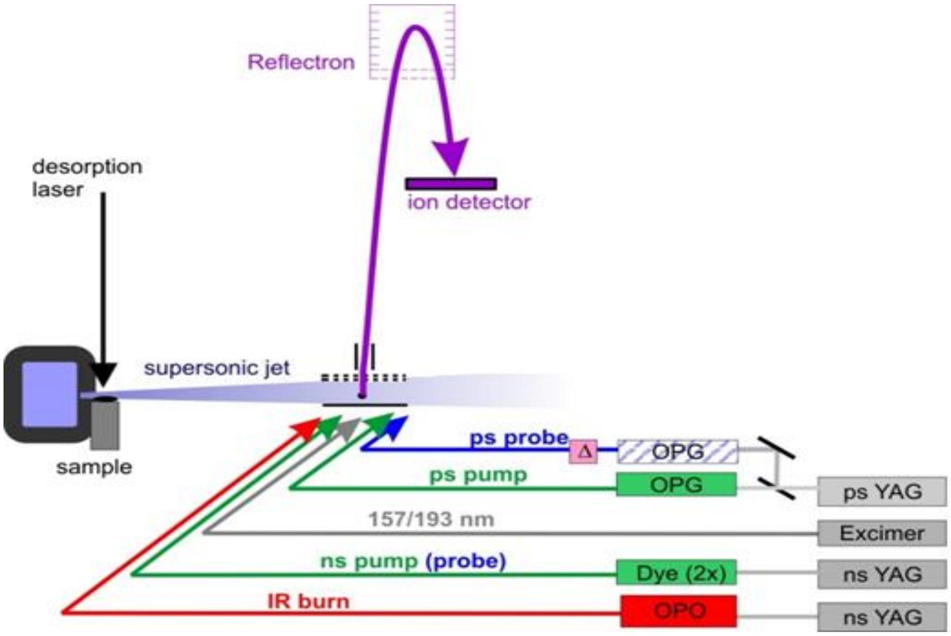

Figure 2.2: Schematic diagram showing the experimental setup of laser desorption supersonic jet-cooling mass spectrometer coupled with various lasers to perform multiple spectroscopic experiments. Laser desorbed molecules are entrained in a supersonic molecular beam of argon. The cold molecules are ionized in the ion source and are subsequently detected by a reflectron time-of-flight mass spectrometer (reTOF-MS).

2.1.1 Laser desorption

In order to study isolated molecules, chemists need to look at them in their gas phase. Therefore, a method is required to vaporize the sample being studied. Heating the sample is one way to encourage molecules into the gas phase but this method is limited to volatile molecules, such as some organic molecules. However, some organic molecules such as biomolecules are more likely to decompose upon heating. To overcome these limitations, laser desorption is used; it uses a laser pulse to vaporize volatile and nonvolatile molecules while avoiding thermal decomposition.

The first use of a high power laser for laser desorption was seen when Honig and Woolston vaporized metal atoms using a ruby laser in 1963 [1]. A few years later, Vastola and Pirone vaporized organic salts using a ruby laser as well [2,3]. In 1974, Beuhler *et al*. were able to laser desorb small quantities of peptides by using a method called “Energy-Sudden”, where neutral species are vaporized with rapid heating from a pulsed laser [4]. However, most of these vaporized molecules ended up fragmenting. In 1978, Pasthumus *et al.* were also able to vaporize nonvolatile, high molecular weight biomolecules [5]. Shortly after, supersonic jet-cooling was coupled with laser desorption, creating an extremely powerful technique. This technique was introduced by Lubman [6,7], Levy [8], Hunziker and de Vries [9–11]. This method helped with the fragmentation issue that Beuhler *et al.* encountered and opened a new window to high resolution spectroscopy of nonvolatile parent molecules.

The way laser desorption works is not well understood and very few experiments were performed to explain this process [12–19]. Experimental parameters such as laser wavelength, laser pulse width, matrix, and substrate, suggest different laser desorption mechanisms. So far, the laser desorption method uses a laser pulse to irradiate some of the surface where the sample is placed. The absorbed energy is converted into heat on the order of picoseconds. In turn, this induces thermal desorption of adsorbates. Using a nanosecond laser, a surface can be heated on a rate of 10^{11} K/s. Compared to other available heating methods, the surfaces are orders of magnitude faster. This rate corresponds to 1000 K in 10 ns laser pulse. Fast rate along with the high energy per laser pulse forces molecules to vaporize instead of thermally fragment as the time scale for heating is shorter than the time scale required to vibrationally excite the bond that leads to fragmentation. Fragmentation is minimized when using laser desorption because most of the laser power is absorbed by the matrix where the sample is embedded rather than the sample itself.

In the de Vries lab, we primarily use graphite as a matrix and occasionally gold. Samples are prepared by cleaning the graphite bar with acetone. Next, the graphite bar is scraped with an abrasive strip. Finally, we rub one side of the graphite bar back and forth on the sample until there is an even distribution of the sample along the sample bar. Better distribution of the sample is achieved when more than two weighing papers are placed on top of each other. This ensures a firm and even base underneath the sample which helps in preparing better samples. Mixing carbon black with samples provides a better sample distribution across the sample bar in addition to signal enhancement, particularly when we are trying to detect clusters with low signal. Woodward *et al*. previously noticed that carbon black improves signal strength and stability [20]. We tried different sample to carbon black ratios and found that the more carbon black added, the more enhanced and homogeneous the signal is. This seems to work as long as the carbon black quantity does not exceed that of the sample. For example, we used to mix 1:1 guanine and cytosine: carbon black by mass in order to get a strong homogenous GC cluster signal. The trick was crushing the sample into a fine powder with the tip of a spatula and mixing it well with carbon black.

In our experiments, we laser desorb a thin layer of sample from graphite substrate in front of a pulsed nozzle. The desorption laser used is a Nd:YAG laser (Continuum Minilite I). It operates at a fundamental wavelength of 1064 nm. This wavelength is optimum because molecules studied in this lab do not interact with this wavelength. The laser is attenuated to about 1 mJ per pulse and focused to a spot of approximately 0.5 mm in diameter on the bar edge closest to the nozzle. The sample bar translates in order get a fresh sample with every laser shot. The sample bar height can also be adjusted to go up or down the molecular beam axis for signal optimization. Ionization efficiency in the laser desorption step is about 10^{-5}; most desorbed molecules remain as neutral species [21–24]. As a result, we are able to study the parent molecules rather than the fragments. The desorption and the ionization step are separated which allows for better control and an independent optimization of each process. The desorbed molecules are sent to the ionization region through supersonic jet-cooling.

2.1.2 Supersonic jet-cooling

The accuracy with which spectroscopy can be measured is governed by the internal temperature of the molecules studied. As a result, cooling the molecules before ionizing them is an important step for selectivity in the REMPI technique.

Large molecules have more complex spectroscopy due to their higher density of states. This results in spectral broadening which is very difficult to analyze. At any relatively high temperature, the rotational and possibly vibrational states of large molecules are populated which leads to spectral complexity. On the other hand, in the solution phase, their spectroscopy is even more complex as solvent interactions contribute to the overall spectrum.

A method is needed to overcome these limitations in order to simplify the spectroscopy of the desorbed molecules. This is done by cooling the molecules being studied. In turn the number of populated rotational and vibrational states is reduced. As a result, supersonic jet-cooling has been used to cool gas-phase molecules and obtain highly resolved spectra, as shown in Figure 2.3.

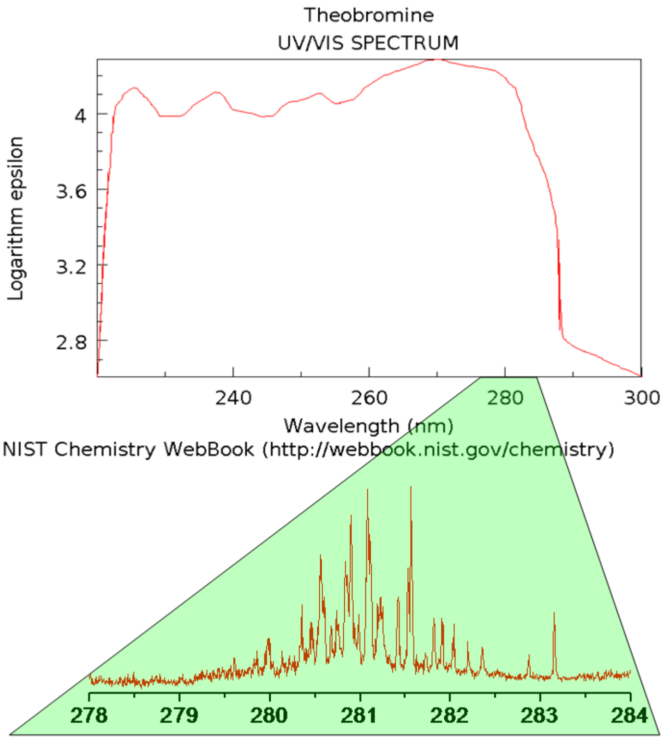

Figure 2.3: A comparison of solution phase spectrum with a jet-cooled spectrum obtained in our lab. Ambient temperatures and solvent-solute interactions lead to broad spectra in the solution phase. On the other hand, jet-cooled molecules in the gas phase have well resolved vibronic features in their spectra.

The supersonic molecular beam was introduced theoretically by Kantrowitz and Grey in 1951 [25]. In the same year, Kistiakowsky and Slichter constructed an apparatus which helped create molecules with narrow velocity distribution [26]. About thirty years later, high speed vacuum pumps made it possible to couple high resolution spectroscopy with supersonic jet-cooling.

Supersonic jet expansion is created when an inert gas such as argon or helium gas is maintained at a high pressure behind a small orifice and then expands into a vacuum chamber, as shown in Figure 2.4. Any molecules entrained with the cold gas molecules become part of this supersonic jet expansion and adopt the energy characteristics of the gas molecules. In a supersonic jet expansion, random thermal motion (rotations and vibrations) of the molecules are converted into direct motion (translation), which results in very low translational temperatures. This energy conversion allows for a more uniform and tight cloud of molecules with a much greater velocity leading to narrower velocity distribution (Figure 2.4).

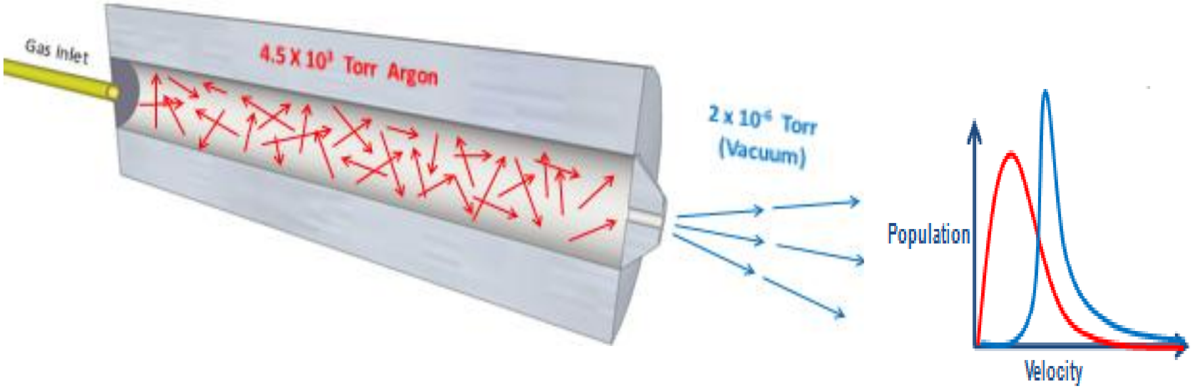

Figure 2.4: High pressure argon gas is expanded into a vacuum through a small nozzle. Random thermal motion of the argon molecules (red arrow) is converted into directed kinetic motion (blue arrow). This results in a low translational temperature (around 1K) which in turn leads to a narrow velocity distribution due to the fact that the width of the velocity distribution is a direct measure of the translational temperature of the gas.

In supersonic jet expansions, translational temperatures less than 1 K are easily attainable [27]. The rate of energy transfer between translation and rotation is fast resulting in efficient cooling and rotational temperatures less than 1 K. On the other hand, the rate of energy transfer between translation and vibrations are not as fast, resulting in vibrational temperatures of 10 to 20 K [10]. Such low temperatures ensure that only a few rotational and vibrational energy states are populated. This results in well-resolved spectra (Figure 2.3).

Near the nozzle where the density of molecules is very high, a high number of inelastic collisions eliminate the internal degrees of freedom and the velocity distribution is relatively narrow. Further away from the nozzle where the density of molecules is low, molecules are free of collisions and the velocity distribution is narrower. A careful optimization of the laser desorption position and multiple jet conditions, such as the pressure and pulse width, are effective in creating clusters. The study of clusters opens up a great type of science where hydrogen bonding, base stacking, and charge transfer can be studied in the gas phase.

The supersonic jet expansion is created by a pulsed nozzle (Amsterdam Cantilever Piezo Valve ACPV2) and is powered by an EDU2 electronic driver unit which is set between 138 and 147 volts. The valve runs at 10 Hz repetition rate and the conical nozzle is 200 μs in diameter. Using argon as a high-purity carrier gas, the cantilever produces a molecular beam at a backing pressure of 4-8 bars. The cold argon molecules entrain the desorbed sample molecules as they expand into the vacuum chamber. After that, the molecules pass through a 3 mm skimmer before reaching the source of the mass spectrometer. Certain pressures must be achieved before the ion source is powered. The source pressure is maintained at 2×10^{-5} torr using a large diffusion pump (Edwards Diffstak 250, pumping speed: 2000 L/s). More importantly, the analyzer pressure is maintained at 2×10^{-6} torr using a small diffusion pump (Edwards Diffstak 100, pumping speed: 535 L/s).

Photoionization, the method used in the de Vries lab to detect desorbed molecules, will be discussed in the next section.

2.1.3 Photoionization

Photoionization is the process of creating ions from atoms or molecules after absorbing photon(s). This process can be done using a single photon or multiple photons, depending on the ionization potential of that specific atom or molecule. In other words, the photoionization cross-section is zero if the photon energy is lower than the ionization threshold but greater than zero if the photoionization cross-section is higher than the ionization threshold. This can be achieved with one photon or more, resonantly or non-resonantly.

2.1.3.A Single photon ionization

The single photon ionization process usually requires a photon in the VUV region that can be generated by commercially available lasers. For example, an excimer may be used. The excimer laser uses a mixture of a noble gas (Ar, Kr, Xe) and a reactive gas (F, Cl) to produce a fixed wavelength below 200 nm that is dependent on the gas mixture.

In order to reach the target ionization potential (IP), the photon must have enough energy (Figure 2.5). Since a large number of the aromatic molecules we study in our research lab have an IP of 7-8 eV, they can be ionized and detected using a VUV source such as the excimer laser. The excimer laser produces 193 nm or 157 nm photons, depending on the gas mixture being used. Since 193 nm corresponds to 6.4 eV, one photon might not be sufficient enough to ionize some of the molecules we study in our lab. In this case, two photons are required. On the other hand, 157 nm (7.9 eV) is sufficient to ionize most of the molecules we study with only one photon.

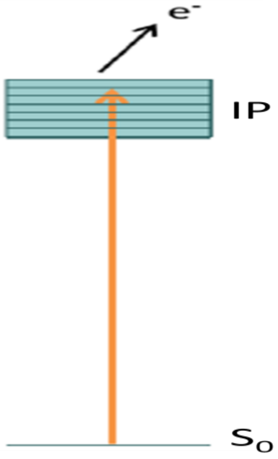

Figure 2.5: Jablonsky diagram for single photon ionization.

Single photon ionization is often used regardless of its lack of selectivity. It does not require the photon to be tuned to the molecule's energy level. Therefore, previous knowledge of the molecule's potential energy surface is not required [28]. This technique can be used to determine whether or not a molecule is present in a sample. For example, single photon ionization may be used in order to gain a general understanding of some of the molecules present in a pottery sample. Monitoring the different masses can narrow down the possible molecular candidates that need to be examined.

2.1.3.B Non-resonant ionization

Non-resonant ionization is a process that requires multiple photons to be simultaneously absorbed by a molecule (Figure 2.6). In order to improve the efficiency of this process, a laser with a high peak power is necessary. This is due to the extremely short-lived characteristic of virtual states. Therefore, a more powerful laser such as the femtosecond laser is required. Using this method for ionization usually leads to unwanted mass fragments to appear due to the use of high power lasers. More importantly, the powerful tool of tautomer (isomer or conformer) specific is lost.

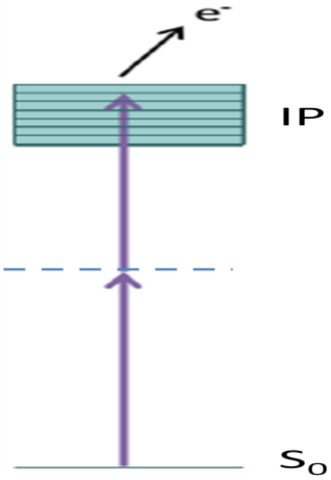

Figure 2.6: Jablonsky diagram for non-resonant ionization

2.1.3.C Resonant ionization

Resonance-enhanced multiphoton ionization (REMPI) is a highly sensitive and state-selective spectroscopic method used to study atoms and molecules in the gas phase. In this process, ionization is achieved through an intermediate state. The energy of that state is resonant with one of the steps in the multi-photon process. Resonant two-photon ionization (R2PI) is the simplest way to perform REMPI. R2PI is a highly effective spectroscopy technique used to study the electronic properties of atoms and molecules. This ionization technique requires one photon to electronically excite the molecule of interest and a second photon to ionize that excited molecule, as shown in Figure 2.7. By scanning the excitation laser in the region of interest and monitoring the ion signal, a UV/VIS mass specific spectrum can be collected. This spectrum is different for every molecule and is the signature for distinguishing between isomers, tautomers, and conformers. The resolved spectrum, due to laser desorption and jet-cooling, contains many bands that are attributed to transitions from the ground state to excited electronic states and to vibrational states within an excited electronic state. The most unique transition band is called the “origin”. It is the transition from the lowest vibrational state in the ground state to the lowest vibrational state in the first electronic state.

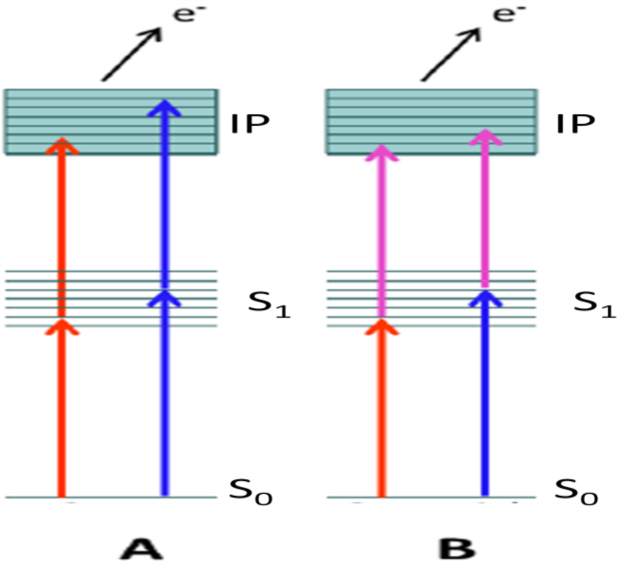

Figure 2.7: Jablonsky diagram for resonant two-photon ionization. One-color R2PI (A) and two-color R2PI (B).

As discussed previously, R2PI generates ions by absorbing of a second photon after tuning the first laser to a molecule’s resonance. This process is possible using one (1-color) or two lasers (2-color), as shown in Figure 2.7 A and B, respectively. Although one-color experiments are easier to perform, they have multiple limitations that can be overcome by using two-color experiments. Two-color experiments require that two lasers overlap both spatially and temporally. One-color experiments can be used on molecules with their first excited state energies higher than half the ionization potential. This means that two photons required for excitation and ionization originate from the same laser. Control over spectral broadening is not possible in one-color experiments because of power saturation. The absorption cross section is 10^{-17} cm^2 for excitation and 10^{-19} cm^2 for ionization [29]. Compared to the excitation process, the ionization process has a smaller cross section. Consequently, this indicates that maximizing ion production results in the saturation of the excitation step. As a result, the use of two lasers allows the researcher to make fine adjustments of each laser separately to minimize the risk of burying valuable information underneath the saturated R2PI peaks. Since the ionization efficiency is greatest just above the ionization potential [29], the second color can be tuned for signal enhancement as shown in Figure 2.8.

In order for a second photon to be absorbed, the molecule under study must have a long-lived excited electronic state. Fast photophysics processes such as internal conversion reduce the excited electronic state population and result in very little ionization signal. Therefore, lasers with extremely narrow spectral bandwidths must be used.

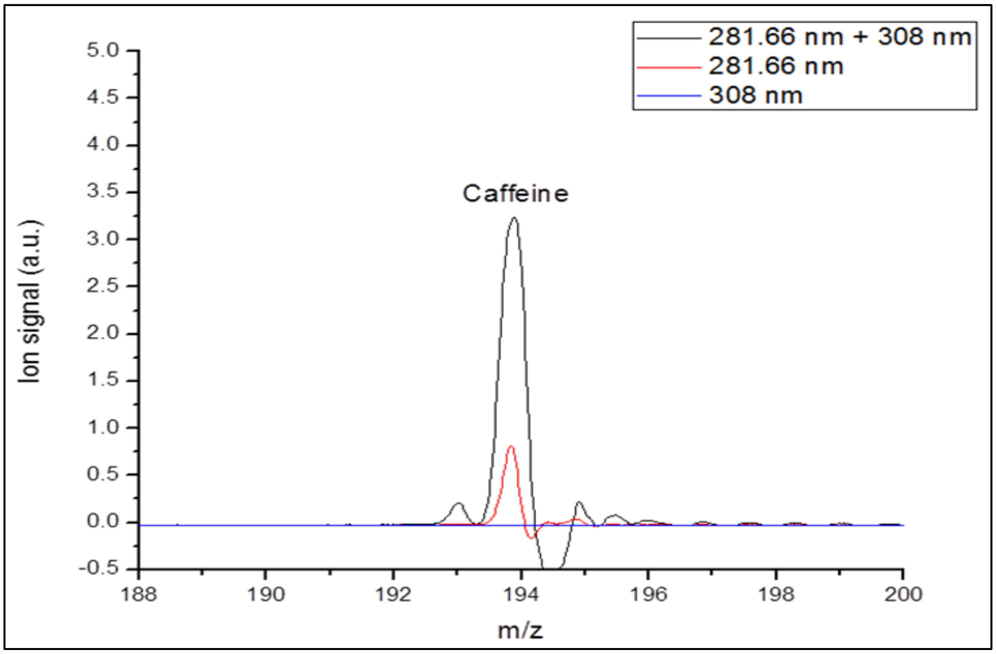

Figure 2.8: One-color vs two-color R2PI for caffeine shows a signal enhancment when a second laser is used for ionization.

Nanosecond R2PI: The system for nanosecond experiments consists of an Nd:YAG laser (Quanta-Ray DCR-2A) producing 7 ns pulses at 532 nm or 6 ns pulses at 355 nm with an energy of ~360 mJ or ~150 mJ, respectively. Then the YAG pumps a tunable dye laser (Lumonics Spectrum Master HD-500). The frequency bandwidth of the dye laser is ~.04 cm^{-1}. The dye laser output provides a large range of wavelengths from 470 to 680 nm. This visible range is sometimes used to collect spectra of some anthraquinone dyes. However, the majority of experiments required that the visible light from the dye laser be doubled by using a beta barium borate (BBO) crystal or a monopotassium phosphate (KD*P) crystal, resulting in 0.015 cm^{-1} bandwidth pulses. The output energy is dependent on the pump frequency, efficiency of the dye, and doubling crystal used. The energy ranges from 0.4 mJ-2.5 mJ/pulse and is attenuated in order to avoid power saturation.

Picosecond R2PI: The system for picosecond experiments consists of a Nd:YAG (EKSPLA PL2441) laser. This laser produces 10-15 ps pulses with energy of ~20 mJ at 355 nm that pumps an (EKSPLA PG401-SH) optical parametric generator (OPG). The frequency bandwidth is ~ 6 cm^{-1}. We are currently splitting out the excess second harmonic of the pump laser and frequency double it to obtain a 266 nm probe beam, or frequency mix it to obtain a 213 nm probe beam. These two outputs are used for the ionization process. The experimental setup to produce 266 and 213 nm will be discussed further in the Pump-Probe section.

It is crucial to remember that REMPI is an action spectroscopy, reflecting not only the excitation from the ground state but also the ionization probability out of the excited state. If the excited state lifetime is significantly shorter than the ionization laser pulse width, the ion signal is reduced. We have found that a typical 10 ns REMPI laser pulse is essentially blind for a molecular species with an excited state that exists less than 10 picoseconds. The picosecond laser setup provides three orders of magnitude shorter pulses, at 10 ps.

Heisenberg’s uncertainty principle, in the form of $\Delta E \Delta t \geq h/4\pi$, forces a trade-off between time resolution and bandwidth. Femtosecond laser pulses are an appropriate tool for measurements in the sub-picosecond time domain; however, they are also inherently broad in the frequency domain and therefore less suited for gas phase spectroscopy. The picosecond regime provides an excellent trade-off between time resolution and spectral resolution. Picosecond laser pulses are short enough in time to perform REMPI and narrow enough in frequency to perform spectroscopy with sufficient resolution to resolve many individual vibronic transitions.

2.1.3.D Double resonance spectroscopy

Biomolecules typically exist in several tautomeric forms which are isolated under gas phase jet-cooled conditions. Each tautomer (isomer or conformer) has unique electronic and vibrational transition energies resulting in distinct peaks in the R2PI spectrum. When several tautomers coexist for a biomolecule, the R2PI spectrum is expected to be complex due to the collection of slightly different vibrational progressions of each tautomer. Many REMPI-based spectroscopic techniques take advantage of the unique S1 ← S0 transition energy of each tautomer to gain tautomer specific data. Double resonance spectroscopy is used to determine the structure of each tautomer; whereas, pump-probe spectroscopy is used to estimate their excited states lifetimes and map their potential energy surfaces.

2.1.3.D.1 UV-UV double resonance spectroscopy

It is not possible to quickly determine the number of tautomers by simply looking at the R2PI spectrum. However, combining the R2PI spectrum with the UV-UV double resonance spectrum can be used to determine the number of tautomers. This experiment requires two UV lasers to be overlapped spatially but 200 ns apart in time, as shown in Figure 2.9. The first laser (burn) resonantly depletes the ground state population. The second laser (probe) is fired 200 ns later to probe the leftover population in the ground state. As the burn laser is scanned, no depletion is seen on the probe signal until the burn laser transition is resonant with that of the tautomer’s transition, selected by the probe laser. If all R2PI peaks are matched with UV-UV dips, then only one tautomer is present. Otherwise, the experiment is to be repeated with a different probe transition; one that has no corresponding dip. The experiment is repeated as many times as necessary until every peak in the R2PI spectrum has corresponding dips in the UV-UV spectrum. The number of scans needed to be done reflects the number of tautomers present in the molecular beam.

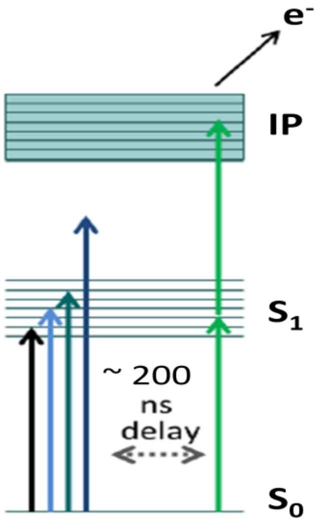

Figure 2.9: Jablonsky diagram for UV-UV double resonance spectroscopy. Multiple arrows indicate that the laser is being scanned.

Figure 2.10 shows an example of UV-UV double resonance spectroscopy [30]. The bottom trace shows a one-color R2PI spectrum. It is common to first set the probe at the origin transition, in this case 289.50 nm. The middle trace was collected when the burn laser was scanned and the probe laser was set at the origin transition. It is clear that not all the R2PI peaks were accounted for in this UV-UV ion-dip scan, most notably the large peak at 289.10 nm. As a result, the experiment was performed again with the probe laser set at 289.10 nm, as shown in the top trace. The combination of the two UV-UV ion-dip scans account for all of the R2PI peaks. This indicates that two tautomers are present in the molecular beam in this spectral region.

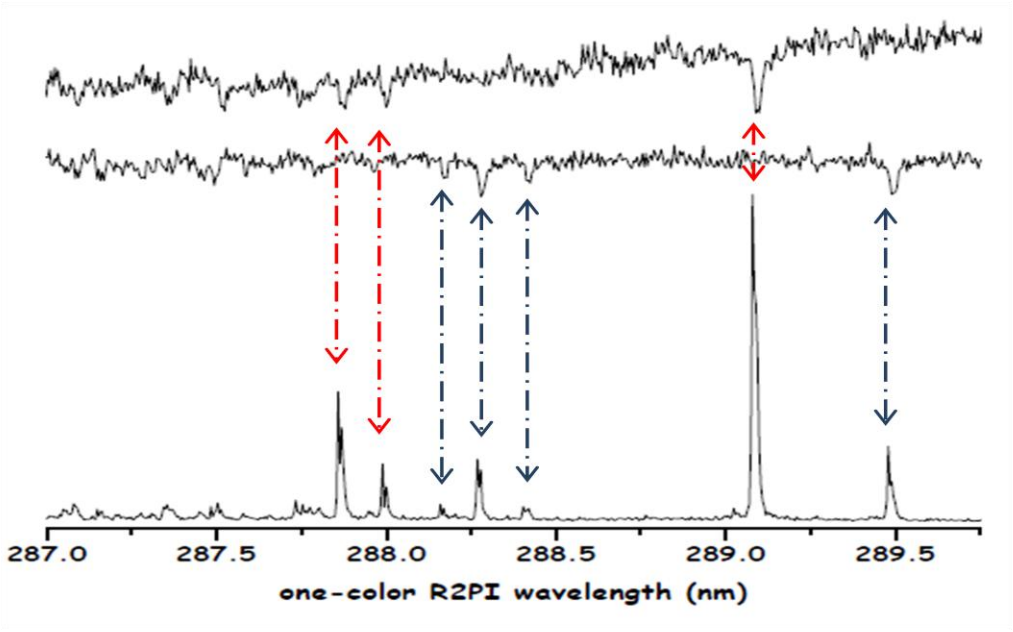

Figure 2.10: R2PI spectrum of vanillic acid (bottom trace) and UV-UV double resonance spectra (top and middle traces)[30]. Two UV-UV double resonance spectra were required to account for all the peaks in the R2PI spectrum. This indicates that two tautomer (conformers or isomers) are present in this spectral region, as indicated by the blue and red arrows.

Terms such as “hole-burning” and “ion-dip” spectroscopy are often used when discussing double resonance spectroscopy. It is worth noting the difference between the two terms. Hole-burning spectroscopy is fixing the burn laser and scanning the probe laser. This method collects a spectrum of all tautomers except for the one selected by the burn laser. On the other hand, ion-dip spectroscopy is fixing the probe laser and scanning the burn laser. This is the common method and is used to determine the number of tautomers in the molecular beam.

2.1.3.D.2 IR-UV double resonance spectroscopy

IR-UV double resonance spectroscopy is a powerful method used to obtain a tautomer-specific IR spectra. This method was first developed in the 1980s [31]. It is analogous to UV-UV double resonance spectroscopy but with the burn UV laser (when performing ion-dip spectroscopy) or the probe UV laser (when performing hole-burning spectroscopy) is replaced with an IR laser as shown in Figure 2.11. The experiment is done in a similar manner with UV-UV spectroscopy. IR-UV ion-dip spectroscopy is used to collect IR spectra for all tautomers separately. This is done by setting the probe laser at one of the transitions in the R2PI spectrum in order to constantly create ion signal. An IR laser OPO/OPA (Laser Vision), 10s-100s ns prior, is scanned in the region of interest, usually the mid IR region, where NH and OH stretches can be detected. When this IR pulse resonantly modifies the vibrational distribution of a specific isomeric population in the molecular beam, we detect this as a change in the ion signal from a selected UV transition peak [32–37]. IR-UV hole-burning spectroscopy is setting the IR laser on a vibrational transition and scanning the UV probe laser. The purpose of this method is similar to UV-UV hole-burning spectroscopy, where the spectrum of all tautomers excluding the one selected by the IR burn laser is collected. In our lab we use this method instead of UV-UV ion-dip spectroscopy in order to determine the number of tautomers in a molecular beam when a long triplet state is present (refer to chapter 5 for more detail).

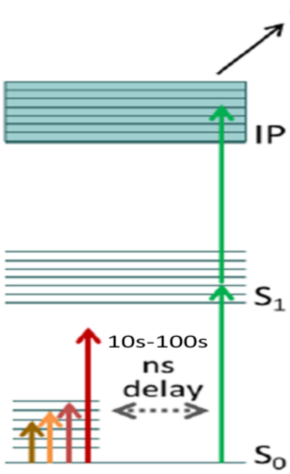

Figure 2.11: Jablonsky diagram for IR-UV double resonance spectroscopy.

As discussed previously, an IR optical parametric oscillator/amplifier (OPO/OPA, bandwidth 3 cm^{-1}) is used to provide tunable mid-IR radiation. This laser system uses a set of nonlinear crystals (KTP/KTA) to convert the fundamental frequency radiation (1064 nm from Nd:YAG DCR-2A) into mid-IR radiation via different frequency mixing. The OH and NH stretching frequencies, in particular, are highly diagnostic for different tautomeric forms and for hydrogen bonded structures. The OPO/OPA system was recently fixed and realigned. Table 2.1 shows IR energies at different frequencies and positions, relative to the OPO/OPA system. These values were collected when the OPO/OPA system was pumped with 550 mJ of horizontally polarized 1064 nm beam.

	Signal	775.4	793.9	825.5
	Mid IR (cm^{-1})	3499.84	3199.95	2717.46
Without the Exit Polarizer	Right out of the OPO/OPA (mJ)	12.5	12.3	12.5
	After the optical tower and right before the beam instrument (mJ)	7.0	7.3	7
With the Exit Polarizer	Right out of the OPO/OPA (mJ)	5.2	4.5	3.9
	After the optical tower and right before the beam instrument (mJ)	2.2	2.0	1.3

Table 2.1: IR energies of the OPO/OPA system when pumped with 550 mJ of horizontally polarized 1064 nm beam. Energy readings were collected in two different spots, right out of the system and right before the instrument. The two spots are ~2.5 meters apart, the path contained two silver mirrors on an optical tower, and one MgF_2 window. The exit polarizer only allowed vertical beam to pass through. All experiments in this dissertation were done with the exit polarizer on and with the IR path purged.

As an example, Figure 2.12 shows the IR-UV ion-dip spectrum for the 6-thioguanine, in the IR region from 3300 to 3650 cm^{-1}. IR bands for isolated molecules in the gas phase are sharp and narrow compared to what is typically seen in this region for the condensed phase. This is due to effects of hydrogen bonding on band shape.

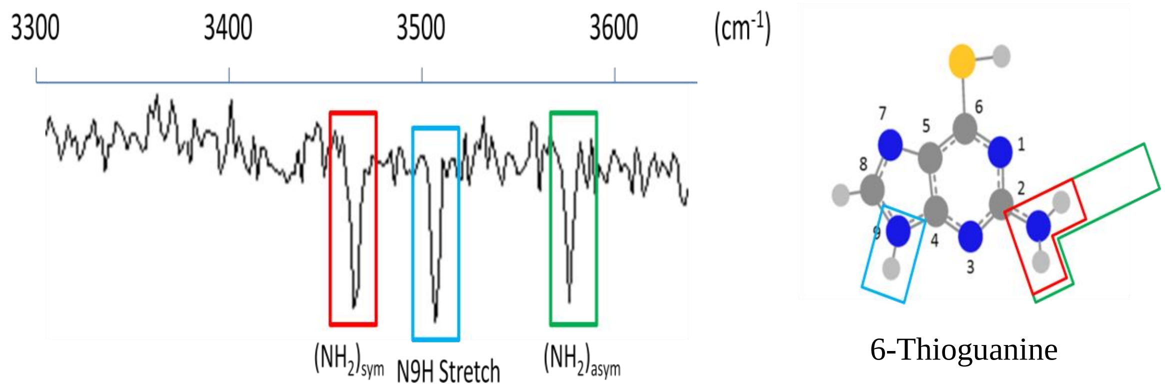

6-Thioguanine

Figure 2.12: IR-UV ion-dip spectrum of 6-thioguanine. Isolated molecules in the gas phase result in narrow and sharp IR bands.

We also performed experiments at the Free-Electron Laser for Infrared eXperiments (FELIX), which is part of the Molecules and Materials Institute at the Radboud University in Nijmegen, the Netherlands. FELIX covers the region (66 – 3600 cm^{-1}) but our experiments focused on the (95 – 880 cm^{-1}) region (see chapter 4 for more detail).

2.1.3.D.3 UV-UV pump-probe spectroscopy

UV-UV pump-probe spectroscopy method is used to measure the excited states' lifetime of specific tautomers. A Jablonsky diagram offers an explanation to this method, as shown in Figure 2.13. By collecting the ion signal while varying the delay between the excitation and the ionization pulses, a decay curve is constructed and then fit with exponential decay functions. In the de Vries lab, we perform both nanosecond and picosecond UV-UV pump-probe spectroscopy.

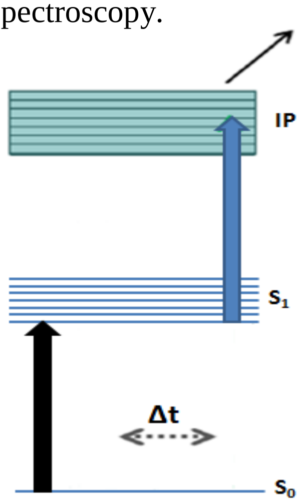

Figure 2.13: Jablonsky diagram for UV-UV pump-probe spectroscopy

<ins>Nanosecond UV-UV pump-probe spectroscopy</ins>: In this technique, the delay is varied electronically between the excited state and the ionization state pulses. The time resolution derives from an instrument function which is determined by the pulse shapes and is typically limited to about half the pulse width of the longest pulse. The range of the nanosecond has

about 5 ns resolution. We can measure lifetimes up to the time it takes for the molecules to exit the interaction region, which is of the order of a few microseconds. In our lab, we use a UV pulse from the dye laser system to excite a molecule and a second UV pulse at 266 nm from the Nd:YAG laser, or the excimer laser at 193 or 157 nm (GAM EX5) to ionize the excited molecule. The excitation and ionization pulses are delayed electronically using a Stanford Research Systems (Model DG645).

Picosecond UV-UV pump-probe spectroscopy: In this technique, the delay is varied by a mechanical delay line between the excited state and the ionization state pulses. For the picosecond range, our resolution is about 15 ps and we can measure up to a few ns. This is limited by the length of our delay stage. In our lab, we use a UV pulse from the EKSPLA picosecond laser system in order to excite a molecule and a second pulse at 266 or 213 nm produced from the excess second harmonic of the pump laser. The two pulses are mechanically delayed mechanically with a retroreflector. Figure 2.14 shows an example of a picosecond pump-probe decay curve for 6-thioguanine along with the exponential decay fit.

In observing Figure 2.15, one can see the scheme of the picosecond pump-probe setup. The 30R/70T beam splitter enables us to increase the 355 nm output. In turn, the 532 and 1064 nm leftover output is increased, without damaging the EKSPLA OPG system. When the laser produces 7-10 mJ of 355nm pump energy, 400-600 μJ of 266 nm beam is generated by doubling the leftover 532 nm using a second harmonic BBO crystal. However, in this process, the leftover 1064 nm beam is separated from the 532 nm beam. Then, it is sent to the 1064 nm port where it is blocked by the beam shutter. The time between the pump and probe pulses is varied when the 266 beam is sent to the UV coated, broadband retroreflector (PLX Inc). The retroreflector is resting on the top of a 300 mm long travel stage with integrated stepper motor controller (Thorlabs LTS 300). The movement of the retroreflector results in 0-1.6 nsec delays, due to the zero position being ~56 mm away from the end of the stage. The probe beam is then collimated with the tunable OPG bean and sent to the instrument. Frequency mixing of 1064 and 266 nm inside the fifth harmonic BBO crystal (EKSPLA) is used to generate ~ 250μJ of 213 nm, with a slightly different path and optics, as shown if Figure 2.15.

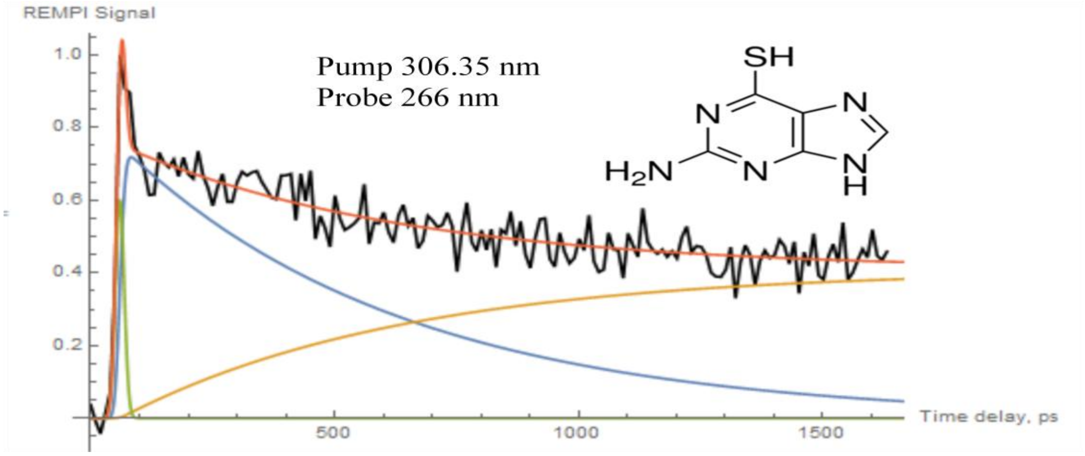

Figure 2.14: Picosecond pump-probe data for 6-thioguanine using 306.35 nm as pump and 266 nm as probe.

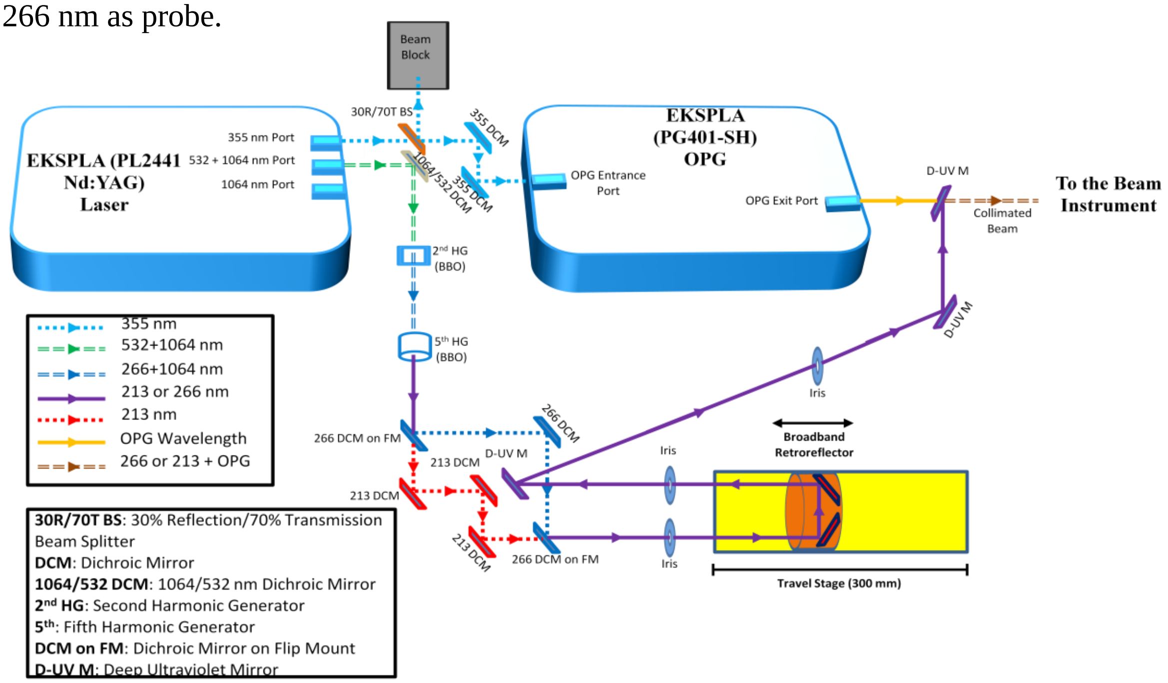

Figure 2.15: A schematic of the picosecond pump-probe setup and (266/213 nm) generation.

2.1.4 Time-of-flight mass spectrometry

As discussed in section 2.1.3, ions are produced through photoionization. These ions are then detected using a reflectron time-of-flight mass spectrometer (reTOF-MS). As the name implies, a time-of-flight mass spectrometer is an instrument that separates ions of different masses based on their different travel time through a field-free region. Once ions are produced, they are accelerated with equal forces. However, the acceleration of each ion is inversely proportional to its mass, according to Newton's second law. Previous experiments have shown that this instrument can be used to study large molecules with a mass range extending >1 MDa, even though an unlimited mass range is theoretically possible [38]. In Figure 2.16, one can note the four parts of the reTOF-MS used in the de Vries laboratory: The ion source, the flight tube (field-free region), the reflectron, and the detector.

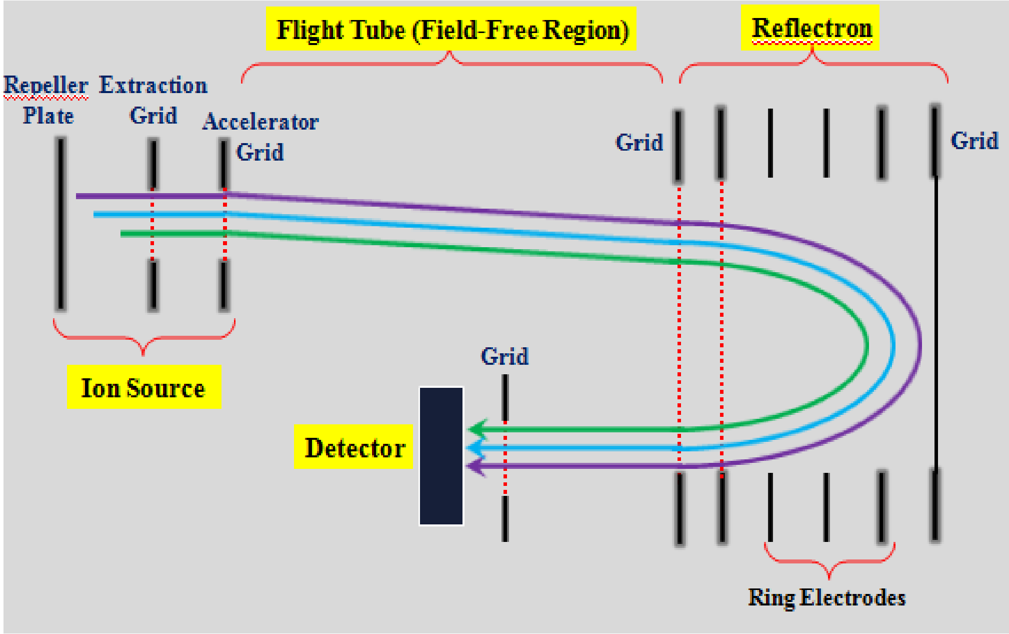

Figure 2.16: A schematic of the reflectron time-of-flight mass spectrometer (reTOF-MS) with the four main parts highlighted in yellow.

2.1.4.A Ion source

In both instruments, we use a dual-stage ion source, developed by Wiley and McLaren [39]. This ion source consists of three planar electrodes: repeller plate, extraction grid, and acceleration grid. Our ion source also consists of a perpendicular set of electrodes called steering plates. Figure 2.17 shows and image of our ion source. The region between the repeller plate and the extraction grid is the first stage and it serves as the extraction region. The second stage serves as the acceleration region and it is the region between the extraction grid and the acceleration grid.

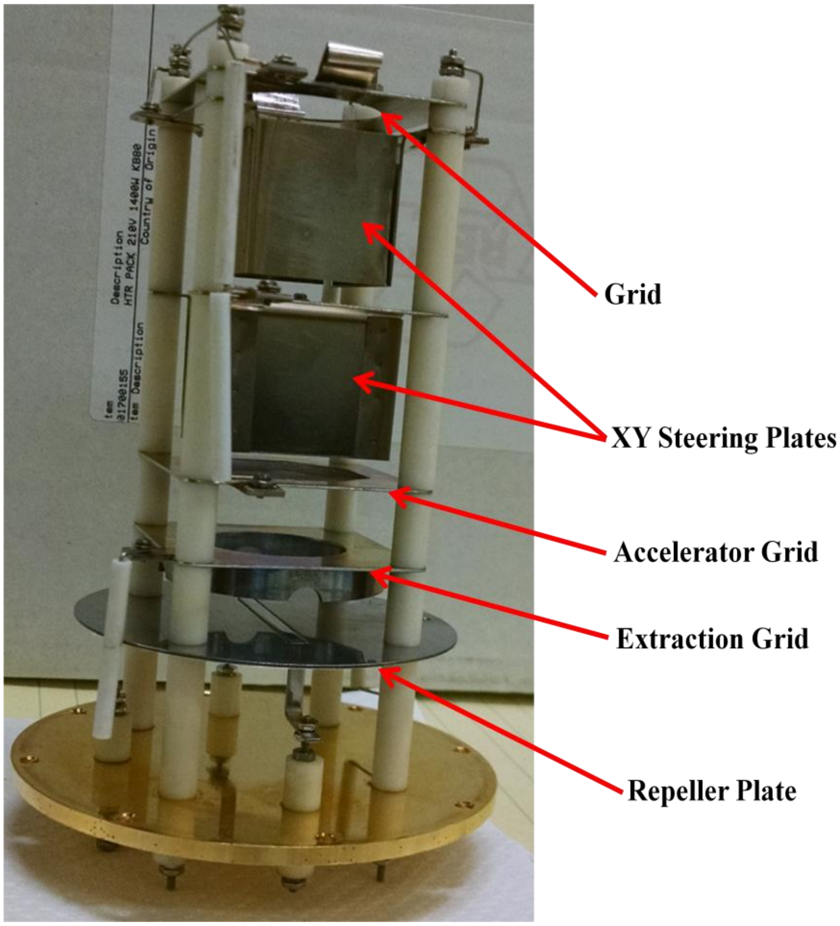

Figure 2.17: An image of our dual-stage ion source. Ions are extracted and then accelerated into the flight tube through the final grid.

Ions must be ejected from the ion source with the same starting point in order for these ions to be suitable for analysis. As a result, the pulsed ion source requires a pulsed laser. When the voltage is switched on rapidly, a group of ions start moving at the same time. This means that ions are produced in the extraction region and then start moving towards and through the extraction grid. The ions then enter the acceleration region with a much stronger field. Here, the ions are accelerated into the flight tube. If the molecules are not static when they are ionized, they could drift away from the axis of the flight tube. As a result, steering plates are used to counteract this issue, as shown in Figure 2.17.

2.1.4.B Flight tube

The flight tube is a vacuum enclosure electric field-free region between the ion source and the detector. All ions, regardless of their masses, are ejected out of the acceleration region with the same kinetic energy. Therefore, a heavy molecule packet will travel slower compared to a light molecule packet resulting in mass separation. The kinetic energy on an ion is given by:

$$\frac{\boldsymbol{mv^2}}{\boldsymbol{2}} = \boldsymbol{zeE} \qquad \text{eqn 1}$$

$\boldsymbol{m}$: mass

$\boldsymbol{v}$: velocity

$\boldsymbol{z}$: number of charges on an ion

$\boldsymbol{e}$: charge on an electron

$\boldsymbol{E}$: electric field

The velocity of the ion equals the distance it travels (ion source to detector) divided by the time it takes to travel, $\boldsymbol{v} = \frac{\boldsymbol{d}}{\boldsymbol{t}}$. By substituting $\boldsymbol{v}$ with $\frac{\boldsymbol{d}}{\boldsymbol{t}}$ and simple rearrangement, the equation can be rewritten as:

$$\boldsymbol{t} = \sqrt{\frac{\boldsymbol{m}}{\boldsymbol{z}}}\ (\boldsymbol{d}/\sqrt{\boldsymbol{2eE}}) \qquad \text{eqn 2}$$

With $\boldsymbol{d}, \boldsymbol{e},$ and $\boldsymbol{E}$ being constants, the ion flight-time is directly proportional to the square root of the mass over charge. Thus, heavier ions travel slower than lighter ions, is mathematically confirmed, assuming that both ions have the same charge.

Ion packet width is governed by two factors, time and position. Time variation, also known as temporal distribution, is when the ionization laser pulse determines the ion packet width. On the other hand, the position variation, also known as spatial distribution, is when the position of the ions created determines the ion packet width. The combination of temporal distribution and spatial distribution results in variation of ion velocities, also known as velocity distribution. In turn, this variation affects the mass resolution of the TOF-MS. Assume two ion packets with the same masses are created in the ion source, as shown in Figure 2.18. The packet closest to the grid will leave first, but will move at a slower rate. Conversely, the packet farthest from the grid will leave last but at a faster rate. Therefore, ions of the same mass will not reach the detector at the same time which will result in similar masses which appear as different peaks.

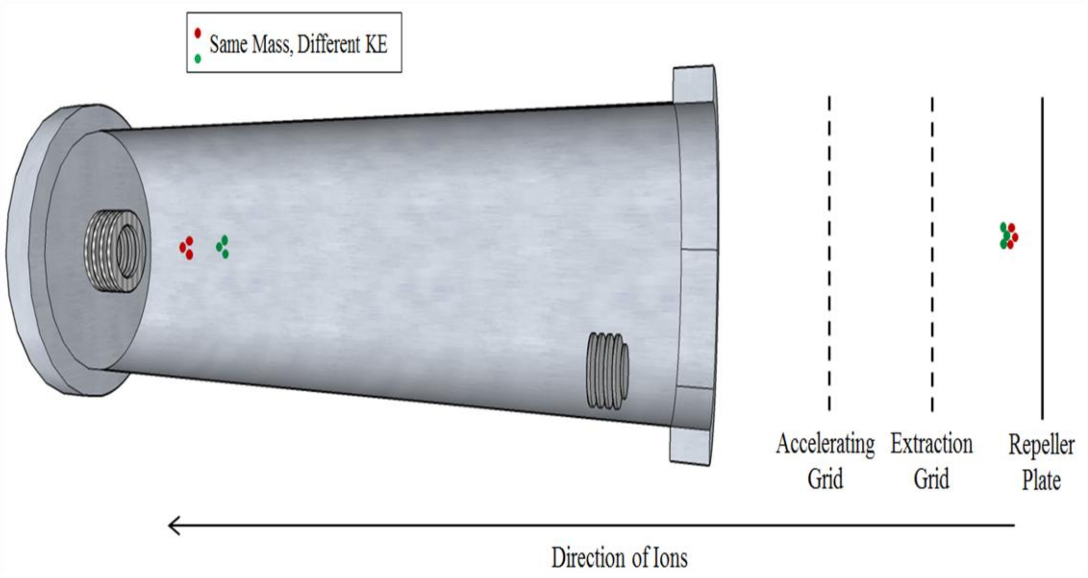

Figure 2.18: A schematic of an ion source and a flight tube. Spatial and temporal distributions in the ion source lead to a velocity distribution in the flight tube. As a result, ions with similar masses are detected at different times.

However, at some point, faster, later ions will eventually catch up with the slower ions. The point in which the ions meet is referred to as the primary focal point. At this point, the width of the ion packet is at its narrowest. Therefore the resolution is at its highest. Mathematically, the resolution is given by

$$\boldsymbol{Resolution} = \frac{\boldsymbol{m}}{\boldsymbol{\Delta m}} = \frac{\boldsymbol{t}}{\boldsymbol{\Delta t}} \qquad \text{eqn 3}$$

$\boldsymbol{m}$: ion mass over charge

$\boldsymbol{\Delta m}$: full width of half-maximum (FWHM) of the ion peak.

$\boldsymbol{t}$: ion travel time

$\boldsymbol{\Delta t}$: full width of half-maximum (FWHM) of arrival times distribution

Using the equation above, the resolution can be improved by increasing the time spent in the flight tube. Specifically, this can either be done by extending the length of the flight tube or by forcing the ions to travel a longer distance in the flight tube.

2.1.4.C Reflectron

As discussed previously, the primary focal point is where the ion packet width is at its narrowest and the resolution is at its highest. Unfortunately, this primary focal point in most instruments is about 100 mm or so [40], which is not enough time for mass separation to occur. At some distance after the focal point, the faster molecules find themselves far away from the slower ones. The result is a wide ion packet. To overcome these limitations, Mamyrin and coworkers developed the reflectron to correct the spread in kinetic energy [41]. A reflectron consists of a series of rings and grids that provide a linear electric field. These rings and grids are employed as electrostatic mirrors to reflect ions back towards the detector [41]. Figure 2.19 illustrates how a reflectron corrects for kinetic energy variation. Ions with more kinetic energy (faster) enter the reflectron sooner and penetrate deeper before they stop and turn around. On the contrary, ions with less kinetic energy (slower) enter the reflectron later and do not penetrate as deep before they turn around, as shown in Figure 2.19. As a result, slower ions spend less time in the detector as they travel a shorter path in the reflectron. In contrast, faster ions spend more time in the detector and therefore leave later [40]. However, by optimizing the voltages on the reflectron, faster will ions will eventually catch up with the slower ones at the detector [41]. Typical mass resolution in our instrument is 500 amu. This number can be increased by a proper optimization of voltages on the ion source and the reflectron.

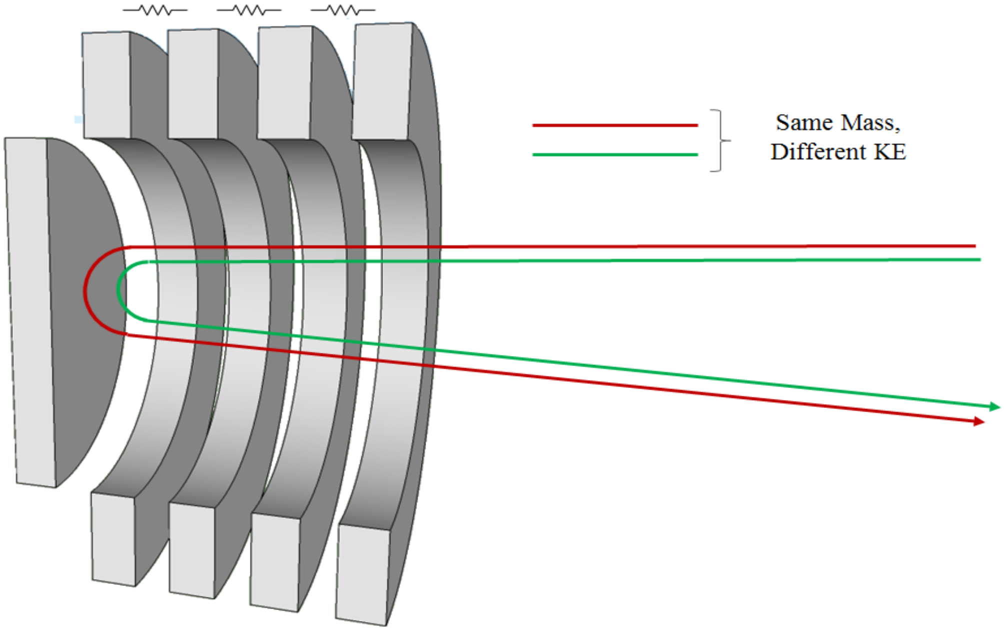

Figure 2.19: A schematic of the reflectron which is used to correct for kinetic energy distribution. The red line represents the faster ion path and the green line represents the slower ion path.

2.1.4.D Detector

Ions are accelerated to a collision with a 2’’ dual microchannel plate (MCP) detector. This detector consists of an array of 10^4-10^7 small electron multipliers oriented parallel to one another. The collision results in one or more electrons to be ejected from the top of the microchannel plate surface. These electrons bounce down a channel in the plate, resulting in more electrons to be ejected at each bounce [40]. The secondary electrons then bounce down the channel and more electrons are created, as shown in Figure 2.20. This process continues all the way through the plates resulting in large gains (10^4-10^7). Next, the electron cascade is collected by an anode that measures the current. The signal is further amplified (10X) by a fast pre-amplifier (custom built at IBM) and then displayed on an oscilloscope (LeCroy, model 9350A, 500 Hz) or a digitizer. Data from the oscilloscope is stored and integrated on a computer using a custom-written LabVIEW program. Two delay generators (Stanford

Research Systems Inc., DG-535 and DG-645 models) are used to time all the events and are set to run the experiment at 10 HZ repetition rate. It is necessary to have proper timing of flashlamp and Q-switch of desorption and ionization lasers, molecular beam pulsed nozzle, picosecond laser sync and pre-trigger when attempting to detect a signal.

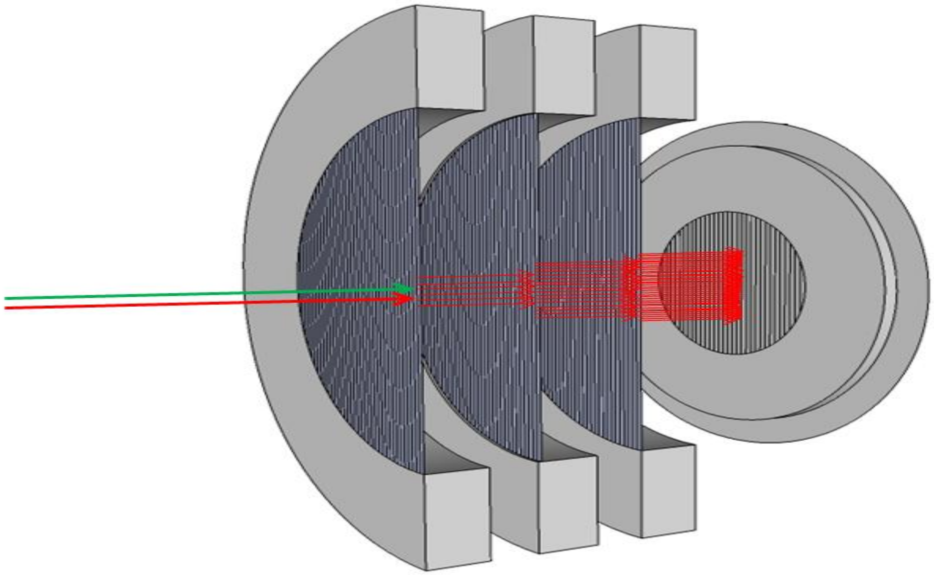

Figure 2.20: Microchannel plate (MCP) detector. An electron cascade is created from an ion impact.

2.2 Second Molecular Beam Instrument

In the de Vries lab, we have been constructing a second molecular beam instrument since 2013, and two years later the instrument was up and running. This was a huge accomplishment because it allowed us to run two different experiments simultaneously.

2.2.1 Instrument and components

Figure 2.21 A and B shows images of the front and the back sides of the second beam instrument, respectively. Although the main beam instrument and the second beam instrument do not share the same, exact components, their functions are nearly identical.

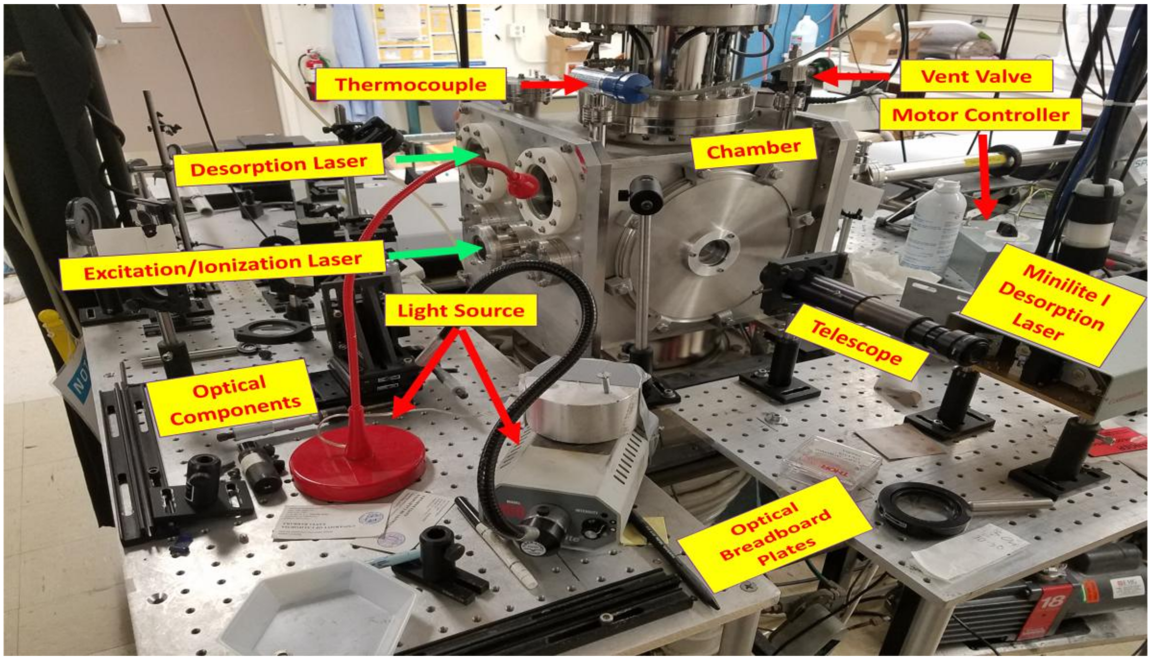

A

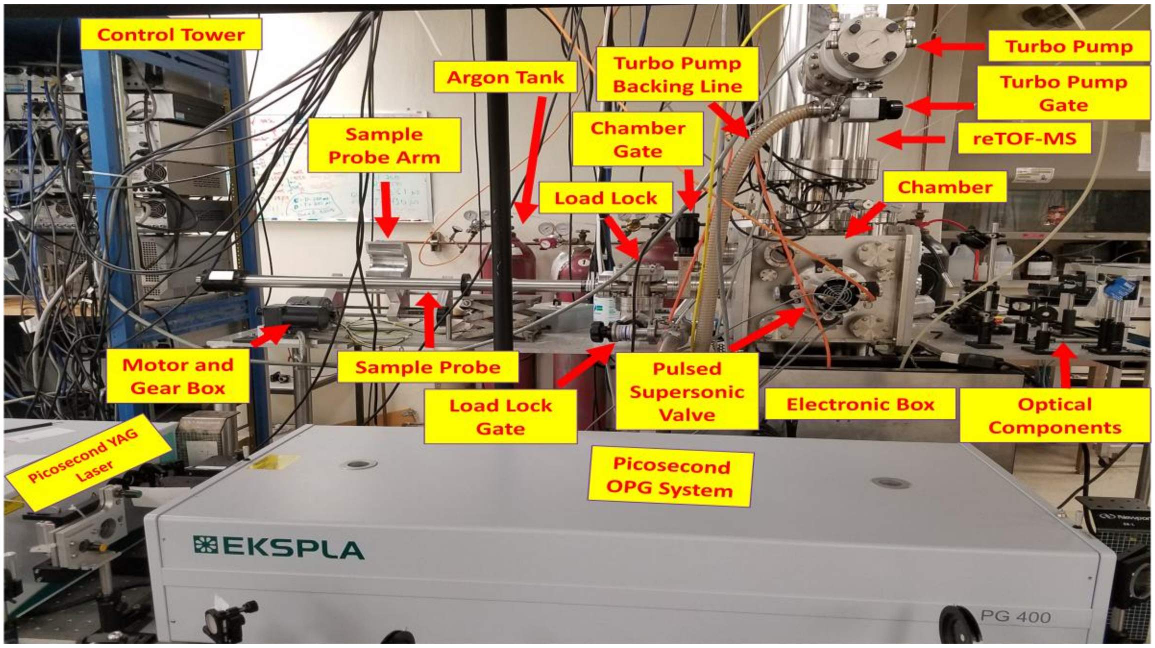

B

Figure 2.21: An image of the second molecular beam instrument, with the main components labeled, showing the front side (A) and the back side (B) of the instrument.

Here are some of the main differences between the two molecular beam instruments:

- The main beam instrument has a liquid nitrogen cooled baffle surrounding the ion source of the TOF in order to reduce noise. However, the second beam instrument does not have this component.
- The main instrument uses a custom built IBM pre-amplifier which smoothes mass dips and inverts them into peaks on the oscilloscope. On the other hand, the second beam instrument uses a commercial pre-amplifier (ORTEC 9306, 1 GHZ), which neither smoothes, nor inverts mass dips.
- The main beam instrument uses a cantilever piezo valve; whereas, the second beam instrument uses a pulsed supersonic valve (PSV) from R.M. Jordan Company. This has proven to be much more sensitive to the sample bar height and the use of carbon black in our sample preparation. Figure 2.21 B shows the outer part of the valve and Figure 2.22 shows the inner part.
- The main beam instrument uses a small diffusion pump (Edwards Diffstak 100, pumping speed: 535 L/s) to maintain the pressure of the analyzer at 2 x 10^{-6} torr, while the second beam instrument uses a turbo pump (Pfeiffer Balzers TPU 240, pumping speed: 240 L/s). The turbo pump can be been seen in Figure 2.21 B.
- Both beam instruments have been using the same type of laser for the desorption process, Nd:YAG laser (Continuum Minilite I) and operate at its fundamental wavelength of 1064 nm. However, the desorption laser for the second beam instrument was recently replaced with a Nd:YAG laser (Quanta-Ray DCR-11) due to multiple issues with the Minilite.
- The sample probe on the main beam instrument is detached once the sample holder is placed onto the sample stage and the height is adjusted using an external knob. On the

contraire, the sample probe on the second beam instrument remains attached onto the sample holder after it is attached onto the sample stage. Therefore, the sample probe is used to adjust the height of the sample bar relative to the valve nozzle. This is done precisely using the graduations on the sample probe. A sample probe arm (built at the University of California Santa Barbara Physics Machine Shop), a motor, and a gearbox (INSCO Corporation) are used to move the sample probe in and out the chamber (Figure 2.21 B).

- The second beam instrument uses a telescope to monitor the position of the sample bar relative to the valve nozzle (Figure 2.21 A). This is done by eye using the main beam instrument. Importantly, the second instrument must have optimum height as the Jordan PSV is much more sensitive to the sample height.
- The distance between the valve nozzle and the tip of the skimmer is 2 cm for the main instrument vs 10 cm for the second instrument, as shown in Figure 2.22. The advantage of this extended distance is discussed in section 2.2.2.

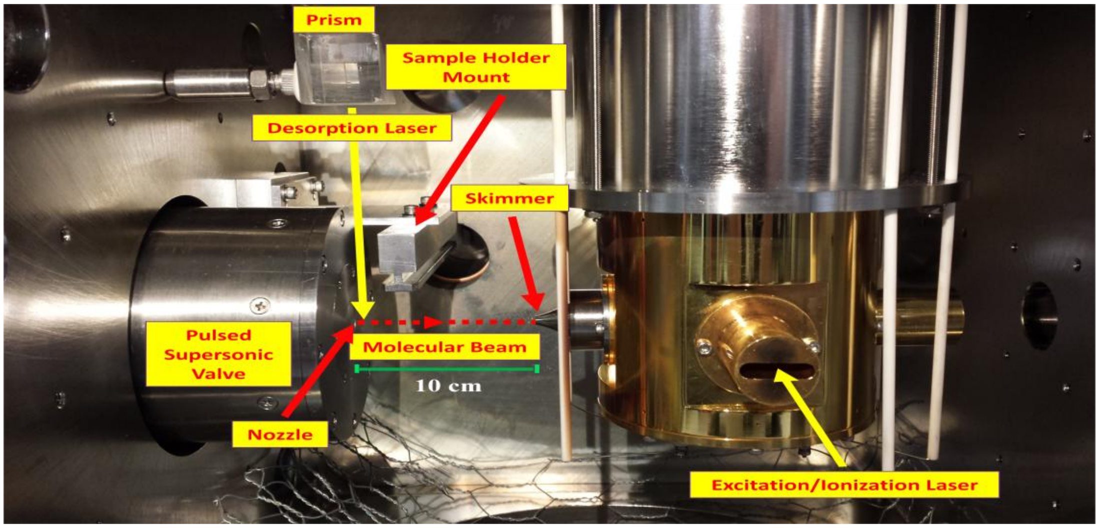

Figure 2.22: An image of the inside of the second molecular beam instrument chamber. The distance between the valve nozzle and the skimmer is 10 cm.

2.2.2 Objectives

In addition to having a backup instrument when one is down, there are a few other purposes for constructing the second beam instrument.

- The second beam instrument forms clusters more easily than the main beam instrument. This result is due to the Jordan pulsed supersonic valve, which provides optimum cooling for cluster formation.
- The second instrument provides more consistent signal because the sample height, relative to the valve nozzle, can be adjusted using a graduated probe. The sample bar height, relative to the valve nozzle, can also be seen using a telescope that we placed across from the nozzle (Figure 2.22 A). We placed all samples at the same height as it makes it easier to compare signal of one sample bar to another, particularly when performing an analytical chemistry project. For example, to determine the relative amount of caffeine to theobromine in pottery Sample #1 to the relative amount of caffeine to theobromine in pottery Sample #2, the same conditions need to be met. Most importantly, the height of the sample bars relative to the valve nozzle which is not trivial to do with the main beam instrument.
- The second beam instrument is suitable in detecting molecules from their dark ground states. Several authors proposed that excited DNA bases follow a curve crossing to a “dark” state which couples with the ground state [42–45]. This rapid internal conversion pathway prevents population of the reactive triplet state and therefore photochemical stability is achieved [42–45]. After internal conversion back to a vibrationally excited S_0 state, intramolecular vibrational relaxation (IVR) occurs, placing molecules in lower but hotter vibrational ground states. Molecules eventually use their internal energies to photo-

fragment; this process is hypothesized to take few microseconds or more to happen. We have proposed multiple experiments where we use the hot ground state fragments to observe molecules with extremely short lifetimes such the biological guanine tautomer. However, this was not possible due to an instrument limitation. In the main beam instrument, molecules are excited before the skimmer (to allow time for the photo-fragmentation process to happen); however, they exit the ionization region before the photo-fragmentation process occurs. As a result, extending the distance between the excitation point and the ionization point would allow enough time for the molecules to photo-fragment before they are ionized from their hot ground states. The second beam instrument resolves this issue with a 10 cm distance between the molecular beam nozzle and the skimmer vs 2 cm for that of the main beam instrument. This allows for the photo-fragmentation process to be completed before the ionization process. Although this experiment is theoretically possible, it has never been attempted with the second beam instrument yet.

2.2.3 Problems and solutions

Constructing an instrument is clearly challenging; however, initiating it and producing signal is equally as challenging. This section addresses the main problems we encountered when trying to produce signal and the steps we used to resolve these issues.

<u>Noise:</u>

Problem: The oscilloscope was displaying a great amount of noise which created challenges in monitoring the mass signal.

Solutions: Originally, we suspected the cause of the noise to be the commercial pre-amplifier. Consequently, we swapped it with the one on the main instrument and unfortunately there was no change. A ground loop appeared to be causing noise which was picked up by the detector and was then enhanced by the pre-amplifier. In an attempt to resolve this issue, we replaced the detector BNC coaxial cable with a triaxial cable (extra insulation layer and a second conducting sheath), shielded that cable and the pre-amplifier with a Faraday cage, and plugged in everything to the same power strip. These attempts proved minor as they were not enough for mass signal to be clearly distinguishable. After a long and careful diagnosis, we discovered that the sample probe drive and motor (Applied Motion Products STM24) was producing radio frequency and causing the noise problem. Therefore, this motor was swapped with a simpler one used by the main instrument and the noise disappeared almost entirely.

Diffuse and moving mass peaks:

Problem: The mass peak was split into multiple peaks and appeared at different places on the oscilloscope, causing the average to fluctuate. Moreover, the mass peak was constantly moving to the right by tens of nanoseconds.

Solutions: Once the instrument was fully constructed, the next step was to get a signal. Running an instrument and optimizing conditions for the first time is not trivial. Therefore, we decided to reduce the number of variables by eliminating the desorption laser and use the argon signal only for optimization. By focusing the 280 nm beam from the dye laser, we were able to detect an argon mass signal. However, the signal was diffuse. Peak appeared at different spots and the average peak was fluctuating and constantly moving to the right. Clearly, multiple problems were happening and they needed to be fixed. We started by adjusting the ion source, reflectron, and detector voltages which would improve the signal for only a few seconds. Next, we replaced the repeller plate (VA1), extraction grid (VA2), and steering plates (VXY) power supply boxes with one Jordan power supply box. This aided in making the signal more stable but the problem was not fully resolved.

Note: The instrument uses a reTOF-MS but the only power supply box available was for a linear TOF-MS (no reflectron) with three detector channels, rather than four. As a result, we had to rearrange channels and ultimately added three external power supply boxes and one home-built detector box. Then, these were replaced with a second Jordan power supply box. When we observed noise which reappeared on the oscilloscope, we decided to turn off the analyzer ion gauge and turn the detector voltage from -3300 to -2100 V. These changes eliminated the noise but lead to an 80% signal depletion.

Using argon for optimization was an obstacle due to plasma formation so we seeded the molecular beam with toluene. In doing so, we detected signal at 37481 cm^{-1} using the picosecond laser. Once we optimized reTOF-MS voltages and events timing, we were able to obtain a narrow 14 nansecond FWHM mass peak on the oscilloscope and then collected a short range R2PI spectrum, as shown in Figure 2.23.The moving mass peak was resolved by grounding the VXY channel and reducing its voltage from 900 to 500 V.

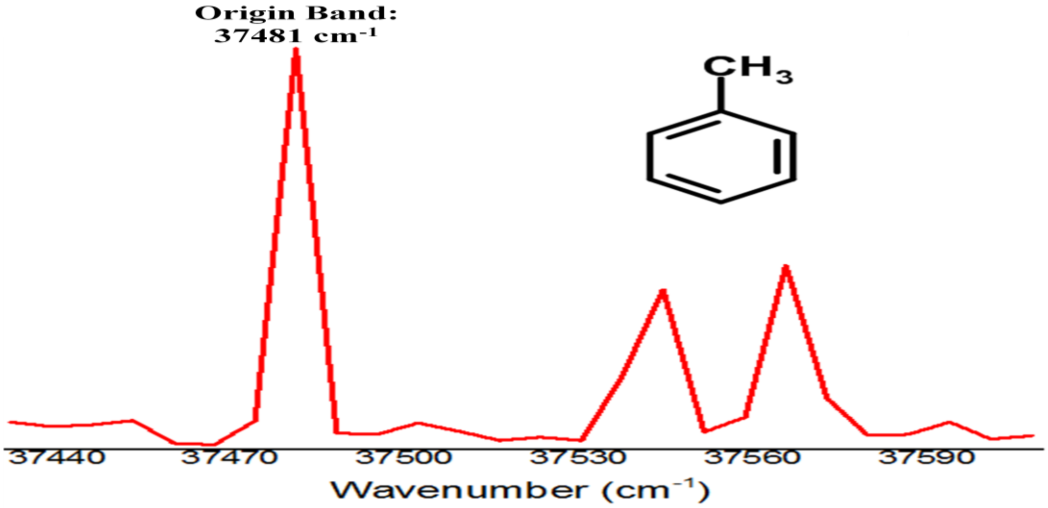

Figure 2.23: One-color R2PI spectrum of toluene using the picosecond laser.

A focused laser beam is required and a poor mass peak profile is produced:

Problem: We only detect signal when the excitation/ionization laser is focused resulting in non-resonance ionization. The Removal of the focusing lens causes the formation of a poor mass peak profile. Moreover, the signal was unstable and inconsistent bar to bar.

Solutions: The next step was including the desorption laser in the optimization process. The molecule we decided to test was theophylline, which is a relatively easy molecule to study when using very low laser power from the picosecond laser. A 16 ns FWHM theophylline mass signal was detected only when the laser beam was focused, which is very peculiar for theophylline. An R2PI scan was also collected but it had poor resolution due to the presence of non-resonance signal. Next, we removed the focusing lens in order to eliminate non-resonance signal; however, once we did so, we lost all signal. Realigning the laser beam through the instrument and readjusting the sample height brought back ~ 20 mV of signal. The signal was broad, square, and consisted of many little peaks. Knowing that the laser energy is sufficient (~100 µJ), we hypothesized that the beam size is what causing the mass peak profile to be broad and featureless. Therefore, we used an iris to cut the beam into a dot. This caused the mass peak to become narrow and the profile was then adjusted by changing the voltages of VA1, VA2, the retarding grid (VR1), the reflector grid (VR2), and VXY. We discovered that the broad and diffuse mass peak is a result of theophylline molecules reaching the detector at different times. As a result, we adjusted the voltage between VA1 and VA2 to be greater and therefore greater spatial distribution in order to resolve the peak profile. VA1 and VA2 were adjusted which required VR1, VR2, and VXY voltages to be corrected. The voltage adjusting process was done by first opening the iris half-way and changing the voltages until the multiple little mass peaks were combined into one narrow 12 nsec FWHM peak, as shown in Figure 2.24. Then, the iris was fully opened and the same procedure was done, resulting in 200 mV of theophylline signal, which is typical at that laser power. VA1 was enhanced from 3600 to 4107 V and the voltage on VA2 was reduced from 3200 to 3053 V. Also, VR1 was enhanced from 2200 to 2478 V, VR2 was reduced from 4200 to 4100 V, and VXY was slightly enhanced from 485 to 525 V. The detector was set to -2100 V in order to avoid detector saturation; this voltage needs to be tuned depending on the molecule being tested. These voltage changes along with molecular beam and desorption firing timings helped improve the peak profile. The voltage difference between A1 and A2 is now over 1000 V vs 700 V before. These approaches resolved signal profile and enhancement.

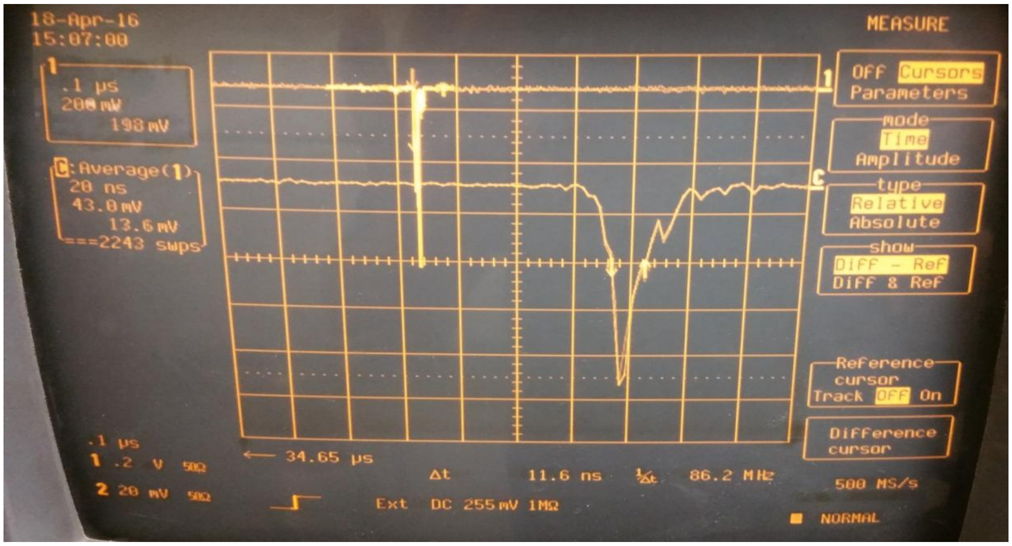

Figure 2.24: Average signal of theophylline (bottom trace, labeled C) and instant signal from channel 1 at 10 Hz (top trace, labeled 1). Two cursors on the average are set to measure the FWHM of the mass peak which is ~ 12nsec wide and the average signal is ~200 mV.

When zooming in onto the mass peak, the signal was not smooth compared to the signal on the main instrument. In consequence, we tested the signal using the custom-built pre-amplifier. The signal was smoother and wider (20 nsec FWHM) but less than 200 mV

(165 mV only). However, the area under the peak was still the same regardless of the pre-amplifier used. As discussed in section 2.2.1, the custom-built pre-amplifier was designed to smooth mass peaks but in return widens them.

Although the peak profile was greatly improved, the signal was still unstable. Moreover, we noticed that we could never completely eliminate off-resonance signal. After an extremely long diagnosis, we determined that the problem was due to a loose optical mount. A prism, placed on the last optical mount in the desorption beam path would slightly move diagonally when we intended to move it back and forth relative to the valve nozzle. As a result, both cold and hot molecules were entrained into the molecular beam, creating an off-resonance and unstable signal.

<u>Signal drop across a sample bar:</u>

Problem: The signal was dropping during scans and the only way to retrieve it was to constantly change molecular beam timing.

Solutions: After collecting scans for easy molecules, we decided to examine guanine, which is a much more difficult molecule to observe. 400 mV of guanine signal was detected on the scope using one-color picosecond laser. Figure 2.25 shows the first ever R2PI spectrum of guanine collected with the second beam instrument. However, we noticed that we continued losing signal during a long scan and the only way to retrieve the signal back was to step the molecular beam timing back by few microseconds. Possible causes of the this problem could have been current instability in the pulse valve, desorption beam movement due to optical board vibrations, bent sample stage, or poorly made sample bars. However, these were later proven not to be the causes of the signal dropping.

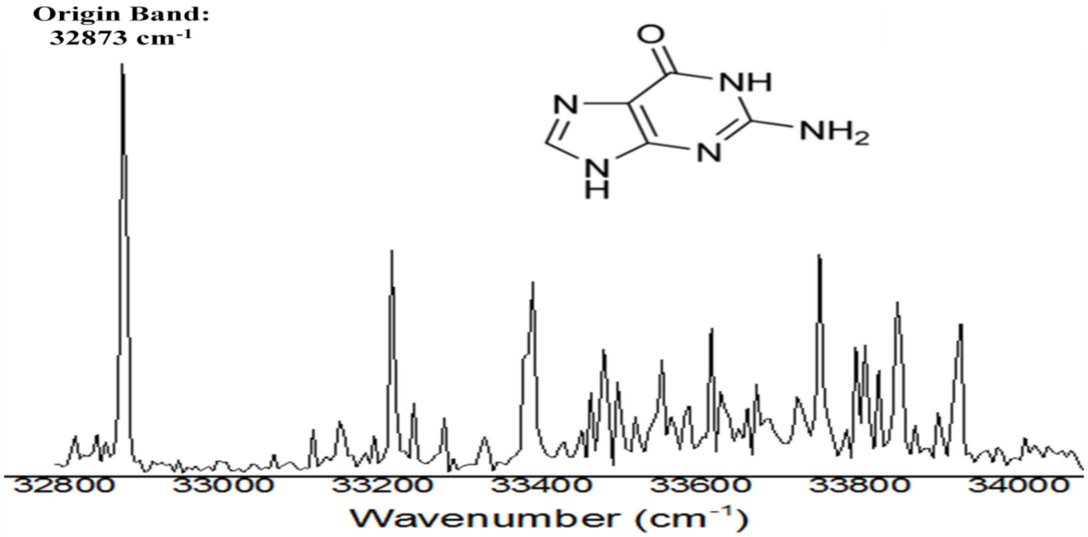

Figure 2.25: One-color R2PI spectrum of 9H-enol guanine using the picosecond laser.

After careful investigation, the cause of the problem was determined to be a bad desorption laser beam profile. The beam was split into two spots and randomly changing shapes, power, and position, requiring us to change molecular beam timing to counteract it. As a result, the desorption laser, Nd:YAG laser (Continuum Minilite I) was replaced with Nd:YAG laser (Quanta-Ray DCR-11). Another cause of the problem could have been the sample bar moving at an inconsistent rate. As a result, we cleaned and lubricated the sample probe arm and claw jig. These two fixes seemed to resolve signal dropping and inconsistency across a sample bar. The instrument is currently being optimized in order to detect clusters.

References

1. Honig, R. E. & Woolston, J. R. Laser-Induced Emission of Electrons, Ions, and Neutral Atoms from Solid Surfaces. *Appl. Phys. Lett.* **2,** 138–139 (1963).

2. Vastola, F. J., Pirone, A. J. & Mumma, R. O. Analysis of Biologically Related Organic Salts by Laser Ionization. *Org. Mass Spectrom.* **1,** 499–500 (1968).

3. Vastola, F. J., Mumma, R. O. & Pirone, A. J. Analysis of organic salts by laser ionization. *Org. Mass Spectrom.* **3,** 101–104 (1970).

4. Beuhler, R. J., Flanigan, E., Greene, L. J. & Friedman, L. Proton transfer mass spectrometry of peptides. Rapid heating technique for underivatized peptides containing arginine. *J. Am. Chem. Soc.* **96,** 3990–3999 (1974).

5. Posthumus, M. A., Kistemaker, P. G., Meuzelaar, H. L. C. & Ten Noever de Brauw, M. C. Laser desorption-mass spectrometry of polar nonvolatile bio-organic molecules. *Anal. Chem.* **50,** 985–991 (1978).

6. Li, L. & Lubman, D. M. Analytical jet spectroscopy of tyrosine and its analogs using a pulsed laser desorption volatilization method. *Appl. Spectrosc.* **42,** 418–424 (1988).

7. Li, L. & Lubman, D. M. Pulsed laser desorption method for volatilizing thermally labile molecules for supersonic jet spectroscopy. *Rev. Sci. Instrum.* **59,** 557–561 (1988).

8. Cable, J. R., Tubergen, M. J. & Levy, D. H. Laser desorption molecular beam spectroscopy: the electronic spectra of tryptophan peptides in the gas phase. *J. Am. Chem. Soc.* **109,** 6198–6199 (1987).

9. Arrowsmith, P., de Vries, M. S., Hunziker, H. E. & Wendt, H. R. Pulsed laser desorption near a jet orifice: concentration profiles of entrained perylene vapor. *Appl. Phys. B* **46,** 165–173 (1988).

10. Meijer, G., De Vries, M. S., Hunziker, H. E. & Wendt, H. R. Laser desorption jet-cooling of organic molecules. *Appl. Phys. B* **51,** 395–403 (1990).

11. Nir, E., Grace, L., Brauer, B. & de Vries, M. S. REMPI Spectroscopy of Jet-Cooled Guanine. *J. Am. Chem. Soc.* **121,** 4896–4897 (1999).

12. Lucchese, R. R. & Tully, J. C. Laser induced thermal desorption from surfaces. *J. Chem. Phys.* **81,** 6313–6319 (1984).

13. Brand, J. L. & George, S. M. Effects of laser pulse characteristics and thermal desorption parameters on laser induced thermal desorption. *Surf. Sci.* **167,** 341–362 (1986).

14. Burgess, D. B., Stair, P. C. & Weitz, E. Calculations of the surface temperature rise and desorption temperature in laser-induced thermal desorption. *J. Vac. Sci. Technol. Vac. Surf. Films* **4,** 1362–1366 (1986).

15. Hall, R. B. Pulsed-laser-induced desorption studies of the kinetics of surface reactions. *J. Phys. Chem.* **91,** 1007–1015 (1987).

16. Zenobi, R., Hahn, J. H. & Zare, R. N. Surface temperature measurement of dielectric materials heated by pulsed laser radiation. *Chem. Phys. Lett.* **150,** 361–365 (1988).

17. Zenobi, R., Hahn, J. H. & Zare, R. N. Reply: Reply to the comment on surface temperature measurement of dielctric materials heated by pulsed laser radiation. *Chem. Phys. Lett.* **186,** 123–124 (1991).

18. Voumard, P., Zenobi, R. & Zhan, Q. Laser-induced thermal desorption of aniline from a quartz surface. *Surf. Sci.* **307–309,** 360–366 (1994).

19. Voumard, P., Zenobi, R. & Zhan, Q. Spectroscopic Probe for Energy Transfer during Laser Desorption from Surfaces. *J. Phys. Chem.* **99,** 11722–11727 (1995).

20. Woodward, J. R., Watanabe, H., Ishiuchi, S.-I. & Fujii, M. A two-color tunable infrared/vacuum ultraviolet spectrometer for high-resolution spectroscopy of molecules in molecular beams. *Rev. Sci. Instrum.* **83,** 14102 (2012).

21. Conzemius, R. J. & Capellen, J. M. A review of the applications to solids of the laser ion source in mass spectrometry. *Int. J. Mass Spectrom. Ion Phys.* **34,** 197–271 (1980).

22. Sherman, M. G., Kingsley, J. R., Hemminger, J. C. & Mclver Jr, R. T. Surface analysis by laser desorption of neutral molecules with detection by fourier-transform mass spectrometry. *Anal. Chim. Acta* **178,** 79–89 (1985).

23. Karas, M. & Bahr, U. Laser desorption mass spectrometry. *TrAC Trends Anal. Chem.* **5,** 90–93 (1986).

24. Mowry, C. D. & Johnston, M. V. Simultaneous detection of ions and neutrals produced by matrix-assisted laser desorption. *Rapid Commun. Mass Spectrom.* **7,** 569–575 (1993).

25. Kantrowitz, A. & Grey, J. A High Intensity Source for the Molecular Beam. Part I. Theoretical. *Rev. Sci. Instrum.* **22,** 328–332 (1951).

26. Kistiakowsky, G. B. & Slichter, W. P. A High Intensity Source for the Molecular Beam. Part II. Experimental. *Rev. Sci. Instrum.* **22,** 333–337 (1951).

27. Levy, D. H. Laser spectroscopy of cold gas-phase molecules. *Annu. Rev. Phys. Chem.* **31,** 197–225 (1980).

28. Pallix, J. B., Schuhle, U., Becker, C. H. & Huestis, D. L. Advantages of single-photon ionization over multiphoton ionization for mass-spectrometric surface analysis of bulk organic polymers. *Anal. Chem.* **61,** 805–811 (1989).

29. Boesl, U., Neusser, H. J. & Schlag, E. W. Multi-photon ionization in the mass spectrometry of polyatomic moleucles: Cross sections. *Chem. Phys.* **55,** 193–204 (1981).

30. Callahan, M. P., Gengeliczki, Z. & de Vries, M. S. Resonant Two-Photon Ionization Mass Spectrometry of Jet-Cooled Phenolic Acids and Polyphenols. *Anal. Chem.* **80,** 2199–2203 (2008).

31. Page, R. H., Shen, Y. R. & Lee, Y. T. Local modes of benzene and benzene dimer, studied by infrared–ultraviolet double resonance in a supersonic beam. *J. Chem. Phys.* **88,** 4621–4636 (1988).

32. Pribble, R. N., Hagemeister, F. C. & Zwier, T. S. Resonant ion-dip infrared spectroscopy of benzene–(methanol) m clusters with m= 1–6. *J. Chem. Phys.* **106,** 2145–2157 (1997).

33. Frost, R. K. *et al.* Fluorescence-dip infrared spectroscopy of the tropolone-H2O complex. *J. Chem. Phys.* **105,** 2605–2617 (1996).

34. Carney, J. R., Hagemeister, F. C. & Zwier, T. S. The hydrogen-bonding topologies of indole–(water)n clusters from resonant ion-dip infrared spectroscopy. *J. Chem. Phys.* **108,** 3379–3382 (1998).

35. Kim, W., Schaeffer, M. W., Lee, S., Chung, J. S. & Felker, P. M. Intermolecular vibrations of naphthalene trimer by ionization-detected stimulated Raman spectroscopy. *J. Chem. Phys.* **110,** 11264–11276 (1999).

36. Janzen, C., Spangenberg, D., Roth, W. & Kleinermanns, K. Structure and vibrations of phenol(H2O)7,8 studied by infrared-ultraviolet and ultraviolet-ultraviolet double-resonance spectroscopy and *ab initio* theory. *J. Chem. Phys.* **110,** 9898–9907 (1999).

37. Carney, J. R. & Zwier, T. S. The Infrared and Ultraviolet Spectra of Individual Conformational Isomers of Biomolecules: Tryptamine. *J. Phys. Chem. A* **104,** 8677–8688 (2000).

38. Wenzel, R. J., Matter, U., Schultheis, L. & Zenobi, R. Analysis of Megadalton Ions Using Cryodetection MALDI Time-of-Flight Mass Spectrometry. *Anal. Chem.* **77,** 4329–4337 (2005).

39. Wiley, W. C. & McLaren, I. H. Time-of-Flight Mass Spectrometer with Improved Resolution. *Rev. Sci. Instrum.* **26,** 1150–1157 (1955).

40. Jordan TOF Products. Inc. *TOP Fundamentals Tutorial*.

41. Mamyrin, B. A., Karataev, V. I., Shmikk, D. V. & Zagulin, V. A. The mass-reflectron, a new nonmagnetic time-of-flight mass spectrometer with high resolution. *J. Exp. Theor. Phys.* **64,** 82–89 (1973).

42. Broo, A. A theoretical investigation of the physical reason for the very different luminescence properties of the two isomers adenine and 2-aminopurine. *J. Phys. Chem. A* **102,** 526–531 (1998).

43. Sobolewski, A. L. & Domcke, W. On the mechanism of rapid non-radiative decay in intramolecularly hydrogen-bonded π systems. *Chem. Phys. Lett.* **300,** 533–539 (1999).

44. Sobolewski, A. L. & Domcke, W. On the mechanism of nonradiative decay of DNA bases: ab initio and TDDFT results for the excited states of 9H-adenine. *Eur. Phys. J. D* **20,** 369–374 (2002).

45. Kang, H., Jung, B. & Kim, S. K. Mechanism for ultrafast internal conversion of adenine. *J. Chem. Phys.* **118,** 6717–6719 (2003).

Chapter 3

Resonance Enhanced Multiphoton Ionization and Quantum Computation to Study the Molecular Structure and Excited State Dynamics of Isolated Thymine and Uracil

3.1 Introduction

Nucleic acid bases are well-known to have ultra-short excited state lifetimes in the gas phase and in solution [1–4]. When absorbing UV radiation, nucleic acid bases eliminate their excitation energies via internal conversion in subpicoseconds. This process protects nucleobases by converting potentially harmful electronic energy to internal energy in the ground state. Internal energy in the form of heat is then dissipated to the environment [5].

This property may have played a selective role in prebiotic chemistry on an early earth, considering that many non-canonical derivatives have long excited state lifetimes and that the intrinsic properties of the nucleobases must have been unchanged since their incorporation in the reproductive machinery. It is thus conceivable that the choice of the genetic alphabet was aided by a photochemical selection that preceded any biological evolution. If that is the case, the photochemical properties of the bases are molecular fossils of prebiotic chemistry. However, for uracil and thymine the electronic relaxation pathway competes with another, incompletely understood, process which causes a very small fraction of excited molecules to populate a ‘‘dark’’ excited state [5].

Computational studies show that the rapid relaxation of photoexcited nucleobases to the ground state proceeds through nonadiabatic transitions via conical intersections on the crossing seam of potential energy surfaces of excited and ground states characterized by strongly ring-puckered structures [6–26]. Several conical intersections were found for naturally occurring nucleobases for which efficiencies depend on the reaction paths from the excited state minima to a particular structure on the crossing seam [5]. A comprehensive study performed by Barbatti *et al*. shows that the purine bases, guanine and adenine, relax with a single-exponential decay along one excited state potential energy surface (PES) leading directly to the intersection with the ground state PES [27].

However, pyrimidines, cytosine, thymine, and uracil exhibit a more complex photophysics from purines. Computational studies explained this complexity with multiple excited states involved in the relaxation process after UV excitation [28–30]. A small portion of the excited state thymine and uracil appears to populate a long-lived "dark state" where they can form covalently-bonded dimers [31]. Photolesions are pyrimidine dimers formed in DNA by photochemical reactions causing the C=C double bonds of pyrimidines to couple and form a four membered ring (Figure 3.1), known as cyclobutane pyrimidine dimer (CPD) [32,33], which can lead to cancers such as melanoma and carcinoma. Experiments concluded that CPD is formed from a vibrationally excited ground state in thymine and a triplet excited state in the adjacent thymine [34,35].

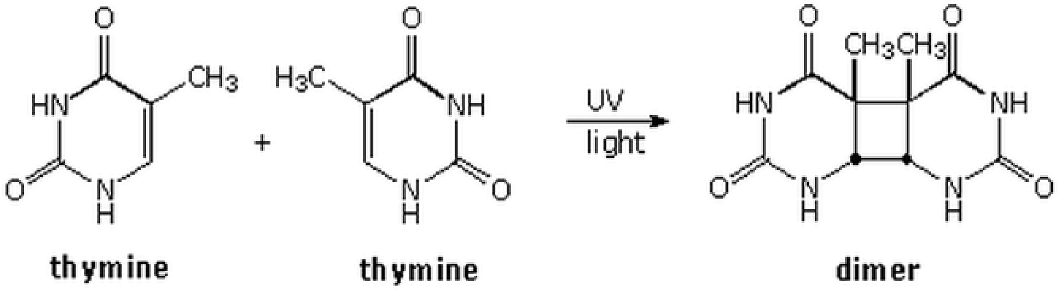

Figure 3.1: Thymine photodimer. C=C double bonds of two isolated thymine molecules couple and form a four membered ring.

Every day, UV light attacks our DNA, causing changes and damages. Although the most dangerous UV light is absorbed by the ozone; UVB still makes its way through and is energetic enough to cause DNA damage. 50-100 reactions can occur during one second of light exposure in each skin cell [33]. The good news is that molecular lesions are repaired immediately by repair enzymes [36]. Two major repair processes are nucleotide excision repair and photoreactivation [33,37–39]. Therefore, understanding the dynamics of pyrimidines is of great importance because the UV damage resistance is not complete and the dark state may act as a precursor to formation of photolesions by dimerization of adjacent pyrimidine bases in DNA.

For thymine which has the longest excited-state lifetime among the nucleobases photodynamics, simulations show that after excitation to the S_2 state of $\pi\pi^*$ character the system relaxes to the minimum of the S_2 state. However, the relaxation is delayed due to the flat character of the PES of this state. The system makes its way to the S_1 state of $n\pi^*$ character via S_2/S_1 intersections where it is trapped an additional delay occurs before internal conversion to the ground state. This entire deactivation mechanism still proceeds on a pico-second timescale [5].

However, many experimental studies have reported an additional sub-nanosecond relaxation pathway to a non-fluorescent (‘‘dark’’) state [1,40,41]. This state was not only observed in bare thymine and uracil, they were also observed for methylated derivatives of thymine and uracil [42,43]. Several candidates for the dark state have been suggested, including the vibrationally ‘‘hot’’ ground state, the S_1 state of $^1(n\pi^*)$ character, and the T_1 state of $^3(\pi\pi^*)$ or $^3(n\pi^*)$ character [28,29,40–44].

As mentioned previously, the excited state dynamics of thymine and uracil exhibit a photo-physics due to the involvement of multiple excited states in the relaxation process. Calculations estimating excitation energies and excited state dynamics show a large geometry change between the S_2 $^1(\pi\pi^*)$ excited state and the ground state as well as multiple internal conversion and intersystem crossings from the initially excited S_2 $^1(\pi\pi^*)$ state which can lead to either a hot ground state, S_1 $^1(n\pi^*)$ state, T_2 $^3(n\pi^*)$ or T_1 $^3(\pi\pi^*)$ states [7–9,12,15]. The complexity is not due to the presence of multiple tautomers as the involvement of different tautomeric forms of thymine was ruled out by Schultz and co-workers on the basis of theoretical calculations [41]. According to the current understanding of the photophysics of thymine, the $^3(\pi\pi^*)$ state is the most likely candidate. Three possible pathways have been suggested to populate this state from the initially excited $^1(\pi\pi^*)$ state: a direct $^1(\pi\pi^*) \rightarrow$ $^3(\pi\pi^*)$ path or one of two indirect pathways: $^1(\pi\pi^*) \rightarrow {}^3(n\pi^*) \rightarrow {}^3(\pi\pi^*)$ or $^1(\pi\pi^*) \rightarrow {}^1(n\pi^*) \rightarrow$ $^3(\pi\pi^*)$ [5,29].

Several authors have interpreted time-resolved pump–probe ionization and vibrational spectra using excited state calculations [7–10,13]. The interpretations are based mainly on characterization of the potential energy surface and the spin–orbit coupling terms [28,29,43]. Etinski *et al.*[28] provided support of the triplet state based on the interpretation of time resolved infrared spectra in acetonitrile solution [44], in particular the peak at 1500 cm^{-1}, resulting from a combination of the C4–C5 stretching and the N1H wagging motions, and the peak near 1350 cm^{-1} due to the ring deformation vibration. These authors reported a 560 ns excited state lifetime, attributed to a triplet state. In solution, excited triplet states are populated in picoseconds after UV excitation where they live for nanoseconds or longer before they decay back to the ground state [44,45].

Here we report on gas phase spectroscopy probing directly that dark excited state in isolated uracil and thymine. The combination of high resolution UV spectroscopy, ground state and excited state double resonance IR-UV spectroscopy, UV-UV pump probe spectroscopy, and ab initio calculations suggest that the dark state is of triplet $^3(\pi\pi^*)$ character. Based on NH vibrational frequencies of the dark state, obtained with double resonant IR-UV spectroscopy of excited state uracil and thymine, we propose an assignment of the long-lived dark state. These frequencies are interpreted using computational studies which include analysis of NH frequencies accounting for the anharmonicity effects [5].

3.2 Methods

3.2.1 Experimental

The instrument and experimental setup have been previously described in detail in chapter two; however, a brief description follows. Samples are placed on a translating graphite substrate directly in front of a pulsed piezo cantilever molecular beam valve [46]. They are laser desorbed by a Nd:YAG laser (1064 nm, ~1 mJ cm^{-1}), then entrained in a supersonic molecular beam of argon (6 atm backing pressure). The cold, neutral molecules are ionized by resonance enhanced multiphoton ionization (REMPI) and are subsequently detected by a reflectron time-of-flight mass spectrometer. For REMPI spectroscopy, the first and resonant photon comes from the frequency doubled output of a tunable dye laser with pulse energy 0.3–0.7 mJ. The second photon comes from an excimer laser (193 nm,1.5–2 mJ per pulse). Using a delay generator, a variable delay between dye laser and excimer laser allows measurement of excited state lifetimes. An additional IR laser is used for IR-UV double resonance spectroscopy in two different pulse sequences, depending on whether the ground state or the dark state is probed, as shown in Figure 3.2. The near-IR output of the OPA/OPA has a pulse energy of 3–5 mJ over the range of 3200–3800 cm^{-1} [5].

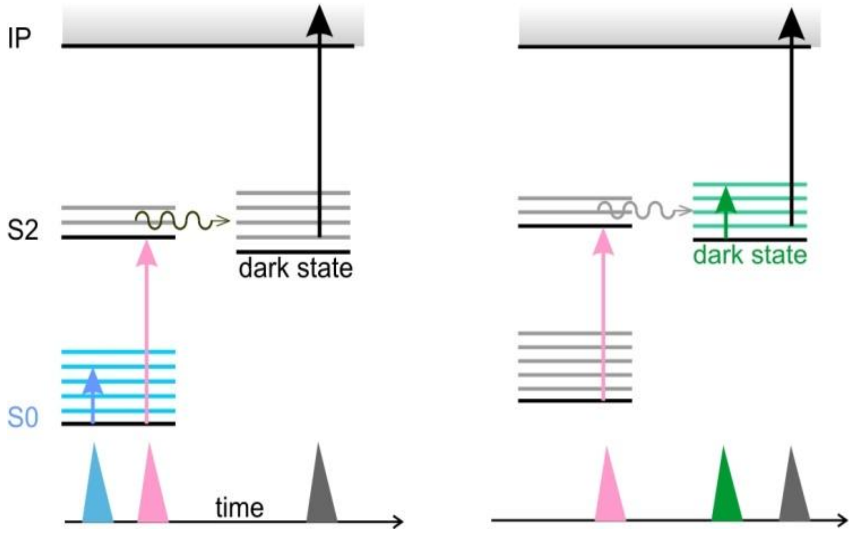

Figure 3.2: Pulse sequence employed to obtain ground state IR (left) and excited state IR (right panel) [5].

3.2.2 Computational

The minimal structure, harmonic and anharmonic frequencies of the ground and excited states were calculated at the Moller-Plesset perturbation theory (MP2) [47] level and with the second-order algebraic diagrammatic construction (ADC(2) method [48,49], with the resolution of identity [50], respectively. The cc-pVTZ basis set [51] was used throughout the calculations. Anharmonic frequency calculations at the second-order perturbation theory (PT2) level were carried out for the ground electronic state using Gaussian09 [52]. One-dimensional NH stretching frequencies (1D-scan) were obtained by solving equation 1 using the Numerov-Cooley integration technique [53].

$$\left\{-\frac{\hbar^2}{2\mu}\frac{\mathrm{d}^2}{\mathrm{d}{r_{NH}}^2}+V(r_{NH})\right\}\chi_n(r_{NH})=E_n\chi_n(r_{NH}) \qquad \text{eqn 1}$$

where

$$\frac{1}{\mu} = \frac{1}{m_N} + \frac{1}{m_H}$$

and $V(r_{NH})$ is a potential energy surface scan over the N-H bond coordinate. Assuming small coupling of the NH stretching motion with other vibrational degrees of freedom, the 1D-scan results should be comparable to one-dimensional anharmonic frequencies evaluated from diagonal anharmonic constants (denoted as 1D-PT2) [5].

3.3 Results

3.3.1 Resonance two-photon ionization spectra

The UV spectrum for both thymine and uracil were first collected over 20 years ago by Brady *et a l* [54]. We have now obtained higher resolution two-photon spectra of thymine and uracil, showing the same onset as reported before, but now also showing some structures as shown in Figure 3.3 [5]. With higher resolution spectra, we are able to analyze and identify vibronic and tautomeric contributions. Although the high resolution R2PI spectra for both thymine and uracil appear to have vibronic transitions from the lowest lying vibrational modes, Franck-Condon calculations via TD-DFT failed to predict any vibronic contributions between S_0 and S_2 which is most likely due to the strong geometry shift between the minimum energy structures [55].

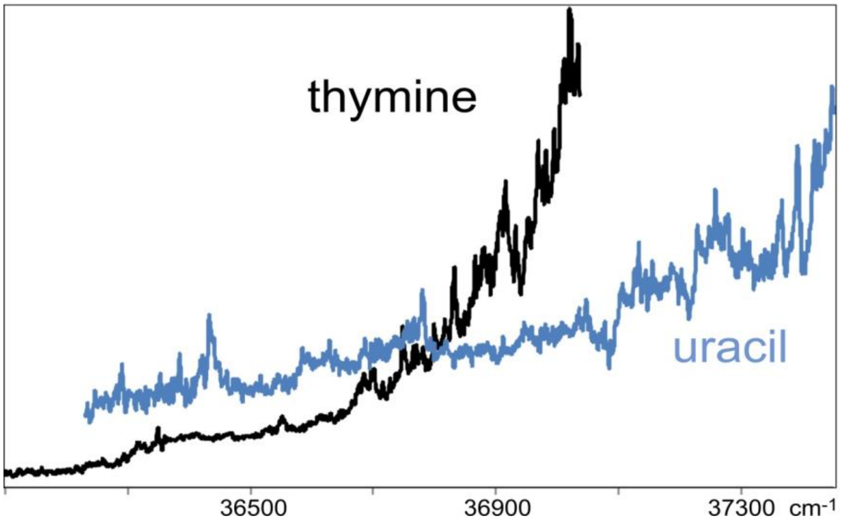

Figure 3.3: Two-color R2PI spectra of thymine and uracil. The second photon is at 193 nm in both cases [5]. The spectrum of thymine shows clear peaks well above the signal to noise level; whereas, uracil peaks are less pronounced due to lower ion signal [55].

The gradual onset and the absence of a dominant origin peak may indicate a large geometry shift between the ground state and the excited state. With an ionization potential of 9.20 eV for thymine and 9.60 eV for uracil, one-color R2PI is not sufficient enough for ionization; these values are more than twice the S_0-S_2 excitation energy. As a result, two-color R2PI, with the second color at 193 nm is used to collect the spectra (Figure 3.3). Even after delaying the second color by up to several nanoseconds, ions can still be observed. We interpret this as ionization out of one or more long-lived dark states, which we shall denote S^*. In other words, the ions we detect result from molecules that have arrived in S^* on nanosecond timescale. Since we are doing action spectroscopy, their structures do not necessarily reflect only the absorption characteristics. Spectral features can be due to absorption resonances but they can also result from potential energy surface dependence of the transitions from the excited state to the dark state(s) [5]. We will consider possible scenarios for this effect in the discussion section.

3.3.2 Ground state and excited state IR spectra

We have obtained the first gas phase IR spectra for thymine (Figure 3.4) and uracil (Figure 3.5), both for the ground state (lower trace) and for the dark state (upper trace) [5]. The pulse sequences employed to obtain these spectra appear in Figure 3.2.

For the ground state, an initial IR pulse is scanned in the NH and OH stretch frequency region and followed by two-step ionization probing. When the IR pulse is resonant with a vibrational frequency this modifies the ground state vibrational population producing a modified Franck–Condon landscape. Usually this modification reduces the ion probe signal, but in this case it increases the ion probe signal. This result suggests a strong geometry change between S_0 and S_2, consistent with the gradual onset of the UV absorption. To obtain a zero background gain spectrum the first UV pulse of the two-step ionization probing was set to 35 714 cm^{-1} where no ionization occurs without IR excitation [5].

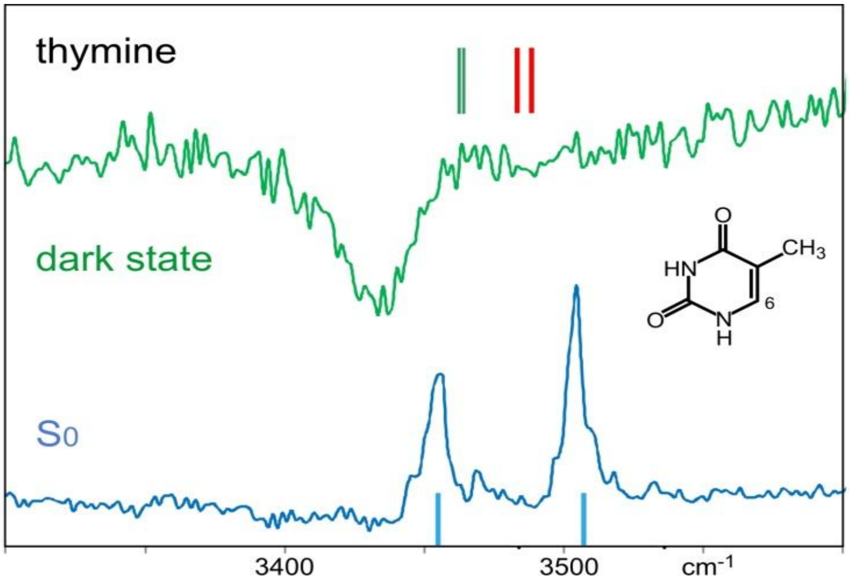

Figure 3.4: IR-UV double resonant spectra of the ground state (blue) and dark excited state of thymine (green). Computed frequencies of the NH stretches are indicated as stick spectra. The frequencies of S_0 state (blue) are obtained with fully-dimensional anharmonic calculations. The S_1 (red) and T_1 (green) frequencies are estimated from the 1D-scan with the assumption of the same corrections for full anharmonicity as for the S_0 state [5]. Scaling factor for all frequencies is 0.991676. [55]

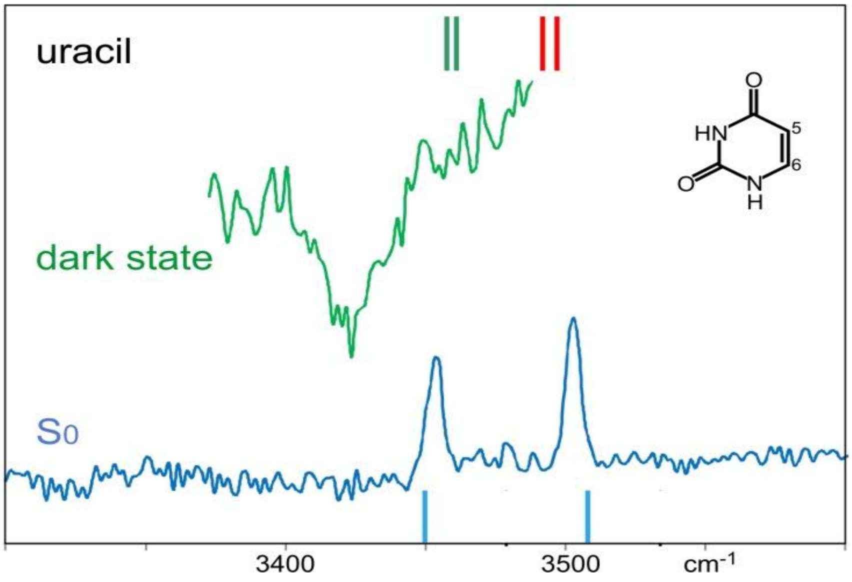

Figure 3.5: Same data as in Figure 3.4 for uracil [5].

For the dark state, the pulse sequence starts with excitation to S_2 (purple pulse, Figure 3.2) followed by rapid relaxation to the dark state. After 20 ns the IR laser is fired (green pulse) followed after another 30 ns by the ionization pulse from the excimer laser (black pulse), serving as the probe. In this sequence the IR laser modifies the dark state vibrational population, producing the green ion-dip spectra [5].

3.3.3 Wavelength-dependent lifetimes

We have obtained lifetimes for the dark state by nanosecond pump-probe measurements. We achieve this by varying the delay between the excitation laser pulse and the ionization laser pulse (purple and black in Figure 3.2). We can fit the decay curves with a single exponential decay plus, in the case of thymine a very long time component. Lifetimes of thymine and uracil at multiple excitation wavenumbers derived from the single exponential decay fits are displayed in Figures 3.6 and 3.7, respectively. Pump-probe spectra for thymine and uracil at multiple excitation wavenumbers are given in appendix 2 (A2.2.1 for thymine and A2.2.2 for uracil).

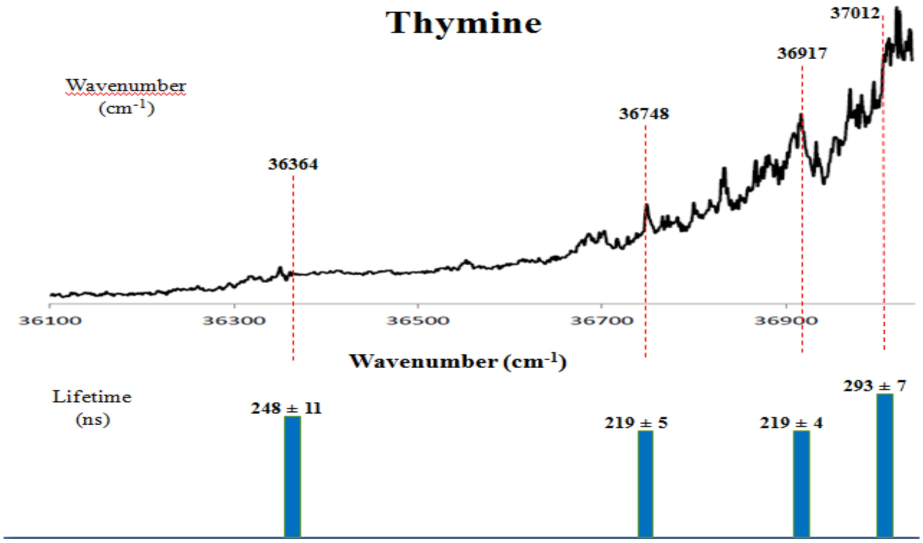

Figure 3.6: Two-color R2PI spectra of thymine (top trace). The red dotted lines show the locations where pump-probe measurements were performed. Lifetime values are given below their probe locations (bottom trace). The column heights resemble the lifetimes relative to each other.

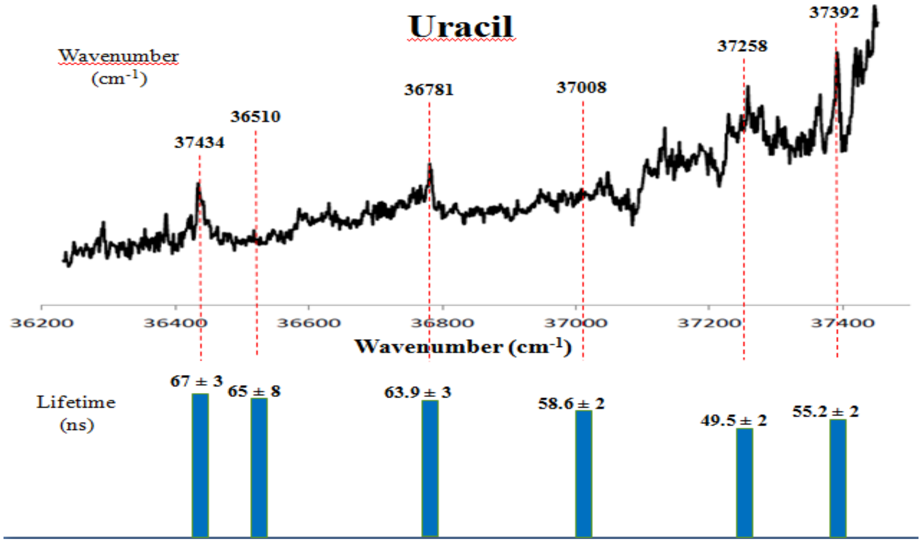

Figure 3.7: Two-color R2PI spectra of uracil (top trace). The red dotted lines show the locations where pump-probe measurements were performed. Lifetime values are given below their probe locations (bottom trace). The column heights resemble the lifetimes relative to each other.

For uracil the lifetime varies from 49 to 64 ns, depending on wavelength. For thymine the lifetime is longer and depends more strongly on excitation wavelength, from 220 ns to 293 ns. For thymine we also observe a very long timescale component. We cannot exclude that this component is due to a long lived excited state, but we interpret it as more likely due to ionization out of the hot ground state, resulting from the rapid internal conversion out of the ππ* state. This would leave the ground state with about 4.5 eV of internal excitation and a very broad Franck–Condon landscape for photo-ionization. Following the pump pulse, the excited molecules move through the probe laser beam spot of about 3 mm in approximately 6 ms. The long lived signal component decreases on that time scale and this indicates a lifetime longer than our experimental window. This time scale is consistent with a hot ground state with a statistical dissociation rate far exceeding that 6 ms window. Within the signal to noise the signal appears to depend linearly on 193 nm power, indicating a single photon process [5].

3.4 Discussion

3.4.1 Broad excitation UV spectra

The spectra collected by Brady *et al.* are similar to the ones collected here with both being broad with some detectable features. They explained the broad and diffuse spectrum of thymine and uracil to the mixing of electronic states or to the large geometry change upon electronic excitation [54]. Since then, several theoretical calculations have studies these two properties in more detail [56–59]. In this experiment, we have collected further data that supports the previous findings.

3.4.2 Ground state

The calculated NH stretching frequencies in the ground state and excited state of thymine and uracil appear in Tables A2.1 and A2.2 (Appendix 2, A2.1), respectively. We evaluated the anharmonic effects for the NH stretching mode for the ground state, both by employing one-dimensional scans of the NH bond length (1D-scan) and from the diagonal anharmonic constants corresponding to NH stretching modes (1D-PT2) [5].

For both systems, the former method gives slightly smaller corrections compared to the 1D-PT2 calculations. The differences are, however, small and justify the reliability of 1D-scan calculations. Both methods yield a blue-shift of about 30 cm^{-1} with respect to the experimentally observed frequencies which are recovered in fully-dimensional anharmonic PT2 calculations. Comparison of the results of PT2 with both 1D-PT2 and 1D-scan indicate a relatively small coupling between NH stretching modes and other degrees of freedom [5]. In addition, these calculations which accounted for full-dimensional anharmonicity provided frequencies in a very good agreement with the experiment, confirming that this is the diketo tautomer as seen in previous experiments [60–65]. The frequencies appear as blue stick spectra in Figures 3.4 and 3.5.

3.4.3 Dark state

To interpret the dark state IR spectra, we performed calculations for both the S_1 and T_1 states. The resulting NH vibrational frequencies for S_1 are nearly degenerate with a splitting of 5 cm^{-1} for both species. The S_1 frequencies obtained with 1D-scan corrections show blue shifts of 29/34 cm^{-1} and 35/40 cm^{-1} with respect to the lower-energy frequency of the ground states of thymine and uracil, respectively, shown in red in Figures 3.4 and 3.5.

Factors such as the structure difference between the ground and the excited state, the amount of internal energy, the anharmonicity constant, and the number/type of modes in the molecule determine the overall shift [66]. Because of the structural similarities at the S_1 and S_0 minima, the effects of anharmonicity may be expected to be similar and, thus, the full-dimensional anharmonic calculations are expected to give very similar effects for S_1 and S_0. Based on these assumptions, the frequencies corresponding to the S_1 state are predicted to fall in the range of 3480–3490 cm^{-1}, i.e. blue-shifted from the lower NH stretching band by about 30–40 cm^{-1} [5].

As in the case of the S_1 minima, the calculations performed for the T_1 minima predict only small splittings of the NH frequencies of 1 and 3 cm^{-1} for thymine and uracil, respectively. The calculated shifts with respect to the lower-energy NH frequencies of the ground states are significantly smaller for the T_1 state, at 8 and 9 cm^{-1} and 2 and 5 cm^{-1} for thymine and uracil, respectively (in green in Figures 3.4 and 3.5). In addition to the global minimum structures of the triplet states, we also investigated the local excited state minima characterized by planar structures. The corresponding NH frequencies are shifted to higher energies with respect to the lower-energy NH vibrations of the ground states by 23 and 26 cm^{-1} for thymine and 30 cm^{-1} for uracil, respectively. These structures are energetically separated from their corresponding global minima by 3.65 and 2.69 kcal mol^{-1} in the case of thymine and uracil, respectively [5].

The prediction of the position of the NH stretching band of the S_1 state, made with the assumption of similar effects of anharmonicity as calculated for the S_0 state, indicate that the observed spectra of both species correspond more likely to the T_1 rather than S_1 states [5].

We also need to consider the possibility of phototautomerization to an enol excited state, which would exhibit a single N–H mode. However, in that case there would be an O–H stretch in the 3600–3700 cm^{-1} range, which we do not observe [5].

3.4.4 Excited state dynamics

We postulate that the wavelength dependence of the dark state lifetime reflects the de-excitation dynamics because the S* internal energy depends on the initial excitation to S_2. This model is further supported by the observation that preceding the UV excitation with an IR excitation modifies the measured dark state lifetime. Figure 3.8 illustrates this observation. Pump–probe data at 37 012 cm^{-1} pump and 193 nm probe wavelengths yields a 293 ns lifetime. Preceding the sequence with an IR pulse at 3504.7 cm^{-1} shortens the lifetime to 164 ns. Both traces, in addition to single exponential decay, have a second lifetime component as well of at least 6 microseconds, which we attribute to ionization out of the hot ground state, following direct internal conversion from S_2 [5]. Repeating the experiment at 36 364 cm^{-1} pump and 193 nm probe results in a similar observation (Figure 3.9). Preceding the sequence with an IR pulse at 3504.7 cm^{-1} shortens the lifetime from 248 ns to 164 ns.

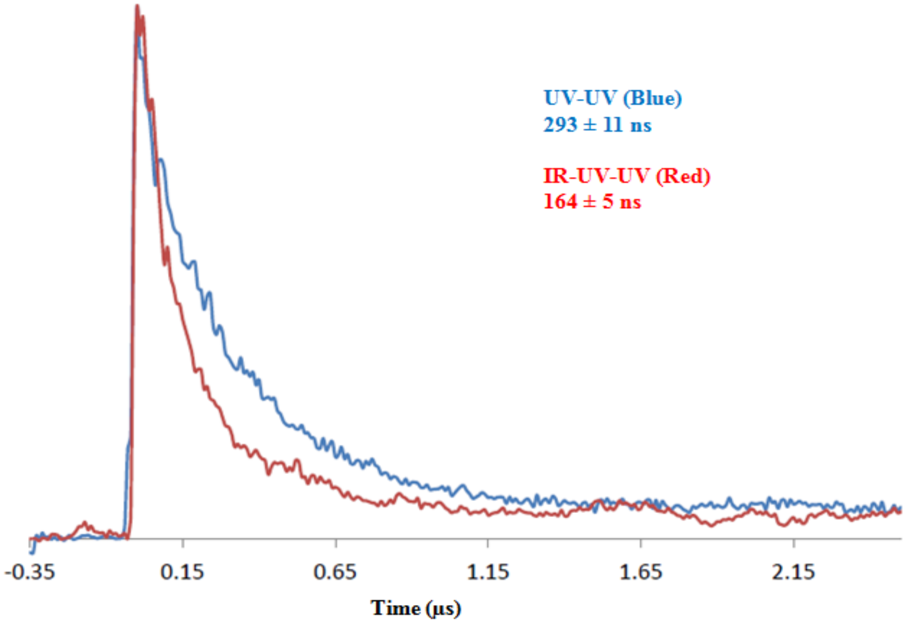

Figure 3.8: Pump-probe spectra for thymine with (red) and without (blue) preceding IR excitation. UV pump wavelength is 37 012 cm^{-1}, UV probe wavelength is 193 nm. IR excitation at 3504.7 cm^{-1} 5.

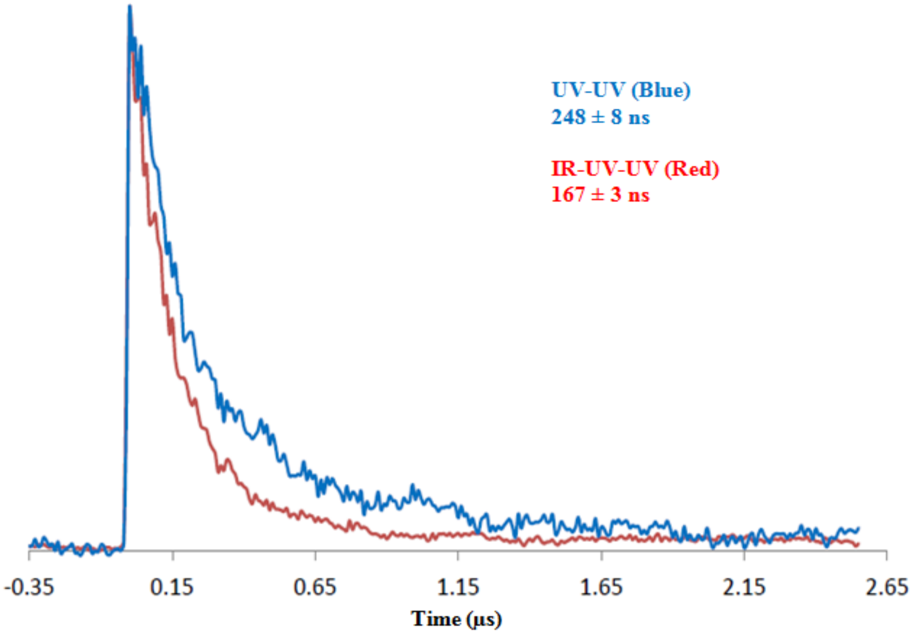

Figure 3.9: Pump-probe spectra for thymine with (red) and without (blue) preceding IR excitation. UV pump wavelength is 36 364 cm^{-1}, UV probe wavelength is 193 nm. IR excitation at 3504.7 cm^{-1} 5.

Because of the jet-cooling in the molecular beam the molecules all start out in v = 0 in the ground state. The IR pulse excites to an NH stretching mode, followed immediately by internal vibrational redistribution to lower frequency modes. In other words, the IR pulse alters the ground state vibrational distribution, resulting in a different S_2 excited state distribution. These data thus suggest that the ensuing excited state dynamics is sensitive to this excited state distribution and affects the population of the dark state. The dark state signal is both increased and shows a shorter lifetime. Although we can fit this decay with a single exponential, it is of course possible that multiple decay paths contribute [5].

In agreement with previously reported studies on thymine and uracil, the minima of the S_1 states of both species are of $n \rightarrow \pi^*$ character with almost planar structure, similar to the ground state minima. The minima of S_2 are characterized by a distortion from planarity with pyramidalization at the C6 atom [6,11,20,56,57].The triplet state minima are of π-π^* character and they are also characterized by pyramidalization of the pyrimidine ring at the C6 atom. Therefore, contrary to the S_1 state, more complex behavior is expected for the T_1 state where the distorted global minimum structures are separated by small barriers from the planar structures. One possible consequence could be dependence of the S_2–S^* coupling on vibrational modes, with enhancement of the interaction in the case of out-of plane vibrational modes that correspond to pyramidalized structures [5].

These barriers could also be responsible for the discrepancy between the experimentally observed and calculated spectral shifts between the S_0 and T_1 states. In particular, the assumption of the same corrections for fully-dimensional anharmonicity as used for S_0 and S_1 states predicts blue shifts of about 9 and 5 cm^{-1} for thymine and uracil, respectively, while we observe small red-shifts of about 10 (thymine) and 20 (uracil) cm^{-1}

experimentally. Due to the complexity of the vibrational dynamics in T_1 states, the low energy vibrations are expected to further influence the coupling with NH stretching modes [5].

3.5 Summary

The ground state and excited state spectra of isolated thymine and uracil confirm the presence of only one species in the molecular beam which is the biologically relevant diketo tautomer. The broad onset in the UV and the ion gain in double resonance spectroscopy suggest that thymine and uracil have a large geometry shift between their ground and excited states. These data confirm the large structural changes predicted by theoretical calculations. Lifetimes of the dark state at different excitation energies in combinations with ab initio calculations suggest that the dark state is if triplet $^3(\pi\pi^*)$ character. Preceding the UV-UV pump probe with an IR pulse seems to shorten the dark state lifetime of thymine; whereas, it increases the dark state signal because the IR pulse alters the ground state vibrational distribution, resulting in a different S_2 excited state distribution which in turn affects the population of the dark state. Figure 3.10 shows a schematic Jablonski diagram, summarizing our current understanding of the excited state dynamics.

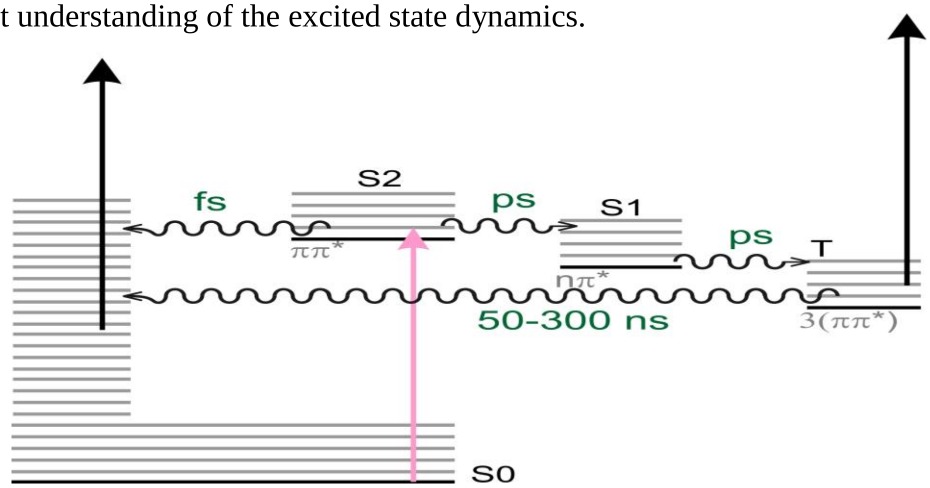

Figure 3.10: Schematic Jablonski diagram of the processes following UV excitation in thymine and uracil [5].

References

1. Kang, H., Lee, K. T., Jung, B., Ko, Y. J. & Kim, S. K. Intrinsic Lifetimes of the Excited State of DNA and RNA Bases. *J. Am. Chem. Soc.* **124,** 12958–12959 (2002).

2. Ullrich, S., Schultz, T., Zgierski, M. Z. & Stolow, A. Electronic relaxation dynamics in DNA and RNA bases studied by time-resolved photoelectron spectroscopy. *Phys. Chem. Chem. Phys.* **6,** 2796 (2004).

3. Canuel, C. *et al.* Excited states dynamics of DNA and RNA bases: Characterization of a stepwise deactivation pathway in the gas phase. *J. Chem. Phys.* **122,** 74316 (2005).

4. Hare, P. M., Crespo-Hernández, C. E. & Kohler, B. Internal conversion to the electronic ground state occurs via two distinct pathways for pyrimidine bases in aqueous solution. *Proc. Natl. Acad. Sci.* **104,** 435–440 (2007).

5. Ligare, M., Siouri, F., Bludsky, O., Nachtigallová, D. & de Vries, M. S. Characterizing the dark state in thymine and uracil by double resonant spectroscopy and quantum computation. *Phys Chem Chem Phys* **17,** 24336–24341 (2015).

6. Hudock, H. R. *et al.* Ab Initio Molecular Dynamics and Time-Resolved Photoelectron Spectroscopy of Electronically Excited Uracil and Thymine. *J. Phys. Chem. A* **111,** 8500–8505 (2007).

7. Chen, H. & Li, S. *Ab initio* study on deactivation pathways of excited 9H-guanine. *J. Chem. Phys.* **124,** 154315 (2006).

8. Perun, S., Sobolewski, A. L. & Domcke, W. Conical Intersections in Thymine. *J. Phys. Chem. A* **110,** 13238–13244 (2006).

9. Perun, S., Sobolewski, A. L. & Domcke, W. Ab Initio Studies on the Radiationless Decay Mechanisms of the Lowest Excited Singlet States of 9H-Adenine. *J. Am. Chem. Soc.* **127,** 6257–6265 (2005).

10. Serrano-Andres, L., Merchan, M. & Borin, A. C. Adenine and 2-aminopurine: paradigms of modern theoretical photochemistry. *Proc. Natl. Acad. Sci.* **103,** 8691–8696 (2006).

11. Matsika, S. Radiationless Decay of Excited States of Uracil through Conical Intersections. *J. Phys. Chem. A* **108,** 7584–7590 (2004).

12. Ismail, N., Blancafort, L., Olivucci, M., Kohler, B. & Robb, M. A. Ultrafast Decay of Electronically Excited Singlet Cytosine via a π,π^* to n_{O},π^* State Switch. *J. Am. Chem. Soc.* **124,** 6818–6819 (2002).

13. Sobolewski, A. L. & Domcke, W. On the mechanism of nonradiative decay of DNA bases: ab initio and TDDFT results for the excited states of 9H-adenine. *Eur. Phys. J. D* **20,** 369–374 (2002).

14. Epifanovsky, E. *et al.* On the Electronically Excited States of Uracil. *J. Phys. Chem. A* **112,** 9983–9992 (2008).

15. Serrano-Andrés, L., Merchán, M. & Borin, A. C. A Three-State Model for the Photophysics of Guanine. *J. Am. Chem. Soc.* **130,** 2473–2484 (2008).

16. Perun, S., Sobolewski, A. L. & Domcke, W. Photostability of 9H-adenine: mechanisms of the radiationless deactivation of the lowest excited singlet states. *Chem. Phys.* **313,** 107–112 (2005).

17. Barbatti, M. & Lischka, H. Nonadiabatic Deactivation of 9 *H* -Adenine: A Comprehensive Picture Based on Mixed Quantum−Classical Dynamics. *J. Am. Chem. Soc.* **130,** 6831–6839 (2008).

18. Fabiano*, E. & Thiel, W. Nonradiative Deexcitation Dynamics of 9H-Adenine: An OM2 Surface Hopping Study. *J. Phys. Chem. A* **112,** 6859–6863 (2008).

19. Marian, C. M. The Guanine Tautomer Puzzle: Quantum Chemical Investigation of Ground and Excited States. *J. Phys. Chem. A* **111,** 1545–1553 (2007).

20. Lan, Z., Fabiano, E. & Thiel, W. Photoinduced Nonadiabatic Dynamics of 9 *H* -Guanine. *ChemPhysChem* **10,** 1225–1229 (2009).

21. Barbatti, M., Szymczak, J. J., Aquino, A. J. A., Nachtigallová, D. & Lischka, H. The decay mechanism of photoexcited guanine − A nonadiabatic dynamics study. *J. Chem. Phys.* **134,** 14304 (2011).

22. Barbatti, M., Aquino, A. J. A., Szymczak, J. J., Nachtigallová, D. & Lischka, H. Photodynamical simulations of cytosine: characterization of the ultrafast bi-exponential UV deactivation. *Phys. Chem. Chem. Phys.* **13,** 6145 (2011).

23. Kistler, K. A. & Matsika, S. Three-state conical intersections in cytosine and pyrimidinone bases. *J. Chem. Phys.* **128,** 215102 (2008).

24. Blancafort, L. & Robb, M. A. Key Role of a Threefold State Crossing in the Ultrafast Decay of Electronically Excited Cytosine. *J. Phys. Chem. A* **108,** 10609–10614 (2004).

25. Sobolewski, A. L. & Domcke, W. Ab initio studies on the photophysics of the guanine–cytosine base pair. *Phys Chem Chem Phys* **6,** 2763–2771 (2004).

26. Zgierski, M. Z., Patchkovskii, S., Fujiwara, T. & Lim, E. C. On the Origin of the Ultrafast Internal Conversion of Electronically Excited Pyrimidine Bases. *J. Phys. Chem. A* **109,** 9384–9387 (2005).

27. Barbatti, M. *et al.* Relaxation mechanisms of UV-photoexcited DNA and RNA nucleobases. *Proc. Natl. Acad. Sci. U. S. A.* **107,** 21453–21458 (2010).

28. Etinski, M., Fleig, T. & Marian, C. M. Intersystem Crossing and Characterization of Dark States in the Pyrimidine Nucleobases Uracil, Thymine, and 1-Methylthymine †. *J. Phys. Chem. A* **113,** 11809–11816 (2009).

29. Serrano-Pérez, J. J., González-Luque, R., Merchán, M. & Serrano-Andrés, L. On the Intrinsic Population of the Lowest Triplet State of Thymine. *J. Phys. Chem. B* **111,** 11880–11883 (2007).

30. Climent, T., González-Luque, R., Merchán, M. & Serrano-Andrés, L. On the intrinsic population of the lowest triplet state of uracil. *Chem. Phys. Lett.* **441,** 327–331 (2007).

31. Lamola, A. A. Excited state precursors of thymine photodimers. *Photochem. Photobiol.* **7,** 619–632 (1968).

32. Setlow, R. B. Cyclobutane-Type Pyrimidine Dimers in Polynucleotides. *Am. Assoc. Adv. Sci.* **153,** 379–386 (1966).

33. Goodsell, D. S. The molecular perspective: ultraviolet light and pyrimidine dimers. *The Oncologist* **6,** 298–299 (2001).

34. Lamola, A. A. & Mittal, J. P. Solution Photochemistry of Thymine and Uracil. *Am. Assoc. Adv. Sci.* **154,** 1560–1561 (1966).

35. Lamola, A. A. & Yamane, T. Sensitized Photodimerization of Thymine in DNA. *Proc. Natl. Acad. Sci. U. S. A.* **58,** 443–446 (1967).

36. Kemmink, J. *et al.* Conformational changes in the oligonucleotide duples d (GCGTTGCG). d (CGCAACGC) induced by formation of a cis-syn thymine dimer. *Eur. J. Biochem.* **162,** 37–43 (1987).

37. Whitmore, S. E., Potten, C. S., Chadwick, C. A., Strickland, P. T. & Morison, W. L. Effect of photoreactivating light on UV radiation-induced alterations in human skin. *Photodermatol. Photoimmunol. Photomed.* **17,** 213–217 (2001).

38. Essen, L. O. & Klar, T. Light-driven DNA repair by photolyases. *Cell. Mol. Life Sci.* **63,** 1266–1277 (2006).

39. Friedberg, E. C. DNA damage and repair. *Nature* **421,** 436–440 (2003).

40. He, Y., Wu, C. & Kong, W. Decay Pathways of Thymine and Methyl-Substituted Uracil and Thymine in the Gas Phase. *J. Phys. Chem. A* **107,** 5145–5148 (2003).

41. González-Vázquez, J., González, L., Samoylova, E. & Schultz, T. Thymine relaxation after UV irradiation: the role of tautomerization and πσ* states. *Phys. Chem. Chem. Phys.* **11,** 3927 (2009).

42. Kunitski, M., Nosenko, Y. & Brutschy, B. On the Nature of the Long-Lived 'Dark' State of Isolated 1-Methylthymine. *ChemPhysChem* **12,** 2024–2030 (2011).

43. Busker, M. *et al.* Electronic and Vibrational Spectroscopy of 1-Methylthymine and its Water Clusters: The Dark State Survives Hydration. *ChemPhysChem* **9,** 1570–1577 (2008).

44. Hare, P. M., Middleton, C. T., Mertel, K. I., Herbert, J. M. & Kohler, B. Time-resolved infrared spectroscopy of the lowest triplet state of thymine and thymidine. *Chem. Phys.* **347,** 383–392 (2008).

45. Salet, C. & Bensasson, R. Studies on thymine and uracil triplet excited state in acetonitrile and water. *Photochem. Photobiol.* **22,** 231–235 (1975).

46. Irimia, D. *et al.* A short pulse (7 μs FWHM) and high repetition rate (dc-5kHz) cantilever piezovalve for pulsed atomic and molecular beams. *Rev. Sci. Instrum.* **80,** 113303 (2009).

47. Møller, C. & Plesset, M. S. Note on an approximation treatment for many-electron systems. *Phys. Rev.* **46,** 618 (1934).

48. Hättig, C. Structure Optimization for Excited States with Correlated Second-Order methods: CC2 and ADC(2). *Adv. Quantum Chem.* **50,** 37–60 (2005).

49. Köhn, A. & Hättig, C. Analytic gradients for excited states in the coupled-cluster model CC2 employing the resolution-of-the-identity approximation. *J. Chem. Phys.* **119,** 5021–5036 (2003).

50. Hättig, C. Geometry optimizations with the coupled-cluster model CC2 using the resolution-of-the-identity approximation. *J. Chem. Phys.* **118,** 7751–7761 (2003).

51. Dunning, T. H. Gaussian basis sets for use in correlated molecular calculations. I. The atoms boron through neon and hydrogen. *J. Chem. Phys.* **90,** 1007–1023 (1989).

52. Barone, V. Anharmonic vibrational properties by a fully automated second-order perturbative approach. *J. Chem. Phys.* **122,** 14108 (2005).

53. Cooley, J. W. An improved eigenvalue corrector formula for solving the Schrödinger equation for central fields. *Math. Comput.* **15,** 363–374 (1961).

54. Brady, B. B., Peteanu, L. A. & Levy, D. H. The electronic spectra of the pyrimidine bases uracil and thymine in a supersonic molecular beam. *Chem. Phys. Lett.* **147,** 538–543 (1988).

55. Ligare, M. Resonance Enhanced Multi-photon Spectroscopy of DNA. (University of California Santa Barbara, 2015).

56. Nachtigallová, D. *et al.* Nonadiabatic Dynamics of Uracil: Population Split among Different Decay Mechanisms. *J. Phys. Chem. A* **115,** 5247–5255 (2011).

57. Szymczak, J. J. *et al.* Photodynamics Simulations of Thymine: Relaxation into the First Excited Singlet State [†]. *J. Phys. Chem. A* **113,** 12686–12693 (2009).

58. Lorentzon, J., Fuelscher, M. P. & Roos, B. O. Theoretical study of the electronic spectra of uracil and thymine. *J. Am. Chem. Soc.* **117,** 9265–9273 (1995).

59. Shukla, M. K. & Mishra, P. C. A gas phase ab initio excited state geometry optimization study of thymine, cytosine and uracil. *Chem. Phys.* **240,** 319–329 (1999).

60. Vaquero, V., Sanz, M. E., López, J. C. & Alonso, J. L. The Structure of Uracil: A Laser Ablation Rotational Study. *J. Phys. Chem. A* **111,** 3443–3445 (2007).

61. Casaes, R. N., Paul, J. B., McLaughlin, R. P., Saykally, R. J. & van Mourik, T. Infrared Cavity Ringdown Spectroscopy of Jet-Cooled Nucleotide Base Clusters and Water Complexes. *J. Phys. Chem. A* **108,** 10989–10996 (2004).

62. Viant, M. R., Fellers, R. S., McLaughlin, R. P. & Saykally, R. J. Infrared laser spectroscopy of uracil in a pulsed slit jet. *J. Chem. Phys.* **103,** 9502–9505 (1995).

63. Puzzarini, C. *et al.* Accurate molecular structure and spectroscopic properties of nucleobases: a combined computational–microwave investigation of 2-thiouracil as a case study. *Phys. Chem. Chem. Phys.* **15,** 16965 (2013).

64. López, J. C., Alonso, J. L., Peña, I. & Vaquero, V. Hydrogen bonding and structure of uracil–water and thymine–water complexes. *Phys. Chem. Chem. Phys.* **12,** 14128 (2010).

65. López, J. C., Isabel Peña, M., Eugenia Sanz, M. & Alonso, J. L. Probing thymine with laser ablation molecular beam Fourier transform microwave spectroscopy. *J. Chem. Phys.* **126,** 191103 (2007).

66. Makarov, A. A., Petrova, I. Y., Ryabov, E. A. & Letokhov, V. S. Statistical inhomogeneous broadening of infrared and Raman transitions in highly vibrationally excited XY6 molecules. *J. Phys. Chem. A* **102,** 1438–1449 (1998).

Chapter 4

Far IR Spectra and Born–Oppenheimer Molecular Dynamics to Structurally Characterize DNA Base Pairs

4.1 Introduction

Isolated purine and pyrimidine molecules are the fundamental building blocks of nucleic acids and spectroscopic knowledge on them in the gas phase has been obtained in recent years [1–9]. Using spectroscopic techniques, one can extend studies to nucleobase clusters and obtain valuable information on the multiple hydrogen-bonded interactions, stabilizing the two DNA stands [10–13]. Unfortunately, Watson-Crick structures have yet to be observed, presumably due to their short excited state lifetime. The 1 ps (or less) excited state lifetime of biological DNA tautomers [3,14–18] protects DNA bases against photochemical damages through internal conversion back to the electronic ground state [19]. Moreover, it is argued that this process played a major role in prebiotic chemistry.

Ever since the structures of DNA and its base pairs were first described, the hydrogen bonding between base pairs, which govern their structures and the relationship between DNA mutation, and tautomerization have been subjects of interest [20–35]. The breaking and re-forming of hydrogen bonds is involved in DNA replication and transcription. An experimental approach to investigating base-pairs and their roles in DNA stabilization is to study them in the gas phase. In contrast to conventional DNA spectroscopy [36–38], gas phase spectroscopy, using laser desorption jet cooling, allows us to study the interaction between molecules in the absence of external effects, such as the solvent or the DNA backbone, which mask important interaction details [1,4,5,9,10,12,39–43].

Recent advances in experimental and computational methods have permitted a deeper understanding of the properties of biological molecules in addition to the forces and dynamics that influence them. For example, the free-electron laser allowed for the mid and far IR region of isolated nucleic acid bases, base pairs, peptides, and other biological molecules to be explored resulting in rich information such as structure, functional properties, and electronic properties [26,44–53]. On the other hand, recent powerful simulations such Born –Oppenheimer Molecular Dynamics (BOMD) helped explain these experimental spectra [46,51,53]. With the spectroscopic data improving theoretical methods of calculations and accurate calculations identifying spectroscopic data, both experimental and computational methods work side by side to aid one another and explore the structures, dynamics, and properties of the different conformers present in the gas phase.

The use of a free electron laser to explore the far IR-region (<800 cm^{-1}) offers yet another piece of information to characterize biomolecules [54,55]. Traditionally the far IR region has been difficult to access both experimentally and computationally [48,55,56]. This region yields new information because it is characterized by large-scale delocalized vibrations that cannot be observed in the mid-IR region. The mid-IR region probes strong localized modes such as NH stretch, C=O stretch, and NH bending vibrations [51,57]. On the other hand, the far-IR region probes large-scale delocalized vibrations. As a result, the mid-IR provides us with local structural information, whereas the far-IR provides us with detailed information on the overall structure. Moreover, the far-IR region probes intrinsic hydrogen bond vibrations directly due to their weak interaction forces [58,59], which is not the case in the mid-IR region.

Here, we use the beam instrument and the free-electron laser to perform IR-UV ion-dip spectroscopy on gas-phase clusters of guanine and cytosine in the far-IR region. We use

BOMD simulation to analyze the great number of peaks observed in that region.

There have been extensive studies, both experimentally and computationally, on isolated guanine and cytosine in addition to the variety of clusters they can form with themselves and with each other. The combination of laser desorption jet cooling experiments of guanine with ab initio calculations or DFT have indicated the presence of two enol and two imino tautomers [6,8,60–62]. In a similar manner, both keto and enol tautomers of cytosine were determined to be present in the molecular beam [5,63]. Initially, REMPI studies on GC clusters indicated the presence of one structure similar to the Watson-Crick with guanine in the 9H-keto form but cytosine in the enol form connected by two hydrogen bonds [10,11,64]. Further measurements in the mid-IR region have later determined the structure of guanine to be the 7H-keto, instead [26]. Scanning the UV excitation further to the red revealed the presence of a second GC structure with the two keto monomers connected by two hydrogen bonds [26].

Force fields, semiempirical methods, and ab initio methods have been employed on the hydrogen-bonded GC and the stacked form with a greater emphasis on the triply hydrogen-bonded GC over the doubly hydrogen-bonded structure [65–72]. These calculations have shown how critical it is to choose the appropriate calculation method and basis set.

Due to their role in proton transfer and thus possible contribution to DNA mutation, vibrations of base pairs are of particular interest. As a result, intermolecular vibrational modes have been computationally studied at the harmonic level [73–75]. Brina Brauer *et al*. have performed RI-MP2/cc-pVDZ and RI-MP2/TZVPP ab initio calculations and anharmonic calculations using adapted PM3 surfaces on 7H-keto G…enol C complex. Combing their results with IR spectra collected by our group in the near and mid IR region

[13,26], they concluded that the CC-VSCF method with adapted PM3 potential surface is the best method for accurate frequency information for biological molecules [76]. They claimed that the inclusion of anharmonicity is necessary for accurate calculations of torsional motions and for understanding the potential surfaces describing the proton transfer between the base pairs [76].

As mentioned previously, hydrogen bond breaking and forming between base-pairs plays an important role in DNA replication and transcription. It is worth noting that the GG dimer is also involved in DNA replication and transcription, although it is less common [77,78]. Sequences of guanine are present in telomeres [79,80]; they form hairpins at the end of linear chromosomes which act as a short DNA or RNA strands and serve as a starting point for the synthesis of complementary DNA strands. Although in this present work, we only investigate the GG complex, mass peaks of multiple guanine sequences were observed but not scanned. Using gas-phase spectroscopy to investigate guanine sequences would be a potential project of extreme interest.

In the present work, we present the IR absorption spectrum of isolated guanine, guanine-guanine clusters, triply hydrogen-bonded guanine-cytosine clusters, doubly hydrogen-bonded guanine-cytosine clusters and 1methyguanine-9ethylguanine clusters, recorded in the 95-870 cm^{-1} region. We also present high-level calculations to interpret the collected data. DFT-MD BLYP-D3 and static harmonic BLYP-D3 are used to assign the major peaks. Wagging motions of hydrogen atoms, delocalized motions, and intermolecular hydrogen vibrations are the major mode groups that dominate the far IR-region. However, here we will focus on the first two groups due to calculation limitations when trying to explore intermolecular hydrogen vibrational modes.

4.2 Methods

4.2.1 Experimental

The experiments reported in this chapter were performed at the Free-Electron Laser for Infrared eXperiments (FELIX) at the Radboud University in the Netherlands. FELIX-1 covers the region 30-150 μm and FELIX-2 covers the region 3-45μm. For this experiment, we use both FELIX-1 and FELIX-2 scanning the region 11.5-105 μm (~ 870-95 cm^{-1}).

The instrument is illustrated in Figure 4.1 and is very similar to both beam instruments in our lab which are described in detail in chapter two along with the experimental setup. Here, the experimental setup is briefly described. Each sample is mixed with an equal amount of carbon black in order to obtain a homogenous mixture and therefore a stable shot-to shot signal. Moreover, we noticed that mixing samples with carbon black led to signal enhancement when trying to monitor clusters with extremely low signal. All chemicals were obtained from Sigma-Aldrich Co. and used without further purifications. The mixture is then placed on a graphite sample bar after it has been cleaned and scraped with an abrasive strip. To ensure a fresh sample is provided on every laser shot, the graphite sample bar is placed on a translation stage directly in front of a pulsed valve (Jordon Co.) with 0.5 mm diameter nozzle. The sample molecules are desorbed by using the fundamental output (1064 nm, ~1 mJ cm^{-1}) from an Nd:YAG laser (Polaris II, New Wave Research.). Then, the cold argon molecules entrain the desorbed sample molecules as they expand into the vacuum chamber. The supersonic molecular beam of argon is produced at a backing pressure of 3 bars. After about 10 cm downstream, the neutral molecules pass through a skimmer before reaching the source of the reflectron time-of-flight mass spectrometer (Figure 4.1). Here, the isolated molecules interact with a UV beam produced by frequency-doubled (BBO) output of a Nd:YAG laser (Quanta-Ray) pumped dye laser (Radiant Dye, Narrowscan) using a laser dye mixture of Rhodamine 610 and Rhodamine 640. Ions are created via one-color R2PI with the UV laser operating at 10 Hz and ~ 1.5 mJ of energy per pulse.

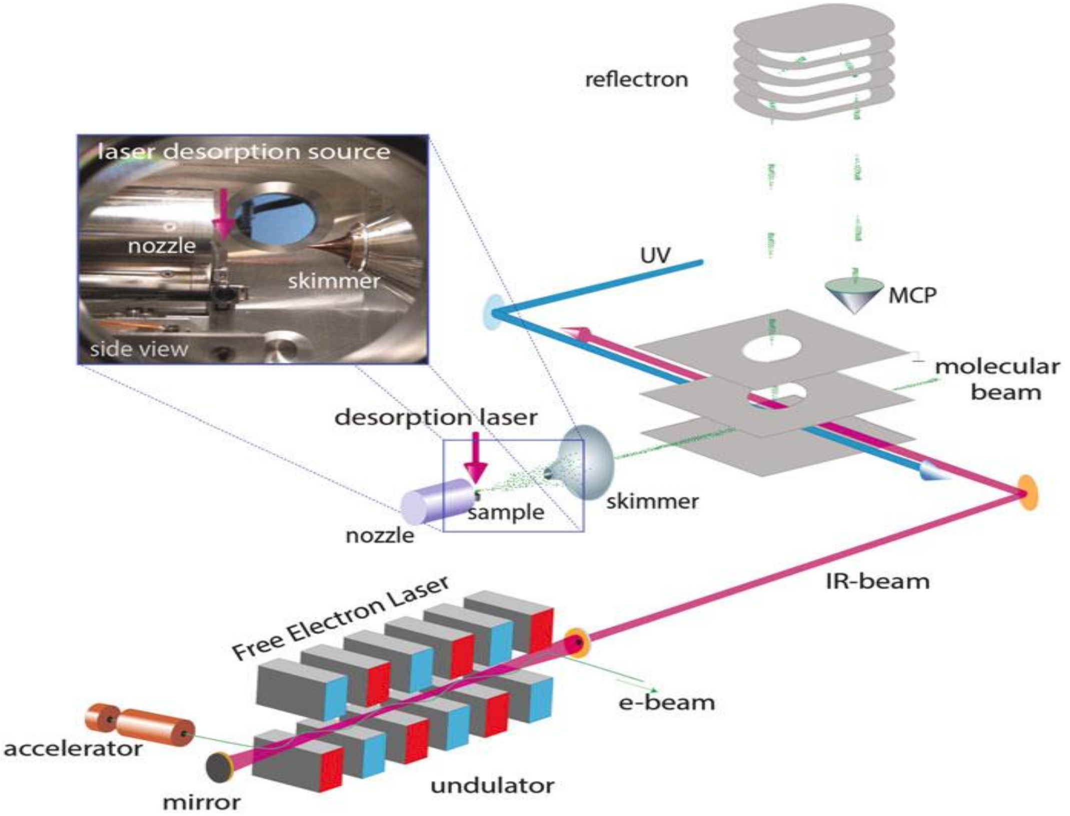

Figure 4.1: A schematic of the beam instrument equipped with the Free-Electron Laser at the FELIX facility.

IR absorption spectra are recorded using IR-UV ion-dip spectroscopy with the UV laser set at 10 Hz repetition rate and tuned to the maximum transition for each molecular system. On the other hand, the IR beam, produced from FELIX, is set at 5Hz repetition rate and spatially overlapped with the UV beam but precedes it by 200 ns. Whenever the IR is resonant with a vibrational transition, the ground state population is depleted due to the transfer of molecules to that vibrational state. The reduction in the number of ions produced leads to a dip in the ion signal produced by R2PI. By varying the IR wavelength, a mass-selected IR ion-dip spectrum is collected and compared to theoretical calculations. Operating the UV and IR lasers at different repetition rates is done to minimize signal fluctuation due to multiple reasons such as UV laser power drift, sample inconsistency, pulse valve voltage fluctuation, or other source conditions. By running the UV laser at double the repetition rate of that of the IR, the signal from the UV is divided into two parts, one with the IR on and one with the IR off. Both signals are recorded separately and then we normalize them by talking the logarithm of the ion signal without the IR divided by the ions signal with IR. The intensity of the IR power varies across a wavelength range; therefore, the IR spectra are renormalized to correct for this intensity variation. The IR spectra were measured in the range of 95-870 cm^{-1} (105-11.5 μm) with a FELIX bandwidth of about 1% (FWHM).

4.2.2 Computational

Theoretical vibrational spectroscopy is performed through DFT-MD simulations (*Density Functional Theory based Molecular Dynamics*) with the CP2K package [81], within the Born-Oppenheimer framework. The BLYP-D3 [82–84] GGA functional has been used for all the results presented here except when explicitly specified. This functional was selected based on previous works on gas-phase different spectral ranges [51,85–87]. The simulations are based on the GPW (*Gaussian Plane Waves*) method [88], with a dual basis set representation constructed here on a plane wave basis set with a 450 Ry energy cutoff and the aug-TZV2P (for the peptidic systems) or m-TZV2PX [89] (for the phenol derivatives and the DNA basis analogues) gaussian basis set . Pseudopotentials of the GTH type (Goedecker-Teter-Hutter) [90] are used. The size of the cubic box is systematically optimized for each family of system to ensure that there is no interaction between the system and its replica. Time-step for the dynamics is 0.4 fs. DFT-MD are performed at 50 K for the best agreement between theory and experiment. Initial structures for the dynamics are re-optimized at our level of theory. Each DFT-MD infrared spectrum is obtained as an average over three separate trajectories (same initial geometry, different initial velocities) of 20 ps each (after thermalisation over 1 ps) in order to obtain converged relative intensities of the absorption peaks. Spectra are therefore calculated over a total 60 ps trajectory. The infrared spectrum can be recalculated as the Fourier Transform of the time correlation function of the fluctuating dipole moment vector of the absorbing molecular system:

$$I(\omega) = \frac{2\pi\beta\,\omega^2}{3cV}\int_{-\infty}^{\infty} \mathrm{d}t\ \langle \delta\mathbf{M}(t)\cdot\delta\mathbf{M}(0)\rangle\ \exp(i\omega t) \qquad \text{eqn 1}$$

where $\beta = 1/kT$, T is the temperature, c is the speed of light in vacuum, V is the volume. The angular brackets represent a statistical average of the correlation function of the molecular dipole moment vector $\mathbf{M}(t)$, where $\delta\mathbf{M}(t) = \mathbf{M}(t) - <\mathbf{M}>$ is the dipole fluctuation, with $<\mathbf{M}>$ the time average of $\mathbf{M}(t)$. This method takes into account the mode coupling and the anharmonicities of the potential energy and dipole surfaces. The vibrational-rotational coupling has been removed within the Eckart-Sayvetz conditions [91,92] when needed. A spectrum is calculated with the Gaussian package [93] with the DFT-MD spectrum. The electronic representation of BLYP-D3/6-311+G(d,p) has been chosen for the best comparison. The normal modes are printed into both cartesian and intra coordinates with the keyword "freq=(Intmodes)".

4.3 Results and Discussion

In addition to hydrogen bonding vibrations, two main families of modes dominate the far-IR absorption spectrum, wagging motions of hydrogen atoms and delocalized motions. In the far-IR region, hydrogen atom wagging motions are characterized as the most intense peaks. They are also local, meaning that one wagging is involved in each normal mode which can have anharmonic behavior. On the other hand, delocalized motions are non-local because they consist of a combination of motions with large amplitude (bending and dihedral motions). Delocalized modes behave harmonically and their peaks are less intense compared to the ones from the wagging modes. In this section, we attempt to explain the collected IR spectra by assigning the experimental peaks to those two dominant mode groups.

4.3.1 Isolated guanine

Figure 4.2 shows the recorded one-color R2PI spectrum of isolated guanine. Here, IR-UV ion-dip spectroscopy is collected by tuning the UV on the origin transition (32854 cm^{-1}) and scanning the IR over the far-IR region. The origin peak belongs to the 9H-enol tautomer [6,8,62]. Calculations were performed on both OH-cis and OH-trans structures (Figure 4.3). The full experimental IR spectrum of guanine monomer (Figure 4.4 A) is divided into two pieces (Figure 4.4 B & C). The region below 500 cm^{-1} (Figure 4.4 C) is scaled up in order to clearly expose the small peaks.

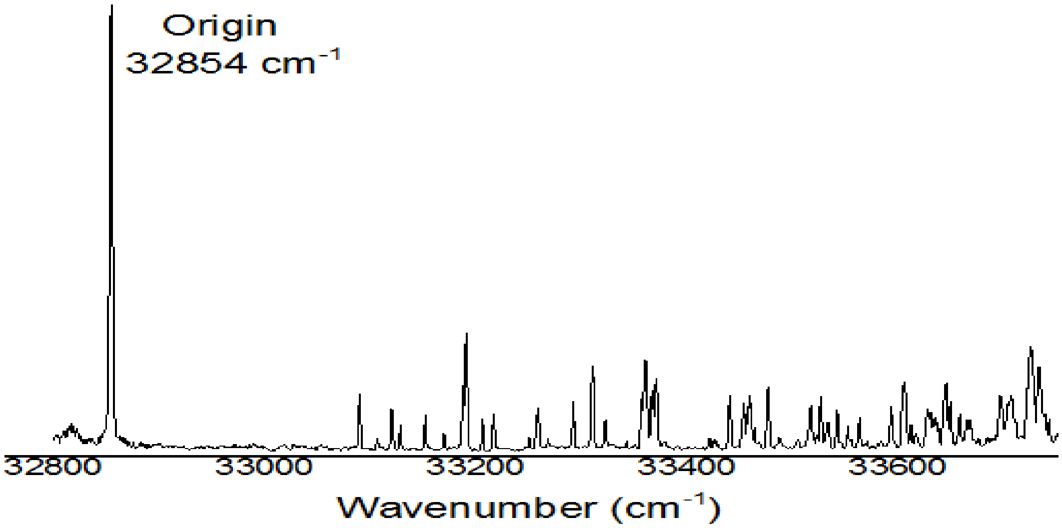

Figure 4.2: One-color resonant two-photon ionization (R2PI) spectrum of guanine monomer. The origin transition (0-0) is at 32854 cm^{-1}.

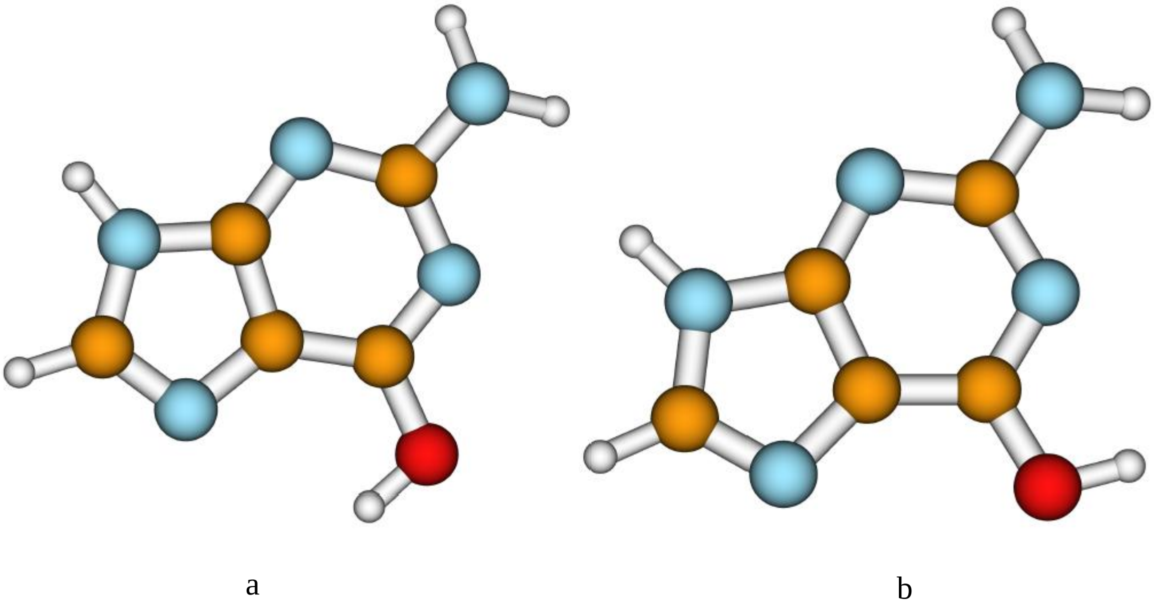

Figure 4.3: The molecular structure of cis-9H-enol guanine (a) and trans-9H-enol guanine (b).

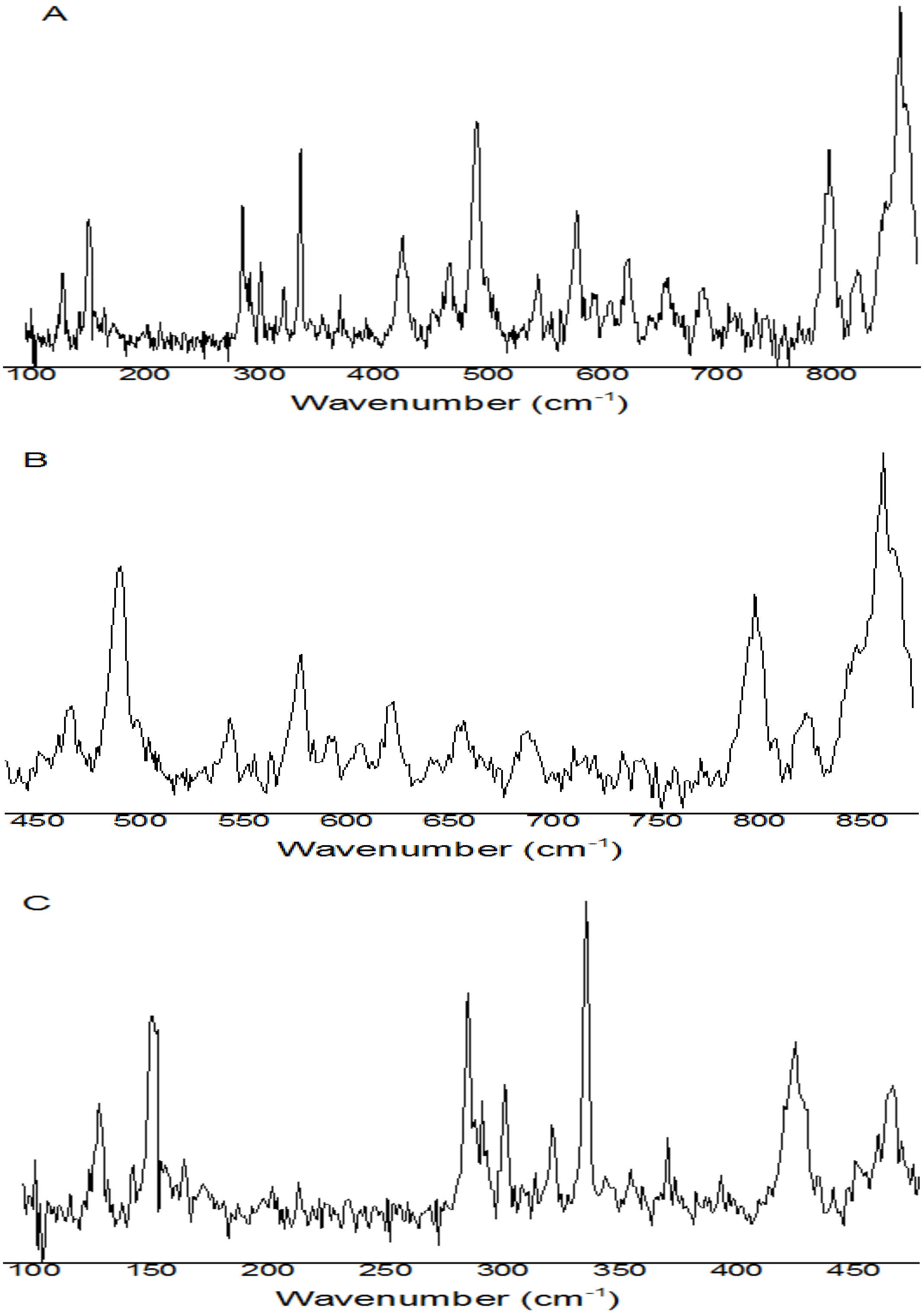

Figure 4.4: Experimental IR spectra of guanine monomer. Full spectrum (A) 450-880 cm^{-1} region (B), and 95-480 cm^{-1} region scaled up (C).

DFT-MD and static harmonic calculations are performed on the guanine system. Unfortunately, there is not a reasonable agreement between experiment and calculations.

In order to analyze the spectrum step by step, we extract the signatures from DFT-MD by using a local analysis tool known as Intra Coordinate Density of States (ICDOS). ICDOS is the Fourier transform of the autocorrelation function of an intra molecular coordinate (distance, angle, or dihedral angle). The mathematical equation (eqn 1) is shown in the theoretical section.

In practice, we use dihedral angles to extract the wagging modes; for example, H-N-C-C. ICDOC of the wagging modes for cis-9H-enol and trans-9H-enol guanine are demonstrated in Figure 4.5. Figure 4.5 a and b show the assignment of modes in the DFT-MD spectra for the cis and trans, respectively.

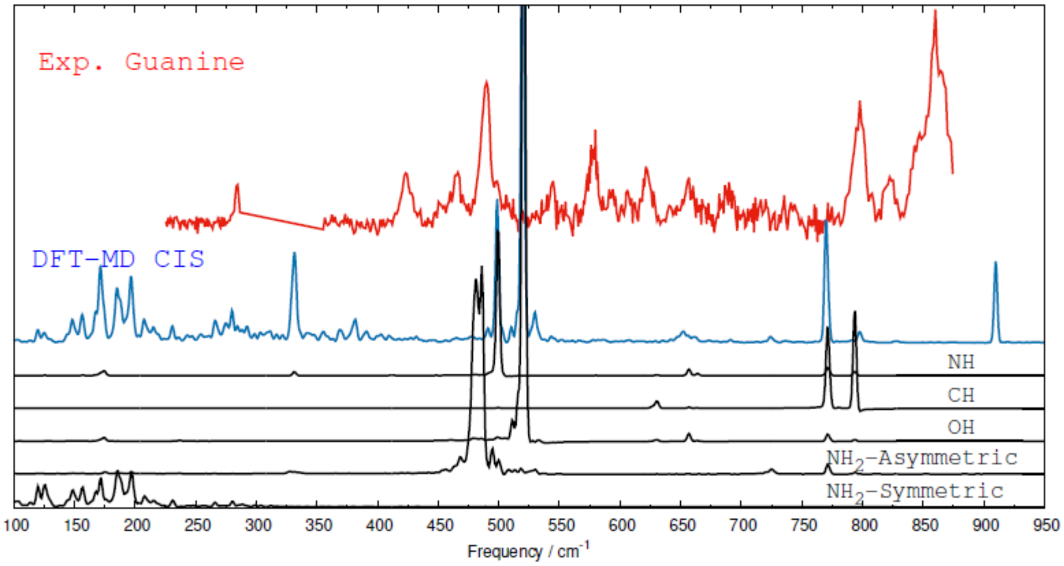

a

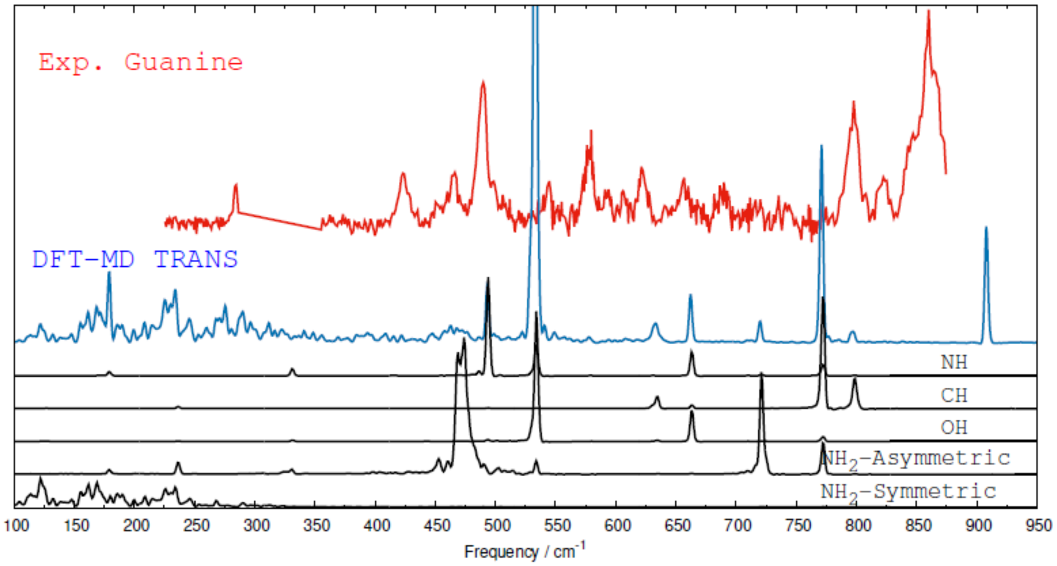

b

Figure 4.5: Identification of peaks in the DFT-MD spectrum (blue) with peaks in the ω(N-H) ω(C-H), ω(O-H), symmetric, and asymmetric NH_2 decomposition (black) for cis-9H-enol G (a) and trans-9H-enol G (b).

Figure 4.6 a and b show the assignment of modes in the harmonic spectra for the cis and trans, respectively.

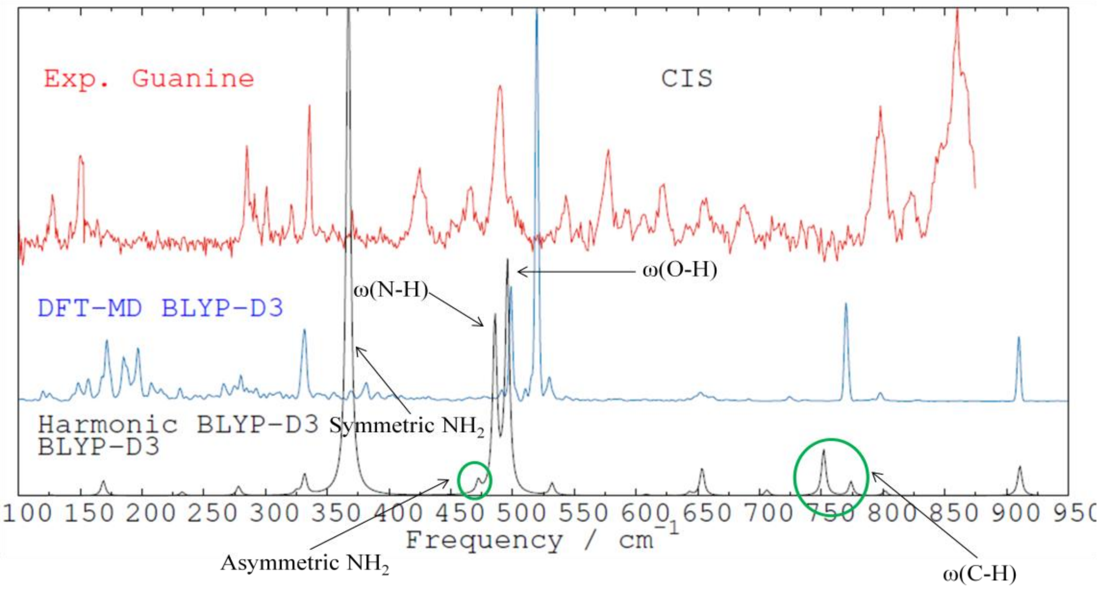

a

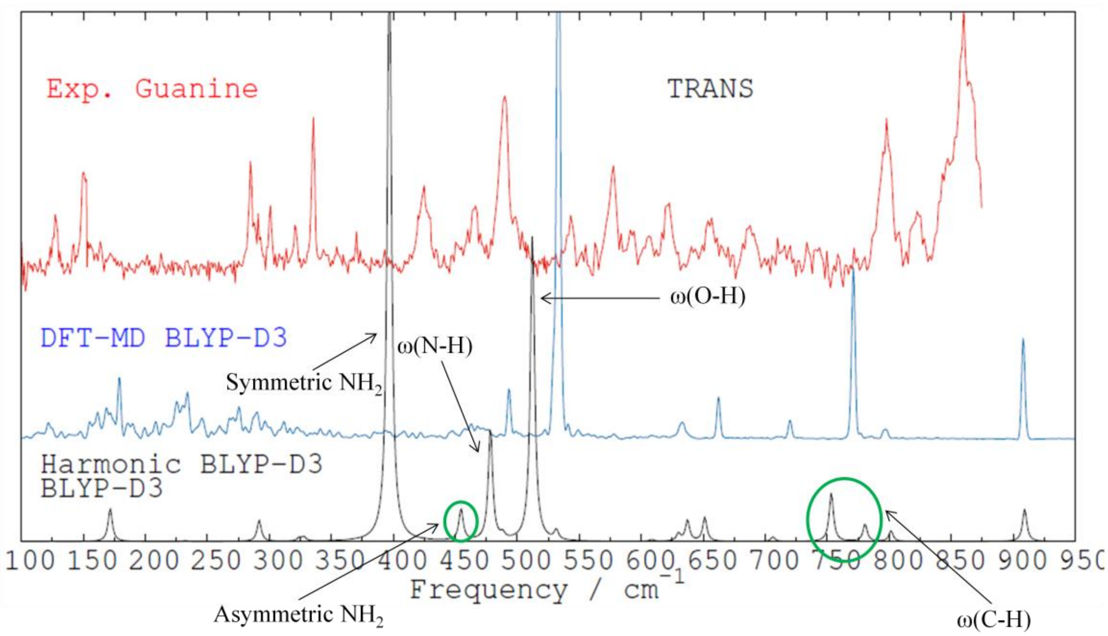

b

Figure 4.6: Assignment of modes in the harmonic spectrum for cis-9H-enol G (a) and trans-9H-enol G (b).

Overall, there is a poor agreement between theory and experiment. Based on the delocalized and harmonic modes between 250 and 350 cm^{-1}, the cis-9H-enol G spectra are in better agreement with the experiment than those of trans-9H-enol G. The NH signature in the DFT-MD spectrum is the only one in good agreement with an experimental peak for both cis and trans structures. We assign the NH wagging to the most intense peak in the experimental spectrum around 480 cm^{-1}. The free NH wagging has anharmonic behavior, similar to the G-G system as shown later. For OH wagging, it is surprising to see that there is no experimental peak that matches in terms of position and intensity. We have no explanation why that is even though the NH wagging is well reproduced.

The main problem here is that there are more intense peaks in the experimental spectrum than in the theoretical spectra. We do expect many overtones and combination bands since those seem common in a small system, such as this. For the other systems shown later, we have no free NH_2 mode for comparison. However, we can assign the two experimental peaks around 125 and 140 cm^{-1} to the NH_2 symmetric signatures despite the corresponding peaks being broad and blue shifted in the DFT-MD spectrum.

Clearly, there is a huge difference between harmonic and DFT-MD spectra for the NH_2 mode. While the asymmetric signatures have small IR intensities and equivalent frequencies for both representations (around 475 cm^{-1}), there is a strong blue shift and broadening of the symmetric signatures in the DFT-MD spectrum. Since the NH_2 function is free of interaction, we would expect tunneling of the lone pair to be much easier compared to bonded-NH_2 (see G-G and 1MeC-9EtG sections). We propose three possibilities to explain the good agreement between theory and experiment for all systems but guanine. 1) No tunneling in any system, 2) tunneling in all systems, or 3) tunneling in only guanine but no effect on the spectrum. If tunneling occurs in all systems, then the tunneling effect is correctly taken into account in the DFT-MD spectrum.

Why there is poor agreement between theory and experiment is not clear. We offer two explanations that might account for that. First, the majority of peaks are due to modes of recombination between overtones, combination bands, and original modes. Second, this guanine monomer might not be 9H-enol, but could be a different tautomer instead. Therefore, we performed conventional DFT and anharmonic correction using VPT2 calculations on cis-9H-enol G, trans-9H-enol G, and trans-7H-enol G (Figure 4.7). For both calculations, the B3LYP-D3 functional and 6-311++ G(d,p) basis set are used.

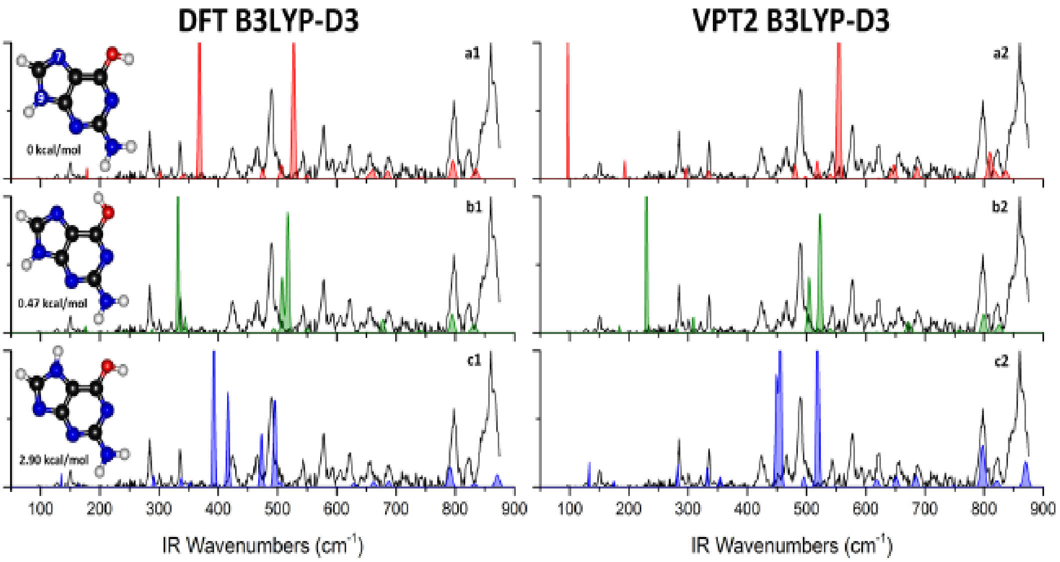

Figure 4.7: Comparison of the experimental spectrum (black) with the computational spectra of cis-9H-enol G (a), trans-9H-enol G (b), and trans-7H-enol G (c). The relative ground state energies are given. Two different computational methods are used, conventional DFT (1) and an anharmonic correction using VPT2 (2). For both calculations the B3LYP-D3 functional and 6-311++G(d,p) basis sets are used.

For both functionals, the computational spectrum of trans-7H-enol G best matches the experimental spectrum, particularly in the 250-350 cm^{-1} and 600-900 cm^{-1} regions. Although Mons *et al.* used methylation to confirm that the tautomer associated with the origin band is 9H-enol [62], more computational work on 7H-enol is called for to conclusively determine what the correct tautomer is.

4.3.2 Guanine-guanine dimer

Figure 4.8 shows the recorded one-color R2PI spectrum for the G-G dimer. In this wavelength range, two isomers of G-G are detected and both structures consist of guanine in the keto tautomeric form despite the presence of enol tautomers in the molecular beam [94]. Here, IR-UV ion-dip spectroscopy is collected by tuning the UV to the origin transition

(33088 cm^{-1}) and scanning the IR over the far-IR region. The origin peak belongs to the triply hydrogen-bonded G-G dimer consisting of 9H- and 7H-keto tautomers of guanine (Figure 4.9). The full experimental IR spectrum of G-G dimer (Figure 4.10 A) is divided into two pieces (Figure 4.10 B & C); the region below 500 cm^{-1} (Figure 4.10 C) is scaled up in order to clearly expose the small peaks.

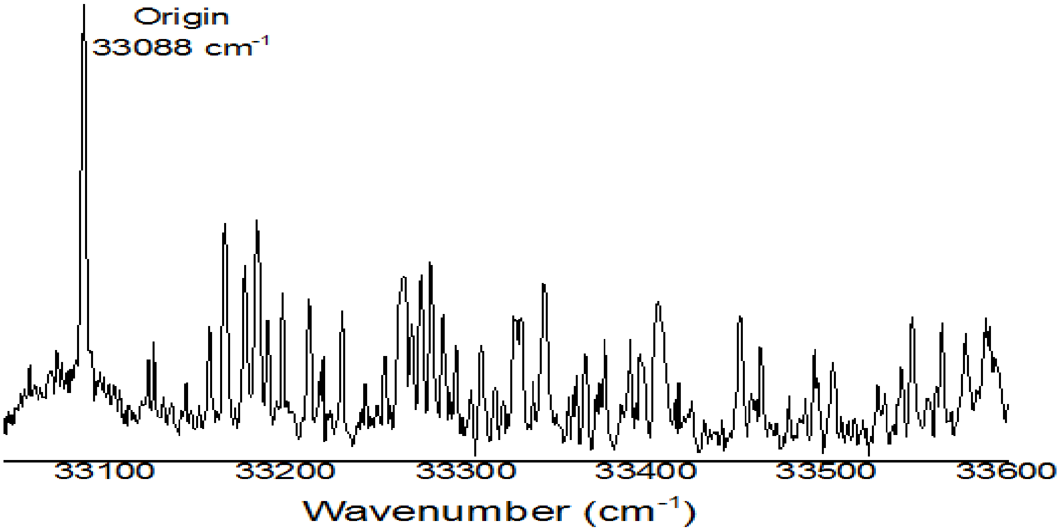

Figure 4.8: One-color resonant two-photon ionization (R2PI) spectrum of G-G dimer. The origin transition (0-0) is at 33088 cm^{-1}.

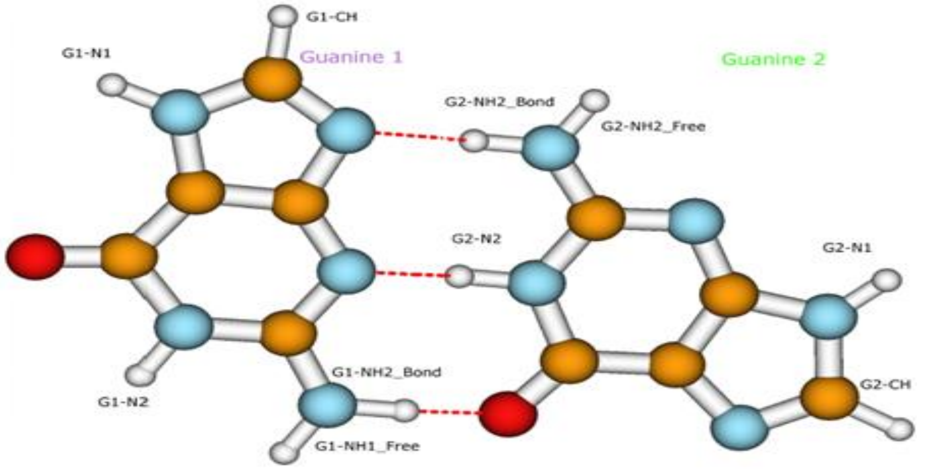

Figure 4.9: The molecular structure of 9H- and 7H-keto guanine dimer with the nomenclature employed. Throughout this section, peaks that originate from guanine 1 (left side) will be highlighted in purple; whereas, peak originating from guanine 2 (right side) will be highlighted in green.

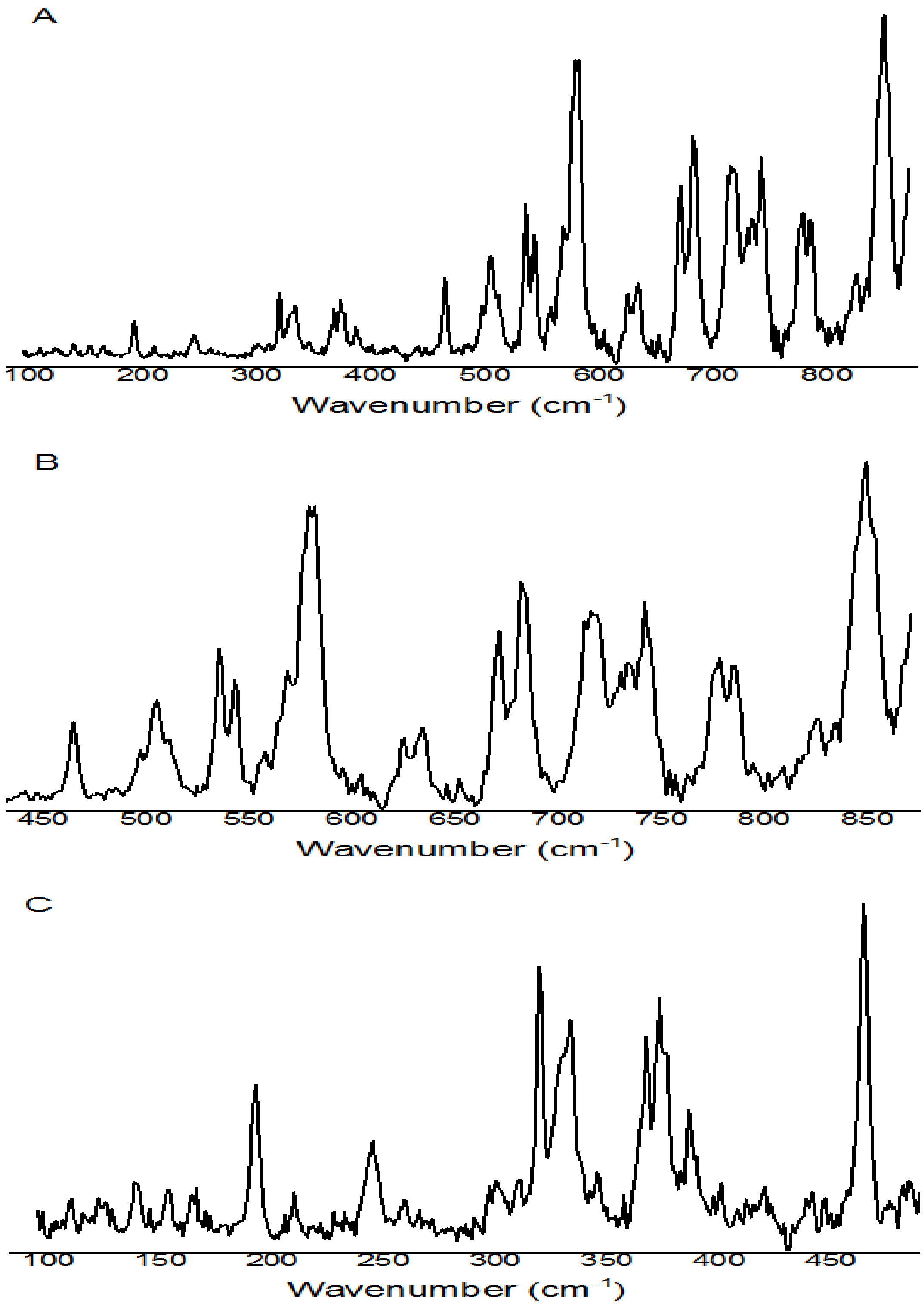

Figure 4.10: Experimental IR spectra of G-G dimer. Full spectrum (A) 450-880 cm^{-1} region (B), and 95-480 cm^{-1} region scaled up (C).

DFT-MD and static harmonic calculations are performed on the G-G system. Overall, there is reasonable agreement between experiment and the DFT-MD spectrum as shown in Figure 4.11. There are however experimental peaks without counterparts in the DFT-MD spectrum (nor in the static harmonic spectrum). These peaks are at ~450, 530, 700-750, and 783 cm^{-1}.

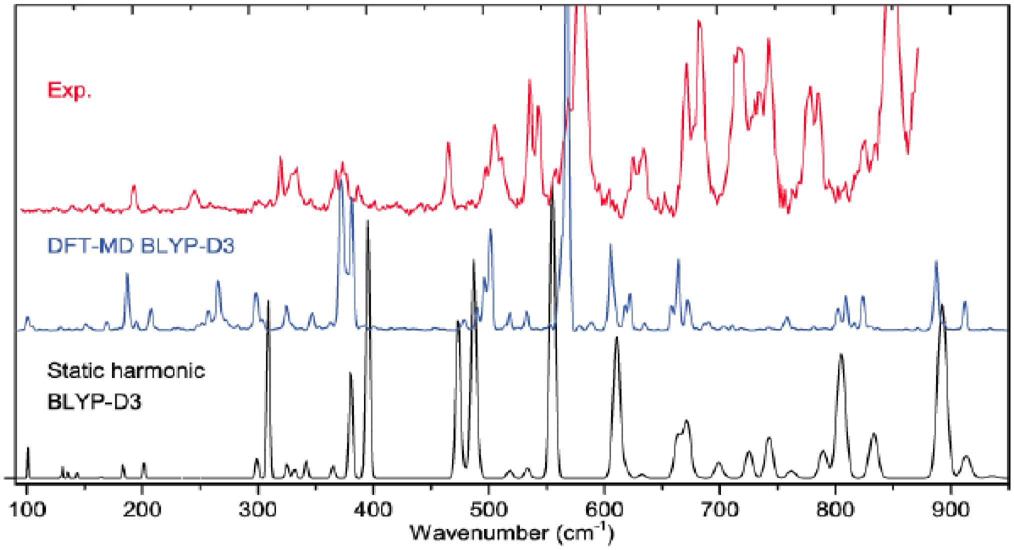

Figure 4.11: Experimental spectrum of G-G dimer (red) in comparison with DFT-MD and static harmonic spectra (blue and black, respectively).

At first sight, the DFT-MD spectrum is slightly improved from the static harmonic spectrum, mostly for frequencies below 600 cm^{-1}. Band shapes and positions in the DFT-MD spectrum seem to match better with those of the experimental ones.

Similar to what was done to the guanine system; we extract the ICDOC to have the signature of each C-H or N-H wagging motion in the G-G system, as shown in Figure 4.12.

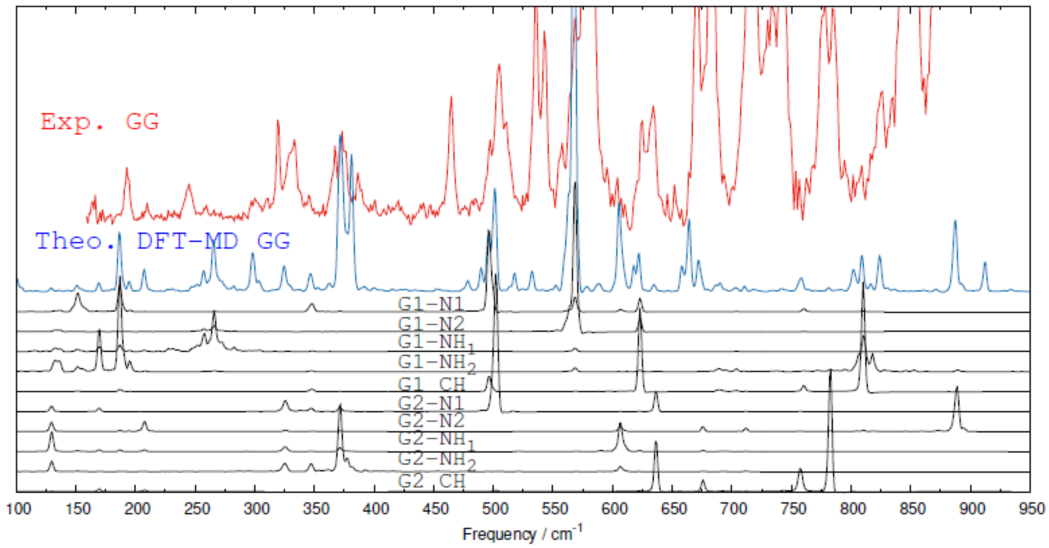

Figure 4.12: Identification of peaks in the theoretical spectrum (blue) with peaks in the ω(N-H) and ω(C-H) decomposition (black) for G-G dimer.

Figure 4.13 shows the mode assignment of the ω(N1-H) for both guanine 1 and guanine 2 in DFT-MD and static harmonic spectra. ω(N1-H) modes refer to the two free N-H groups G1-N1 and G2-N1 (Figure 4.9).

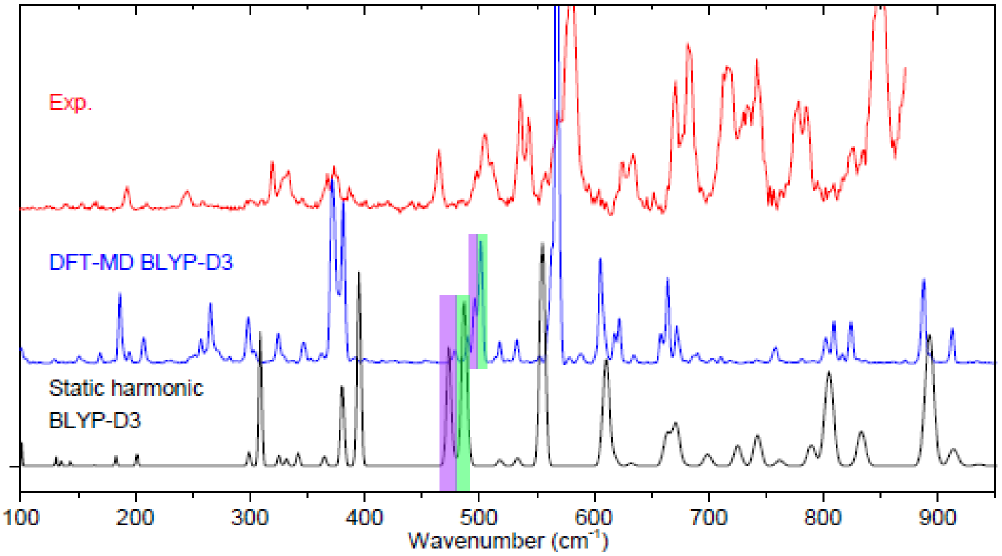

Figure 4.13: Mode assignment of ω(N1-H) in G-G dimer. Mode of guanine 1 is highlighted in purple and mode of guanine 2 is highlighted in green.

After taking the anharmonicities into account, we have a blue shift of 21 and 17 cm^{-1} from harmonic frequencies for ω(N1-H) G1-N1 and G2-N1, respectively. We conclude that the broad peak around 506 cm^{-1} in the experiment arises from the G1-N1 and G2-N1 ω(N1-H) modes.

Next, we show the mode assignment of the ω(N2-H) for both guanine 1 and guanine 2 in DFT-MD and static harmonic spectra (Figure 4.14). ω(N2-H) modes refer to the free N-H group G1-N2 and the H-bonded N-H group G2-N2 (Figure 4.9).

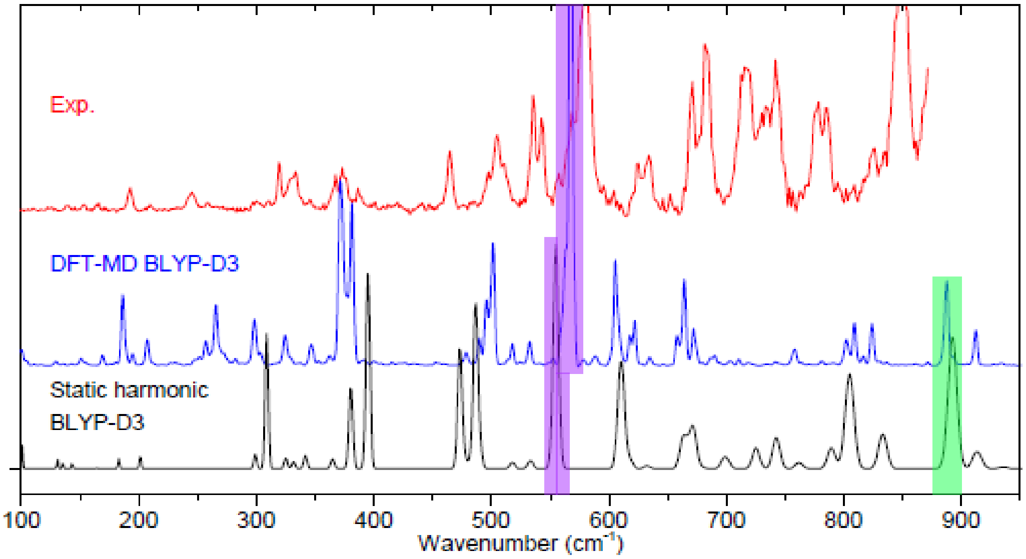

Figure 4.14: Mode assignment of ω(N2-H) in G-G dimer. Mode of guanine 1 is highlighted in purple and mode of guanine 2 is highlighted in green.

After taking the anharmonicities into account, we have a blue shift of 22 cm^{-1} for ω(N2-H) G1-N2 and a red shift of 8 cm^{-1} for G2-N2 from harmonic values. We can conclude that the intense peak at 581 cm^{-1} in the experiment arises from the ω(N2-H) G1-N2, while the ω(N2-H) G2-N2 produces signatures slightly out of the range of the measured experimental spectrum. Although G1-N2 is a free N-H (as G1-N1), its frequency is blue-shifted by

~75 cm^{-1}. We explain this shift by the different chemical environment around both N-H groups.

Now, we show the mode assignment of the ω(N-H) of NH2-Free and NH2-Bond modes for guanine 1 in DFT-MD and static harmonic spectra (Figure 4.15). ω(N-H) modes of NH2-Free and NH2-Bond refer to the G1-NH2_Free and G1-NH2_Bond, respectively (Figure 4.9).

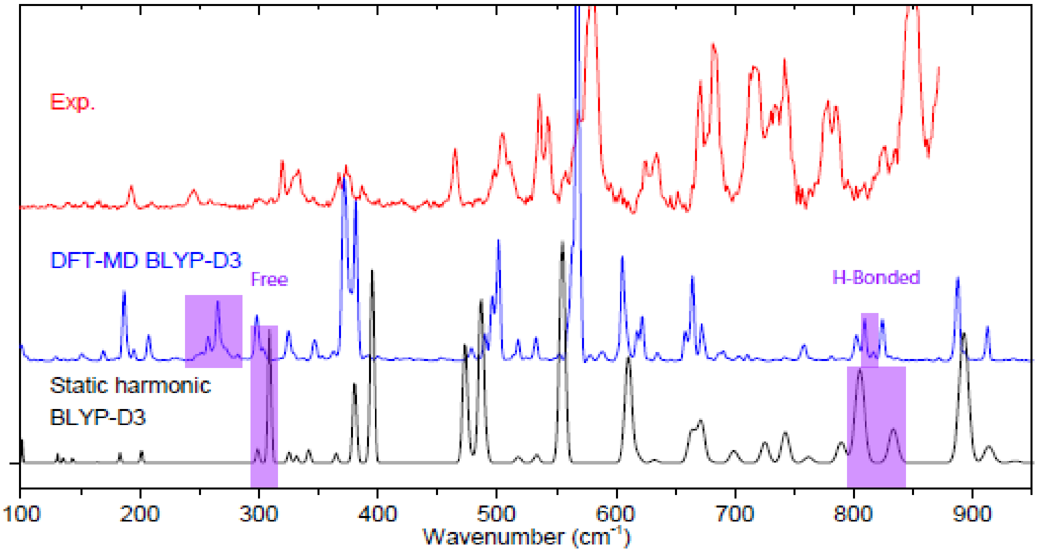

Figure 4.15: Mode assignment of ω(N-H) of NH2-Free and NH2-Bond modes for guanine 1 in G-G dimer.

We can combine free and H-bonded contributions into symmetric and asymmetric contributions (not done here). After taking the anharmonicities into account, we have a red shift of 43 cm^{-1} for ω(N-H) G1-NH2_Free and no shift for G1-NH2_Bond from harmonic values. We can conclude that the intense peak at 246 cm^{-1} in the experiment arises from the G1-NH2_Free mode while the G1-NH2_Bond mode produces a peak at 809 cm^{-1} in the DFT-MD spectrum, exactly between two experimental peaks, which makes the assignment complicated. We assume here that the theoretical band is red shifted from the experimental spectrum; therefore, we assign the peak to the one at 850 cm^{-1} in the experiment.

Finally, we show the mode assignment of the ω(N-H) of NH2-Free and NH2-Bond modes for guanine 2 in DFT-MD and static harmonic spectra (Figure 4.16). ω(N-H) modes of NH2-Free and NH2-Bond refer to the G2-NH2_Free and G1-NH2_Bond, respectively (Figure 4.9).

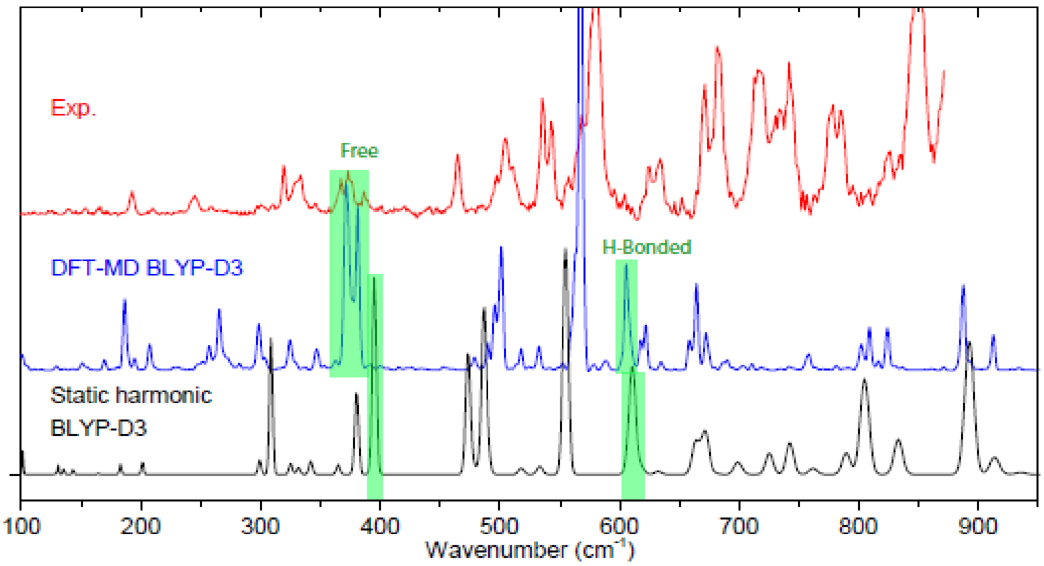

Figure 4.16: Mode assignment of ω(N-H) of NH2-Free and NH2-Bond modes for guanine 2 in G-G dimer.

Just like the case with guanine 1 shown above, we can combine free and H-bonded contributions into symmetric and asymmetric contributions. After taking the anharmonicities into account, we have a red shift of 20 cm^{-1} for ω(N-H) G2-NH2_Free that produces the double peak around 378 cm^{-1} in the DFT-MD spectrum and a red shift of 5 cm^{-1} for G2-NH2_Bond from harmonic values. We conclude that the broad peak located around 375 cm^{-1} in the experiment arises from ω(N-H) G2-NH2_Free while the ω(N-H) G2-NH2_Bond produces the experimental peak ~636 cm^{-1}.

The overall assignment of the experimental peaks is shown in Figure 4.17.

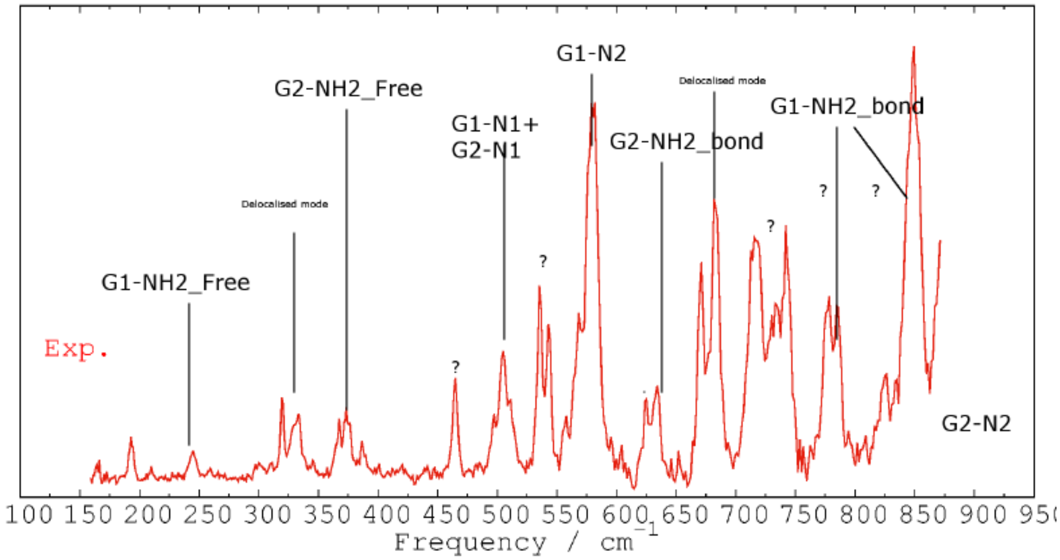

Figure 4.17: Assignment of G-G experimental peaks. Question mark symbols (?) are placed on peaks with no counterparts in DFT-MD spectrum.

The experimental peaks located at 246, 375, 506, 581, 636, and 850 cm^{-1} are assigned to ω(N-H) wagging modes. ω(N-H) modes are characterized by high intensity peaks; whereas, ω(C-H) modes are characterized by low intensity peaks. Therefore, ω(N-H) modes are the dominant ones in the far-IR region. The broad massif of peaks experimentally located around ~725 cm^{-1} has no counterpart in the DFT-MD spectrum but could be explained by three peaks present in the static harmonic spectrum at 699, 725, and 742 cm^{-1}, respectively. These three peaks have nonetheless far too low intensity in comparison to the experiment. The first peak arises from a delocalized mode located on guanine 1. The second peak consists of the wagging of guanine 1 backbone around the central carbon with contribution of G1-NH2_Bond. The third peak arises from the G2-CH wagging mode, which includes delocalized vibrations on guanine 2.

The two experimental peaks at 671 and 682 cm^{-1} (and 664 cm 672 cm^{-1} in the DFT-MD spectrum) are explained by delocalized modes that also provide signatures at 663, 668, and 672 cm^{-1} in the harmonic static spectrum. The mode at 663 cm^{-1} consists of G1-NH2, G1-N1, and G1-N2 motions in-plane, which include in-plane motions in G2-NH2 and G2-N2. The mode at 668 cm^{-1} consists of wagging G2-NH2_Bond wagging, which induces delocalized motions across guanine 2. At 672 cm^{-1}, the mode consists of G2-NH2 and G2-N2 motions in-plane, which induces delocalized in-plane motions in guanine 1 and 2.

The double peaks located in the experiment at 535 and 543 cm^{-1} are assigned to the peaks at 517 and 533 cm^{-1} and correspond to delocalized modes across guanine 1 and 2 with ring deformations. These two peaks have nonetheless for too low intensity in comparison to the experiment. We provide no explanation for the peak at 466 cm^{-1} as there are no corresponding peaks in the DFT-MD spectrum or the static harmonic calculation.

The broad massif of peaks between 321 and 355 cm^{-1} is explained by delocalized modes, corresponding to the peaks at 325, 332, and 342 cm^{-1}. The modes at 325 and 342 cm^{-1} correspond to a butterfly-like motion in guanine 2 and 1, respectively. The peak at 332 cm^{-1} arises from the in-plane motion of G2-NH2, G2-N1, and G2-CH, which induces the in-plane motion of G1-NH2.

Although we assigned most of the peaks, indicated with a question mark, to delocalized motions, calculations with the Gaussian-VPT2 method suggests that these peaks could be due to overtones or combination bands as shown in Figure 4.18.

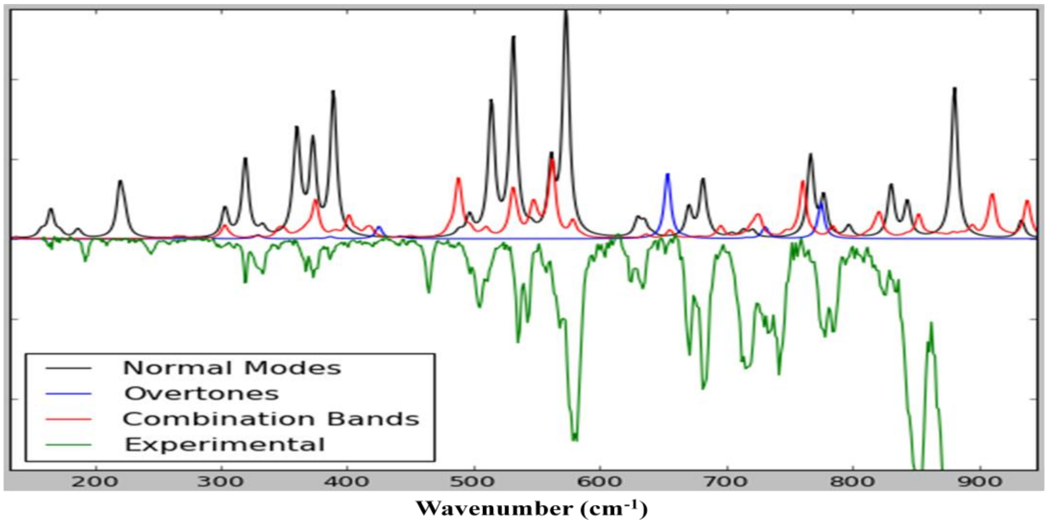

Figure 4.18: Gaussian-VPT2 method of calculation showing the experimental spectrum (green) vs the calculated spectra with normal modes in black, overtones in blue, and combination bands in red.

The question therefore remains; can we trust the static harmonic spectrum to explain our experimental data? Previous calculations on ω(N-H) modes of peptides have shown that ω(N-H) modes have a strong anharmonic behavior. However, it seems that for rigid molecules like guanine, ω(N-H) modes are more harmonic since the peak shifts between static harmonic and DFT-MD are less. ω(N-H) modes of the free NH functions are not highly harmonic with a blue shift of 21, 16, and 22 cm^{-1} for G1-N1, G2-N1, and G1-N2 modes, respectively from the static harmonic to the DFT-MD values. The G2-N2 ω(N-H) mode of the strongly H-bonded NH function appears highly harmonic with a red shift of 8 cm^{-1} going from static harmonic to DFT-MD. Geometry optimization provides a hydrogen bond length of 1.86 Å. For G1-NH2 we have a red shift of 43 cm^{-1} from static harmonic to DFT-MD for ω(N-H) of the free hydrogen atom and no shift for the H-bonded hydrogen atom. On the other hand, for G2-NH2 we have a red shift of 20 cm^{-1} for the free hydrogen atom and a red shift of 5 cm^{-1} for the H-bonded hydrogen atoms. Geometry optimization gives hydrogen bond lengths of 1.76 Å for H....O and 2.05 Å for H….N.

4.3.3 Methylated guanine-cytosine cluster

Figure 4.19 shows the recorded one-color R2PI spectrum for the 9EtG-1MeC cluster. In this wavelength range, one isomer is detected where 9-ethylguanine and 1-methylcytosine are in the keto tautomeric form [13], as shown in figure 4.20. This Watson-Crick (WC) structure exhibits a broad UV absorption feature in contrast to the sharp UV spectra by non-WC structures. This broad absorption spectrum can be explained by a presence of a pathway for rapid internal conversion [95]. Assuming that broadening is solely due to lifetime, the WC structure excited state lifetime is about 2 orders of magnitude shorter than that for non-WC structures [13]. As a result, the WC structure would be more photo-stable than other base-pair structures and this photochemical mechanism may have protected it from harsh environmental conditions at the time of the origin of life.

Here, IR-UV ion-dip spectroscopy is collected by tuning the UV on a strong transition (33071 cm^{-1}) and scanning the IR over the far-IR region. The full experimental IR spectrum of 9EtG-1MeC dimer (Figure 4.21 A) is divided into two pieces (Figure 4.21 B & C); the region below 500 cm^{-1} (Figure 4.21 C) is scaled up in order to clearly expose the small peaks.

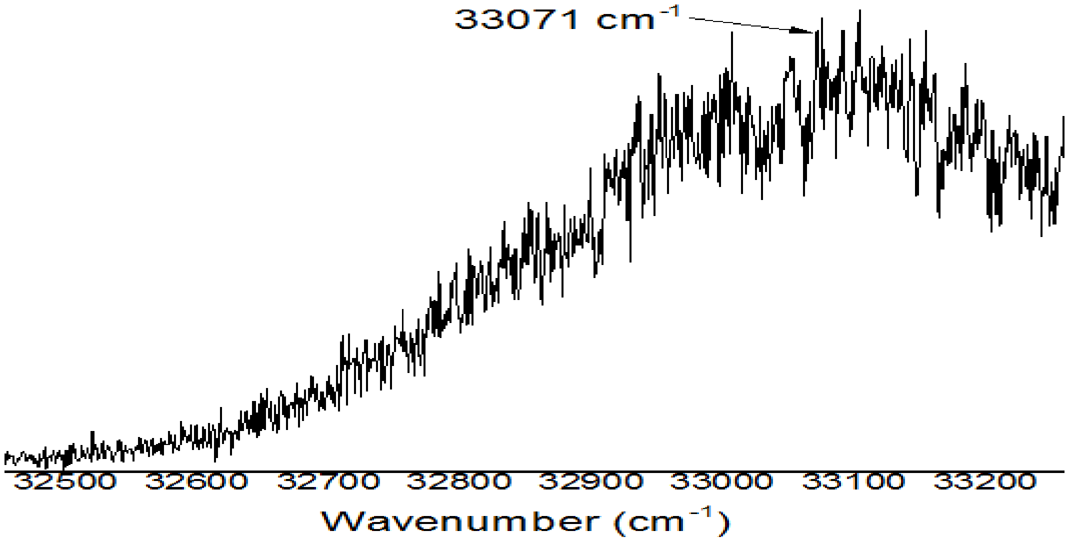

Figure 4.19: One-color resonant two-photon ionization (R2PI) spectrum of 9EtG-1MeC dimer. IR-UV is performed on 33071 cm^{-1} transition.

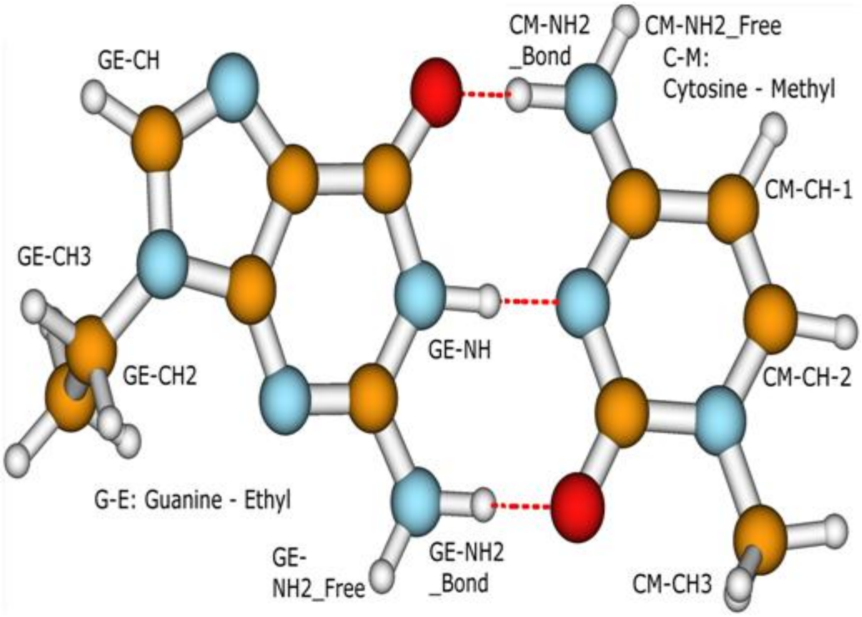

Figure 4.20: The molecular structure of 9EtG-1MeC dimer with the nomenclature employed. Throughout this section, peaks that originate from 9EtG will be highlighted in purple; whereas, peak originating from 1MeC will be highlighted in green.

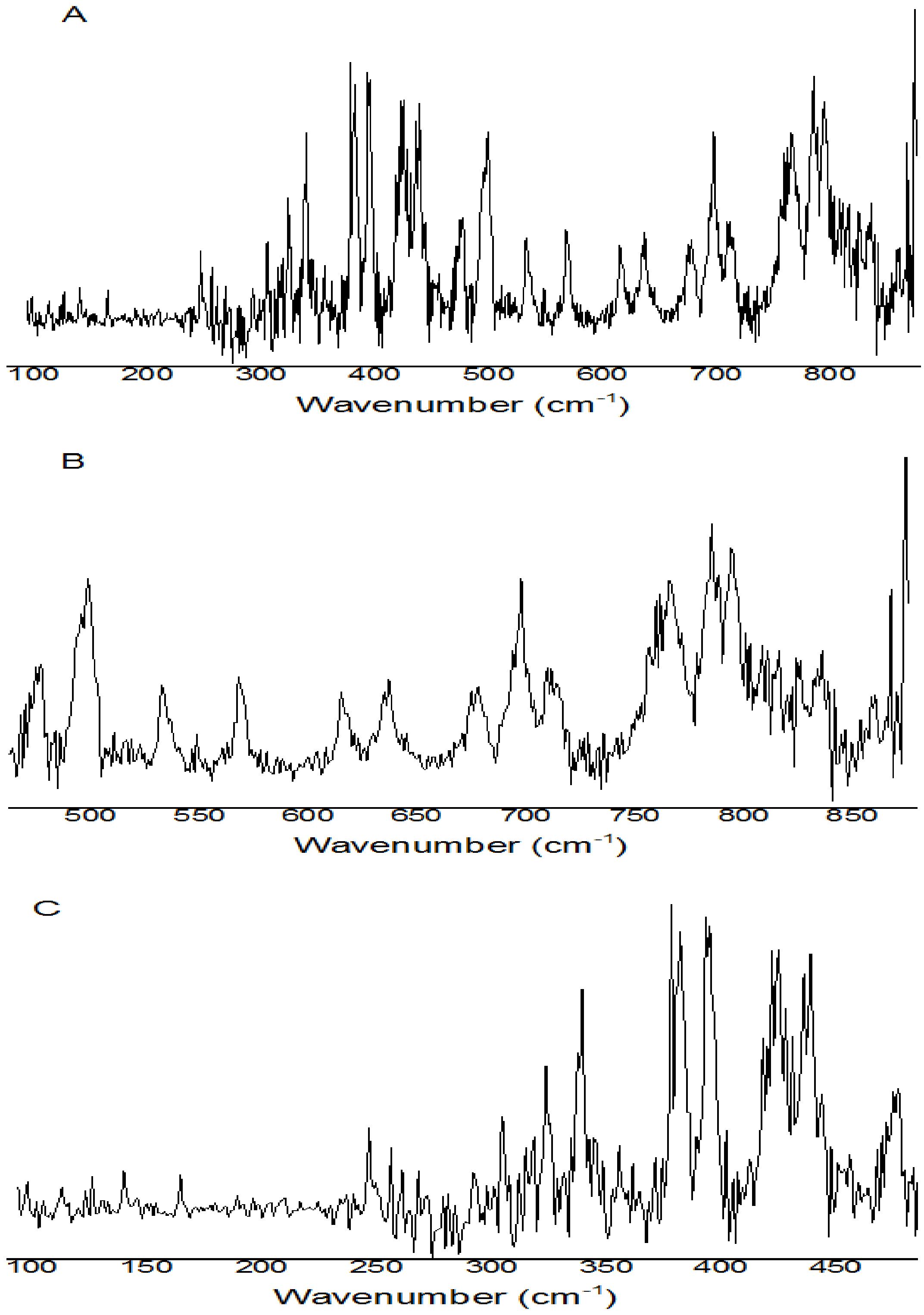

Figure 4.21: Experimental IR spectra of 9EtG-1MeC dimer. Full spectrum (A), 470-880 cm^{-1} region (B), and 95-480 cm^{-1} region scaled up (C).

DFT-MD and static harmonic calculations are performed on the 9EtG-1MeC system. Overall, there is reasonable agreement between experiment and the DFT-MD spectrum (Figure 4.22). The Figure also shows that DFT-MD and harmonic spectra are somewhat identical. There are however experimental peaks without counterparts in the DFT-MD spectrum (nor the static harmonic spectrum). These peaks are 424, 533, 713, 785, and 796 cm^{-1}. When comparing these peaks with those of G-G's (~450, 530, 700-750, and 783 cm^{-1}), we notice that they are located at almost equivalent frequencies.

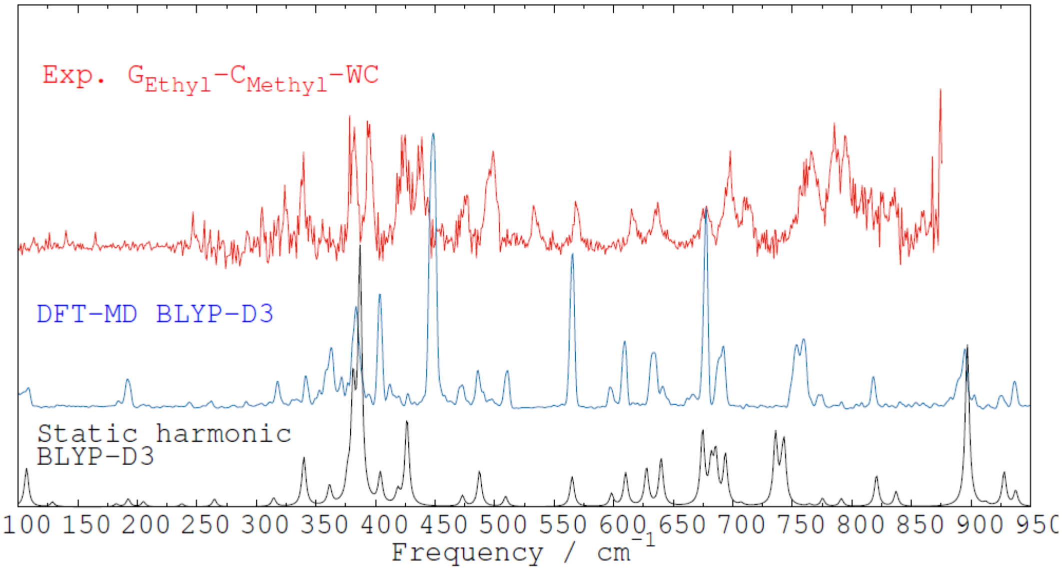

Figure 4.22: Experimental spectrum of 9EtG-1MeC dimer (red) in comparison with DFT-MD and static harmonic spectra (blue and black, respectively).

Similar to what was done to the G-G system, we extract the ICDOC to have the signature of each C-H or N-H wagging motion in the 9EtG-1MeC system, as shown in Figure 4.23.

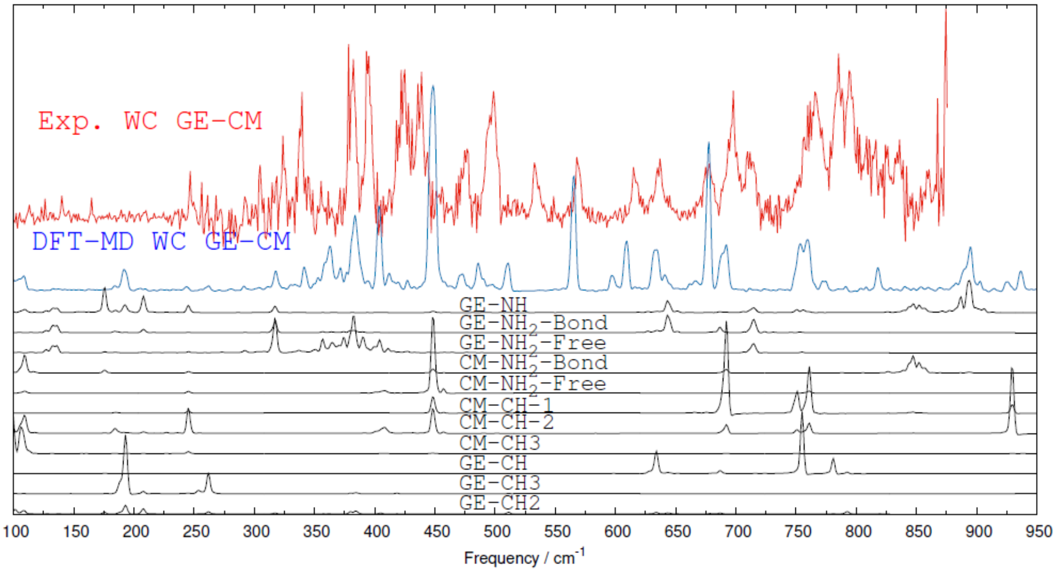

Figure 4.23: Identification of peaks in the theoretical spectrum (blue) with peaks in the ω(N-H) and ω(C-H) decomposition (black) for 9EtG-1MeC dimer.

First, we focus our attention on N-H wagging modes. Figure 4.24 shows the mode assignment of the ω(GE-NH) for 9ETG in DFT-MD and static harmonic spectra. ω(GE-NH) modes refer to the strong H-bonded group on 9EtG (Figure 4.20).

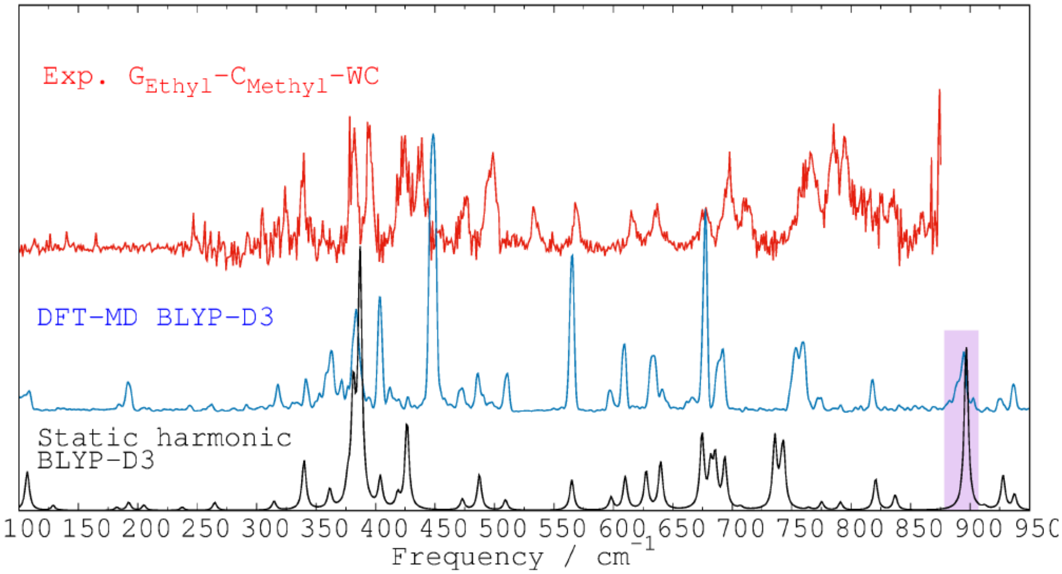

Figure 4.24: Mode assignment of ω(GE-NH) for 9EtG in 9EtG-1MeC dimer, highlighted in purple.

The length of the H-bond formed by this NH function with a nitrogen atom is 1.89 Å. For comparison, the length of the H-bond formed by the equivalent NH in the G-G system is 1.86 Å. After taking the anharmonicities into account, we see almost no shift indicating that this mode is anaharmonic. The corresponding experimental peak is probably outside the range of the measured spectrum. In G-G system, the signature of the strongly H-bonded N-H is located in the same position, ~900 cm^{-1}.

Now, we show the mode assignment of the ω(N-H) of NH2-Free and NH2-Bond modes for 9MeG in DFT-MD and static harmonic spectra (Figure 4.25). ω(N-H) modes of NH2-Free and NH2-Bond refer to the GE-NH2_Free and GE-NH2_Bond, respectively (Figure 4.20).

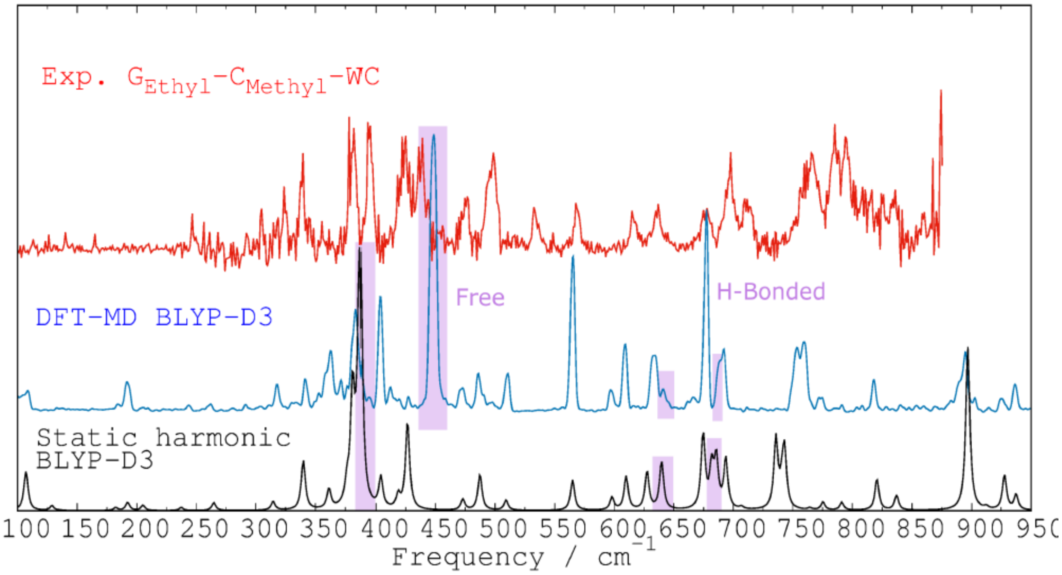

Figure 4.25: Mode assignment of ω(N-H) of NH2-Free and NH2-Bond modes for 9EtG in 9EtG-1MeC dimer.

This NH_2 function is involved in a hydrogen bond with the oxygen atom on the 1MeC; this hydrogen bond is 1.89 Å in length with no equivalence in the G-G system. The two hydrogen atoms (bonded and free) are not coupled together (no shared signatures) and it makes no sense to mix these motions together into symmetric and asymmetric contributions. We see the same behavior for the G-G dimer. For the H-bonded hydrogen atom, we have multiple signatures in different normal modes. The H-bonded hydrogen atom related modes have a harmonic behavior, while the mode for the free hydrogen atom is blue-shifted by 62 cm^{-1} after taking anharmonicities into account. As a result, we offer the following assignments. The 440 cm^{-1} experimental peak arises from ωGE-NH2_Free (DFT-MD value is 449 cm^{-1}). The 700 cm^{-1} experimental peak and the shoulder around 640 cm^{-1} arise from ωGE-NH2_Bond (DFT-MD values are 690 and 642 cm^{-1} for the shoulder).

For the final N-H wagging modes, we show the mode assignment of the ω(N-H) of NH2-Free and NH2-Bond modes for1MeC in DFT-MD and static harmonic spectra (Figure 4.26). ω(N-H) modes of NH2-Free and NH2-Bond refer to the CM-NH2_Free and CM-NH2_Bond, respectively (Figure 4.20).

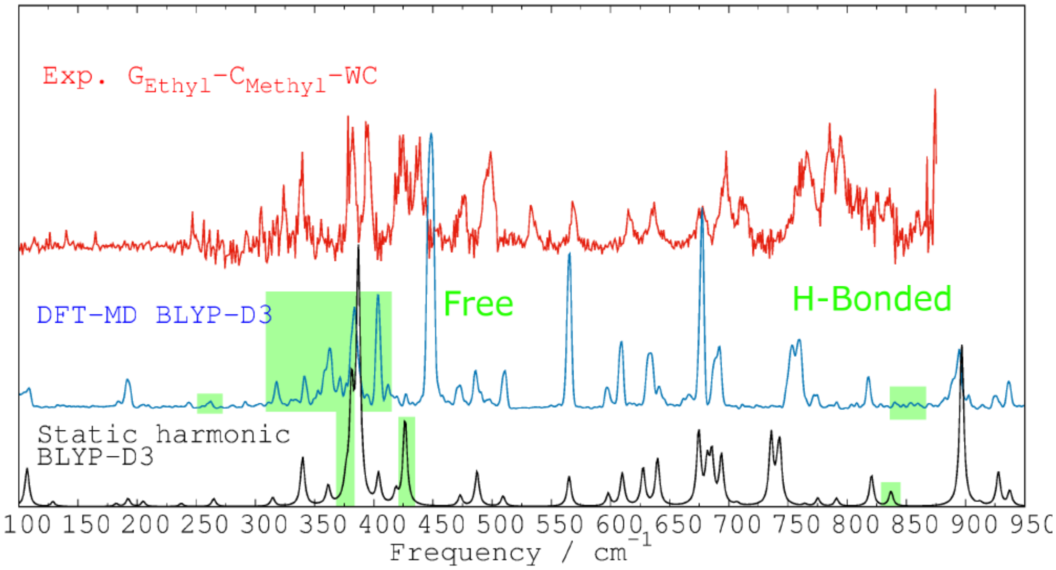

Figure 4.26: Mode assignment of ω(N-H) of NH2-Free and NH2-Bond modes for 1MeC in 9EtG-1MeC dimer, highlighted in green.

This NH_2 function is involved in a hydrogen bonding with the oxygen atom on the 9EtG; this hydrogen bond is 1.75 Å in length with no equivalence in the G-G system. Similar to 9EtG, the two hydrogen atoms are not coupled together and it makes no sense to mix these motions together into symmetric and asymmetric contributions. We see a small red shift for ωCM-NH2_Free and a small blue shift for ωCM-NH2_Bond after taking anharmonicities into account. We also notice similar behavior for equivalent H-bonded NH_2 in the G-G system. Due to the multiple peaks in the DFT-MD representation, no exact shift could be measured. We offer the following assignments: experimental peaks between 230 and 400 cm^{-1} are assigned to modes with strong contribution from ωCE-NH2_Free. Signatures arising from ωCE-NH2_Bond have very weak intensity so we do not assign any experimental peaks to this motion.

Now, we focus our attention on C-H wagging modes. Figure 4.27 shows the mode assignment of ωCH and ωCH_3 in DFT-MD and static harmonic spectra.

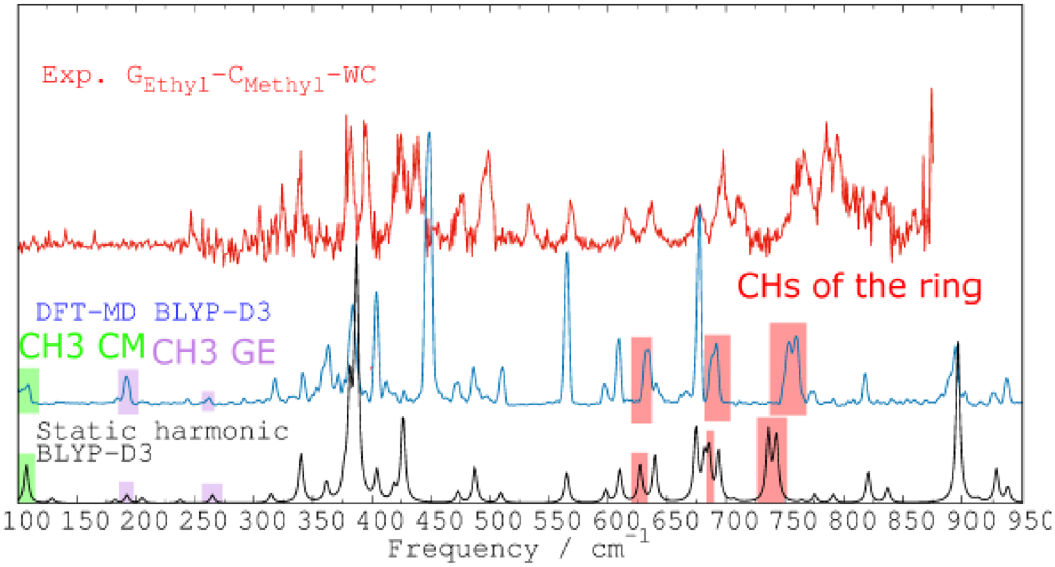

Figure 4.27: Mode assignment of ωCH and ωCH_3 in 9EtG-1MeC dimer. CHs of the rings are highlighted in red.

The CH_3 rotational mode is sensitive to its environment. The CH_3 group of the MeC is linked to an atom with an sp^2 hybridization and has its signature at ~100 cm^{-1} in the DFT-MD spectrum. On the other hand, the CH_3 group of the EtG is linked to an atom with an sp^3 hybridization and signatures at 194 and 262 cm^{-1}. No counterparts for the CH_3 signatures present in the DFT-MD can be found in the experimental spectrum. All the modes with CH wagging participation have harmonic behaviors. The 2 CH waggings in the MeC are coupled together while the CH wagging in the EtG is independent. Compared to the experiment, these modes are slightly red shifted.

For the rest of the peaks, there is a good correspondence between DFT-MD and the harmonic spectrum. In other words, those peaks have a strong harmonic behavior. This confirms our previous conclusion that delocalized modes have harmonic behaviors (at least in the BLYP-D3 representation). The overall assignment of the experimental peaks is shown in Figure 4.28.

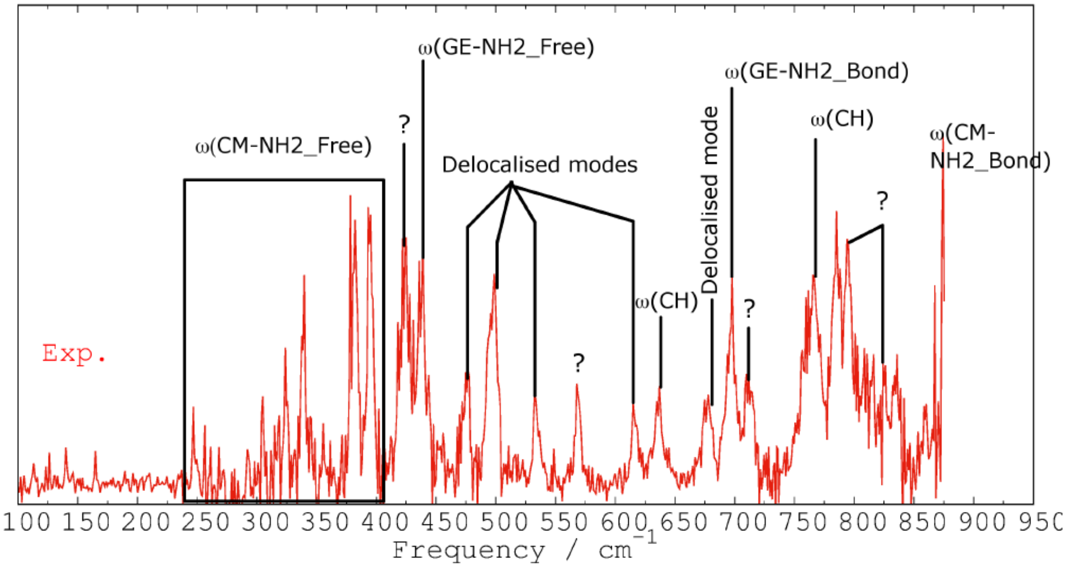

Figure 4.28: Assignment of 1MeC-9EtG experimental peaks. Question mark symbols (?) are placed on peaks with no counterparts in DFT-MD spectrum.

In summary, the experimental peaks located between 230 and 400, 440, and 700 cm^{-1} are assigned to normal modes with strong ω(N-H) wagging contributions. The peaks located at 638 and 768 cm^{-1} are assigned to normal modes with strong ω(N-H) wagging contributions. The peaks at 478, 500, 570, 616, and 679 cm^{-1} are explained by delocalized modes; these modes are mainly composed of bending motions. There are no counterparts in the theoretical spectra for the experimental peaks at 424, 533, 713, 785, and 796 cm^{-1}. In the G-G system, the missing peaks are explained by overtones or combinations bands calculated with the Gaussian-VPT2 method.

We have a consistent agreement (with the same systematic errors) between the DFT-MD and the experimental spectra for the two systems, G-G and 1MeC-9EtG. It is unclear why there is a poor agreement between experiment and theory in the region below 250 cm^{-1} for the 1MeC-9EtG system.

4.3.4 Triply hydrogen-bonded guanine-cytosine cluster.

Figure 4.29 shows the recorded one-color R2PI spectrum for the triply hydrogen bonded G-C dimer. In this wavelength range, one tautomer of GC is detected and the structure consists of cytosine in the enol form and guanine in the keto form with the hydrogen on the 7-psosition (7H-keto) [26], as shown in figure 4.30. Here, IR-UV ion-dip spectroscopy is collected by tuning the UV on the origin transition (33297 cm^{-1}) and scanning the IR over the far-IR region. The full experimental IR spectrum of the GC cluster (Figure 4.31 A) is divided into two pieces (Figure 4.31 B & C); the region below 500 cm^{-1} (Figure 4.31 C) is scaled up in order to clearly expose the small peaks.

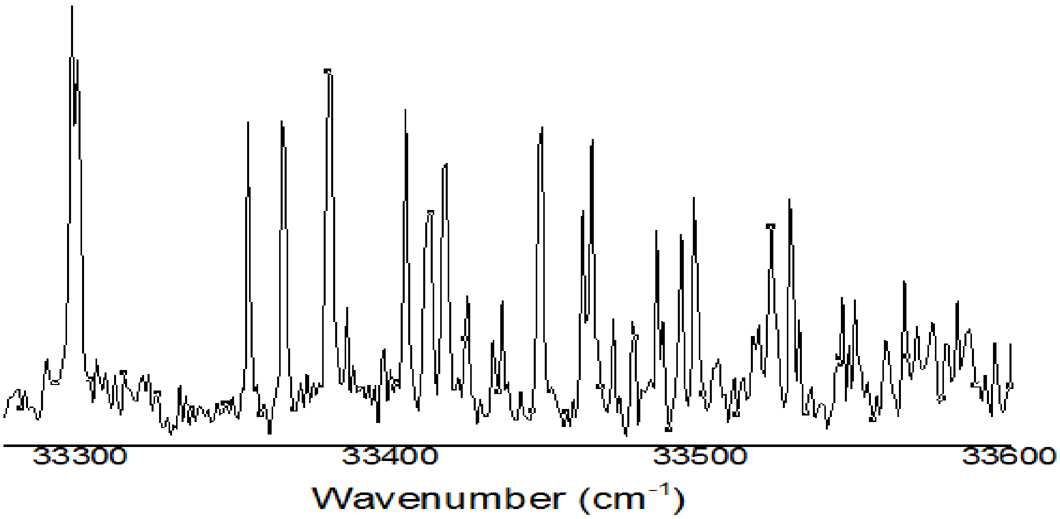

Figure 4.29: One-color resonant two-photon ionization (R2PI) spectrum of the triply hydrogen-bonded G-C dimer. The origin transition (0-0) is at 33297 cm^{-1}.

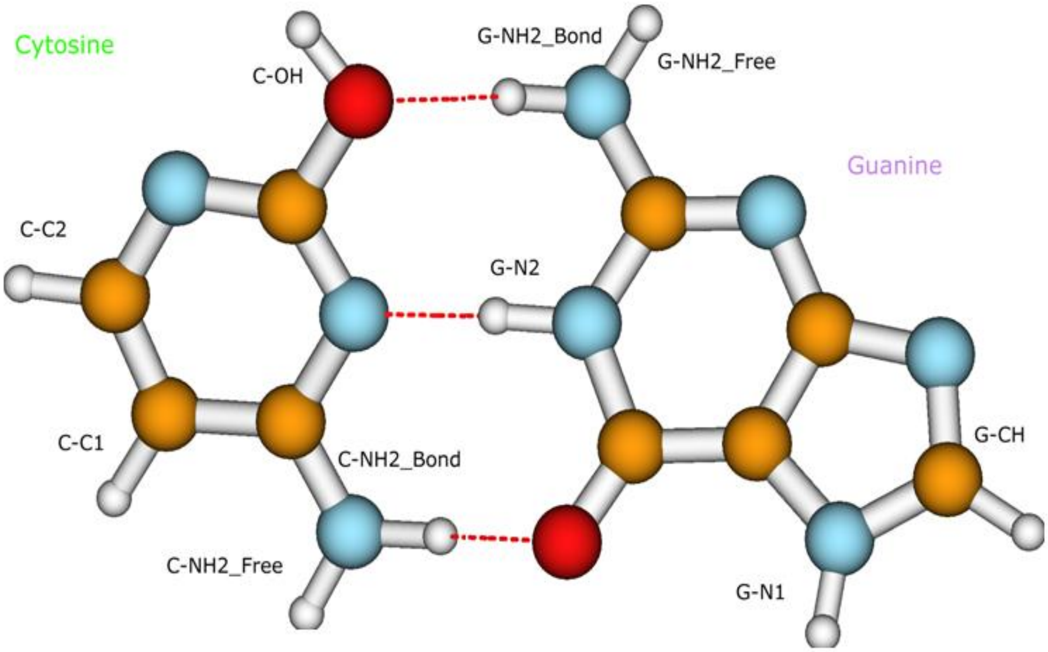

Figure 4.30: The molecular structure of enol cytosine and 7H-keto guanine dimer with the nomenclature employed.

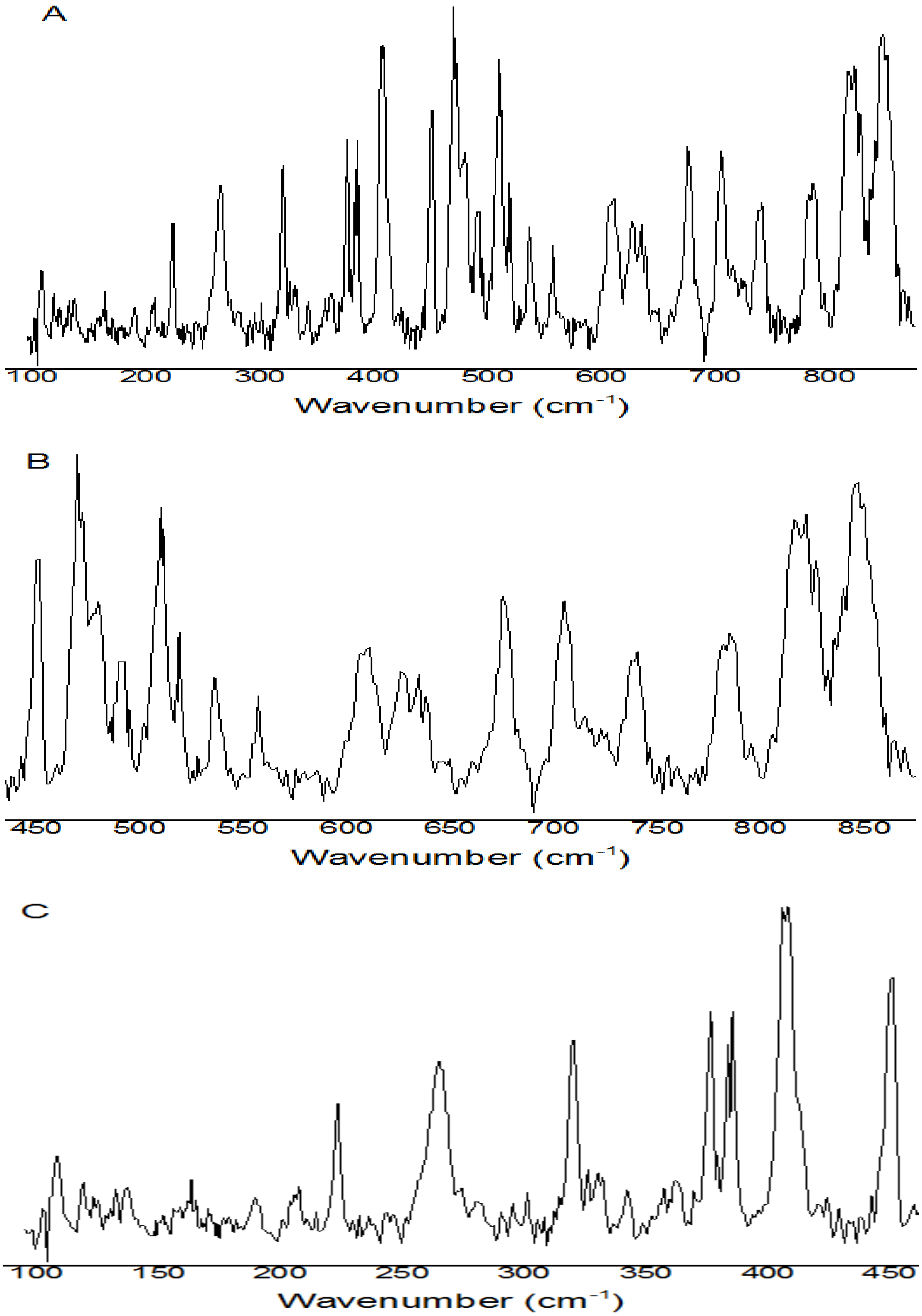

Figure 4.31: Experimental IR spectra of triply hydrogen-bonded GC dimer. Full spectrum (A), 470-880 cm^{-1} region (B), and 95-480 cm^{-1} region scaled up (C).

DFT-MD and static harmonic calculations are performed on the G-C system. Overall, there is reasonable agreement between experiment and the DFT-MD spectrum as shown in Figure 4.32. There are however experimental peaks without counterparts in the DFT-MD spectrum (nor static harmonic spectrum). These peaks are 459, 613, 628-641, and 741 cm^{-1}.

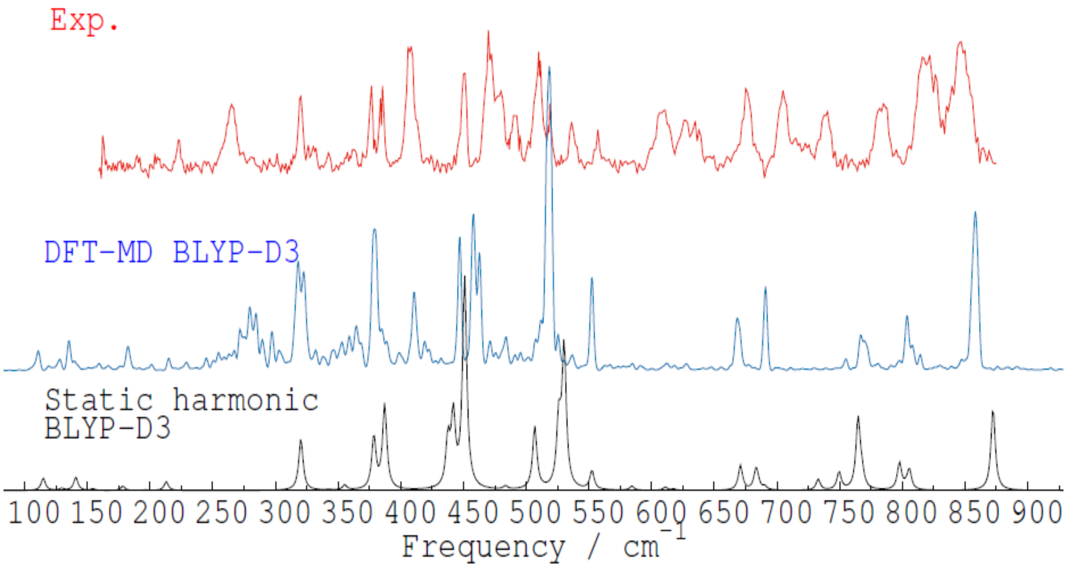

Figure 4.32: Experimental spectrum of G-C dimer (red) in comparison with DFT-MD and static harmonic spectra (blue and black, respectively).

At first sight, the DFT-MD spectrum is slightly improved from the static harmonic spectrum in terms of band shapes and positions.

Similar to what was done to the guanine system; we extract the ICDOC to have the signature of each C-H or N-H wagging motion in the G-C system, as shown in Figure 4.33.

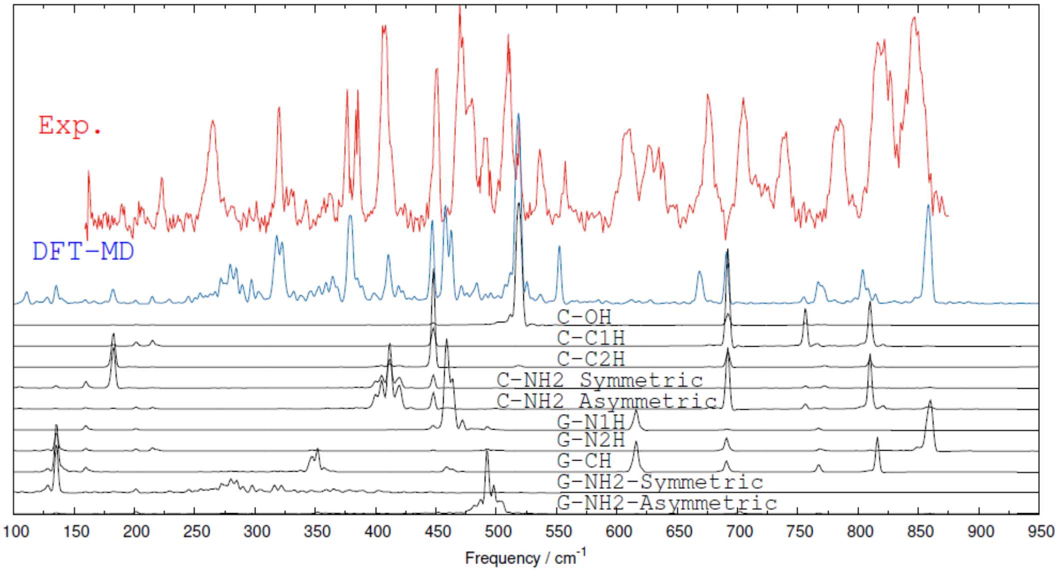

Figure 4.33: Identification of peaks in the theoretical spectrum (blue) with peaks in the ω(N-H) and ω(C-H) decomposition (black) for G-C dimer.

Figure 4.34 shows that mode assignment of the ω(N1-H) and ω(N2-H) for guanine in DFT-MD and static harmonic spectra. ω(N1-H) mode refers to the free N-H group, labeled as G-N1 and ω(N2-H) refers to the H-bonded N-H, labeled as G-N2. (Figure 4.30).

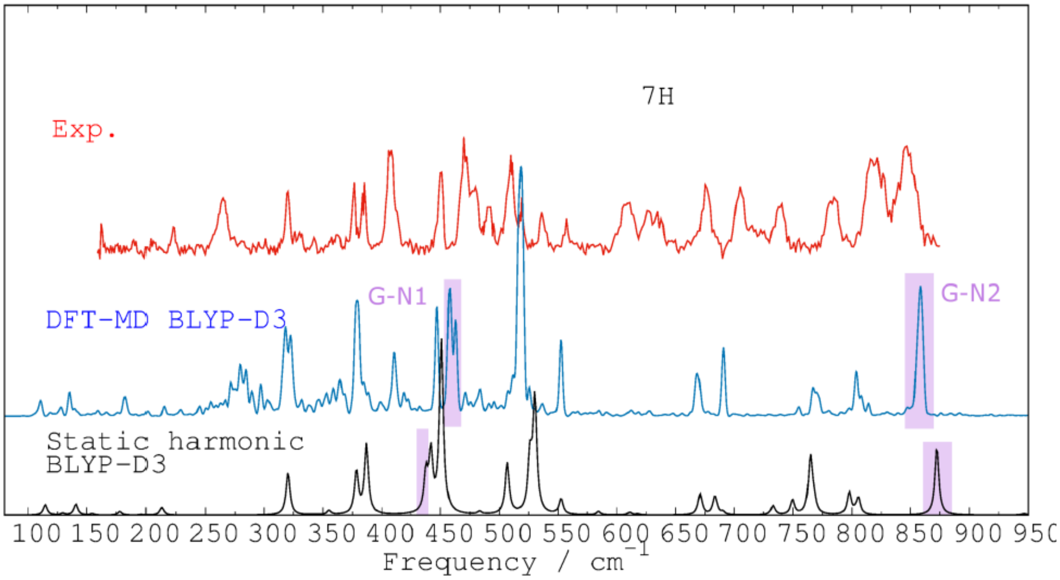

Figure 4.34: Mode assignment of ω(N1-H) and ω(N2-H) for guanine in G-C dimer.

We assign the experimental peak at 847 cm^{-1} to the ω(G-N2) mode of the strongly bonded NH function. Equivalent NH functions are present in the 1MeC-9EtG and the G-G clusters but with stronger H-Bond (In the harmonic calculation: 1.89 Å and 1.86 Å respectively instead of 1.93 Å here). The signatures for the other clusters are blue-shifted at ~900 cm^{-1} in the DFT-MD spectra. In this system and the previous ones, a small red-shift of few wavenumbers in the DFT-MD spectrum is observed in comparison with the static spectrum.

We assign the experimental peak at 471 cm^{-1} to the ω(G-N1) mode. The DFT-MD peak is red-shifted in comparison with the experiment (in G-G, we have no shift between the assigned peak of the experimental spectrum and the DFT-MD peak). Here, we observe a blue shift after taking the anharmonicities into account. We see this behavior for the equivalent function in the G-G system.

Next, we show the mode assignment of the ω(CH) for guanine and ω(C1H) and ω(C2H) for cytosine in DFT-MD and static harmonic spectra (Figure 4.35).

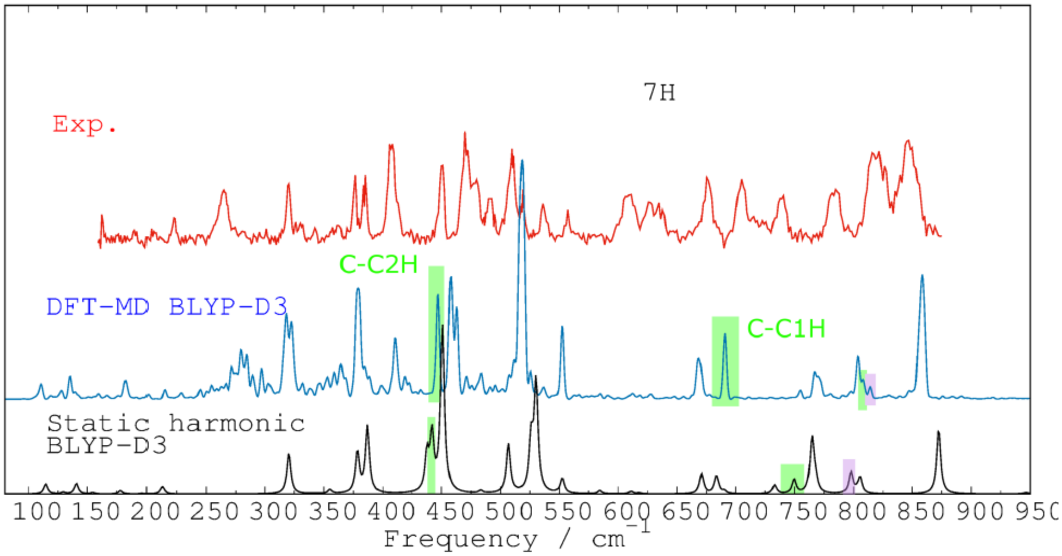

Figure 4.35: Mode assignment of ω(CH) for guanine and ω(C1H) and ω(C2H) for cytosine in G-C dimer. Modes of guanine are highlighted in purple and modes of cytosine are highlighted in green.

We assign the experimental peak at 452 cm^{-1} to the ω(C2H) mode. The mode is harmonic and both DFT-MD and harmonic spectra give well positioned signatures. The guanine mode ω(CH) does not provide an intense signature in the DFT-MD spectrum and no experimental peak is assigned to this mode. ω(C1H) wagging is the most interesting mode and we will discuss it later in more detail.

Finally, we show the mode assignment of the ω(O-H) and ω(N-H) of NH2-Free and NH2-Bond waggings for guanine and cytosine in DFT-MD and static harmonic spectra (Figure 4.36).

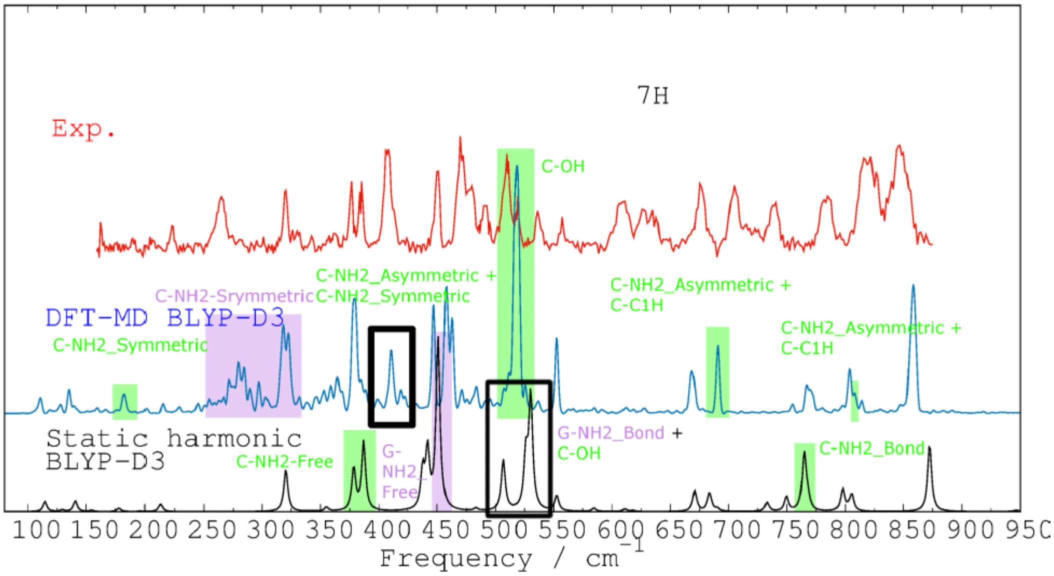

Figure 4.36: Mode assignment of ω(OH) and ω(N-H) of NH2_Free and NH2_Bond waggings for guanine and cytosine in G-C dimer. Modes of guanine are highlighted in purple and moded of cytosine are highlighted in green.

For these modes, we have strong differences between the harmonic and DFT-MD spectra. In the G-G and 1MeC-9EtG clusters, we have strong hydrogen bonds and no coupling between the waggings ω($NH2_{Bond}$) and ω($NH2_{Free}$). In the guanine system where the NH_2 function is free, the coupling between the two waggings is strong so we used the symmetric and asymmetric contributions. For the current system, we are probably at the turning point between the two possibilities. For the harmonic calculations, we still have strong enough hydrogen bonds to have the $\omega(\mathrm{NH2_{Bond}})$ / $\omega(\mathrm{NH2_{Free}})$ decouple. For the DFT-MD spectrum, we put enough energy in the system to weaken the hydrogen bonds and couple the $\omega(\mathrm{NH2_{Bond}})$ / $\omega(\mathrm{NH2_{Free}})$ waggings.

In the static spectrum, the $\omega(\mathrm{NH2_{Bond}})$ and $\omega(\mathrm{NH2_{Free}})$ waggings of the cytosine function are located around 760 and 360 $\mathrm{cm^{-1}}$ respectively. The NH_2 function is engaged in a strong hydrogen bond (1.79 Å after geometry optimization) and can be directly compared to $NH_2\cdots OH$ hydrogen bond present in G-G and 1MeC-9EtG systems (1.75 Å for both cluster after geometry optimization). After taking anharmonicities into account for the previous systems, we have a small blue shifts for the $\omega(\mathrm{NH2_{Bond}})$ signature, an important red-shift, and an enlargement of the signatures for $\omega(\mathrm{NH2_{Free}})$. This is more complicated in this DFT-MD spectrum, mostly because of coupling of these waggings with the ω(C1H) wagging. We therefore assign the experimental peaks at 821 and 705 $\mathrm{cm^{-1}}$ to a combination of $\omega(\mathrm{NH2_{Asymmetric}})$ and ω(C1H) and the experimental peak at 408 $\mathrm{cm^{-1}}$ to a combination of the $\omega(\mathrm{NH2_{Asymmetric}})$ and $\omega(\mathrm{NH2_{Symmetric}})$ contributions.

In the static spectrum, the $\omega(\mathrm{NH2_{Free}})$ gives a signature at 450 $\mathrm{cm^{-1}}$ while the $\omega(\mathrm{NH2_{Bond}})$ couples with the ω(OH) wagging to provide two peaks around 520 $\mathrm{cm^{-1}}$. The associated NH_2 function is involved in a weak hydrogen bond (2.04 Å after geometry optimization) that can be directly compared to the $NH_2\cdots OH$ hydrogen bond present in the G-G cluster (2.04 Å after geometry optimization). In the G-G system, we have signatures around 380 and 600 $\mathrm{cm^{-1}}$ in the DFT-MD spectrum for $\omega(\mathrm{NH2_{Bond}})$ and $\omega(\mathrm{NH2_{Free}})$ respectively, slightly red shifted in comparison with the harmonic spectrum. For G-C, the ω(NH2$_{\text{Asymmetric}}$) signature is located near 500 cm^{-1} but does not provide intense signatures in the DFT-MD spectrum. The ω(OH) is not coupled with other motions as in the harmonic calculation but it is not clear whether it should be assigned to the 511 or 538 cm^{-1} peak in the experimental spectrum. The two peaks at 265 and 321 cm^{-1} in the experimental spectrum are assigned to the ω(NH2$_{\text{Symmetric}}$) mode and the DFT-MD spectrum reproduces those two experimental peaks.

The overall assignment of the experimental peaks is shown in Figure 4.37.

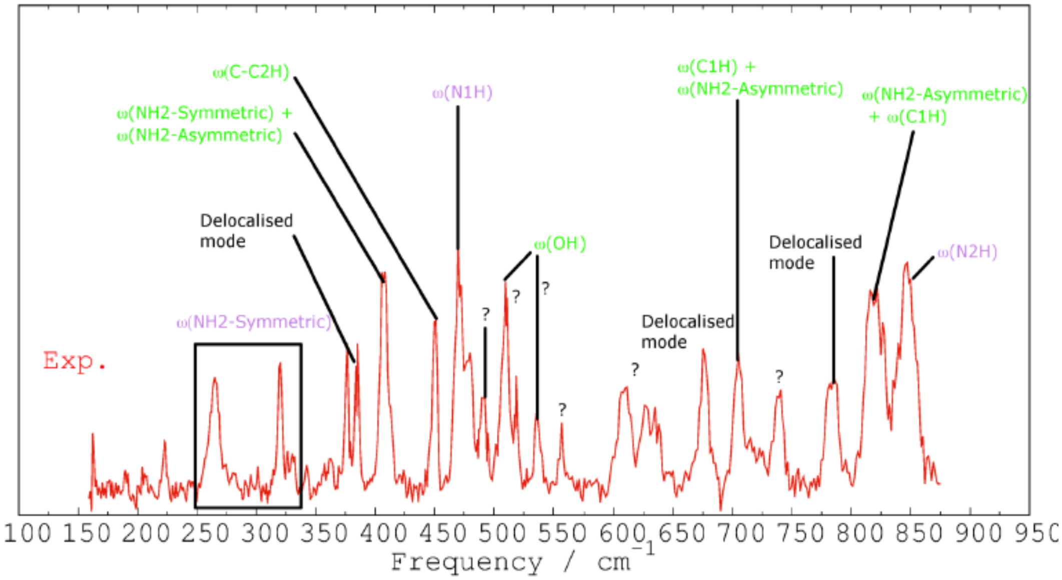

Figure 4.37: Assignment of G-C experimental peaks. Question mark symbols (?) are placed on peaks with no counterparts in DFT-MD spectrum.

To summarize, the experimental peaks located at 265, 321, 408, 471, 705 and 821 cm^{-1} are assigned to ω(N-H) wagging modes. The 452 cm^{-1} experimental spectrum is assigned to ω(C-H) motion which also has important contributions in the 705 and 821 cm^{-1} modes. It is not clear whether the ω(OH) mode has to be assigned to the 511 or to the 538 cm^{-1} experimental peak. The peaks located at 491, 559, 613 and 741 cm^{-1} in the experimental spectrum and the massif between 628 and 641 cm^{-1} have no counterparts in the

DFT-MD spectrum. The experimental peaks at 378 or 387, 676 and 784 cm^{-1} are assigned to delocalized modes; these modes are mainly composed of bending motions. In this system, the main differences between the harmonic and DFT-MD spectra come from the NH_2 signatures. We find the same anharmonicities for comparable functions except for the NH_2 function of the guanine in the G-C system, which provides something not found in the other systems.

4.3.5 Doubly hydrogen-bonded guanine-cytosine dimer

Figure 4.38 shows the recorded one-color R2PI spectrum for the double hydrogen bonded G-C dimer. In this wavelength range, one tautomer of G-C is detected and the structure consists of both cytosine and guanine in the keto form with the hydrogen on guanine positioned at the 9th nitrogen atom (9H-keto) [26], as shown in figure 4.39. Here, IR-UV ion-dip spectroscopy is collected by tuning the UV to the origin transition (32813 cm^{-1}) and scanning the IR over the far-IR region. The full experimental IR spectrum of the doubly H-bonded G-C dimer (Figure 4.40 A) is divided into two pieces (Figure 4.40 B & C); the region below 500 cm^{-1} (Figure 4.40 C) is scaled up in order to clearly expose the small peaks.

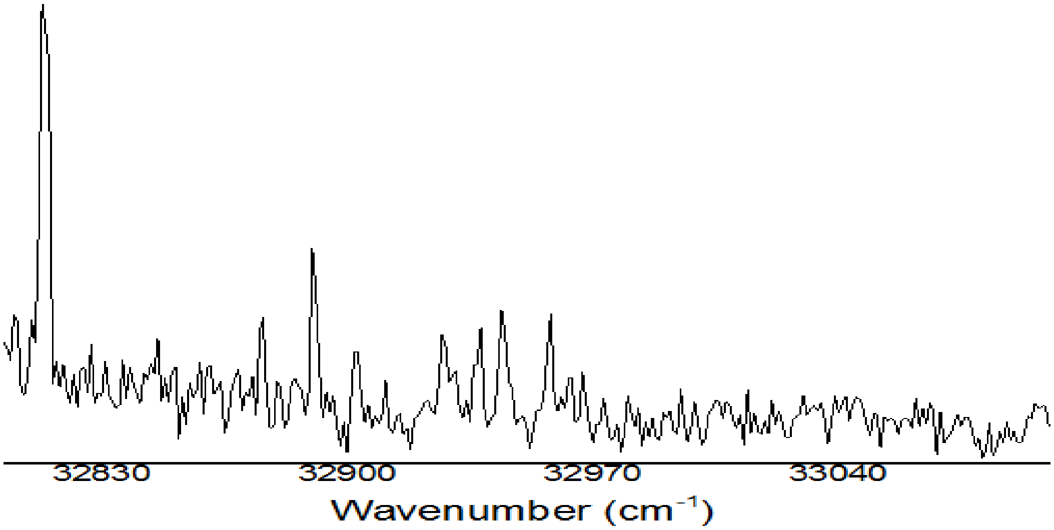

Figure 4.38: One-color resonant two-photon ionization (R2PI) spectrum of the doubly hydrogen-bonded G-C dimer. The origin transition (0-0) is at 32813 cm^{-1}.

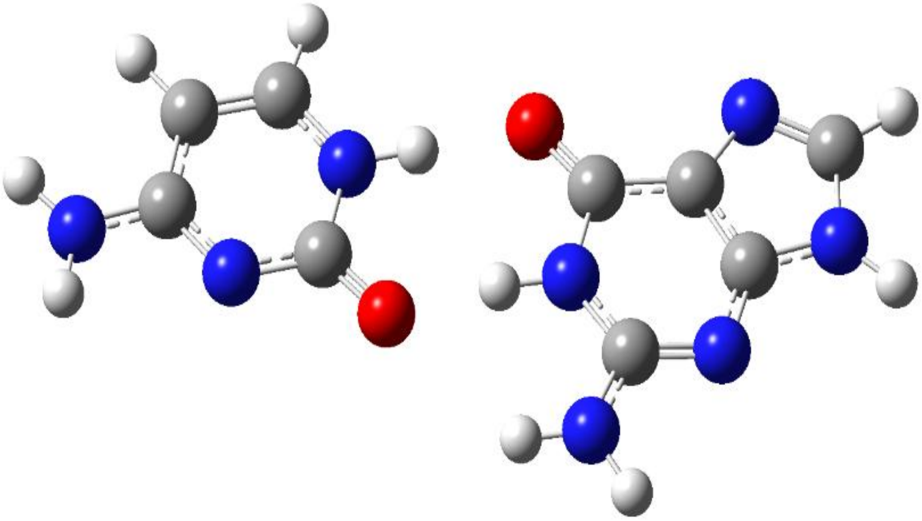

Figure 4.39: The molecular structure of the doubly hydrogen-bonded G-C dimer. Both cytosine and guanine are in the keto form.

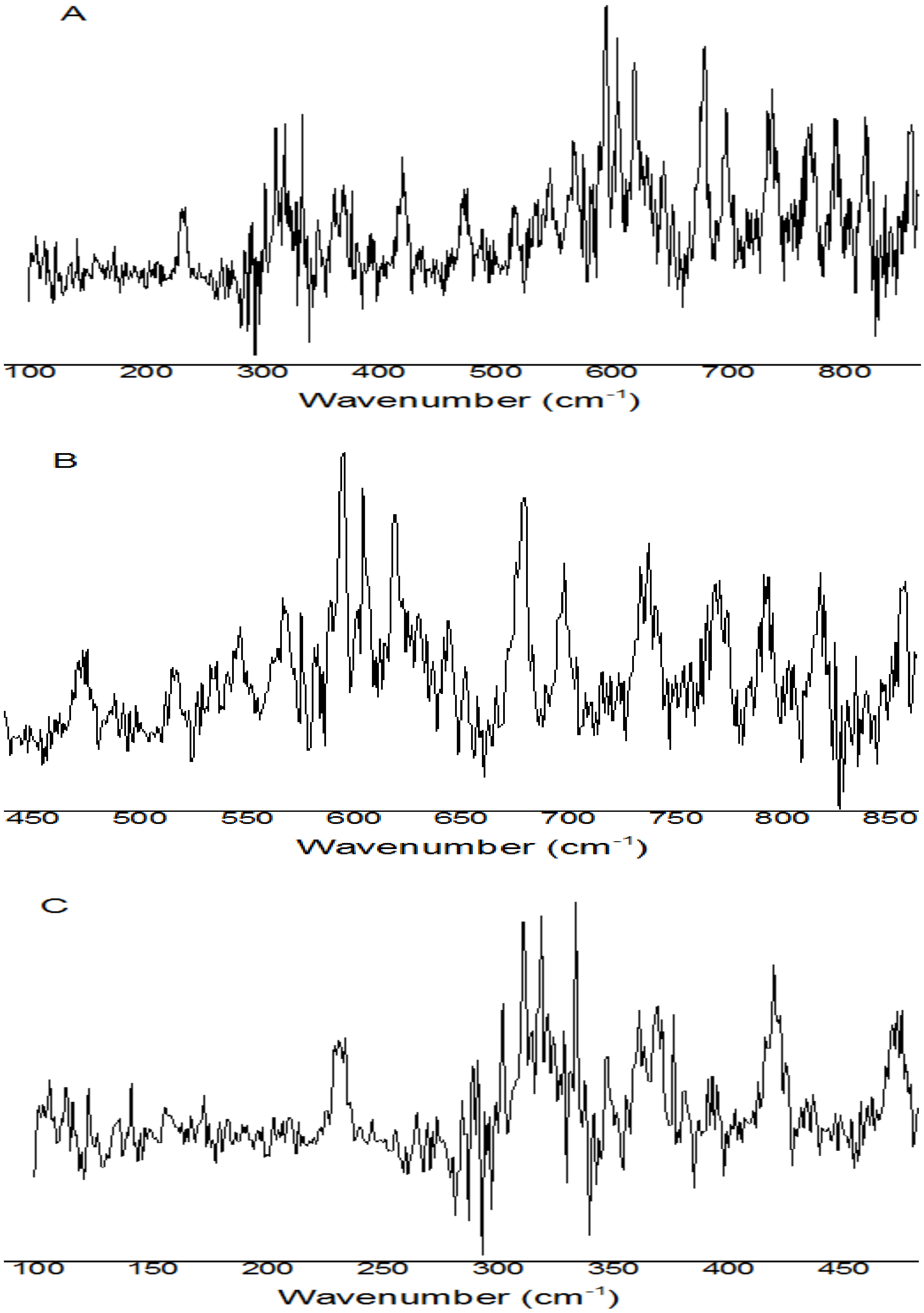

Figure 4.40: Experimental IR spectra of the doubly hydrogen-bonded G-C dimer. Full spectrum (A), 470-880 cm^{-1} region (B), and 95-480 cm^{-1} region scaled up (C).

Theoretical calculations on this system are currently in progress.

4.4 Summary

We used the free electron laser and the IR-UV ion-dip technique to collect the ground state IR spectra for several guanine-cytosine base pairs in the gas phase. To structurally characterize these base pairs, we performed BOMD simulations because this method does not rely on harmonic approximations and therefore it is ideal for assignments in the far-IR region. BOMD simulation seems to work better for clusters compared to monomers. Although BOMD was capable of assigning most of the peaks in the IR spectra, there are few limitations to this method. It had difficulties assigning peaks in the region below 250 cm^{-1} which is an important region because it provides information on intermolecular hydrogen bonding signatures. BOMD was not able to assign all peaks which other calculations assigned to combinations bands and overtones. Overall, BOMD is the first attempt to explain the experimental data and we seem to be on the right track. In the future, we are seeking an improved method which will hopefully explain every single peak. Moreover, we will perform excited state calculations on these systems. This will provide us with information on how these base pairs respond to UV light and how their structures and the hydrogen bonding vibrations change with and without UV light.

References

1. Nir, E., Grace, L., Brauer, B. & de Vries, M. S. REMPI Spectroscopy of Jet-Cooled Guanine. *J. Am. Chem. Soc.* **121,** 4896–4897 (1999).

2. Kim, N. J. *et al.* Resonant two-photon ionization and laser induced fluorescence spectroscopy of jet-cooled adenine. *J. Chem. Phys.* **113,** 10051–10055 (2000).

3. Lührs, D. C., Viallon, J. & Fischer, I. Excited state spectroscopy and dynamics of isolated adenine and 9-methyladenine. *Phys. Chem. Chem. Phys.* **3,** 1827–1831 (2001).

4. Plützer, C., Nir, E., de Vries, M. S. & Kleinermanns, K. IR–UV double-resonance spectroscopy of the nucleobase adenine. *Phys. Chem. Chem. Phys.* **3,** 5466–5469 (2001).

5. Nir, E., Müller, M., Grace, L. I. & De Vries, M. S. REMPI spectroscopy of cytosine. *Chem. Phys. Lett.* **355,** 59–64 (2002).

6. Chin, W. *et al.* Tautomer contributions to the near UV spectrum of guanine: towards a refined picture for the spectroscopy of purine molecules. *Eur. Phys. J. D* **20,** 347–355 (2002).

7. Choi, M. Y. & Miller, R. E. Four Tautomers of Isolated Guanine from Infrared Laser Spectroscopy in Helium Nanodroplets. *J. Am. Chem. Soc.* **128,** 7320–7328 (2006).

8. Mons, M., Piuzzi, F., Dimicoli, I., Gorb, L. & Leszczynski, J. Near-UV resonant two-photon ionization spectroscopy of gas phase guanine: evidence for the observation of three rare tautomers. *J. Phys. Chem. A* **110,** 10921–10924 (2006).

9. Ligare, M., Siouri, F., Bludsky, O., Nachtigallová, D. & de Vries, M. S. Characterizing the dark state in thymine and uracil by double resonant spectroscopy and quantum computation. *Phys Chem Chem Phys* **17,** 24336–24341 (2015).

10. Nir, E., Kleinermanns, K. & de Vries, M. S. Pairing of isolated nucleic-acid bases in the absence of the DNA backbone. *Nature* **408,** 949–951 (2000).

11. Nir, E., Janzen, C., Imhof, P., Kleinermanns, K. & de Vries, M. S. Pairing of the nucleobases guanine and cytosine in the gas phase studied by IR–UV double-resonance spectroscopy and ab initio calculations. *Phys. Chem. Chem. Phys.* **4,** 732–739 (2002).

12. Plützer, C., Hünig, I., Kleinermanns, K., Nir, E. & de Vries, M. S. Pairing of Isolated Nucleobases: Double Resonance Laser Spectroscopy of Adenine-Thymine. *ChemPhysChem* **4,** 838–842 (2003).

13. Abo-Riziq, A. *et al.* Photochemical selectivity in guanine–cytosine base-pair structures. *Proc. Natl. Acad. Sci. U. S. A.* **102,** 20–23 (2005).

14. Daniels, M. & Hauswirth, W. Fluorescence of the Purine and Pyrimidine Bases of the Nucleic Acids in Neutral Aqueous Solution at 300 K. *Am. Assoc. Adv. Sci.* **171,** 675–677 (1971).

15. Callis, P. R. Electronic states and luminescence of nucleic acid systems. *Annu. Rev. Phys. Chem.* **34,** 329–357 (1983).

16. Peon, J. & Zewail, A. H. DNA/RNA nucleotides and nucleosides: direct measurement of excited-state lifetimes by femtosecond fluorescence up-conversion. *Chem. Phys. Lett.* **348,** 255–262 (2001).

17. Kang, H., Jung, B. & Kim, S. K. Mechanism for ultrafast internal conversion of adenine. *J. Chem. Phys.* **118,** 6717–6719 (2003).

18. Crespo-Hernández, C. E., Cohen, B., Hare, P. M. & Kohler, B. Ultrafast Excited-State Dynamics in Nucleic Acids. *Chem. Rev.* **104,** 1977–2020 (2004).

19. Broo, A. A theoretical investigation of the physical reason for the very different luminescence properties of the two isomers adenine and 2-aminopurine. *J. Phys. Chem. A* **102,** 526–531 (1998).

20. Watson, J. D. & Crick, F. H. C. A Structure for Deoxyribose Nucleic Acid. *Nature* **171,** 737–738 (1953).

21. Franklin, R. E. & Gosling, R. G. Molecular Configuration in Sodium Thymonucleate. *Nature* **171,** 740–741 (1953).

22. Watson, J. D. & Crick, F. H. C. Genetical Implications of the structure of Deoxyribonucleic Acid. *Nature* **171,** 964–967 (1953).

23. Löwdin, P.-O. Proton tunneling in DNA and its biological implications. *Rev. Mod. Phys.* **35,** 724 (1963).

24. Hanus, M. *et al.* Correlated ab Initio Study of Nucleic Acid Bases and Their Tautomers in the Gas Phase, in a Microhydrated Environment and in Aqueous Solution. Guanine: Surprising Stabilization of Rare Tautomers in Aqueous Solution. *J. Am. Chem. Soc.* **125,** 7678–7688 (2003).

25. Hanus, M., Kabeláč, M., Rejnek, J., Ryjáček, F. & Hobza, P. Correlated ab Initio Study of Nucleic Acid Bases and Their Tautomers in the Gas Phase, in a Microhydrated Environment, and in Aqueous Solution. Part 3. Adenine. *J. Phys. Chem. B* **108,** 2087–2097 (2004).

26. Bakker, J. M. *et al.* The mid-IR absorption spectrum of gas-phase clusters of the nucleobases guanine and cytosine. *Phys Chem Chem Phys* **6,** 2810–2815 (2004).

27. Kool, E. T., Morales, J. C. & Guckian, K. M. Mimicking the Structure and Function of DNA: Insights into DNA Stability and Replication. *Angew Chem Int Ed Engl* **39,** 990–1009 (2000).

28. Goodman, M. F. Hydrogen bonding revisited: geometric selection as a principal determinant of DNA replication fidelity. *Proc. Natl. Acad. Sci.* **94,** 10493–10495 (1997).

29. Noguera, M., Sodupe, M. & Bertran, J. Effects of protonation on proton-transfer processes in guanine?cytosine Watson?Crick base pairs. *Theor. Chem. Acc.* **112,** (2004).

30. Nedderman, A., Stone, M., Williams, D., Lin, P. & Brown, D. Molecular basis for methoxyamine-initiated mutagenesis: 1H magnetic resonance studies of oligonucleotide duplexes containing base-modified cytosine residues. *J Mol Biol* **230,** 1068–1076 (1993).

31. Gorb, L. *et al.* A quantum-dynamics study of the prototropic tautomerism of guanine and its contribution to spontaneous point mutations in Escherichia coli. *Biopolymers* **61,** 77–83 (2001).

32. Podolyan, Y., Gorb, L. & Leszczynski, J. *Ab initio study of the prototropic tautomerism of cytosine and guanine and their contribution to spontaneous point mutations*. (Molecular Diversity Preservation International, 2003).

33. Leszczynski, J. The potential energy surface of guanine is not flat: an ab initio study with large basis sets and higher order electron correlation contributions. *J. Phys. Chem. A* **102,** 2357–2362 (1998).

34. Gorb, L., Podolyan, Y., Dziekonski, P., Sokalski, W. A. & Leszczynski, J. Double-Proton Transfer in Adenine−Thymine and Guanine−Cytosine Base Pairs. A Post-Hartree−Fock ab Initio Study. *J. Am. Chem. Soc.* **126,** 10119–10129 (2004).

35. Tofazzal, H. M. *et al.* Crystallographic studies on damaged DNAs IV. N4-methoxycytosine shows a second face for Watson-Crick base-pairing, leading to purine transition mutagenesis. *Nucleic Acids Res.* **29,** 4949–3954 (2001).

36. Fodor, S., Rava, R. P., Copeland, R. A. & Spiro, T. G. H2 Raman-shifted YAG laser ultraviolet Raman spectrometer operating at wavelengths down to 184 nm. *J. Raman Spectrosc.* **17,** 471–475 (1986).

37. Urabe, H. *et al.* Collective vibrational modes in molecular assembly of DNA and its application to biological systems. Low frequency Raman spectroscopy. *J. Chem. Phys.* **82,** 531–535 (1985).

38. Cocco, S. & Monasson, R. Theoretical study of collective modes in DNA at ambient temperature. *J. Chem. Phys.* **112,** 10017–10033 (2000).

39. Brady, B. B., Peteanu, L. A. & Levy, D. H. The electronic spectra of the pyrimidine bases uracil and thymine in a supersonic molecular beam. *Chem. Phys. Lett.* **147,** 538–543 (1988).

40. Viant, M. R., Fellers, R. S., McLaughlin, R. P. & Saykally, R. J. Infrared laser spectroscopy of uracil in a pulsed slit jet. *J. Chem. Phys.* **103,** 9502–9505 (1995).

41. Yanson, I. K., Teplitsky, A. B. & Sukhodub, L. F. Experimental studies of molecular interactions between nitrogen bases of nucleic acids. *Biopolymers* **18,** 1149–1170 (1979).

42. Dey, M., Moritz, F., Grotemeyer, J. & Schlag, E. W. Base Pair Formation of Free Nucleobases and Mononucleosides in the Gas Phase. *J. Am. Chem. Soc.* **116,** 9211–9215 (1994).

43. Dey, M., Grotemeyer, J. & Schlag, E. W. Pair Formation of Free Nucleobases and Mononucleosides in the Gas Phase. *Z Naturforsch* **49,** 776–784 (1994).

44. Ligare, M. R. *et al.* Resonant Infrared Multiple Photon Dissociation Spectroscopy of Anionic Nucleotide Monophosphate Clusters. *J. Phys. Chem. B* **119,** 7894–7901 (2015).

45. Rijs, A. M., Kay, E. R., Leigh, D. A. & Buma, W. J. IR Spectroscopy on Jet-Cooled Isolated Two-Station Rotaxanes. *J. Phys. Chem. A* **115,** 9669–9675 (2011).

46. Jaeqx, S., Oomens, J., Cimas, A., Gaigeot, M.-P. & Rijs, A. M. Gas-Phase Peptide Structures Unraveled by Far-IR Spectroscopy: Combining IR-UV Ion-Dip Experiments with Born-Oppenheimer Molecular Dynamics Simulations. *Angew. Chem. Int. Ed.* **53,** 3663–3666 (2014).

47. Constantinidis, P., Schmitt, H.-C., Fischer, I., Yan, B. & Rijs, A. M. Formation of polycyclic aromatic hydrocarbons from bimolecular reactions of phenyl radicals at high temperatures. *Phys Chem Chem Phys* **17,** 29064–29071 (2015).

48. Cirtog, M. *et al.* Far/Mid-Infrared Signatures of Solvent–Solute Interactions in a Microhydrated Model Peptide Chain. *J. Phys. Chem. Lett.* **3,** 3307–3311 (2012).

49. Bakker, D. J., Peters, A., Yatsyna, V., Zhaunerchyk, V. & Rijs, A. M. Far-Infrared Signatures of Hydrogen Bonding in Phenol Derivatives. *J. Phys. Chem. Lett.* **7,** 1238–1243 (2016).

50. Tan, E. M. M. *et al.* Conformational Heterogeneity of Methyl 4-Hydroxycinnamate: A Gas-Phase UV–IR Spectroscopic Study. *J. Phys. Chem. B* **117,** 4798–4805 (2013).

51. Mahé, J., Jaeqx, S., Rijs, A. M. & Gaigeot, M.-P. Can far-IR action spectroscopy combined with BOMD simulations be conformation selective? *Phys Chem Chem Phys* **17,** 25905–25914 (2015).

52. Yatsyna, V., Bakker, D. J., Feifel, R., Rijs, A. M. & Zhaunerchyk, V. Aminophenol isomers unraveled by conformer-specific far-IR action spectroscopy. *Phys Chem Chem Phys* **18,** 6275–6283 (2016).

53. Bakker, D. J. *et al.* Anharmonic, dynamic and functional level effects in far-infrared spectroscopy: phenol derivatives. *J. Mol. Spectrosc.* (2017). doi:10.1016/j.jms.2017.02.004

54. Carney, J. R., Hagemeister, F. C. & Zwier, T. S. The hydrogen-bonding topologies of indole–(water)n clusters from resonant ion-dip infrared spectroscopy. *J. Chem. Phys.* **108,** 3379–3382 (1998).

55. Bakker, J. M., Aleese, L. M., Meijer, G. & von Helden, G. Fingerprint IR Spectroscopy to Probe Amino Acid Conformations in the Gas Phase. *Phys. Rev. Lett.* **91,** (2003).

56. Çarçabal, P. *et al.* Hydrated complexes of tryptophan: ion dip infrared spectroscopy in the 'molecular fingerprint' region, 100–2000 cm $^{-1}$. *Phys Chem Chem Phys* **6,** 4546–4552 (2004).

57. *Gas-Phase IR Spectroscopy and Structure of Biological Molecules*. **364,** (Springer International Publishing, 2015).

58. Falconer, R. J. & Markelz, A. G. Terahertz Spectroscopic Analysis of Peptides and Proteins. *J. Infrared Millim. Terahertz Waves* **33,** 973–988 (2012).

59. Itoh, K. & Shimanouchi, T. Far-infrared spectra of N-methylacetamide and related compounds and hydrogen-bond force constants. *Biopolymers* **5,** 921–930 (1967).

60. Seefeld, K., Brause, R., Häber, T. & Kleinermanns, K. Imino Tautomers of Gas-Phase Guanine from Mid-Infrared Laser Spectroscopy. *J. Phys. Chem. A* **111,** 6217–6221 (2007).

61. Nir, E., Janzen, C., Imhof, P., Kleinermanns, K. & de Vries, M. S. Guanine tautomerism revealed by UV–UV and IR–UV hole burning spectroscopy. *J. Chem. Phys.* **115,** 4604–4611 (2001).

62. Mons, M., Dimicoli, I., Piuzzi, F., Tardivel, B. & Elhanine, M. Tautomerism of the DNA Base Guanine and Its Methylated Derivatives as Studied by Gas-Phase Infrared and Ultraviolet Spectroscopy. *J. Phys. Chem. A* **106,** 5088–5094 (2002).

63. Nir, E., Hünig, I., Kleinermanns, K. & de Vries, M. S. The nucleobase cytosine and the cytosine dimer investigated by double resonance laser spectroscopy and ab initio calculations. *Phys Chem Chem Phys* **5,** 4780–4785 (2003).

64. Nir, E., Plützer, C., Kleinermanns, K. & de Vries, M. Properties of isolated DNA bases, base pairs and nucleosides examined by laser spectroscopy. *Eur. Phys. J. D* **20,** 317–329 (2002).

65. Šponer, J. & Hobza, P. Molecular Interactions of Nucleic Acid Bases. A Review of Quantum-Chemical Studies. *Collect. Czechoslov. Chem. Commun.* **68,** 2231–2282 (2003).

66. Hobza, P., Kabeláč, M., Sponer, J., Mejzlik, P. & Vondrasek, J. Performance of Empirical Potentials (AMBER, CFF95, CVFF, CHARMM, OPLS, POLTEV), Semiempirical Quantum Chemical Methods (AM1, MND)/M, PM3), and Ab Initio Hartee-Fock Method for Interaction od DNA Bases: Comparison with Nonempirical Beyond Hartee-Fock Results. *J. Comput. Chem.* **18,** 1136–1150 (1997).

67. Šponer, J., Jurečka, P. & Hobza, P. Accurate Interaction Energies of Hydrogen-Bonded Nucleic Acid Base Pairs. *J. Am. Chem. Soc.* **126,** 10142–10151 (2004).

68. Shishkin, O., Šponer, J. & Hobza, P. Intramolecular flexibility of DNA bases in adenine–thymine and guanine–cytosine Watson–Crick base pairs. *J. Mol. Struct.* **477,** 15–21 (1999).

69. Burda, J. V., Šponer, J., Hrabáková, J., Zeizinger, M. & Leszczynski, J. The Influence of N $_7$ Guanine Modifications on the Strength of Watson−Crick Base Pairing and Guanine N $_1$ Acidity: Comparison of Gas-Phase and Condensed-Phase Trends. *J. Phys. Chem. B* **107,** 5349–5356 (2003).

70. Danilov, V. I. & Anisimov, V. M. Post Hartree-Fock Studies of the Canonical Watson-Crick DNA Base Pairs: Molecular Structure and the Nature of Stability. *J. Biomol. Struct. Dyn.* **22,** 471–482 (2005).

71. Kabanov, A. V., Komarov, V. M., Yakushevich, L. V. & Teplukhin, A. V. Low-frequency intra- and intermolecular vibration modes of H-bonded nucleobases in oligonucleotide double helixes and hydrated nucleotide duplex: Application of the PM3 method. *Int. J. Quantum Chem.* **100,** 595–609 (2004).

72. JureÄ • ka, P., Nachtigall, P. & Hobza, P. RI-MP2 calculations with extended basis setsâ€”a promising tool for study of H-bonded and stacked DNA base pairs. *Phys. Chem. Chem. Phys.* **3,** 4578–4582 (2001).

73. Florián, J., Leszczynski, J. & Johnson, B. G. On the intermolecular vibrational modes of the guanine··· cytosine, adenine··· thymine and formamide··· formamide H-bonded dimers. *J. Mol. Struct.* **349,** 421–426 (1995).

74. Špirko, V., Šponer, J. & Hobza, P. Anharmonic and harmonic intermolecular vibrational modes of the DNA base pairs. *J. Chem. Phys.* **106,** 1472–1479 (1997).

75. Grunenberg, J. Direct Assessment of Interresidue Forces in Watson−Crick Base Pairs Using Theoretical Compliance Constants. *J. Am. Chem. Soc.* **126,** 16310–16311 (2004).

76. Brauer, B. *et al.* Vibrational Spectroscopy of the G· · ·C Base Pair: Experiment, Harmonic and Anharmonic Calculations, and the Nature of the Anharmonic Couplings. *J. Phys. Chem. A* **109,** 6974–6984 (2005).

77. Henderson, E., Hardin, C. C., Walk, S. K., Tinoco, I. & Blackburn, E. H. Telomeric DNA oligonucleotides form novel intramolecular structures containing guanine· guanine base pairs. *Cell* **51,** 899–908 (1987).

78. Wellinger, R. J. & Sen, D. The DNA structures at the ends of eukaryotic chromosomes. *Eur. J. Cancer* **33,** 735–749 (1997).

79. Blackburn, E. H. Structure and function of telomeres. *Nature* **350,** 569–573 (1991).

80. Gualberto, A., Patrick, R. M. & Walsh, K. Nucleic acid specificity of a vertebrate telomere-binding protein: evidence for GG base pair recognition at the core-binding site. *Genes Dev.* **6,** 815–824 (1992).

81. VandeVondele, J. *et al.* Quickstep: Fast and accurate density functional calculations using a mixed Gaussian and plane waves approach. *Comput. Phys. Commun.* **167,** 103–128 (2005).

82. Becke, A. D. Density-functional exchange-energy approximation with correct asymptotic behavior. *Phys. Rev. A* **38,** 3098–3100 (1988).

83. Lee, C., Yang, W. & Parr, R. G. Development of the Colle-Salvetti correlation-energy formula into a functional of the electron density. *Phys. Rev. B* **37,** 785–789 (1988).

84. Grimme, S., Antony, J., Ehrlich, S. & Krieg, H. A consistent and accurate *ab initio* parametrization of density functional dispersion correction (DFT-D) for the 94 elements H-Pu. *J. Chem. Phys.* **132,** 154104 (2010).

85. Jaeqx, S., Oomens, J., Cimas, A., Gaigeot, M.-P. & Rijs, A. M. Gas-Phase Peptide Structures Unraveled by Far-IR Spectroscopy: Combining IR-UV Ion-Dip Experiments with Born-Oppenheimer Molecular Dynamics Simulations. *Angew. Chem. Int. Ed.* **53,** 3663–3666 (2014).

86. Schindler, B. *et al.* Distinguishing isobaric phosphated and sulfated carbohydrates by coupling of mass spectrometry with gas phase vibrational spectroscopy. *Phys. Chem. Chem. Phys.* **16,** 22131–22138 (2014).

87. Brites, V., Nicely, A. L., Gaigeot, M.-P. & Lisy, J. M. High energy conformers of M+(APE)(H2O)0–1Ar0–1 clusters revealed by combined IR-PD and SFt-MD anharmonic vibrational spectroscopy. *Phys. Chem. Chem. Phys.* **16,** 13086–13095 (2014).

88. Lippert, G., Hutter, J. & Parrinello, M. A hybrid Gaussian and plane wave density functional scheme. *Mol. Phys.* **92,** 477–488 (1997).

89. VandeVondele, J. & Hutter, J. Gaussian basis sets for accurate calculations on molecular systems in gas and condensed phases. *J. Chem. Phys.* **127,** 11415 (2007).

90. Goedecker, S., Teter, M. & Hutter, J. Separable Dual Space Gaussian Pseudo-potentials. *Phys. Rev. B* **54,** 1703 (1996).

91. Yanai, T., Tew, D. P. & Handy, N. C. A new hybrid exchange-correlation functional using the Coulomb-attenuating method (CAM-B3LYP). *Chem. Phys. Lett.* **393,** 51–57 (2004).

92. Adamo, C. & Scuseria, G. E. Accurate excitation energies from time-dependent density functional theory: Assessing the PBEO model. *J. Chem. Phys.* **111,** 2889–2899 (1999).

93. Andersson, Y., Langreth, D. C. & Lundqvist, B. I. van der Waals Interactions in Density-Functional Theory. *Phys. Rev. Lett.* **76,** 102–105 (1996).

94. Nir, E., Janzen, C., Imhof, P., Kleinermanns, K. & de Vries, M. S. Pairing of the nucleobase guanine studied by IR–UV double-resonance spectroscopy and ab initio calculations. *Phys. Chem. Chem. Phys.* **4,** 740–750 (2002).

95. Sobolewski, A. L. & Domcke, W. Ab initio studies on the photophysics of the guanine–cytosine base pair. *Phys Chem Chem Phys* **6,** 2763–2771 (2004).

Chapter 5

Excited State Dynamics of 6-Thioguanine

5.1 Introduction

The DNA and RNA bases have a built-in protection mechanism against UV radiative damage. When they absorb UV light, they return safely to the electronic ground state in less than a picosecond by internal conversion (IC). This ultrafast IC dominates alternative relaxation pathways, such as intersystem crossing (ISC), so potentially harmful photochemical processes are averted. The availability of rapid IC pathways depends critically on molecular structure. This dependence results from the fact that the conical intersections that mediate IC occur at molecular geometries that differ strongly from ground state minimum geometries. Therefore the excited state dynamics of nucleobases can differ drastically for different derivatives [1–9], analogues [10–12], and even tautomers [13–15]. Many derivatives and analogues of the canonical nucleobases that could serve as alternative bases lack the UV protection afforded by rapid internal conversion. This difference suggests a possible prebiotic photochemical selection of nucloebases on an early earth. In the case of guanine (G), the keto tautomer, which is prevalent in DNA, is characterized by rapid IC in contrast to enol and imino tautomers [15–24]. When the oxygen atom in DNA is replaced with a sulfur atom, the photochemistry changes dramatically due to the heavy atom effect on spin-forbidden transitions [25]. Canonical DNA bases absorb UVB (290-320 nm); whereas, sulfur substituted DNA analogues such as 6-thioguanine (6-TG), absorb UVA (320-400 nm) [12,26–28]. The comparison of the excited state dynamics of G versus 6-TG has so-far been limited to their keto and corresponding thione tautomers [29,30]. The photoproducts and photochemistry of the enol and corresponding thiol tautomers have not been studied in great detail. In this work we find significant transition rates to a dark state, most likely a triplet state, with estimated quantum yields of the order of 25% for enol G and considerably higher rates for thiol 6-TG.

6-TG and other thiopurines are effective anti-inflammatory, anticancer, and immunosuppressive drugs used for over 50 years [31], however, prolonged treatment with 6-TG has been associated with a 65-250 times increased risk of skin cancer [32]. 6-TG is of interest because it can be incorporated into a patient's DNA [33], increasing skin sensitivity to UVA radiation. Once 6-TG is converted into 6-TG nucleotide, it replaces the guanine in the patient's DNA [34]. Excitation of DNA-6TG with UVA radiation generates a series of reactions leading to the formation of reactive oxygen [35] species such as singlet oxygen that can damage both DNA and proteins [36,37]. Other consequences of UVA interaction with DNA 6-TG includes DNA and protein oxidation, DNA-protein cross linking, DNA strand breakage, and DNA interstrand cross linking [38].

Guanine is known to relax to the ground state by internal conversion with lifetimes of 140 fs and 2.3 ps [39]**,** and no triplet yield has been measured to date. These fast relaxation times are indicative of a nucleobase that efficiently dissipates internal energy introduced through UV excitation. However, these femtosecond pump-probe experiments were performed with a 267 nm excitation pulse and 400 nm probe pulse and therefore do not map out the complete excited state dynamics. Furthermore these experiments lack tautomer selectivity. In solution guanine is primarily in the keto form. In the gas phase, four guanine tautomers were detected in molecular beams, two iminos and two enols [40,41]. Choi *et al*. observed keto tautomers in helium droplets [42]. In the present work, we evaluate the excited state lifetime of the 9-H enol guanine and compare it with that of thiol 6-TG. Research on 6-TG has focused on exploring the excited state dynamics of the thione tautomer, but no studies have been reported on the thiol tautomer [43–46]. Reichardt *et al*. investigated the excited state dynamics of 6-thioguanosine in phosphate buffer and in acetonitrile solutions via femtosecond broadband transient absorption spectroscopy coupled with quantum chemical calculations [43]. They determined that in the aqueous buffer solution, ~ 80% of the S_2 ($\pi\pi^*$) excited state population decays by ultrafast intersystem crossing to T_3 (nπ^*) which is ~0.1 eV below the S_2 FC region, suggesting a strong spin-orbit coupling between these two states. However, Martínez-Fernández *et al* have later argued that the proposed channel is not the correct pathway to the triplet manifold [44,45] . Instead, they used ab initio calculations to show that the dominant pathway is $S_2 \rightarrow S_1 \rightarrow T_2 \rightarrow T_1$. Moreover, Martínez-Fernández *et al.* assigned T_3 as ($\pi\pi^*$) instead of (nπ^*). As a result, Martínez-Fernández *et al.* determined that the S_2 state ($\pi\pi^*$) and T_3 state ($\pi\pi^*$) negligibly coupled at the FC and S_2 minimum structures. Both authors however agreed that internal conversion and intersystem crossing compete in the relaxation mechanism to the ground state with the intersystem crossing pathway being the major pathway and $S_2 \rightarrow S_1 \rightarrow S_0$ being the minor pathway.

Here we present the tautomeric characterization and excited state dynamics of jet-cooled guanine in the enol form (G_e) and of 6-thioguanine (6-TG) as an alternative nucleobase and as a case study into heavy-atom effects on ISC and application of El-Sayed's rules [47]. We collected 1 and 2-color R2PI on isolated 6-TG, with IR-UV characterization, and performed nanosecond and picosecond pump probe spectroscopy on G_e and 6-TG to determine IC and ISC rates from the origin up to ~900 cm^{-1} excess internal energy.

5.2 Methods

5.2.1 Experimental

The instrument and experimental setup have been described in detail in chapter 2. Samples (6-thioguanine, TCI 95%) are mixed with carbon black and placed on a graphite substrate. One-color nanosecond R2PI was carried out with the frequency doubled output of a Lumonics HD-300 tunable dye laser (2 mJ/pulse, 8 ns pulse length, 0.04 cm^{-1} spectral linewidth).

The picosecond R2PI spectroscopic and pump-probe delay measurements are performed with an Ekspla PL2251 Nd:YAG laser system producing ~ 30 ps laser pulses. The 355 nm output pumps an Ekspla PG401 tunable optical parametric generator (OPG) (UV output of 80-120 μJ/pulse, 30 ps pulse length, ~ 6 cm^{-1} spectral linewidth). 6-TG is excited by the OPG UV and ionized by 266 nm, fourth harmonic of the ps pump laser, which is mechanically delayed up to 1.5 ns before colineation with the OPG beam. A variable delay between OPG UV laser and an excimer laser (193 nm, 1.5-2 mJ/pulse) is used for pump-probe measurements in the nanosecond range.

For IR-UV double resonant spectroscopy a Laser Vision optical parametric oscillator/amplifier (OPA/OPA) (near-IR output over the range 3200-3800 cm^{-1} of ~3-5 mJ/pulse, 3 cm^{-1} spectral linewidth) precedes the ns R2PI by 200 ns. We perform two different double resonant schemes in this report, (I) we scan the IR at a fixed UV probe wavelength and (II) we scan the UV with a fixed IR burn wavelength. In scheme I the IR laser is scanned while the UV laser is fixed on one vibronic transition and signal depletes when the IR laser becomes resonant with that ground state population. The resulting ion-dip spectrum represents the ground state IR spectrum of a single tautomer, selected by the UV probe wavelength. This IR spectrum can be compared with calculated IR frequencies to determine the specific tautomer of the selected vibronic transition. In scheme II the IR laser is set to a tautomer specific vibrational resonance and we scan the UV laser, comparing spectra with IR laser on and off. The difference spectrum identifies peaks that arise from the same tautomer.

5.2.2 Computational

Starting structures for both thiol and thione structures were optimized using the B3LYP hybrid functional with a 6-31+G(2d,p) basis set. The shorthand notation of these structures will include a number, 7 or 9, which indicates which nitrogen is sp^3 hybridized, and a letter, e or k, which indicates whether the structure is a thiol or thione, respectively. This nomenclature was adopted to be consistent with the equivalent enol and keto designations for guanine. These structures were then further optimized using MP2/6-31+G(2d,p), which were then used to perform an anharmonic frequency analysis where ground state minima were confirmed by the absence of imaginary frequencies. The simulated spectra arise from anharmonic frequencies with harmonic intensities using a Lorentzian shape and FWHM of $1 cm^{-1}$. The MP2 optimized structures were used for single point energy calculations at the CCSD and EOM-CCSD level with the same basis set. These levels of theory provide good accuracy electronic energies for the ground and electronically excited states, respectively. These computations were performed by using *Gaussian 09* [48].

Ab initio molecular dynamic simulations were performed using surface hopping including arbitrary couplings (SHARC) [49,50]. The package developed by Gonzalez and coworkers performs high accuracy *ab initio* calculations and modifies nuclear positions as a function of time to obtain molecular dynamic information. The quantum calculations within SHARC were performed with the *Molpro* interface [51]. 10 trajectories were run which included three singlet and triplet electronic states, so that intersystem crossing information could be obtained as well as singlet internal conversion. Once an internal conversion (IC) or intersystem crossing (ISC) geometry was found in a *SHARC* trajectory, the CI was verified by performing a single point energy calculation with *Gaussian 09*, followed by a linear interpolation of internal coordinates (LIIC) from the Frank-Condon geometry to the intersection of interest. Both *Gaussian 09* and *Molpro* simulations employed the state averaged complete active space self-consistent field method (SA-CASSCF). The active space used in this method consisted of 10 electrons in 10 orbitals (10,10), and used the 6-31G* basis set.

5.3 Results

5.3.1 R2PI

Figure 5.1 shows the R2PI spectrum of jet-cooled 6-TG in the frequency range 32 330-33 330 cm^{-1}.

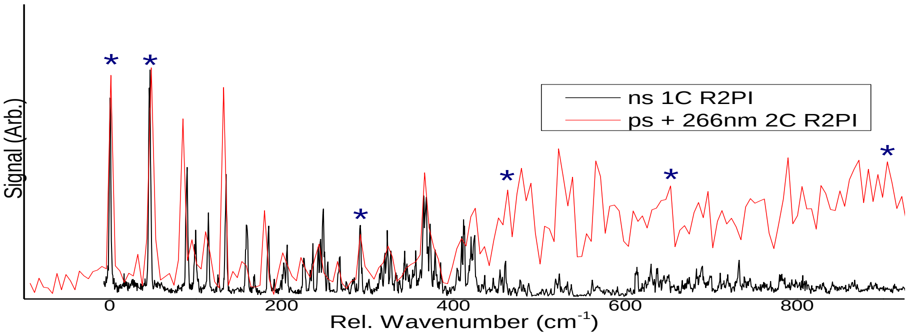

Figure 5.1: One-color resonant two-photon nanosecond ionization spectrum of jet-cooled 6-thioguanine is shown in black and two-color resonant two-photon picosecond ionization spectrum of jet-cooled 6-thioguanine is shown in red. The wavenumber scale is relative to the 0_0^0 band at 32 343 cm^{-1} and asterisks mark where pump probe was performed.

The top panel shows nanosecond one-color (1C) R2PI. The spectrum exhibits a sharp red-most band at 32 343 cm^{-1}, which we assume to be a 0_0^0 band and similarly sharp vibronic bands up to +290 cm^{-1}, after which the spectral features lose intensity and congest. The bottom panel shows the same spectrum with picosecond excitation. In this case the signal is lower so we used two-color (2C) R2PI in which the second color consisted of 266 nm picosecond pulses. Two-color ionization with nanosecond 193 nm ionization is not shown but shows features identical to ionization at 266 nm. The excitation laser in the 2C-R2PI has a spectral linewidth of 6 cm^{-1}, as opposed to 0.04 cm^{-1} for the laser in the 1C scan. Above 500 cm^{-1} the nanosecond signal is strongly reduced in contrast to the picosecond signal. This observation points to a decrease in excited state lifetime with increasing excitation energy, corresponding to a deactivation pathway with a barrier of the order of 500 cm^{-1}.

5.3.2 Tautomer determination

Figure 5.2 shows a double resonant spectrum per scheme I, with the UV probe laser fixed at 32,343 cm^{-1} together with calculated anharmonic IR frequencies for four different tautomers. The optimized structures of the different tautomers are found in Figure 5.3. The simulated spectra of both thiol structures fit the experimental spectrum, while none of the thione spectra fit, which was previously confirmed by Kasende[52].

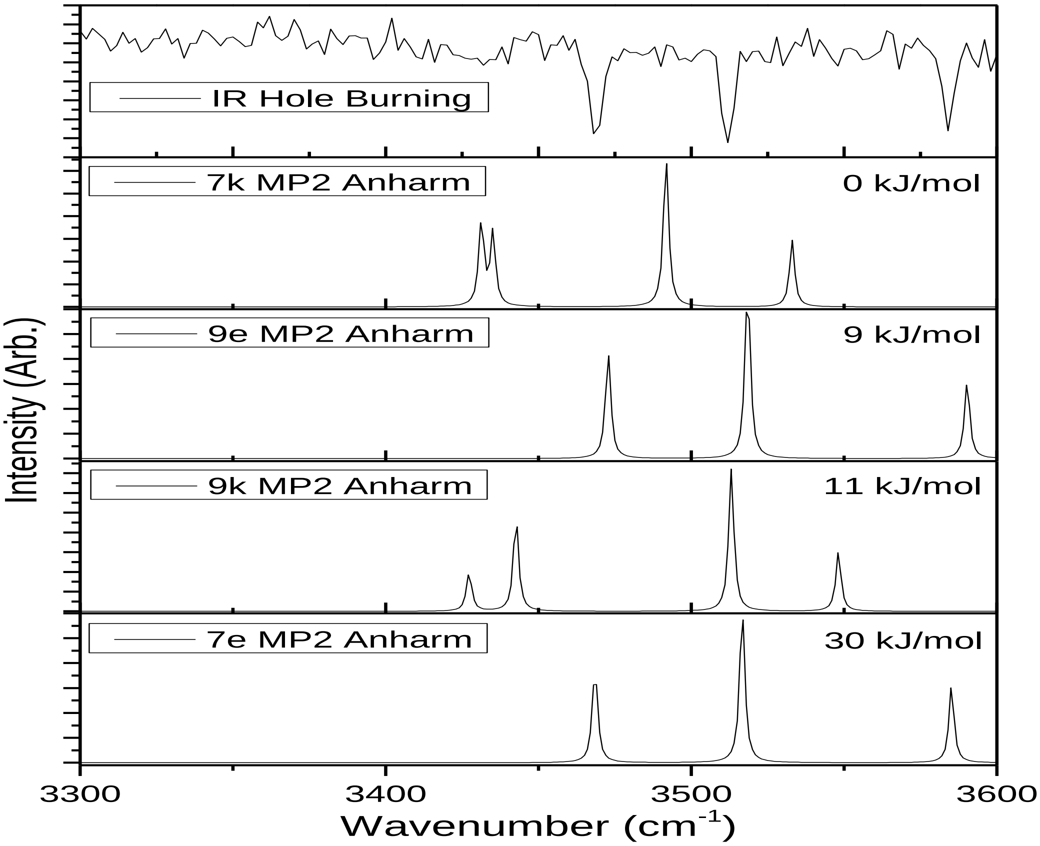

Figure 5.2: Experimental IR hole spectrum via scheme I (*top*) and theoretical IR bands calculated at the anharmonic MP2/6-31+G(2d,p) level. Energies shown calculated at CCSD/6-31+G(2d,p).

6-TG thiones have 2 bands in the red part of the spectrum, whereas only one band is present in the thiols (3470 cm^{-1}), representing the $(NH_2)_{sym}$ stretch. Moreover, the thione bands do not line up with the experimental data, particularly the highest energy band, the $(NH_2)_{sym}$ stretch, which appears ~50 cm^{-1} higher than the highest frequency measured. The calculated and measured intensities are well matched with the N7H/N9H stretch band at 3510 cm^{-1}, which is the most intense, followed by the $(NH_2)_{sym}$ stretch at 3470 cm^{-1} and $(NH_2)_{asym}$ stretch at 3584 cm^{-1} with nearly identical intensities but slightly more intense at 3470 cm^{-1}. We did search for the SH stretch which is calculated to be around 2662 cm^{-1}. However, we did not detect the peak in that region which is most likely due to a weak oscillator strength which we calculated to be less than 10% of the least intense NH/NH_2 peaks.

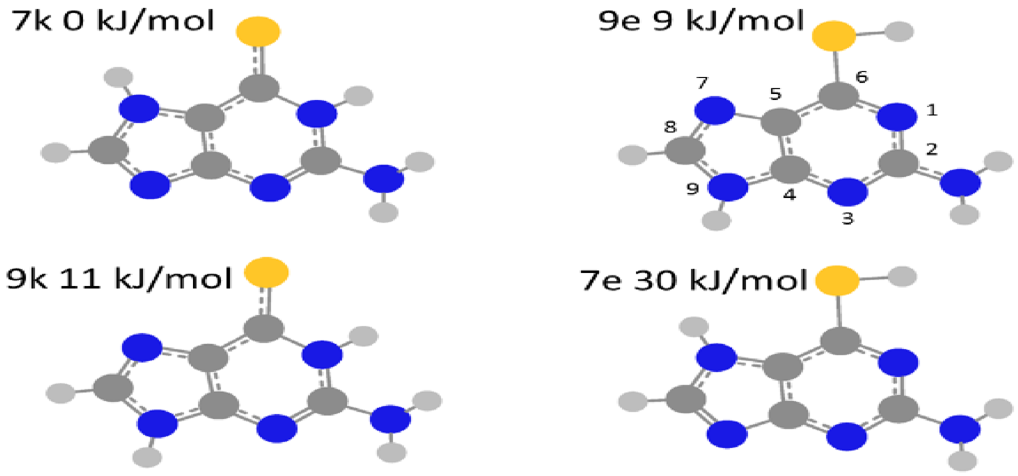

Figure 5.3: Ground state (Frank-Condon) structures optimized at MP2/6-31+G(2d,p). The atom number scheme is shown on the 9e tautomer. Energies shown calculated at CCSD/6-31+G(2d,p).

Vibrational analysis is typically the most direct way of determining which tautomer(s) are present in the molecular beam; however, Figure 5.2 shows that it is difficult to distinguish whether the tautomer is the 7e or 9e form. As calculated, (Figure 5.3**)**, the 9e is ~9 kJ/mol higher in energy than the lowest energy tautomer, and the 7e is ~30 kJ/mol higher in energy than the lowest energy tautomer. Past work in our lab on the nucleobase adenine showed that only the lowest energy tautomer was present, where the next lowest energy tautomer was calculated to be at ~33 kJ/mol higher energy than the one observed [53]. For this reason, we tentatively assign the tautomer present here as the 9e, however, we do not rule out the possibility of 7e 6-TG being present. The discussion will proceed focusing on 9e, but keeping 7e in consideration. Moreover, we cannot exclude the possibility of other tautomers outside the UV measured region.

So far, we have shown that 9e and possibly 7e are the tautomers present when probing at the origin. Typically, UV-UV hole burning spectroscopy is used to determine the number of tautomers in a REMPI scan; however, the presence of a long-lived triplet state, which we discuss below, interferes with this approach. The probe laser should only produce ions from the ground state and this signal should be reduced when the ground state is depleted resonantly by the burn laser. However, when the burn laser populates a long-lived triplet state, the probe laser still produces ions from that triplet state even at the burn laser resonances. Since it is not practical to perform double resonant spectroscopy by scheme I, scanning the IR with the UV wavelength fixed, at each successive UV peak, we performed double resonant spectroscopy with scheme II.

We set the burn laser to 3584 cm^{-1} 200 ns prior to the UV probe laser which was then scanned to record the IR-UV hole burning spectrum. We chose the $(NH_2)_{asym}$ stretch because it is a good thiol indicator (Figure 5.2). There is no marker frequency that can distinguish between 7e and 9e tautomers as they share very similar IR spectra. We obtained spectra with IR laser off and IR laser on, where a decrease in signal indicated shared IR resonance with the origin transition and therefore the same tautomer. The result, shown in Figure 5.4, indicates that the entire UV spectrum in this range correlates with the same IR marker frequency and thus exclusively with thiol tautomers.

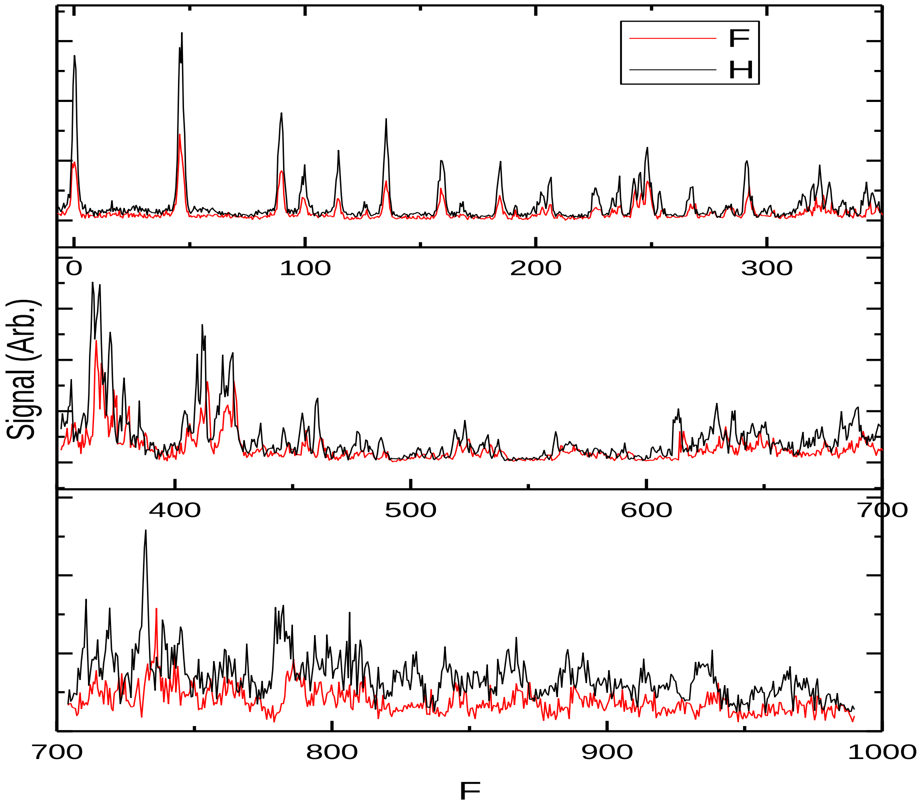

Figure 5.4: IR laser set to 3584 cm^{-1} 200 ns prior to scanning UV. Decrease in signal indicates shared IR resonance with the origin transition.

5.3.3 Pump-probe

6-Thioguanine

We performed pump probe experiments on both the nanosecond and picosecond timescale to determine which types of processes are occurring in this system; the peaks investigated are marked with asterisks in Figure 5.1. By combining information from both time domains and monitoring lifetimes as a function of excitation energy, it is possible to gain an understanding of the excited state dynamics involved in deactivation. The behavior as a function of time of each decay channel derives from the kinetic equations and from solving the system of ordinary differential equations with boundary conditions (eqn 1), where p(t) refers to a primary pathway which is populated at zero delay time and fills a secondary pathway, s(t), which then decays with a time constant τ_m. Since measurements are made with a finite pulse width laser, the measured response is a convolution of the instrument response function (IRF) with each of the pump and probe pulses where the IRF is represented by a Gaussian centered around t_0. The standard deviation of the Gaussian is fitted for each profile rather than using a single value, as reported by Lipert *et al.* [54] and results in FWHM values which ranged from half to full width of the experimental laser pulses. After convoluting the exponential decays, which gives the excitation profile, the profile is convoluted again with the probe pulse as performed by Spesyvtsev [55] and shown in equations 2a-b. The excitation profile, P(t), consists of a sum of all primary and secondary pathways, where the secondary pathways are multiplied by an ionization efficiency factor (ϕ_{ion}) relative to the primary pathway, as shown in equation 2a. The excitation profile is convolved with 2 Gaussians centered at different t_0 with standard deviation σ in equation 2b. This double convolution is then scaled with a factor f which accounts for the signal intensity being in arbitrary units. The data are fit using a sum of the convolutions in 2b and a Gaussian centered around max signal, as performed by Kang *et al.* [56]. We performed all fitting with the Mathematica 10 package [57] which employed the Levenberg–Marquardt algorithm for least squares fitting.

$$\boldsymbol{\frac{dp}{dt} = -\frac{1}{\tau_n} p(t, \tau_n),} \qquad \boldsymbol{\frac{ds}{ds} = -p(t, \tau_n) - \frac{1}{\tau_m} s(t, \tau_m)} \qquad \text{eqn 1}$$

$$\boldsymbol{P(t) = \sum_{n=1}^{N} \sum_{m=1}^{M} p(t, \tau_n) + \phi_{ion}\, s(t, \tau_m)} \qquad \text{eqn 2a}$$

$$\boldsymbol{I(t) = f \int_0^t G\left(t - t'', t_0^{probe}, \sigma\right) \int_0^t G\left(t - t', t_0^{pump}, \sigma\right) P(t)\, dt'\, dt''} \qquad \text{eqn 2b}$$

In the following discussion, we refer to the UV excitation peaks by their energy relative to the origin at 32,343 cm^{-1}.

Table 5.1 lists fitting parameters from the picosecond and nanosecond pump probe experiments. When fitting the picosecond pump-probe traces, shown in Figure 5.5**,** all traces except for 47 cm^{-1} and 290 cm^{-1} are fit with a primary decay (τ_1) that decays on the order of hundreds of picoseconds and populates a secondary state. The lifetime of the secondary state (τ_2) can only be determined at excess energies greater than 462 cm^{-1} and is of the order of 1 ns. The 47 cm^{-1} and 290 cm^{-1} traces, however, can only be fit with a single primary decay of about 4 ns. It cannot be determined on the picosecond timescale whether or not this 4 ns decay fills a secondary state, so we move to the nanosecond timescale to obtain more information.

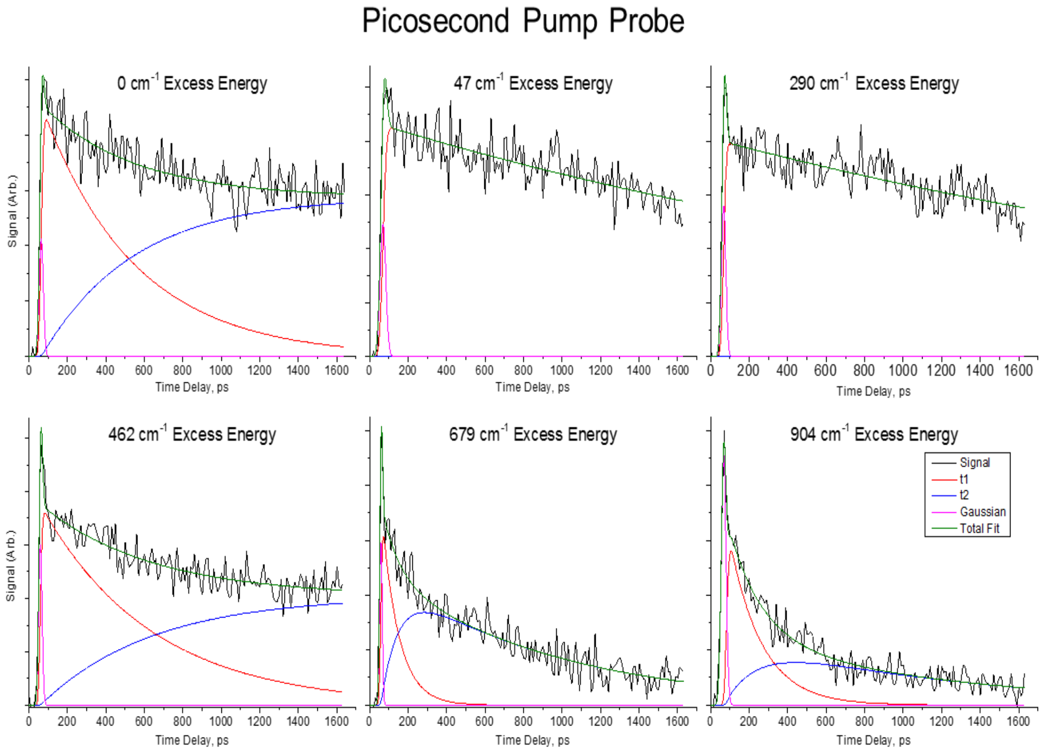
Picosecond Pump Probe

0 cm^{-1} Excess Energy

47 cm^{-1} Excess Energy

290 cm^{-1} Excess Energy

462 cm^{-1} Excess Energy

679 cm^{-1} Excess Energy

904 cm^{-1} Excess Energy

Figure 5.5: Picosecond pump probe traces with fitting for 0, 47, 290, 462, 679, and 904 cm^{-1}. Fitting parameters are marked as ^{a} in Table 2**.**

Fitting Parameters for 6-Thioguanine

Excess Energy cm^{-1}	**ISC τ_1, ps**	**T_2 Decay τ_2, ns**	**T_2 Decay τ_{2b}, ns**	**T_1 Decay τ_3, ns**
0	481 [a]	6.1 [b]	▨	2025 [b]
47	3920 [ab]	▨	▨	3033 [b]
290	4330 [ab]	▨	▨	2000 [b]
462	577 [a]	5.7 [b]	▨	2590 [b]
679	87 [a]	0.9 [a]	24 [b]	878 [b]
904	168 [a]	1.1 [a]	21.5 [b]	462 [b]

Table 5.1: Summary of fitting parameters where [a] denotes a value from picosecond fit and [b] denotes a value from a nanosecond fit.

The nanosecond lasers are too slow to measure dynamics that occur on shorter timescales, but can be used to fit longer lived pathways. Upon inspection of the nanosecond pump probe traces (Figure 5.6**)**, it is evident that a long lived secondary state is populated which returns to the ground state on the order of a few microseconds (τ_3). This means that the secondary state in the picosecond experiments that decays within 1 ns (τ_2) is most likely a triplet state (T_2) that feeds another triplet state (T_1) which is observed in the nanosecond experiment. The nanosecond pump probe was fit with primary and secondary decays, however, in this case the primary decay is the T_2 state which decays with time constant τ_2 into T_1 with a lifetime τ_3. The 1 ns T_2 decay for peaks 679 cm^{-1} and 904 cm^{-1} are too fast to be measured by the nanosecond pump probe, but an additional primary decay of ~20 ns was needed to fit the 679 cm^{-1} and 904 cm^{-1} traces, denoted τ_{2b}, implying a double exponential decay to T_1.

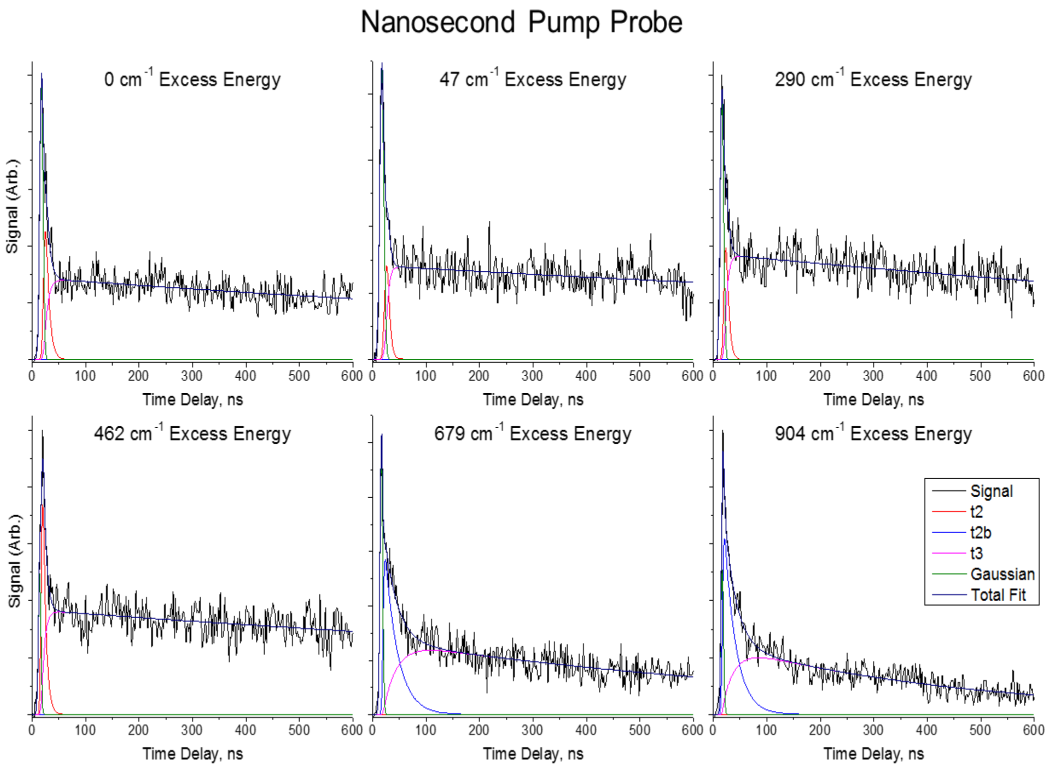

Figure 5.6: Nanosecond pump probe traces with fitting for 0, 47, 290, 462, 679, and 904 cm^{-1}. Fitting parameters are marked as ^{b} in Table 1.1.

9-enol Guanine

We performed Pump probe experiments on 9e-guanine to compare dynamics with 9e 6-thioguanine. The excitation wavelength of 304.2 nm selects the origin of this tautomer, based on previous results [58,59]. Measurements in the picosecond range show in a flat line, indicating that there are no fast dynamics to capture at that timescale. Figure 5.7 shows the nanosecond trace of the 9e-guanine origin 32873 cm^{-1} revealing two long lifetime components. One decay path with a 40 ns lifetime feeds a secondary state while the other goes directly to the ground state with a 13 ns lifetime. Fluorescence experiments performed by Polewski *et al*. in cold argon matrix found a 9 ns fluorescence lifetime when guanine was excited at 304 nm [60]. We therefore interpret the faster decay as fluorescence and the slower decay as populating a dark state. Since in solution guanine exists predominantly in the keto form this is to our knowledge the first observation of such a dark state in enol guanine. This dark state could be a triplet state and if these are the only two processes then the ISC quantum yield is about 25%.

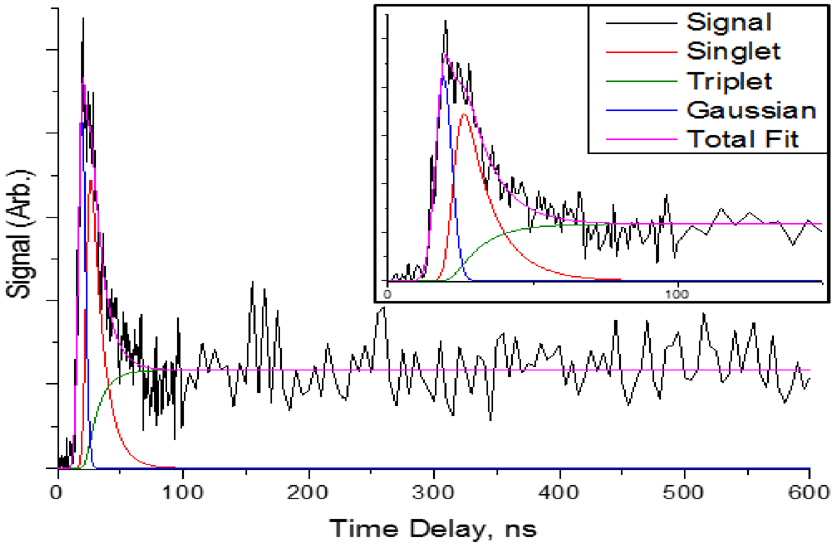

Figure 5.7: Nanosecond pump probe trace of 9-enol guanine at its origin of 32873 cm^{-1}. The singlet lifetime is fit as a bi-exponential of fluorescence (13 ns) and ISC (40 ns) which feeds a triplet with a lifetime longer than the experiment allows. The inset shows a magnified portion of the fitting.

5.3.4 Computational Results

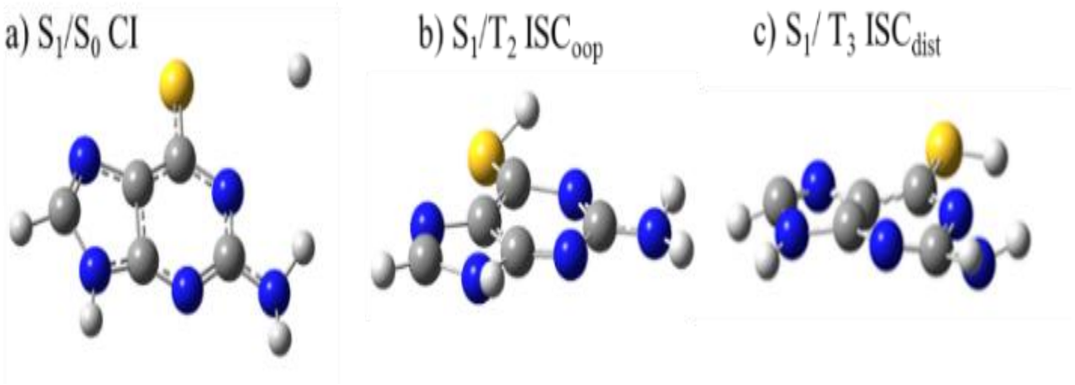

Figure 5.8: Structures are geometries leading to hops in the SHARC simulation. All structures are calculated at SA-CASSCF(10,10)/6-31G(d) level.

The CCSD energy calculations for the excited states indicate that excitation is to the S_1 state based on oscillator strengths (table 5.2).

a)

Ground State		S_1		S_2	
Tautomer	**Rel. kJ/mol**	**Character**	**Vert. E, eV**	**Character**	**Vert. E, eV**
9e	9.0	ππ*	4.66 (0.193)	nπ*	5.17 (0.004)
7e	29.8	ππ*	4.44 (0.159)	nπ*	4.95 (0.004)

b)

Ground State		T_1		T_2		T_3	
Tautomer	**Rel. kJ/mol**	**Character**	**Vert. E, eV**	**Character**	**Vert. E, eV**	**Character**	**Vert. E, eV**
9e	9.0	ππ*	3.598	ππ*	4.698	nπ*	4.909
7e	29.8	ππ*	3.591	ππ*	4.306	nπ*	4.672

Table 5.2: a) Singlet and b) triplet excited state analysis at CCSD/6-31+G(2d,p) for ground state and EOM-CCSD/6-31+G(2d,p) for excited states. Values in parenthesis correspond to oscillator strengths of the transition. Ground state energies are relative to 7k tautomer.

This conclusion rules out the option that τ_1 could be the decay of S_2 to S_1 and instead suggests that τ_1 describes ISC, populating a triplet state. The fast ISC can be further explained when combined with information from CASSCF calculations. From the 10 SHARC trajectories, one conical intersection for S_1/S_0 internal conversion and two relevant intersystem crossing geometries for El-Sayed allowed $S_1(\pi\pi^*)/T_3(n\pi^*)$ and forbidden $S_1(\pi\pi^*)/T_2(\pi\pi^*)$ crossing were found (Figure 5.8**)**. The CI involves the loss of the SH hydrogen, where the S_1/T_3 ISC path involves a distortion of the heterocycle (ISC_{dist}), and the S_1/T_2 path is an out of plane rotation of the thiol group (ISC_{oop}). LIIC plots were constructed by stepping the internal coordinates from FC geometry to the CI/ISC of interest, and may be found in Figure 5.9. It can be seen that the path to the CI has no barrier, and can be accessed from all excitations beyond the FC region. The LIIC for ISC_{oop} (Figure 5.9b) results in a barrierless path for a S_1/T_2 crossing being located well below the FC region. The transition is forbidden, but with larger spin orbit coupling due to the sulfur, could be much faster than without it. It also appears that this path results in the singlet and second triplet state being in close proximity throughout the path which could increase the probability of making the transition. The ISC_{dist} pathway (Figure 5.9c) involves a crossing seam which starts around 0 cm^{-1} of excess energy, and extends to nearly 9000 cm^{-1}. Since this ISC transition is El-Sayed allowed, ultrafast ISC is expected if the crossing is reached which may not be the case considering IVR in the excited state will distribute energy across all modes rather than in the direction of the LIIC.

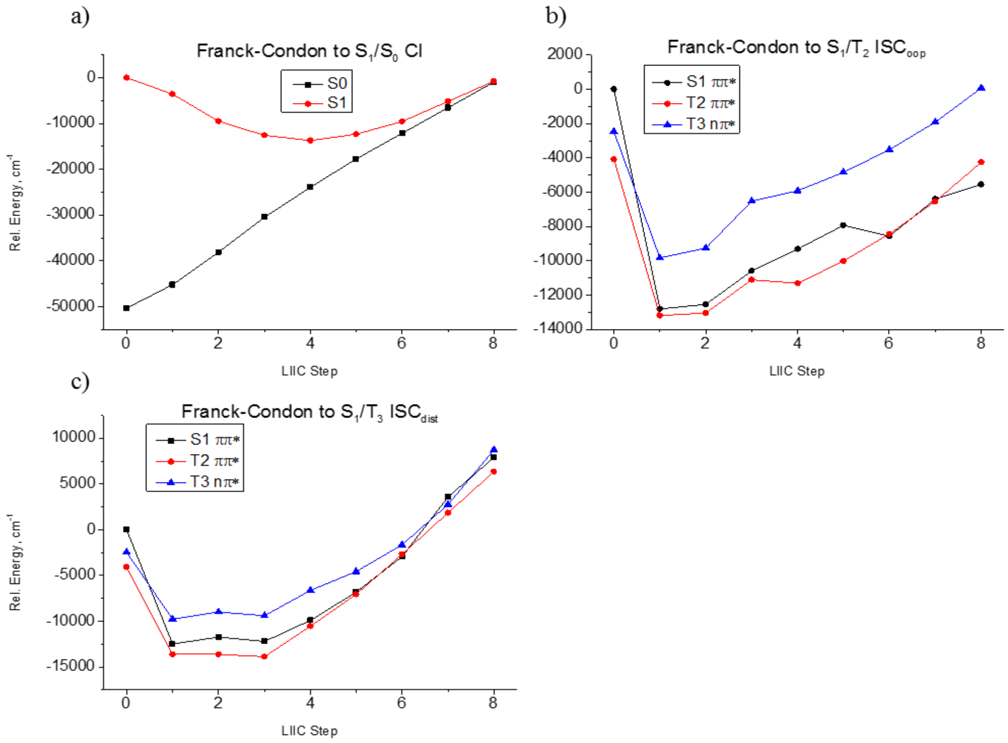

Figure 5.9: LIIC curves using SA-CASSCF(10,10)/6-31G* from the Frank-Condon geometry to the a) conical intersection, b) ISC path to ISC_{oop}, and c) ISC path to ISC_{dist}

5.4 Discussion

Intersystem crossing is typically a slow process due to the required spin flip, but may be ultrafast when spin orbit coupling is large. Increases in spin orbit coupling may happen in various ways, such as a change in symmetry or through the heavy atom effect [47,61]. We measured excited state lifetimes with increasing excess energy to learn more about possible decay pathways in 6-TG. We performed SHARC simulations initiating in the S_2 state so that internal conversion to S_1 produces a hot excited state. By performing simulations in this manner, we can find crossing geometries that have an activation barrier, which may be accessed with larger amounts of internal energy.

Based on the assumption that the excitation results in S_1 population (table 5.2a), the initial decay can go to either the ground state (IC) or a triplet state (ISC). The picosecond pump probe data show that the initial decay populates a secondary state, indicating that fast ISC is occurring. It is interesting that IC is not observed, because Figure 5.9a shows that there is a conical intersection located below the Frank-Condon region. It may be that IC occurs quicker than the laser pulse widths, obscuring this pathway. Without certainty that all processes are observed we cannot derive quantum yields from the rates, but we can compare ISC rates with those of the 9-enol tautomer of guanine.

Figure 5.10 summarizes a tentative interpretation of the pump-probe observations with two cases. Case (a) corresponds to excitation at 0, 462, 679, and 904 cm^{-1} and case (b) corresponds to excitation at 47 and 290 cm^{-1}. A possible explanation for the difference is that these are excitations of two different enol tautomers which exhibit different excited state behavior. In this model in both cases the first decay τ_1 represents ISC from S_1, which for case (a) decreases with excitation energy from around 500 ps at the origin to about 100 ps at 904 cm^{-1} excess energy and for case (b) fits a lifetime of about 4 ns. In both cases τ_3 is the lifetime of the long lived T_1 triplet state, ranging from about 2-3 μs below 500 cm^{-1} and about 0.5-0.9 μs above 500 cm^{-1}. This decrease in triplet lifetime has been observed in other systems [62,63] when internal energy of about 3500 cm^{-1} was added prior to pump probe. In case (b) T_1 is populated directly from S_1 but in case (a) there is an intermediate state, which could be T_2, with a lifetime τ_2, measured to be about 5 ns at excess energies of 0 and 462 $cm^{-1}$and about 1 ns for 679 and 904 cm^{-1}. At the higher energies an additional decay of ~20 ns is required for a good fit (τ_{2b}). This could correspond to an additional pathway populating T_1, possibly *via* a crossing with a large barrier. So case (a), applying to excitation at 0, 462, 679, 904 cm^{-1}, fits the model in Figure 5.8a, involving ISC to T_2 which decays through 2 pathways to T_1 on the order of nanoseconds. Case (b), applying to excitation at 47 and 290 cm^{-1} do not reveal any other short pathways, and are consistent with ISC of ~4 ns which feeds T_1, which decays in 2-3 μs. Figure 5.9b shows that S_1/T_2 crossing occurs below the Frank-Condon geometry, and Figure 5.9c shows S_1/T_3 crossing occurs well above the Frank-Condon geometry with S_1 and T_2 intersecting along this path as well. This suggests that ISC is occurring quickly to T_2 at the energies probed here, and that with even more energy, maybe T_3 may be accessed which would provide access to an El Sayed allowed transition. The difference in excited state behavior between the different peaks suggests that both enol tautomers are present in our experiments.

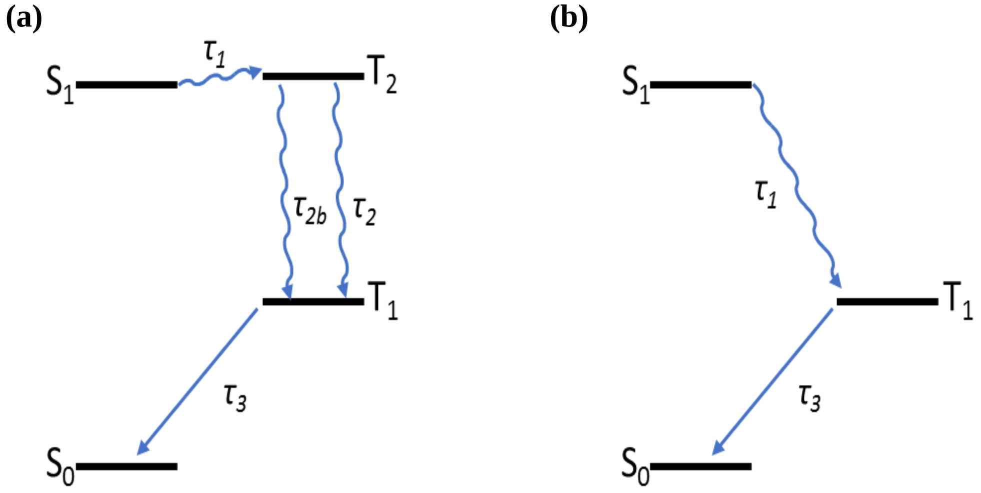

Figure 5.10: Proposed decay pathways where (a) corresponds to excitation at 0, 462, 679, and 904 cm^{-1} and (b) corresponds to excitation 47 and 290 cm^{-1}.

When comparing the dynamics of the thiol system studied here with the aqueous phase femtosecond study of the thione-nucleoside by Reichardt *et al.*[43] interpreted by Martínez-Fernández *et al.*[44,45], the rates for ISC are 300-1000 times lower for the thiol.

Reichardt also saw internal conversion occurring on the tens of picoseconds timescale, which we do not see in the thiol in the gas phase. While there could be an unobserved IC component faster than our time resolution, a larger ISC rate is expected because the thiol triplet transition is spin-forbidden while excitation to S_2 ($\pi\pi^*$) in the thione allows for ultrafast IC to S_1($n\pi^*$) which then allows for ultrafast ISC to T_2 ($\pi\pi^*$). In this scenario the singlet-triplet transition can occur on the sub-nanosecond timescale because the sulfur increases spin-orbit coupling in the system. We demonstrated the effect on ISC of replacing the oxygen in guanine with a sulfur by comparing the pump probe results of 9e 6-TG with those of 9e guanine, G_e. As mentioned earlier, the guanine data correspond to ISC and fluorescence lifetimes of 40 ns and 13 ns, respectively. The rate for ISC in 9e 6-TG is 80 times greater at the origin compared to 9e guanine. No fluorescence decay was measured for 6-TG, most likely due to fast ISC quenching this pathway [60].

5.5 Summary

We investigated 6-thioguanine excited state dynamics on the picosecond and nanosecond timescale. IR-UV double resonant spectroscopy showed the presence of 1 or 2 thiol tautomers in the experiment. Modeling the pump-probe data fits two cases, possibly corresponding to two tautomers. The first case, likely 9e, undergoes fast ISC on the 100-500 ps timescale from S_1 to T_2, which decays in 1-5 ns to T_1 which in turn lives for 0.5-2 μs (Figure 7a). Excess energies of 679 and 904 cm^{-1} result in an additional T_2 of about 20 ns, which could be due to an additional pathway with a conical intersection with a large barrier. The second case, likely 7e, undergoes ISC in ~4 ns from S1 to T_1, which lives for 2-3 μs (Figure 7b). When comparing 9e 6-TG with 9e guanine, we find that the ISC is 80 times greater which is likely due to additional spin-orbit coupling from the sulfur substitution. The difference in the excited state landscape between the thione and thiol can be understood in the sense that the thione has an El-Sayed allowed transition from S_1 (nπ*) to T_2 (ππ*), where thiol excitation results in S_1 (ππ*) population while the ^{3}(nπ*) triplet state is higher in energy.

References

1. He, Y., Wu, C. & Kong, W. Decay Pathways of Thymine and Methyl-Substituted Uracil and Thymine in the Gas Phase. *J. Phys. Chem. A* **107,** 5145–5148 (2003).

2. Gengeliczki, Z. *et al.* Effect of substituents on the excited-state dynamics of the modified DNA bases 2,4-diaminopyrimidine and 2,6-diaminopurine. *Phys. Chem. Chem. Phys.* **12,** 5375 (2010).

3. Etinski, M., Fleig, T. & Marian, C. M. Intersystem Crossing and Characterization of Dark States in the Pyrimidine Nucleobases Uracil, Thymine, and 1-Methylthymine [†]. *J. Phys. Chem. A* **113,** 11809–11816 (2009).

4. Trachsel, M. A., Lobsiger, S., Schär, T. & Leutwyler, S. Low-lying excited states and nonradiative processes of 9-methyl-2-aminopurine. *J. Chem. Phys.* **140,** 044331 (2014).

5. Kunitski, M., Nosenko, Y. & Brutschy, B. On the Nature of the Long-Lived 'Dark' State of Isolated 1-Methylthymine. *ChemPhysChem* **12,** 2024–2030 (2011).

6. Nir, E., Kleinermanns, K., Grace, L. & de Vries, M. S. On the Photochemistry of Purine Nucleobases. *J. Phys. Chem. A* **105,** 5106–5110 (2001).

7. Malone, R. J., Miller, A. M. & Kohler, B. Singlet Excited-state Lifetimes of Cytosine Derivatives Measured by Femtosecond Transient Absorption¶. *Photochem. Photobiol.* **77,** 158 (2003).

8. Trachsel, M. A. *et al.* The excited-state structure, vibrations, lifetimes, and nonradiative dynamics of jet-cooled 1-methylcytosine. *J. Chem. Phys.* **145,** 134307 (2016).

9. Brister, M. M. & Crespo-Hernández, C. E. Direct Observation of Triplet-State Population Dynamics in the RNA Uracil Derivative 1-Cyclohexyluracil. *J. Phys. Chem. Lett.* **6,** 4404–4409 (2015).

10. Lobsiger, S., Frey, H.-M. & Leutwyler, S. Supersonic jet UV spectrum and nonradiative processes of the thymine analogue 5-methyl-2-hydroxypyrimidine. *Phys. Chem. Chem. Phys.* **12,** 5032–5040 (2010).

11. Nachtigallová, D. *et al.* The effect of C5 substitution on the photochemistry of uracil. *Phys. Chem. Chem. Phys.* **12,** 4924–4933 (2010).

12. Pollum, M., Martínez-Fernández, L. & Crespo-Hernández, C. E. in *Photoinduced Phenomena in Nucleic Acids I* (eds. Barbatti, M., Borin, A. C. & Ullrich, S.) **355,** 245–327 (Springer International Publishing, 2014).

13. Tomić, K., Tatchen, J. & Marian, C. M. Quantum Chemical Investigation of the Electronic Spectra of the Keto, Enol, and Keto−Imine Tautomers of Cytosine. *J. Phys. Chem. A* **109,** 8410–8418 (2005).

14. Plützer, C. & Kleinermanns, K. Tautomers and electronic states of jet-cooled adenine investigated by double resonance spectroscopy. *Phys Chem Chem Phys* **4,** 4877–4882 (2002).

15. Marian, C. M. The Guanine Tautomer Puzzle: Quantum Chemical Investigation of Ground and Excited States. *J. Phys. Chem. A* **111,** 1545–1553 (2007).

16. Canuel, C. *et al.* Excited states dynamics of DNA and RNA bases: Characterization of a stepwise deactivation pathway in the gas phase. *J. Chem. Phys.* **122,** 074316 (2005).

17. Nachtigallová, D., Hobza, P. & Špirko, V. Assigning the NH Stretches of the Guanine Tautomers Using Adiabatic Separation: CCSD(T) Benchmark Calculations. *J. Phys. Chem. A* **112,** 1854–1856 (2008).

18. Seefeld, K., Brause, R., Häber, T. & Kleinermanns, K. Imino Tautomers of Gas-Phase Guanine from Mid-Infrared Laser Spectroscopy. *J. Phys. Chem. A* **111,** 6217–6221 (2007).

19. Mons, M., Piuzzi, F., Dimicoli, I., Gorb, L. & Leszczynski, J. Near-UV resonant two-photon ionization spectroscopy of gas phase guanine: evidence for the observation of three rare tautomers. *J. Phys. Chem. A* **110,** 10921–10924 (2006).

20. Černý, J., Špirko, V., Mons, M., Hobza, P. & Nachtigallová, D. Theoretical study of the ground and excited states of 7-methyl guanine and 9-methyl guanine: comparison with experiment. *Phys Chem Chem Phys* **8,** 3059–3065 (2006).

21. Hare, P. M., Crespo-Hernández, C. E. & Kohler, B. Internal conversion to the electronic ground state occurs via two distinct pathways for pyrimidine bases in aqueous solution. *Proc. Natl. Acad. Sci.* **104,** 435–440 (2007).

22. Serrano-Andrés, L. & Merchán, M. Are the five natural DNA/RNA base monomers a good choice from natural selection? *J. Photochem. Photobiol. C Photochem. Rev.* **10,** 21–32 (2009).

23. Yamazaki, S., Domcke, W. & Sobolewski, A. L. Nonradiative Decay Mechanisms of the Biologically Relevant Tautomer of Guanine. *J. Phys. Chem. A* **112,** 11965–11968 (2008).

24. Mons, M., Dimicoli, I. & Piuzzi, F. in *Radiation Induced Molecular Phenomena in Nucleic Acids* 343–367 (Springer, 2008).

25. Koziar, J. C. & Cowan, D. O. Photochemical Heavy-Atom Effects. *Am. Chem. Soc.* **11,** 334–341 (1978).

26. Rubin, Y. V., Blagoi, Y. P. & Bokovoy, V. A. 6-Thioguanine luminescence probe to study DNA and low-molecular-weight systems. *J. Fluoresc.* **5,** 263–272 (1995).

27. Ashwood, B., Jockusch, S. & Crespo-Hernández, C. Excited-State Dynamics of the Thiopurine Prodrug 6-Thioguanine: Can N9-Glycosylation Affect Its Phototoxic Activity? *Molecules* **22,** 379 (2017).

28. Stewart, M. J., Leszczynski, J., Rubin, Y. V. & Blagoi, Y. P. Tautomerism of thioguanine: From gas phase to DNA. *J. Phys. Chem. A* **101,** 4753–4760 (1997).

29. Martínez-Fernández, L., Corral, I., Granucci, G. & Persico, M. Competing ultrafast intersystem crossing and internal conversion: a time resolved picture for the deactivation of 6-thioguanine. *Chem. Sci.* **5,** 1336 (2014).

30. Kang, H., Lee, K. T., Jung, B., Ko, Y. J. & Kim, S. K. Intrinsic Lifetimes of the Excited State of DNA and RNA Bases. *J. Am. Chem. Soc.* **124,** 12958–12959 (2002).

31. Karran, P. & Attard, N. Thiopurines in current medical practice: molecular mechanisms and contributions to therapy-related cancer. *Nat. Rev. Cancer* **8,** 24–36 (2008).

32. Euvrard, S., Kanitakis, J. & Claudy, A. Skin cancers after organ transplantation. *N. Engl. J. Med.* **348,** 1681–1691 (2003).

33. Kaplan, H., Kendric, S. & Patricia, T. Radiosensitization of E coli by purine and pyrimidine analagous incorporated in deoxyribonucleic acid. *Nature* **190,** 794–796 (1961).

34. Cuffari, C., Li, D. Y., Mahoney, J., Barnes, Y. & Bayless, T. M. Peripheral blood mononuclear cell DNA 6-thioguanine metabolite levels correlate with decreased interferon-γ production in patients with Crohn’s disease on AZA therapy. *Dig. Dis. Sci.* **49,** 133–137 (2004).

35. Zhang, X. *et al.* Novel DNA lesions generated by the interaction between therapeutic thiopurines and UVA light. *DNA Repair* **6,** 344–354 (2007).

36. O’Donovan, P. *et al.* Azathiopurine and UVA Light Generate Mutagenic Oxidative DNA Damage. *Science* **309,** 1868–1871 (2005).

37. Montaner, B. *et al.* Reactive oxygen-mediated damage to a human DNA replication and repair protein. *EMBO Rep.* **8,** 1074–1079 (2007).

38. Attard, N. R. & Karran, P. UVA photosensitization of thiopurines and skin cancer in organ transplant recipients. *Photochem Photobiol Sci* **11,** 62–68 (2012).

39. Mons, M., Dimicoli, I. & Piuzzi, F. in *Radiation Induced Molecular Phenomena in Nucleic Acids* 343–367 (Springer, 2008).

40. Nir, E., Janzen, C., Imhof, P., Kleinermanns, K. & de Vries, M. S. Guanine tautomerism revealed by UV–UV and IR–UV hole burning spectroscopy. *J. Chem. Phys.* **115,** 4604–4611 (2001).

41. Seefeld, K., Brause, R., Häber, T. & Kleinermanns, K. Imino Tautomers of Gas-Phase Guanine from Mid-Infrared Laser Spectroscopy. *J. Phys. Chem. A* **111,** 6217–6221 (2007).

42. Choi, M. Y. & Miller, R. E. Four Tautomers of Isolated Guanine from Infrared Laser Spectroscopy in Helium Nanodroplets. *J. Am. Chem. Soc.* **128,** 7320–7328 (2006).

43. Reichardt, C., Guo, C. & Crespo-Hernández, C. E. Excited-State Dynamics in 6-Thioguanosine from the Femtosecond to Microsecond Time Scale. *J. Phys. Chem. B* **115,** 3263–3270 (2011).

44. Martínez-Fernández, L., González, L. & Corral, I. An ab initio mechanism for efficient population of triplet states in cytotoxic sulfur substituted DNA bases: the case of 6-thioguanine. *Chem. Commun.* **48,** 2134 (2012).

45. Martínez-Fernández, L., Corral, I., Granucci, G. & Persico, M. Competing ultrafast intersystem crossing and internal conversion: a time resolved picture for the deactivation of 6-thioguanine. *Chem. Sci.* **5,** 1336 (2014).

46. Mai, S. *et al.* The origin of efficient triplet state population in sulfur-substituted nucleobases. *Nat. Commun.* **7,** 13077 (2016).

47. El-Sayed, M. A. Spin—Orbit Coupling and the Radiationless Processes in Nitrogen Heterocyclics. *J. Chem. Phys.* **38,** 2834 (1963).

48. Frisch, M. *Gaussian 09*. (Gaussian Inc., 2009).

49. Mai, S. *et al. SHARC: Surface Hopping Including Arbitrary Couplings – Program Package for Non-Adiabatic Dynamics*. (2014).

50. Richter, M., Marquetand, P., González-Vázquez, J., Sola, I. & González, L. SHARC: *ab Initio* Molecular Dynamics with Surface Hopping in the Adiabatic Representation Including Arbitrary Couplings. *J. Chem. Theory Comput.* **7,** 1253–1258 (2011).

51. Werner, H.-J., Knowles, P. J., Knizia, G., Manby, F. R. & Schütz, M. Molpro: a general- purpose quantum chemistry program package. *WIREs Comput Mol Sci* **2,** 242–253 (2012).

52. Kasende, O. E. Infrared spectra of 6-thioguanine tautomers. An experimental and theoretical approach. *Spectrochim. Acta. A. Mol. Biomol. Spectrosc.* **58,** 1793–1808 (2002).

53. Plützer, C., Nir, E., de Vries, M. S. & Kleinermanns, K. IR–UV double-resonance spectroscopy of the nucleobase adenine. *Phys. Chem. Chem. Phys.* **3,** 5466–5469 (2001).

54. Lipert, R. J., Bermudez, G. & Colson, S. D. Pathways of S1 decay in phenol, indoles, and water complexes of phenol and indole in a free jet expansion. *J. Phys. Chem.* **92,** 3801–3805 (1988).

55. Spesyvtsev, R. Experimental investigation of ultrafast internal conversion in aniline and 1,4-diazabicyclo[2.2.2]octane (DABCO). (University College London, 2013).

56. Kang, H., Lee, K. T., Jung, B., Ko, Y. J. & Kim, S. K. Intrinsic Lifetimes of the Excited State of DNA and RNA Bases. *J. Am. Chem. Soc.* **124,** 12958–12959 (2002).

57. Wolfram Research, Inc. *Mathematica, Version 10.0*. (2014).

58. Nir, E., Grace, L., Brauer, B. & de Vries, M. S. REMPI Spectroscopy of Jet-Cooled Guanine. *J. Am. Chem. Soc.* **121,** 4896–4897 (1999).

59. Nir, E., Janzen, C., Imhof, P., Kleinermanns, K. & de Vries, M. S. Guanine tautomerism revealed by UV–UV and IR–UV hole burning spectroscopy. *J. Chem. Phys.* **115,** 4604–4611 (2001).

60. Polewski, K., Zinger, D., Trunk, J., Monteleone, D. C. & Sutherland, J. C. Fluorescence of matrix isolated guanine and 7-methylguanine. *J. Photochem. Photobiol. B* **24,** 169–177 (1994).

61. Koziar, J. & Cowan, D. Photochemical Heavy-Atom Effects. *J. Am. Chem. Soc.* **11,** 334–341 (1978).

62. He, Y., Wu, C. & Kong, W. Decay Pathways of Thymine and Methyl-Substituted Uracil and Thymine in the Gas Phase. *J. Phys. Chem. A* **107,** 5145–5148 (2003).

63. Ligare, M., Siouri, F., Bludsky, O., Nachtigallová, D. & de Vries, M. S. Characterizing the dark state in thymine and uracil by double resonant spectroscopy and quantum computation. *Phys Chem Chem Phys* **17,** 24336–24341 (2015).

Appendix 1

Direct Analysis of Xanthine Stimulants in Archaeological Vessels by Laser Desorption Resonance Enhanced Multiphoton Ionization

Abstract

Resonance enhanced multiphoton ionization spectroscopy (REMPI) generates simultaneous vibronic spectroscopy and fragment free mass spectrometry to identify molecules within a complex matrix. We combined laser desorption with REMPI spectroscopy to study organic residues within pottery sherds from Maya vessels (600−900 CE) and Mississippian vessels (1100−1200 CE), successfully detecting three molecular markers, caffeine, theobromine, and theophylline, associated with the use of cacao. This analytical approach provides a high molecular specificity, based on both wavelength and mass identification. At the same time, the high detection limit allows for direct laser desorption from sherd scrapings, avoiding the need for extracting organic constituents from the sherd matrix.

A1.1 Introduction

Analysis of organic compounds in pottery sherds traditionally relies on the use of infrared spectroscopy [1], separation techniques such as gas chromatography−mass spectrometry (GC−MS) [2,3] high-performance liquid chromatography (HPLC) [4], and liquid chromatography−mass spectrometry (LC−MS) [2,5–7]. Chromatographic techniques, while providing a wealth of information, often cannot be routinely applied to cultural heritage artifacts, e.g., pottery sherds, due to the relatively large sample-size and sample consumption required by most GC and LC techniques [7]. Typically, pieces of several cm^3 in size may be needed to yield 500 mg of material for extraction. Fourier transform-infrared (FT-IR) spectroscopy of pottery samples can provide functional group identification of organic, as well as some inorganic, compounds but can be challenging since the organic materials often are present as part of an extremely complex mixture [1]. While these techniques provide important information, they often lack the capability to identify unique compounds or require hundreds of milligrams of sample to do so. Therefore, there remains a need for techniques that require less sample, thus causing less physical damage to the object, while maintaining high molecular selectivity. Here we describe a technique for organic tracer molecule analysis for archaeometry, in a specialized form of laser mass spectrometry. A laser-desorption jet-cooling source is followed by resonance enhanced multiphoton ionization (REMPI) and time-of-flight (TOF) mass spectrometry. This approach combines the selectivity of resonant laser spectroscopy with the sensitivity of mass spectrometry and is therefore simultaneously highly specific and sensitive [8–16].

As a member of the theobroma genus, the cacao bean (Theobroma cacao) originates from a tree confined to within the tropical regions of South America and Mesoamerica [17]. The seeds, or pods, produced by the tree were ground up and mixed with other ingredients (water, maize, honey) to make a drink that had a mild stimulating effect [18]. It was a particularly important cultural icon in Mesoamerican society and has been consumed by the Maya as early as 600 BCE [18] in addition to being the precursor to modern day chocolate [19].

Figure A1.1 shows the three molecules associated with the cacao bean, caffeine (1,3,7trimethylxanthine), theobromine (3,7-dimethylxanthine), and theophylline (1,3-dimethylxanthine); these have been found in pottery sherds found in the Mesoamerican region [2,18,20–23]. These compounds are still very common today in stimulant drinks such as coffee, tea, and yerba mate. Serving as natural pest deterrents, these three methylxanthines are found in over 13 orders of plants, comprising well over 100 different plant species and are often used as molecular markers to identify geo-cultural origins of pottery sherds, particularly cacao [3,24].

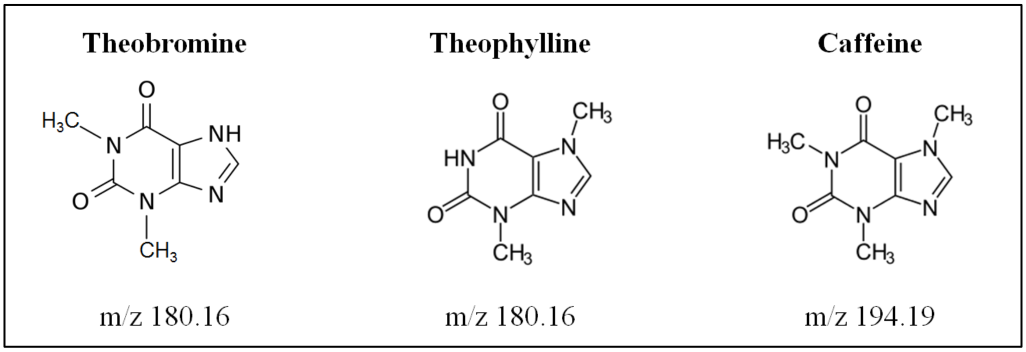

Figure A1.1: The three methylxanthine molecules associated with the cacao bean.

Similar to cacao in MesoAmerican culture, people from regions around the American gulf coast prepared a black tea made from the yaupon holly (I. vomitoria) as well as the dahoon holly (I. cassine). These species contain caffeine and theobromine but are not believed to contain theophylline [3,7,25]. Further, yerba mate (I. paraguariensis), guarana fruit (P. cupana), and the yoco vine (P. yoco) is widespread in South America and contains caffeine, theobromine, and/or theophylline [24,26–28]. Figure A1.2 shows a map marking the geographical origin of these plants [29]. Because of the shared occurrence of caffeine, theobromine, and/or theophylline it is clear that analytical tools need to go beyond positive identification of these molecules within complex matrixes and need to consider the relative occurrence to identify the organic origin of the residue in question [19].

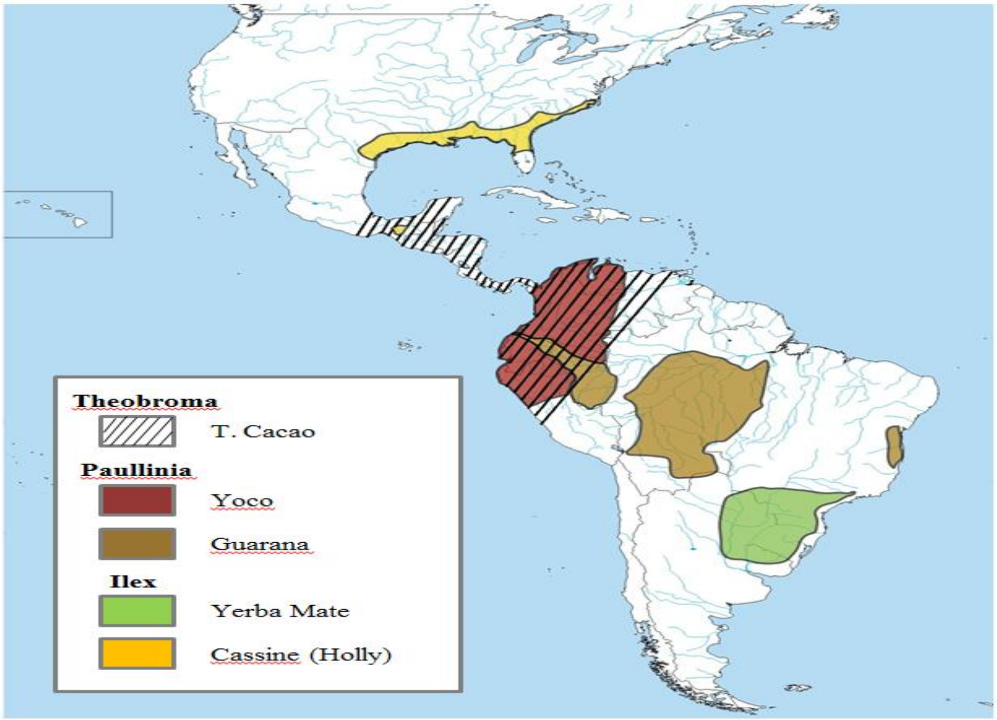

Figure A1.2: A map showing the origin of methylxanthine containing plants [29] .

Each plant species has a characteristic concentration of each methylxanthine (Table A1.1) [29], which is commonly used to narrow down the species of plant serving as the source of the organic residues in question. The method presented here can positively confirm the presence of methylxanthines with a reasonably high analytical detection limit and may pragmatically identify cacoa residue from pottery samples excavated where cacao and holly species are geolocated. The complete attribution of concentration ratios of the different marker molecules to specific plants is complicated because the distribution and concentration of these molecules in different plants is somewhat contentious given all the variable conditions. Moreover, the extraction dynamics can affect the ratios observed [26]. Previous analysis of pottery from Central America has identified theobromine in residue from the inside of ceramic vessels from Honduras, Guatemala, and Belize dating from 1500 BCE to

480 CE [2,18,22]. The identifications were made by GC−MS and HPLC−MS. Recent research has also suggested the presence of all three molecular markers in sherds found in Northwestern New Mexico and the Central Illinois River Valley, with the authors suggesting a previously unknown trade network with MesoAmerican cultures [7,30,31].

Genus	Species	Theobromine	Theophylline	Caffeine
		(mass % of dry weight)		
Theobroma	*T. cacao*	1.4% - 2%	0.3% - 0.4%	0.2% - 0.9%
Ilex	*I. paraguariensis* (yerba mate)	0.3% - 0.9%	trace	1% - 2%
	I. cassine (holly)	0.22%	ND	0.12%
	I. vomitoria (holly)	0.11%	ND	0.56%
Paullinia	*P. yoco*	0.05%	ND	0.3% - 0.4%
	P. cupana (guarana fruit)	0.015%	0.01%	4.28%

Table A1.1: Concentration of methyxanthine in each relevant plant species [29].

In the following sections we will detail the technique by which we identify these molecular markers in pottery sherds, followed by a first example of the identification of methylxanthine markers in organic residues in Maya and Mississippian pottery sherds [19].

A1.2 Experimental Section

A1.2.1 Two-step laser mass spectrometry

The instrument and experimental setup have been previously described in detail in chapter two. The sample obtained from the pottery sherd can be either an extract deposited onto a sample bar or sherd scrapings placed on a sample bar from which we laser desorb directly. The desorption laser is focused using either a cylindrical lens or a spherical lens, generating desorption spot sizes of 0.50 mm × 3.0 mm or 0.75 mm diameter, respectively.

A1.2.2 REMPI

Resonance-enhanced multiphoton ionization has been previously described in detail in chapter two; however, a brief description follows. REMPI combines optical spectroscopy with mass spectrometry. This dramatically enhances the specificity for selected compounds and allows for distinction of structural isomers, tautomers, and enantiomers [32]. One-color REMPI is performed on the methylxanthine molecules presented in this study with both photons originating from the doubled output of a Lumonics HD-300 tunable dye laser (spectral line width ≈ 0.04 cm^{-1}, pulse energy ≈ 0.3−0.7 mJ in 8 ns pulses). We have demonstrated that with REMPI technique we can detect compounds at the femtomole level and in favorable cases down to the 100 attomole level [9]. We can further improve REMPI sensitivity by two color ionization in which the excitation and ionization steps are performed at different wavelengths. We can further improve overall detection limits without sacrificing selectivity if we employ a different wavelength for the second step at higher laser fluence. We have demonstrated this principle for perylene, obtaining an overall 0.25 photoionization efficiency resulting in a 30 femtogram detection limit [9].

The combination of laser spectroscopy and mass spectrometry provides analytical information in two dimensions: wavelength and mass. Generally spectroscopic resolution, which is typically fractions of wavenumbers is several orders of magnitude higher than the mass resolution that can be obtained in conventional mass spectrometry [32]. To fully capitalize on these advantages it is necessary that the spectroscopy of the analyte molecule is known in a predetermined spectral library. We can find a needle in a haystack, provided we know what the needle looks like [19].

A1.2.3 Detection limit

We previously reported data for a series of test samples with different concentrations of vanillic acid, a marker for peonidin in grape wine [33]. There the ion signal was linear with concentration (r = 0.9994), allowing (a) quantitative measurements when using internal standards and (b) establishment of a lower limit of detection. The latter will differ from compound to compound because it depends on the ionization efficiency. In the case of vanillic acid with one color ionization at 289.192 nm, we obtained a detection limit at S/N = 3 of 60 picograms per laser shot. To put this limit in perspective, 250 pg of vanillic acid corresponds to a few microliters of modern wine and indeed we have detected vanillic acid in a 5 μL droplet of wine. Even if only 0.1% of the original peonidin content of the wine can be recovered and converted to vanillic acid, we would still only need a milliliter of residue, from for example an amphora, to be able to detect it. For the current study of methylated xanthines, a detection limit of 4 picograms per 10 laser shots average was determined. Theophylline ion signal desorbed from graphite substrate at quantities of 0.05, 0.5, 5, and 50 ng detected by 1C REMPI at 280.71 nm fit a linear regression of the form log y = m log x + b, where m is slope, x is concentration, b a fitting constant, and y is signal. Extrapolating this fit down to the signal limit, corresponding to the background signal of desorbed blank graphite sample, provided the limit of detection with a S/N of 3. This fit is shown in Figure A1.3 [19].

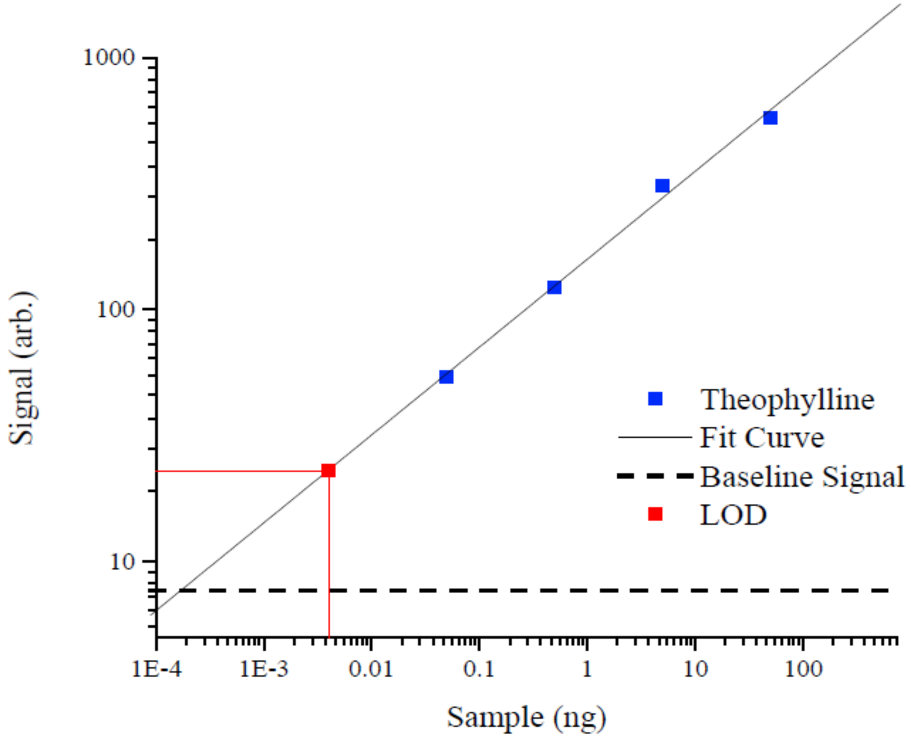

Figure A1.3: Theophylline ion signal at quantities of 0.05, 0.5, 5.0, and 50.0 ng detected by 1C REMPI @ 280.71 nm and desorbed from graphite substrate. The dashed line represents baseline background signal. A detection sensitivity of 4.0 picograms per 10 laser shot average was determined by extrapolation of theophylline ion signal by linear fit m*log(x)+b=log(y) with S/N=3. m=0.348 b=2.20 and log[S/N]=1.36. The log-log plot corresponds to signal being a function of concentration to a power m, where m is the slope in the plot. For a linear dependence we would expect m to equal 1 and we do not know why apparently the details of the desorption process cause the power (and thus the slope) to be less than 1. At this point we merely use the empiric dependence to establish the LOD [19].

If additional detection sensitivity is required, 2C REMPI is used. The ionization wavelength of 308 nm was found to maximize ionization efficiency and minimize fragmentation of the analytes, increasing signal by at least a factor of 2 (shown in Figure A1.4). Substrate does have an effect on detection efficiency, and we have tested graphite bars, gold plated bars, stainless steel pegs, and double-sided tape. Of these, graphite bars provide the greatest detection sensitivity but they suffer from sample carryover due to graphite's ability to readily absorb either organic sample or organic solvated sample. We used new graphite bars to negate the possibility of sample contamination between runs, which we also controlled for by analysis of blanks [19].

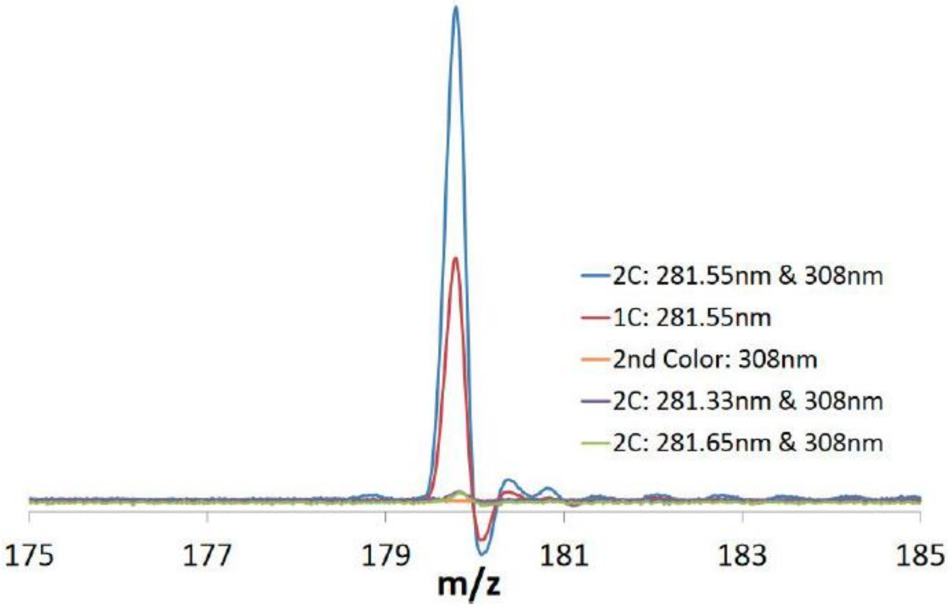

Figure A1.4: Example of ionization efficiency at different wavelength combinations for theobromine. The amount of signal observed in the resonant wavelength 2C-R2PI is double that in the 1C-R2PI (blue and red traces), while off-resonant wavelengths do not ionize theobromine (orange, purple, and green traces) [19].

A1.2.4 Sample preparation

We purchased standards of theobromine, theophylline, and caffeine from Sigma-Aldrich and used them without further purification. Standards are directly applied to graphite sample bars as a thin solid layer. The spectra for standards were collected using separate graphite bars to ensure each spectrum is free of any other standards. We analyzed pottery samples directly from the pottery material and from extracts when concentration was necessary. The extracts are made by using a 3:1 mixture of acetone and water. Approximately 400 mg of ground pottery is added to 5 mL of solution and allowed to sit at room temperature for 72 h. The supernatant liquid is then filtered by a Whatman 13 mm GD/X disposable filter, polypropylene filter media with polypropylene housing, 0.45 mm pore size. The extract is then concentrated by gentle heating (25−35 °C) under dry nitrogen flow. The extracts are concentrated approximately 5-fold then deposited dropwise on the ends of 0.75 mm diameter disposable stainless steel pegs mounted to the sample bar. Gentle heating (35−45 °C) is used to speed up evaporation of solvent. The dried, concentrated extracts are then immediately inserted into the instrument for analysis. Direct desorption analysis of the samples is done by applying small amounts (0.5−1.0 mg) of either ground or surface pieces of pottery material to double-sided tape mounted on gold sample bars. A new, clean disposable razor blade was used to scrape sherd fragments directly onto the tape for each sherd tested. Direct desorption does not lend itself to samples in need of concentration; however, it does allow for the most immediate and unaltered analysis of a sample's composition, avoiding possible unintended chemical rearrangements that can occur in an extraction, condensation, or solvated separation step. Direct analysis also makes it possible to separately sample different parts, for example, to compare surface versus inside areas [19].

A1.3 Results

We previously reported the detailed REMPI spectra of all three molecular markers [34], identifying unique resonances for the selective ionization of each of the markers. The left-hand side of Figure A1.5 shows the REMPI spectra obtained from each standard. The wavelength range marked by a black box indicates the part of the spectra used for subsequent sample analysis. In order to optimize conditions for each target methylxanthine, we chose a wavelength correlating to a strong REMPI transition and unique to each to perform optically selected mass spectrometry. Figure A1.5 shows mass spectra obtained at the resonant ionization wavelengths indicated in the figure with asterisks, clearly determining the parent mass with virtually no fragmentation. The peak at mass 40 is from the argon carrier gas of the molecular beam. When comparing theobromine and theophylline signal directly from the same sample, we scanned the wavelength range indicated by the black box. This small part of the spectrum contains distinct and spectrally well separated peaks of each of these compounds. We examined samples from three different archeological sites: (1) A Puerto Escondido vessel extract which has previously tested positive for theobromine by HPLC−MS (Provided by Dr. Patrick McGovern from the Molecular Archaeology lab at the University of Pennsylvania Museum.). (2) Thirteen base sherds of unique Late Classic period (~600− 900 CE) Maya vessels from the El Pilar area, located on the border of Guatemala and Belize. (3) Seven sherds from the early Mississippian period (~1100−1200 CE) vessels, located from the Central Illinois River Valley in Fulton County, Illinois [19].

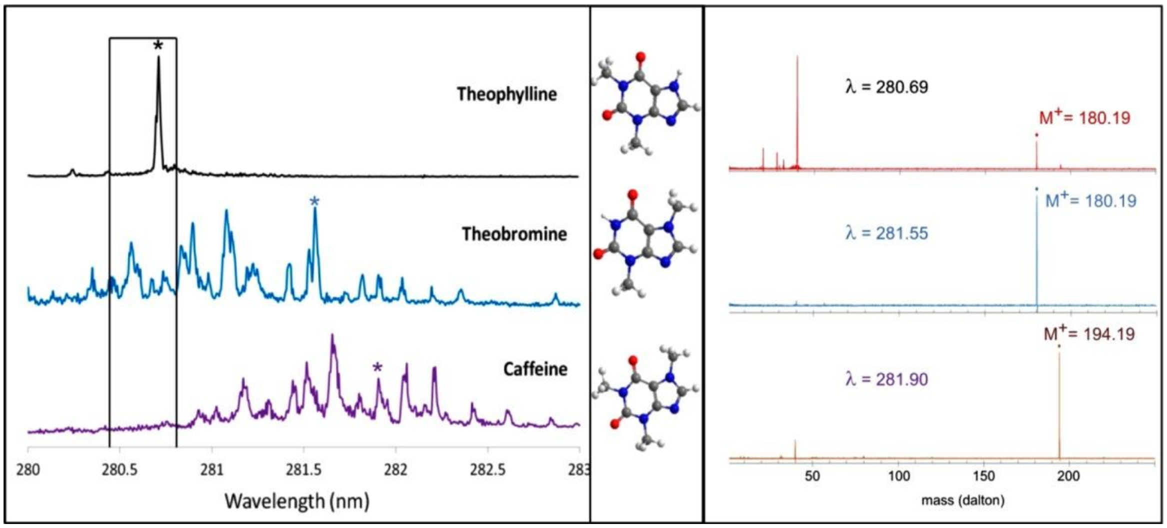

Figure A1.5: Spectra of methylxanthine standards. Left panel: REMPI spectra recorded on the parent mass, indicated in the right panel. Black box marks the region scanned for the pottery sherds. Right panel: mass spectra recorded at the indicated resonant wavelength, marked for each compound with an asterisk in the left panel. Y-axis for both panels in arbitrary units of ion intensity [19].

Puerto Escondido Extract. We analyzed extracts provided by Dr. McGovern for theobromine using 2C-REMPI (resonant excitation at 281.55 nm, ionization at 308.00 nm). We detected theobromine in each of these extracts confirming previously published findings [2].

Maya Sherds. Thirteen samples from different ranked Maya archeological dig sites were analyzed. Rank houses may be associated with different social strata in different areas of the Maya settlement [35]. The data from the analysis of extract revealed some levels of all three methylxanthines in each sherd, excluding sherd one from a small rank house, which tested negative for all three markers. The sherds from the Small Rank and High Rank House show much lower levels of theobromine than theophylline, with caffeine being the most abundant of the three markers. Samples from a median rank house and from a small center exhibit more theobromine relative to the other samples [19].

In order to investigate the potential of directly desorbing from sherd material, we examined scrapings of the sherds for methylxanthines. The large amount of material required for extraction (≈400 mg) often prevents any analysis of pottery sherds, as many of these items are essentially priceless. In addition, solubility differences can impact the rate at which each respective molecule is extracted from the sherd matrix. Figure A1.6 shows REMPI spectra, collected at m/z 180, obtained directly off scrapings from two different sherds, a cylindrical vessel from a minor center and a pedestal base vessel from a median rank house. For comparison, Figure A1.6 shows pure control samples of theobromine and theophylline which have been scaled in relative intensity to represent equimolar quantities. It is clear that the sherd samples exhibit different theobromine to theophylline residue ratios. This observation suggests a different history for these vessels. The presence of both dimethylxanthine isomers with relatively high theobromine abundance is a positive indication of cacao present in the cylindrical but not the pedestal base vessel [19].

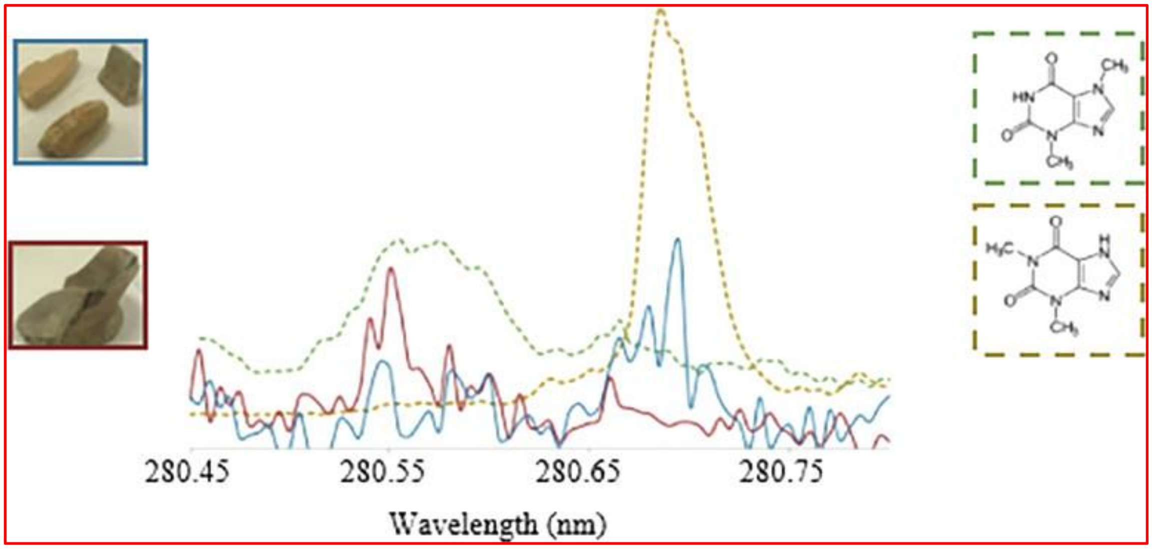

Figure A1.6: REMPI spectra of two different vessels (cylindrical vessel, blue trace, and pedestal vessel, red trace) performed directly on sherd material. Dotted lines are REMPI spectra of pure standards of theobromine (green trace) and theophylline (yellow trace). Standard spectra have been scaled to represent equimolar intensities (y-axis is ion signal in arbitrary units)[19].

Mississippi Sherds. We analyzed seven sherds from what is present day Fulton County, Illinois, collected from bluff tops on the western side of the Central Illinois River Valley flood plain. The sherds originated from a Mississippian culture and date back to between 1100 and 1200 CE. We analyzed these samples using the same procedures established with the Maya sherds but only using direct desorption from sherd material. All seven of these samples showed a strong presence of caffeine and theophylline, while six displayed the presence of some theobromine [19]. The presence of all three methylxanthenes from these Northern American findings suggests the presence of various plant residues. The presence of theophylline could argue against “black” beverage, which would be based on holly native to the area. This conclusion would not be in agreement with past studies except two recent research studies suggesting the presence of cacao residue in vessels obtained north of Mesoamerica and possibly indicating a previously unknown trade network [7,31].

A1.4 Summary

The attribution of the geo-cultural origins of pottery sherds is a very complex task, requiring a deep understanding of numerous factors that can affect the presence of certain organic residues. Some of these factors are unavoidable, e.g., physical and biological environmental impacts, solubility differences leading to different leaching rates over time, various clays impacting the affinity for long-term storage of organic molecules, but others are manageable. For example, the initial washing and storage process can be controlled. To preserve water-soluble markers, it can be helpful to avoid the use of water. To minimize the risk of cross contamination sherds can be collected in individual containers. The metabolic n-demethylation of these methylxanthines by soil bacteria can be identified by the products paraxanthine and 7-methylxanthine [30,36], molecules well suited to REMPI analysis, which we have shown previously in publishing the REMPI spectrum of 7-methylxanthine [34]. The ubiquity of the compounds used as biomarkers in museum, laboratory, and storage spaces can be controlled for by the use of blanks both during analysis and in predictive in situ monitoring of an object’s journey from excavation to storage [30].

We present a new method for analysis of molecular markers of stimulant containing beverages. Pottery sherds from both Central and North America tested positive for all three xanthine alkaloids: caffeine, theobromine, and theophylline. Although the method is not yet quantitative, relative amounts of caffeine to theobromine or caffeine to theophylline are consistent throughout the data set at their respective resonant wavelengths for the direct desorption method. This method is more sensitive than previous methods by identifying all three xanthine stimulants in multiple samples, requiring much smaller sample sizes. The three major advantages of this technique are reduced sample sizes needed for positive identification, the ability to directly analyze samples in complex matrixes such as clay from pottery without extraction, and simultaneous positive identification both my mass and spectral signature. We are undertaking a systematic study of a larger set of pottery samples to evaluate if it will be possible to derive conclusions about their use from this type of measurement [19].

References

1. Shillito, L. M., Almond, M. J., Wicks, K., Marshall, L.-J. R. & Matthews, W. The use of FT-IR as a screening technique for organic residue analysis of archaeological samples. *Spectrochim. Acta. A. Mol. Biomol. Spectrosc.* **72,** 120–125 (2009).

2. Henderson, J. S., Joyce, R. A., Hall, G. R., Hurst, W. J. & McGovern, P. E. Chemical and archaeological evidence for the earliest cacao beverages. *Proc. Natl. Acad. Sci.* **104,** 18937–18940 (2007).

3. Reber, E. A. & Kerr, M. T. The persistence of caffeine in experimentally produced black drink residues. *J. Archaeol. Sci.* **39,** 2312–2319 (2012).

4. Pura Naik, J. Improved High-Performance Liquid Chromatography Method to Determine Theobromine and Caffeine in Cocoa and Cocoa Products. *J. Agric. Food Chem.* **49,** 3579–3583 (2001).

5. Guasch-Jané, M. R., Ibern-Gómez, M., Andrés-Lacueva, C., Jáuregui, O. & Lamuela-Raventós, R. M. Liquid Chromatography with Mass Spectrometry in Tandem Mode Applied for the Identification of Wine Markers in Residues from Ancient Egyptian Vessels. *Anal. Chem.* **76,** 1672–1677 (2004).

6. Mottram, H. R., Dudd, S. N., Lawrence, G. J., Stott, A. W. & Evershed, R. P. New chromatographic, mass spectrometric and stable isotope approaches to the classification of degraded animal fats preserved in archaeological pottery. *J. Chromatogr. A* **833,** 209–221 (1999).

7. Crown, P. L. *et al.* Ritual drinks in the pre-Hispanic US Southwest and Mexican Northwest. *Proc. Natl. Acad. Sci.* **112,** 11436–11442 (2015).

8. Arrowsmith, P., Vries, M. S., Hunziker, H. E. & Wendt, H. R. Pulsed laser desorption near a jet orifice: concentration profiles of entrained perylene vapor. *Appl. Phys. B Lasers Opt.* **46,** 165–173 (1988).

9. Meijer, G., Vries, M. S. de, Hunziker, H. E. & Wendt, H. R. Laser desorption jet-cooling of organic molecules. *Appl. Phys. B Lasers Opt.* **51,** 395–403 (1990).

10. Nir, E., Hunziker, H. E. & de Vries, M. S. Fragment-Free Mass Spectrometric Analysis with Jet Cooling/VUV Photoionization. *Anal. Chem.* **71,** 1674–1678 (1999).

11. de Vries, M. S., Elloway, D. J., Wendt, H. R. & Hunziker, H. E. Photoionization mass spectrometer with a microscope laser desorption source. *Rev. Sci. Instrum.* **63,** 3321–3325 (1992).

12. Mahajan, T. B., Plows, F. L., Gillette, J. S., Zare, R. N. & Logan, G. A. Comparison of microprobe two-step laser desorption/laser ionization mass spectrometry and gas chromatography/mass spectrometry studies of polycyclic aromatic hydrocarbons in ancient terrestrial rocks. *J. Am. Soc. Mass Spectrom.* **12,** 989–1001 (2001).

13. Seb Gillette, J., Ghosh, U., Mahajan, T. B., Zare, R. N. & Luthy, R. G. Microprobe laser mass spectrometry studies of polycyclic aromatic hydrocarbon distributions on harbor sediments and coals. *Isr. J. Chem.* **41,** 105–110 (2001).

14. Mahajan, T. B., Ghosh, U., Zare, R. N. & Luthy, R. G. Microscale detection of polychlorinated biphenyls using two-step laser mass spectrometry. *Int. J. Mass Spectrom.* **212,** 41–48 (2001).

15. Boesl, U. *et al.* Resonance-enhanced multi-photon ionization: a species-selective ion source for analytical time-of-flight mass spectroscopy. *Chemosphere* **29,** 1429–1440 (1994).

16. Hafner, K., Zimmermann, R., Rohwer, E. R., Dorfner, R. & Kettrup, A. A Capillary-Based Supersonic Jet Inlet System for Resonance-Enhanced Laser Ionization Mass Spectrometry: Principle and First On-line Process Analytical Applications. *Anal. Chem.* **73,** 4171–4180 (2001).

17. Ogata, N. in *The Lowland Maya Area: Three Millennia at the Human-Wildland Interface* 415–438 (The Haworth Press Inc, 2003).

18. Hurst, W. J., Tarka, S. M., Powis, T. G., Valdez, F. & Hester, T. R. Archaeology: cacao usage by the earliest Maya civilization. *Nature* **418,** 289–290 (2002).

19. Owens, S. C. *et al.* Direct Analysis of Xanthine Stimulants in Archaeological Vessels by Laser Desorption Resonance Enhanced Multiphoton Ionization. *Anal. Chem.* **89,** 2838–2843 (2017).

20. Brunetto, M. del R. *et al.* Determination of theobromine, theophylline and caffeine in cocoa samples by a high-performance liquid chromatographic method with on-line sample cleanup in a switching-column system. *Food Chem.* **100,** 459–467 (2007).

21. Hall, G. D., Tarka, S. M., Hurst, W. J., Stuart, D. & Adams, R. E. W. Cacao Residues in Ancient Maya Vessels from Rio Azul, Guatemala. *Am. Antiq.* **55,** 138–143 (1990).

22. Hurst, W. J., Martin, R. A., Tarka, S. M. & Hall, G. D. Authentication of cocoa in Maya vessels using high-performance liquid chromatographic techniques. *J. Chromatogr. A* **466,** 279–289 (1989).

23. Coco, F. L., Lanuzza, F., Micali, G. & Cappellano, G. Determination of theobromine, theophylline, and caffeine in by-products of cupuacu and cacao seeds by high-performance liquid chromatography. *J. Chromatogr. Sci.* **45,** 273–275 (2007).

24. Ashihara, H., Kato, M. & Crozier, A. in *Methylxanthines* **200,** 11–31 (Springer Berlin Heidelberg, 2011).

25. Edwards, A. L. & Bennett, B. C. Diversity of Methylxanthine Content inIlex cassine L. andIlex vomitoria Ait.: Assessing Sources of the North American Stimulant Cassina. *Econ. Bot.* **59,** 275–285 (2005).

26. Saldaña, M. D. A., Mohamed, R. S., Baer, M. G. & Mazzafera, P. Extraction of Purine Alkaloids from Maté (Ilex paraguariensis) Using Supercritical CO2. *J. Agric. Food Chem.* **47,** 3804–3808 (1999).

27. Meinhart, A. D. *et al.* Methylxanthines and Phenolics Content Extracted during the Consumption of Mate (*Ilex paraguariensis* St. Hil) Beverages. *J. Agric. Food Chem.* **58,** 2188–2193 (2010).

28. Schimpl, F. C., da Silva, J. F., Gonçalves, J. F. de C. & Mazzafera, P. Guarana: Revisiting a highly caffeinated plant from the Amazon. *J. Ethnopharmacol.* **150,** 14–31 (2013).

29. Owens, S. High Resolution Laser Spectroscopy and Nanoscale Proximal Probe Desorption of Historically Significant Molecules. (University of California Santa Barbara, 2015).

30. Washburn, D. K., Washburn, W. N., Shipkova, P. A. & Pelleymounter, M. A. Chemical analysis of cacao residues in archaeological ceramics from North America: considerations of contamination, sample size and systematic controls. *J. Archaeol. Sci.* **50,** 191–207 (2014).

31. Washburn, D. K., Washburn, W. N. & Shipkova, P. A. The prehistoric drug trade: widespread consumption of cacao in Ancestral Pueblo and Hohokam communities in the American Southwest. *J. Archaeol. Sci.* **38,** 1634–1640 (2011).

32. Imasaka, T., Moore, D. S. & Vo-Dinh, T. Critical assessment: Use of supersonic jet spectrometry for complex mixture analysis. *Pure Appl. Chem.* **75,** (2003).

33. Callahan, M. P., Gengeliczki, Z. & de Vries, M. S. Resonant Two-Photon Ionization Mass Spectrometry of Jet-Cooled Phenolic Acids and Polyphenols. *Anal. Chem.* **80,** 2199–2203 (2008).

34. Callahan, M. P. *et al.* Non-standard base pairing and stacked structures in methyl xanthine clusters. *Phys. Chem. Chem. Phys.* **10,** 2819–2826 (2008).

35. Ford, A. & Fedick, S. Prehistoric Maya Settlement Patterns in the Upper Belize River Area: Initial Results of the Belize River Archaeological Settlement Survey. *J. Field Archaeol.* **19,** 35 (1992).

36. Summers, R. M., Louie, T. M., Yu, C. L. & Subramanian, M. Characterization of a broad-specificity non-haem iron N-demethylase from Pseudomonas putida CBB5 capable of utilizing several purine alkaloids as sole carbon and nitrogen source. *Microbiology* **157,** 583–592 (2011).

Appendix 2

Supplementary Information for Resonance Enhanced Multiphoton Ionization and Quantum Computation to Study the Molecular Structure and Excited State Dynamics of Isolated Thymine and Uracil

A2.1 The Calculated NH Stretching Frequencies in the Ground State and Excited State of Thymine and Uracil.

A2.1.1 Thymine

State	Method		NH Stretching	
S_0	Experiment		**3505**	**3455**
	MP2	ω	3669	3616
	1D-Scan	Δν	-133	-132
	1D-PT2	Δν	-136	-136
	PT2[a]	Δν	-164	-163
		ν	**3505**	**3453**
S_1	CC2	ω	3652	3646
	1D-Scan	Δν	-134	-133
		ν[b]	**3487**	**3482**
T_1	CC2	ω	3627	3625
	1D-Scan	Δν	-135	-132
		ν[b]	**3461**	**3462**

Table A2.1: Vibrational frequencies (cm^{-1}) of the NH stretching modes of thymine. [a]full-dimensional anharmonic calculations, [b]1D-anharmonic model corrected for the anharmonic coupling from the PT2 calculations on the ground state [1].

A2.1.2 Uracil

State	Method		NH Stretching	
S_0	Experiment		**3503**	**3453**
	MP2	ω	3669	3616
	1D-Scan	$\Delta\nu$	-132	-132
	1D-PT2	$\Delta\nu$	-136	-135
	PT2[b]	$\Delta\nu$	-163	-165
		ν	**3506**	**3451**
S_1	CC2	ω	3657	3651
	1D-Scan	$\Delta\nu$	-133	-132
		ν[b]	**3493**	**3486**
T_1	CC2	ω	3622	3620
	1D-Scan	$\Delta\nu$	-136	-131
		ν[b]	**3455**	**3456**

Table A2.2: Vibrational frequencies (cm^{-1}) of the NH stretching modes of uracil. [a]full-dimensional anharmonic calculations, [b]1D-anharmonic model corrected for the anharmonic coupling from the PT2 calculations on the ground state [1].

These calculations were done using Gaussian 09 Program [2].

A2.2 Pump-Probe Spectra

A2.2.1 Thymine

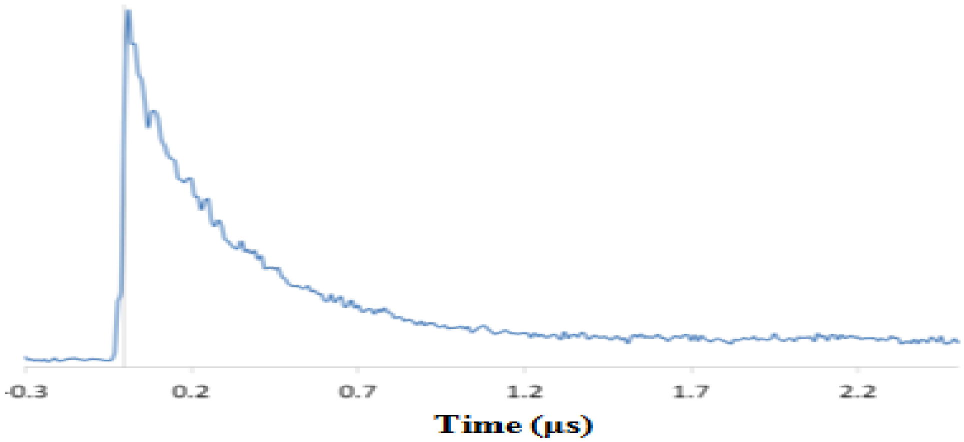

Figure A2.1: Pump-probe spectrum of thymine at 37 012 cm^{-1} UV excitation energy.

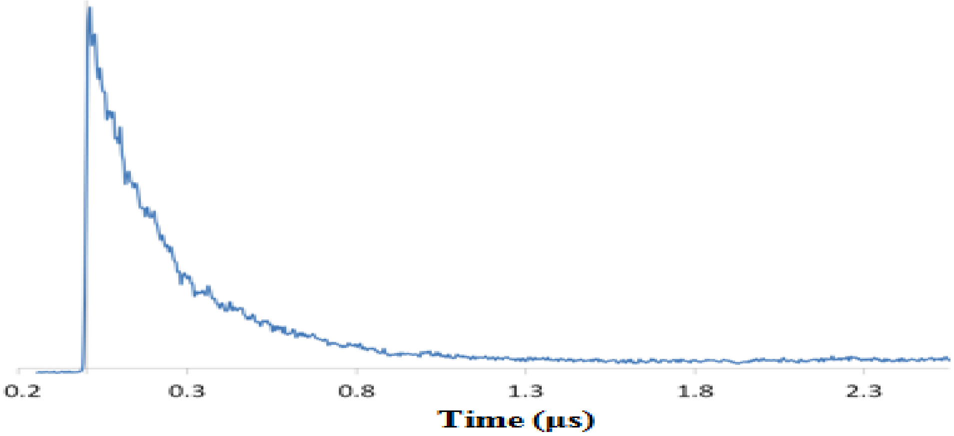

Figure A2.2: Pump-probe spectrum of thymine at 36 917 cm^{-1} UV excitation energy.

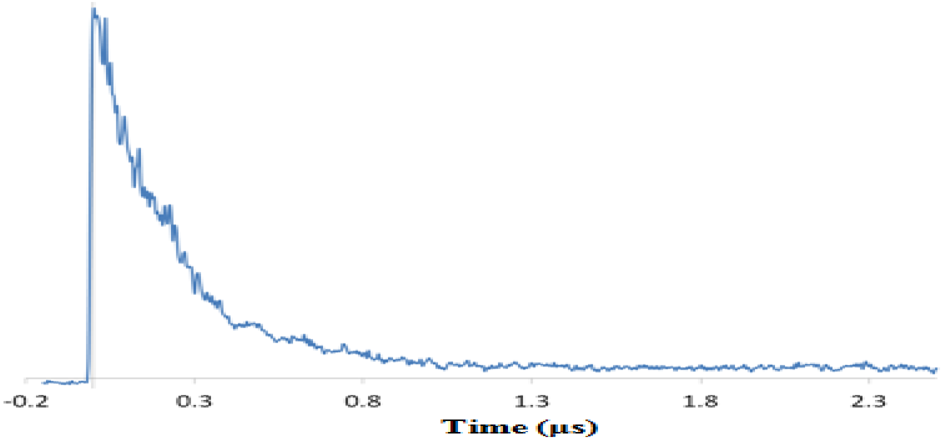

Figure A2.3: Pump-probe spectrum of thymine at 36 748 cm^{-1} UV excitation energy.

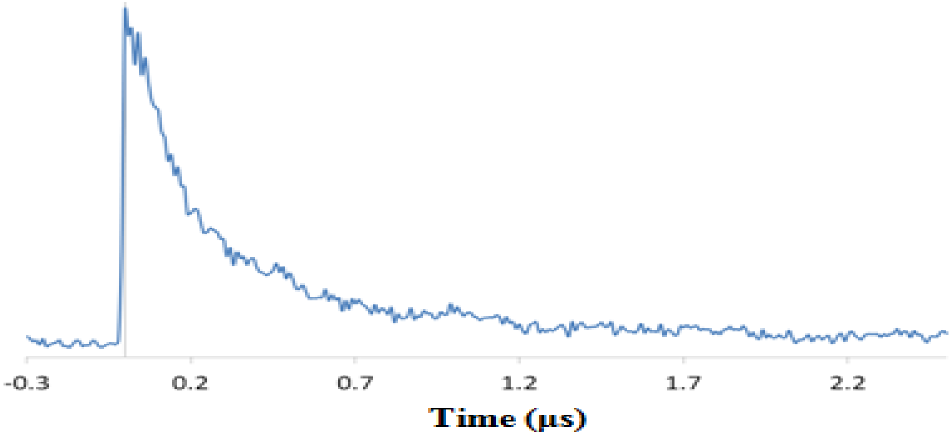

Figure A2.4: Pump-probe spectrum of thymine at 36 364 cm^{-1} UV excitation energy.

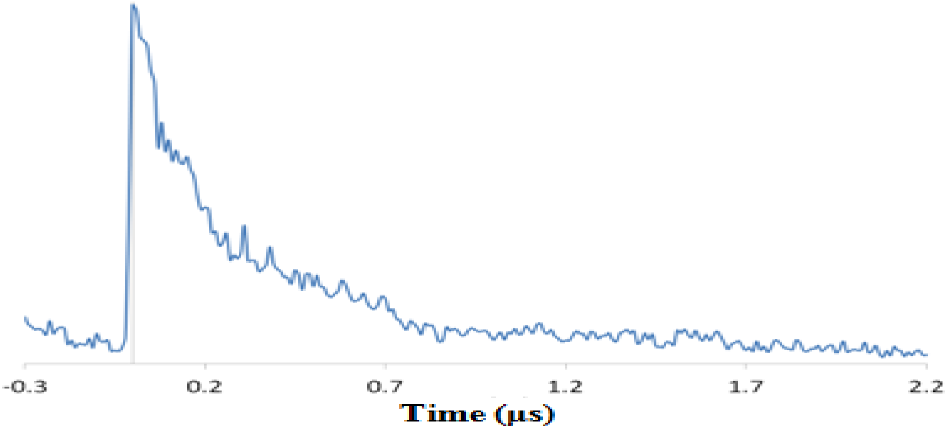

Figure A2.5: Pump-probe spectrum of thymine at 36 101 cm^{-1} UV excitation energy.

A2.2.2 Uracil

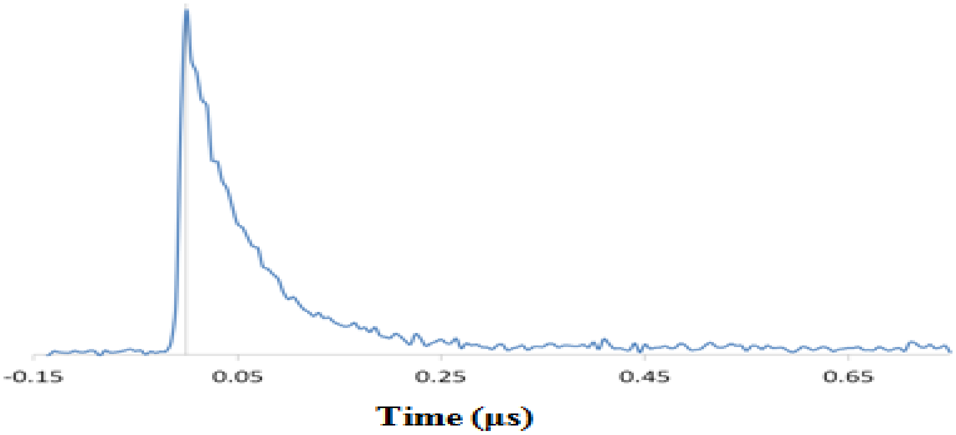

Figure A2.6: Pump-probe spectrum of uracil at 37 392 cm^{-1} UV excitation energy.

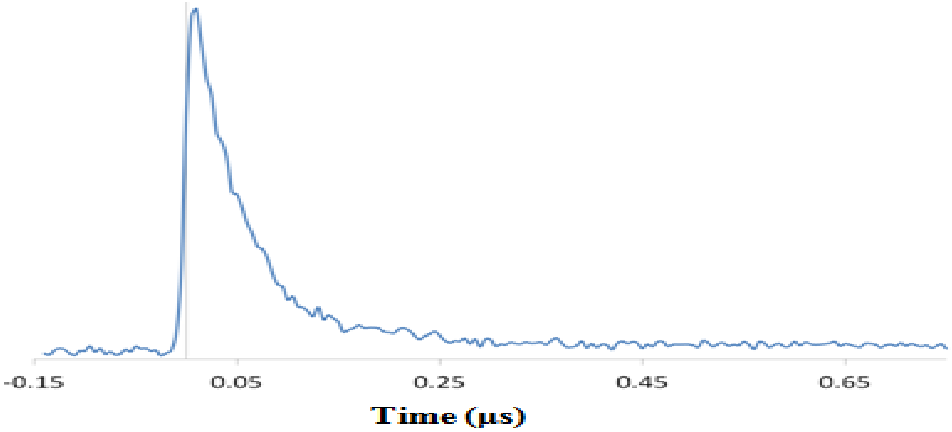

Figure A2.7: Pump-probe spectrum of uracil at 37 258 cm^{-1} UV excitation energy.

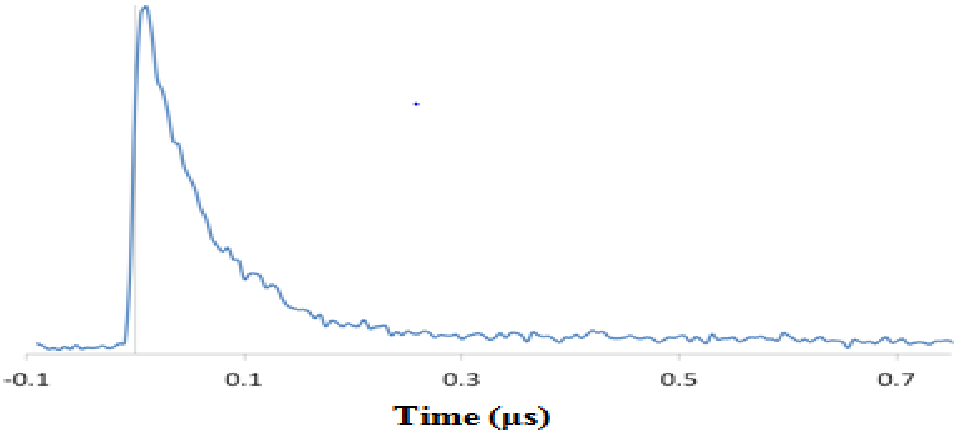

Figure A2.8: Pump-probe spectrum of uracil at 37 021 cm^{-1} UV excitation energy.

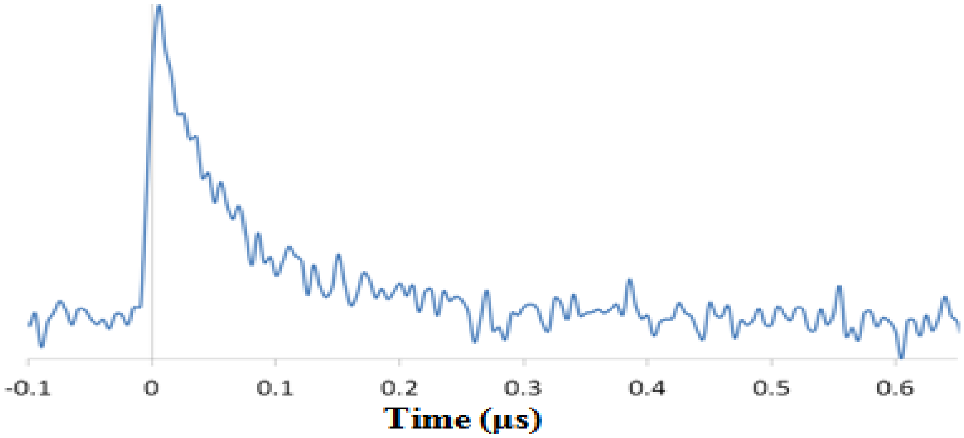

Figure A2.9: Pump-probe spectrum of uracil at 36 510 cm^{-1} UV excitation energy.

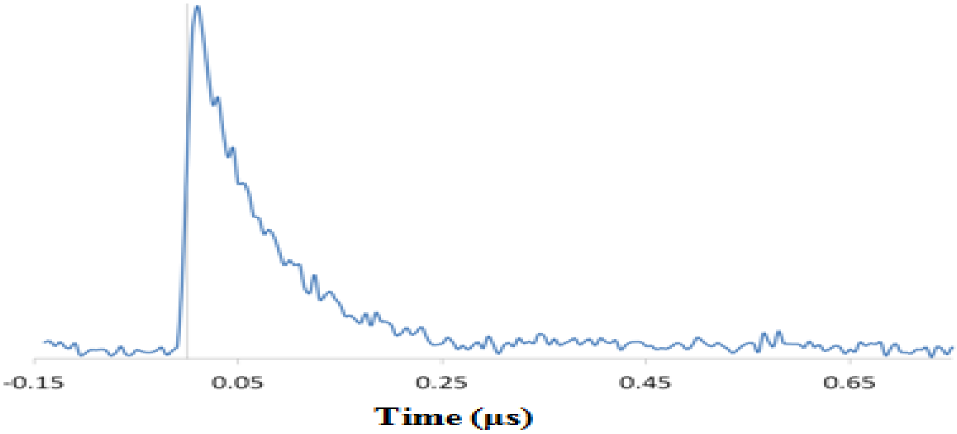

Figure A2.10: Pump-probe spectrum of uracil at 36 430 cm^{-1} UV excitation energy.

References

1. Ligare, M., Siouri, F., Bludsky, O., Nachtigallová, D. & de Vries, M. S. Characterizing the dark state in thymine and uracil by double resonant spectroscopy and quantum computation. *Phys Chem Chem Phys* **17,** 24336–24341 (2015).

2. Frisch, M. J. *et al. Gaussian 09*. (Gaussian, Inc., Wallingford CT, 2009).